GALILEO GALILEI (GG)
FINAL REPORT
DRL/DRD: DEL-13

and

SATELLITE DETAILED ARCHITECTURE REPORT
DRL/DRD: DEL-34/41

Written by	***Responsibility***
A. ANSELMI	Author (for the GG study team)
Verified by	
n.a.	Checker
Approved by	
	Product Assurance
	Configuration Control
	Design Engineer
	System Engineering Manager
A. ANSELMI	Study Manager
Documentation Manager	
R. Cavaglià	

The validations evidence are kept through the documentation management system.

ISSUE	DATE	§ CHANGE RECORDS	AUTHOR
01	8-Jun-09	First issue submitted to PRR	

TABLE OF CONTENTS

LIST OF FIGURES

LIST OF TABLES

1. SCOPE AND PURPOSE

This document is submitted in partial fulfillment of Work Package 1A-AA of the GG Phase A2 Study. It comprises the Final Report (DRL item DEL-13) and the Satellite Detailed Architecture report (DEL-34).

The purpose of the document is to provide a comprehensive description of the design adopted for the GG satellite at the end of the Phase A2 Study. The trade-offs leading to the design described in this document are summarized in a companion report [RD 9].

2. REFERENCES

2.1 Applicable Documents

[AD 1] ASI, “Progetto Galileo Galilei-GG Fase A-2, Capitolato Tecnico”, DC-IPC-2007-082, Rev. B, 10-10-2007 and applicable documents defined therein

2.2 Standards

[SD 1] ECSS-M-00-02A, Space Project Management – Tailoring of Space Standards, 25 April 2000

[SD 2] ECSS-E-ST-10C, Space Engineering - System Engineering General Requirements, 6 March 2009

[SD 3] ECSS-E-10-02A, Space Engineering – Verification

[SD 4] ECSS-Q-00A, Space Product Assurance - Policy and Principles, and related Level 2 standards.

2.3 ASI Reference Documents

[RD 1] GG Phase A Study Report, Nov. 1998, revised Jan. 2000, available at: http://eotvos.dm.unipi.it/nobili/ggweb/phaseA/index.html

[RD 2] Supplement to GG Phase A Study (GG in sun-synchronous Orbit) “Galileo Galilei-GG”: design, requirements, error budget and significance of the ground prototype”, A.M. Nobili et al., Physics Letters A 318 (2003) 172–183, available at: http://eotvos.dm.unipi.it/nobili/documents/generalpapers/GG_PLA2003.pdf

[RD 3] A. Nobili, DEL001: GG Science Requirements, Pisa, September 2008

2.4 GG Phase A2 Study Notes

[RD 4] SD-RP-AI-0625, GG Final Report / Satellite Detailed Architecture Report, Issue 1

[RD 5] SD-RP-AI-0626, GG Phase A2 Study Executive Summary, Issue 1

[RD 6] SD-TN-AI-1163, GG Experiment Concept and Requirements Document, Issue 3

[RD 7] SD-RP-AI-0620, GG System Performance Report, Issue 2

[RD 8] SD-TN-AI-1167, GG Mission Requirements Document, Issue 2

[RD 9] SD-RP-AI-0590, GG System Concept Report (Mission Description Document), Issue 3

[RD 10] SD-SY-AI-0014, GG System Functional Specification and Preliminary System Technical Specification, Issue 1

[RD 11] SD-RP-AI-0631, GG Consolidated Mission Description Document, Issue 1

[RD 12] SD-TN-AI-1168, GG Mission Analysis Report, Issue 2

[RD 13] GG-TN-DTM-002, Galileo Galilei Satellite - Design & Structural Analysis Report, Issue 1

[RD 14] SD-RP-AI-0627, GG Thermal Design and Analysis Report, Issue 1

[RD 15] SD-RP-AI-0268, GG System Budgets Report, Issue 1

[RD 16] SD-RP-AI-0621, Technical Report on Drag and Attitude Control, Issue 2

[RD 17] TL25033, Payload Architectures and Trade-Off Report, Issue 3

[RD 18] SD-RP-AI-0629, Technical Report on Simulators, Issue 1

[RD 19] GG.ALT.TN.2003, FEEP Microthruster System Technical Report, Issue 1

[RD 20] TASI-FI-44/09, Cold Gas Micro Thruster System for Galileo Galilei (GG) Spacecraft - Technical Report, Issue 1, May 2009

[RD 21] SD-RP-AI-0630, Spin Sensor Design, Development and Test Report, Issue 1

[RD 22] SD-TN-AI-1169, GG Launcher Identification and Compatibility Analysis Report, Issue 1

[RD 23] ALTEC-AD-001, GG Ground Segment Architecture and Design Report, Issue 1

[RD 24] SD-TN-AI-1218, GG Preliminary Product Tree, Issue 1

[RD 25] SD-PL-AI-0227, GG System Engineering Plan (SEP), Issue 2

[RD 26] TAS-I, Payload Development and Verification Plan, Issue 1

[RD 27] SD-PL-AI-0228, GG System Verification and Validation Plan, Issue 1

[RD 28] SD-TN-AI-1219, Report on Frequency Management Issues, Issue 1

[RD 29] SD-RP-AI-0632, GG Mission Risk Assessment And Mitigation Strategies Report, Issue 1

[RD 30] SD-RP-AI-0633, Report on Mission Costs Estimates, Issue 1

2.5 External Reference Documents

[RD 31] VEGA User's Manual, Issue 3/ Revision 0, March 2006

[RD 32] E. Fischbach, C. L. Talmadge: The Search for Non-Newtonian Gravity; Springer- Verlag, New York, 1998

[RD 33] Plasma effects in GG, G. Vannaroni, 19 March 2009

3. MISSION AND EXPERIMENT SUMMARY

GG is a small scientific satellite mission with the objective of testing the equivalence principle (EP) to 1 part in 10^{17}, four orders of magnitude better than the best experiments to date. The experiment consists in testing the universality of free fall by means of two concentric hollow cylinders of different composition (the test masses) in orbit in the gravitational field of the Earth.

The cylinders spin around their common axis, perpendicular to the orbit plane, at a rate (1 Hz) much larger than the orbit rate. Weak suspensions constrain the motion to the plane perpendicular to the spin axis. Suitable sensors (capacitance plates) located between the test masses detect the relative displacements. A violation of EP would manifest itself as a displacement of the order of 1 pm, constant in the orbit frame and directed toward the centre of the Earth.

The test bodies, their mechanical coupling and the capacitance read-out are the core of the mission. Once the experimental design has been conceived, the required features of the spacecraft and its attitude and orbit follow. The spacecraft must provide a suitable accommodation to the experiment, provide specific and stable mass properties, shield it from thermal and dynamic perturbations within specified limits. The spin axis must be nearly perpendicular to the orbit plane, gyroscopic stiffness providing stability against external attitude disturbances. The orbit must be near circular, near-equatorial, the altitude and inclination being selected as the best compromise between experiment needs and technical and cost considerations.

The description of the orbital mission is provided in [RD 11]. A detailed analysis of the experiment requirements was carried out in Phase A2 and is documented in a preliminary experiment requirements specification [RD 6], published as an addendum to the mission requirements [RD 8].

4. PAYLOAD DESCRIPTION

4.1 Payload Main Elements

The GG payload is housed inside the “spinning top (see further on, Figure 5.2-4). It contains in a nested configuration −and always respecting the cylindrical symmetry, as well as “top/down” symmetry with respect to the center of mass of the whole system− the following main elements:

- the PGB laboratory, with its central shaft, connected to the “spinning top” by mechanical springs at its “top” and “bottom” (see details on the springs in Figure 4.1-1, Figure 4.1-2)
- the differential accelerometer for EP testing with U shaped laminar suspensions connecting its coupling arm (see below) to the PGB shaft/tube at its center
- a perfectly symmetric coupling arm made of two pieces, arranged inside each other in order to guarantee the required symmetry; each piece is connected at the center to the PGB shaft via U shaped laminar suspensions (see Figure 4.1-3 and Figure 4.1-4)
- two coaxial concentric test cylinders, each one connected to the coupling arm described above via U shaped laminar suspensions. Note that the test cylinders are not directly connected to the PGB, otherwise they could not form a balance and reject common mode effects. They are connected to the PGB only through the coupling arm, which is indeed the beam of the balance
- two opposite pairs of capacitance plates located halfway in between the test cylinders forming two capacitance bridges and rigidly connected to the PGB shaft
- small capacitance plates (arranged as capacitance bridges) to sense the relative motion (in all 3 directions) of the PGB wrt the spacecraft which provides the input signal to the drag free control loop. They also serve as actuators to damp the whirl motion of the PGB
- small capacitance plates (arranged as capacitance bridges) similar to those described above, between each test cylinder and the PGB shaft. They are used as sensors and actuators within the whirl control loop (to damp the whirl motion of the test cylinders relative to the PGB).

The PGB accommodates also the electronics of the capacitance read-out system, while data from the accelerometer will be transmitted by an optical link (the same in the lab prototype). The PGB springs will allow the required power to be provided from the spacecraft to the accelerometer (read out electronics and inchworms).

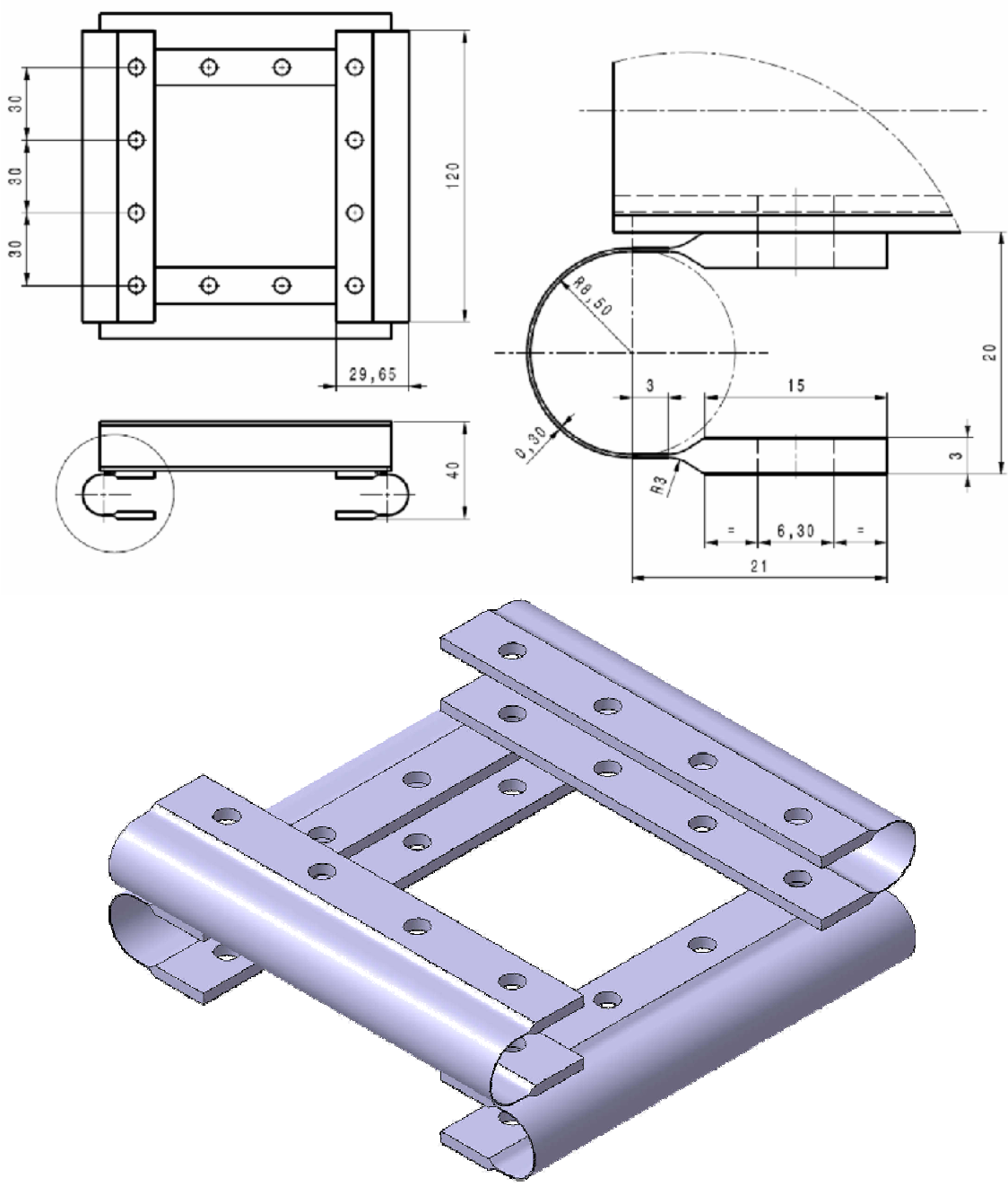

Figure 4.1-1: Construction details of the springs connecting the PGB to the spacecraft

Flessione di una sbarretta con un'estremita' fissa

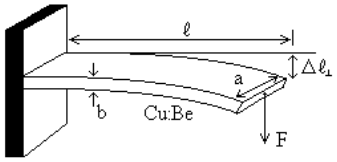

$$\Delta\ell_\perp = \frac{4}{Y}\cdot\frac{F\,\ell^3}{a\,b^3}$$

Energia elastica del sistema

$$E = \int_0^{\Delta\ell_\perp} F(x)dx$$

Y = Young's modulus

Y(Pure Cu) = $12\cdot10^{11}$ dyne/cm^2
Y(Cu:Be) ~ $19\cdot10^{11}$ dyne/cm^2
Y(Steel) = $21\cdot10^{11}$ dyne/cm^2

Def. $F \equiv k\cdot\Delta\ell$ $\qquad k_\perp = \frac{Y\,a\,b^3}{4\,\ell^3}$

Per una molla a forma di U e con un braccio rigido di lunghezza L si ha:

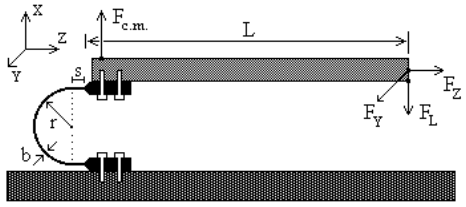

r = 0.25 cm
s = 0.1 cm
$\ell = \pi\cdot r + 2s \cong 1$ cm
$b = 5\cdot10^{-3}$ cm
L = 20 cm
a = 0.5 cm

$k_\ell = \frac{Y\,a\,b^3}{4\,\ell^3} \cong 3\cdot10^4$ dyne/cm $\qquad k_L = \frac{Y\,a\,b^3}{4\,\ell\,L^2} \cong 74$ dyne/cm

$k_Z \cong \frac{1}{2}\frac{Y\,a\,b^3}{4\,r_{+s}^3} \cong 9.5\cdot10^5$ dyne/cm $\qquad k_{c.m.} \cong k_Z$

$k_{c.m.}/k_\ell \cong 32$ $\qquad k_{c.m.}/k_L \cong 12800$ $\qquad k_Y \cong k_L$

Prove sperimentali effettuate con un pezzetto di lamella di Cu:Be di spessore $b = 50\,\mu$

Con: a = 1 cm r = 0.4 cm s = 0.1 cm L = 8 cm F_L = 50 mgr ≃ 50 dyne
si ha: $\Delta\ell \simeq 0.5$ cm $\Longrightarrow$ $k_L \simeq 100$ dyne/cm Y ~ $19\cdot10^{11}$ dyne/cm^2

Con $F_Y = 1$ gr	si ha:	$\Delta\ell_Y \simeq 1.54$ cm	$k_Y/k_L \simeq 6.5$
Con $F_{c.m.} = 8$ gr	si ha:	$\Delta\ell_{c.m.} = 0.05$ cm	$k_{c.m.}/k_L \cong 1600$
Con $F_Z = 10$ gr	si ha:	$\Delta\ell_Z = 0.1$ cm	$k_Z/k_L \cong 1000$
Con: a = 0.5 cm	$F_Y = 1$ gr	$\Delta\ell_Y \simeq 2.6$ cm	

Per una lamella fatta con un nastro di Rame-Berillio inizialmente piano, poi curvata a forma di U senza superare il suo limite di elasticita' e tenuta compressa fra due piani paralleli da una forza F_Z si ha:

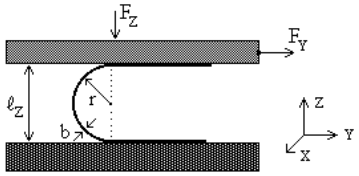

$\ell_Z = 2r$

$$\Delta\ell = \frac{4}{Y}\cdot\frac{F\,\ell^3}{a\,b^3}$$

Per far scorrere in direzione Y la superficie superiore rispetto all'altra, come se fosse su una ruota, non occorre nessuna forza F_Y. Infatti durante tale moto la molla mantiene inalterata la sua energia elastica (se r non varia) in quanto si flette ad una estremita' del diametro verticale aumentando l'energia elastica, e si rilascia (si srotola) dall'altra, diminuendo l'energia di una uguale quantita'.

Percio', in linea di principio, se le superfici sono piane, pulite, e se la molla e' omogenea, il k_Y di questa molla e' zero.

In pratica si potra' ottenere un k_Y positivo o negativo se le superfici sono rispettivamente un po' concave o un po' convesse.

Figure 4.1-2: Mechanical properties of the springs designed to connect the PGB to the spacecraft

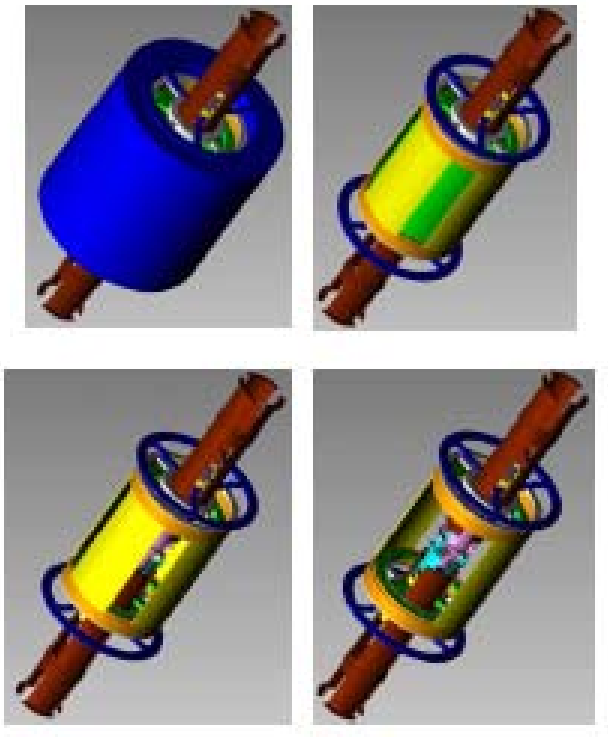

Figure 4.1-3: Details from the engineering drawings of the GG differential accelerometer

The figures proceed from "outside" to "inside". The brown central tube is the PGB shaft. The blue and green cylinders are the test masses, the yellow plates are the capacitance bridge plates to measure the relative displacements of the test cylinders. Note that the outer diameter of the blue test cylinders is about 23 cm.

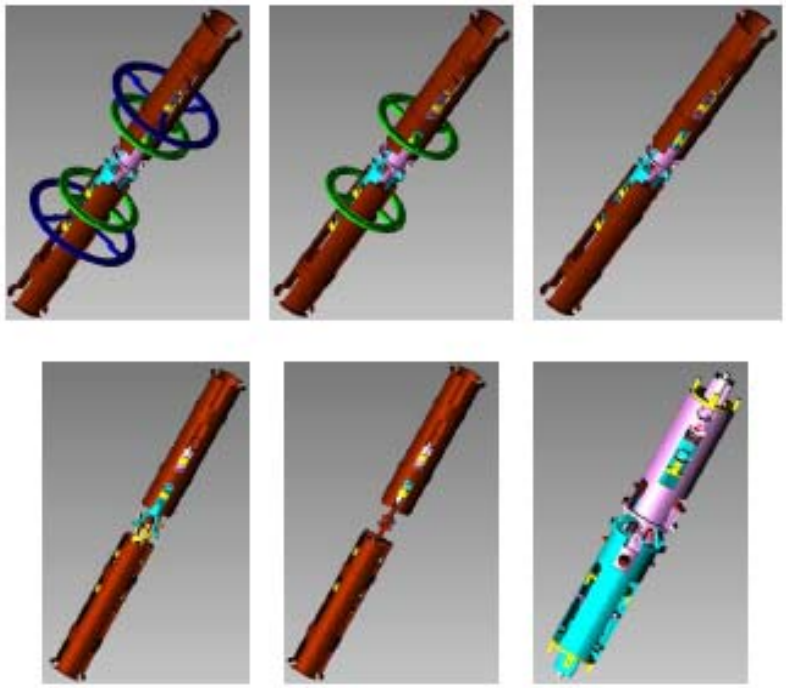

Figure 4.1-4: Further details from the engineering drawings of the GG differential accelerometer

Continuing from the previous figure, further details are revealed after removing components one by one. In the last picture only the coupling arm remains, and it is clear how it is made symmetric by putting together the two parts (pink and light blue). In the figure before the last, the PGB shaft is well visible, showing its centre where the two pieces of the coupling are connected, each one with 3 U shaped laminar suspensions at 120° from each other.

4.2 Lock/Unlock Mechanisms

The PGB, the test cylinders and the coupling arms −being weakly suspended− will have a static launch lock mechanism in order to withstand large accelerations at launch, to be unlocked once in orbit (1-shot). In addition, by design, each suspended mass is constrained by mechanical stops to only slight movements in all directions, as it is apparent from the 3D drawings shown in Figure 4.1-3 and Figure 4.1-4.

Finally a refined lock/unlock system, with inch-worms and pressure sensors, has been designed for the system in orbit (shown and described in Figure 4.2-1) in order to gently release the test masses and the PGB in absence of weight. Unlike the static lock, this system can be re-used during the whole mission to lock/unlock the bodies in orbit should the need occur.

The single shot static lock is a “brute force” lock to be used only once but obviously crucial to the experiment; special care is being devoted to it by DTM Technologies, a company with considerable expertise and a long successful record of collaboration with Thales Alenia Space for issues related space mechanics and Ferrari for ground mechanics.

The finer mechanism is no matter of concern because of the very small forces involved at zero-g and the high reliability of inch-worms (based on PZTs).

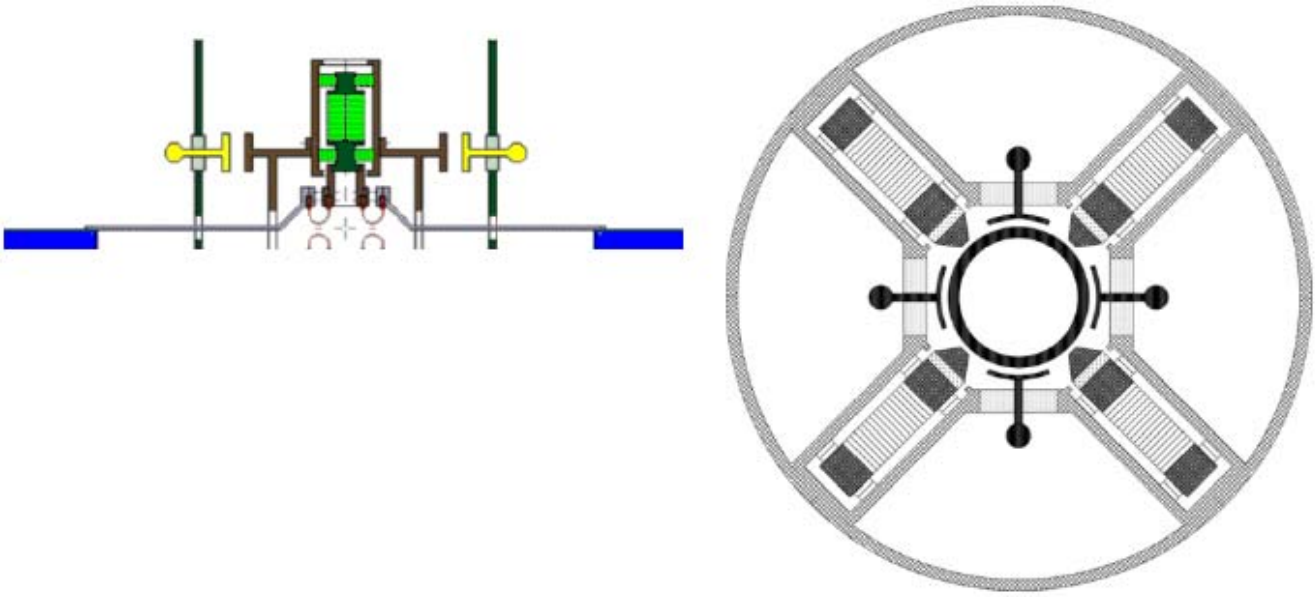

Figure 4.2-1: Schematics of the fine lock/unlock mechanisms

(right) Top view (across the spin/symmetry axis) of one set of 4 inch-worm actuators for fine unlocking of the suspended GG bodies; (left) Section through the symmetry axis showing the detailed location of this fine lock/unlock device for one of the test cylinders. The figure on the right refers to unlocking the PGB from the spacecraft. The inner tube of about 10 cm radius (belonging to the PGB) encloses one of the PGB suspension spring. This system is located at the top (or bottom) of the PGB suspensions. Each suspended cylinder needs 2 sets like the one shown here placed at its two axial ends.

4.2.1 Locking devices - Acceleration loads evaluation

From the VEGA User's Manual Issue 3 [RD 31] we selected the worst-case conditions as far as the launch accelerations (longitudinal and transversal) are concerned.

From the results of this analysis the most demanding conditions result to be the ones recalled on case number 6, defined as "Stage Ignition" leading to a g value along the symmetry x axis (see Figure 4.2-2) equal to 5 g's, while on the two other perpendicular axes y and z the load values are both equal to 0,2 g's.

Obviously, these values are increased due to the amplification phenomena going from the external outer structure of the satellite towards the symmetry axis. The highest level of acceleration occurs on the inner delicate and strategic components of the experiment. Fortunately the corresponding mass of these just mentioned parts is very limited, so the resulting vector of the resulting force is nevertheless acceptable, leading to a design of the whole locking system still acceptable for the GG project, both in terms of added masses and necessary accommodation volumes.

We have then:

g (x) = 5 g's

g (y) = 0,2 g's

g (z) = 0,2 g's

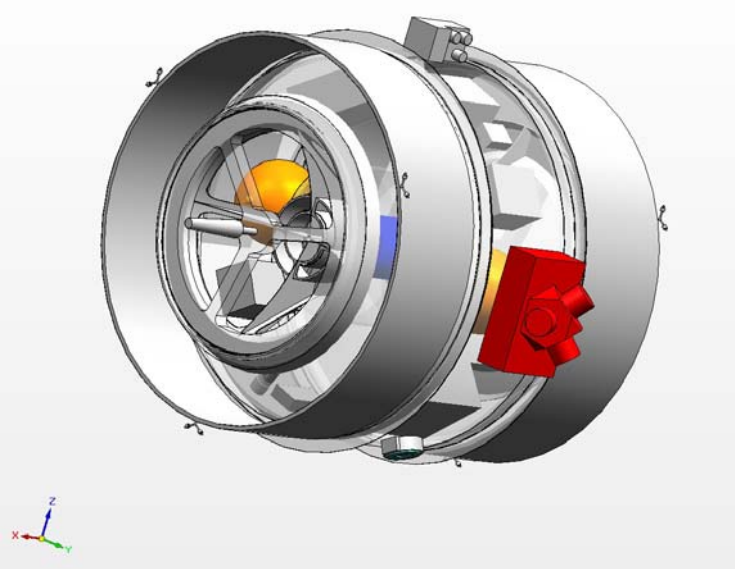

Figure 4.2-2: GG spacecraft axes definition

In consideration of the most recent mass budget evaluation, we have consequently a reaction load to be applied through the set of mechanisms we are presently developing equal to approximately 1500 Newton.

Due to the above consideration, and also to the analysis of the layout of the GG scientific key-components, we developed a specific set of mechanisms, simple, reliable and light as much as possible, based on electronically controlled linear actuators whose knowledge is a long DTM tradition, being the same kind of devices already successfully tested in previous Space missions, both manned and unmanned.

The reliability of the mechanisms subsystem has been a key point for the selection and design of the mechanisms, since in the following and more detailed program phases one of the mandatory issues to be immediately faced will be the failure mode analysis. The development of the mechanical project based on the assumptions of the failure mode analysis requires redundancy, avoiding single-point failure conceptual design; the approach to the GG locking mechanisms design is then compliant to this mandatory design approach.

The above is a blocking point for the further design development, so we believe since now the design of the mechanisms must take care of these safety and reliability requirements.

Also, due to the analysis of the satellite preliminary layout, it has been decided to keep as simple as possible also the accommodation and orientation of the above mentioned locking / unlocking devices, which are now axially positioned. As a further advantage, this disposition of the mechanisms inside the satellite structure allows to have a very simple and straightforward electronic control design/ implementation.

Locking devices levels.

There are four “nested” levels of locking systems; they are, starting from the outer side of the satellite structure:

- Locking of the whole PGB (including PGB structure and science inner components)
- Locking of the external test mass
- Locking of the internal test mass (concentric to the previous one)
- Locking of the very sensitive inner mechanisms, connected to both test masses via very thin laminae (cantilever springs), which are the key components used for science data measurement (relative displacement of the two test masses).

4.2.2 Design of the locking mechanisms. Locking of the test masses

Being the design approach of all the locking devices envisaged as the same for the four levels of locking, in this section the attention is manly focused on the most inner mechanisms, namely the ones used to lock for launch configuration the delicate measuring devices used to investigate on test masses relative displacement.

Figure 4.2-3 shows the concept envisaged for the test masses launch locking. The locking of both outer and inner test masses (the second one is represented in Figure 4.2-3) is based on two sets of identical non-magnetic actuators able to overcome the launch acceleration forces.

The load components acting in the plane perpendicular to the satellite symmetry axis are dealt by custom made “tips” of the actuator plungers matching with corresponding “indents” (whose small protrusion shall be obviously dictated by the PI not to affect science aspects) of the counterpart to be locked.

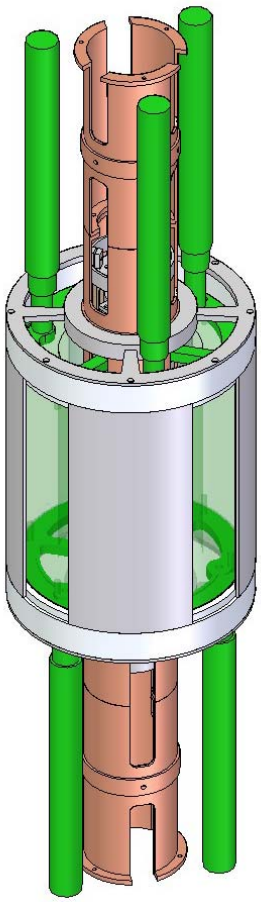

Figure 4.2-3: Test masses locking concept

4.2.3 Locking of the inner differential measuring devices

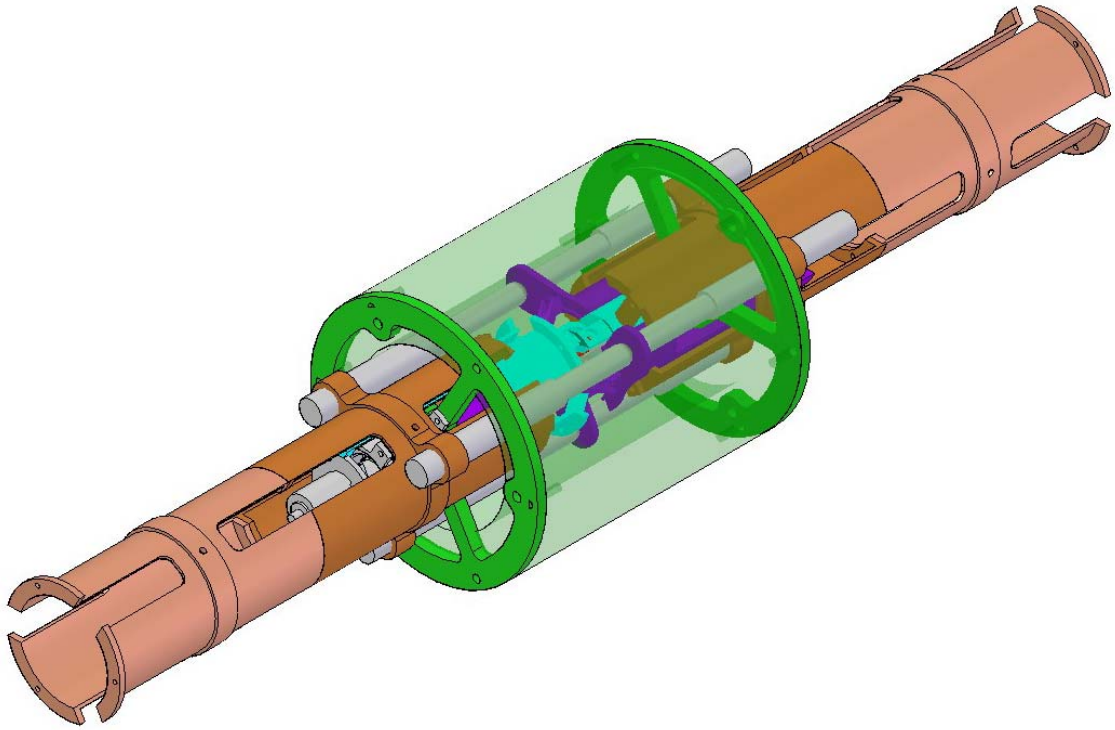

Figure 4.2-4: Inner differential measuring devices locking concept

Figure 4.2-4 shows an image of the three axial non-magnetic actuators accommodated as a crown with respect to the differential measuring device; the assembly is partly hidden because of the inner test mass, here in light green colour.

The relatively long actuators are accommodated in such a way not to generate interference w.r.t. the test mass; as a mater of fact they are placed in between the “spokes” of the two wheels supporting the axial-symmetric mass.

Figure 4.2-5 is a detail of the previous image, showing more clearly the matching area between the actuators (in light grey) and the “bunny ears” of the measuring device.

The next two images Figure 4.2-6 and Figure 4.2-7 show in bi-dimensional section view the inner assembly. This first image includes also the upper and lower cylinders, in light-brown colour, supporting the whole “science section” of GG. The inner delicate components of the differential measuring devices – shown in Figure 4.2-7 in purple and sky blue – are the ones analysed with finite element programs, and described in the next section of the report.

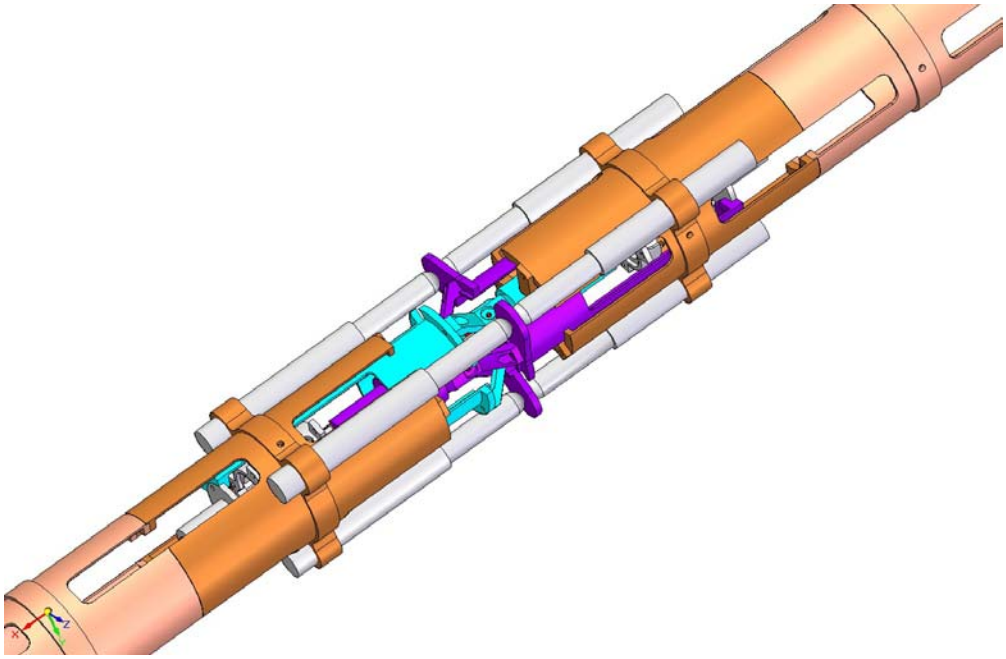

Figure 4.2-5: Inner differential measuring devices locking concept (detail)

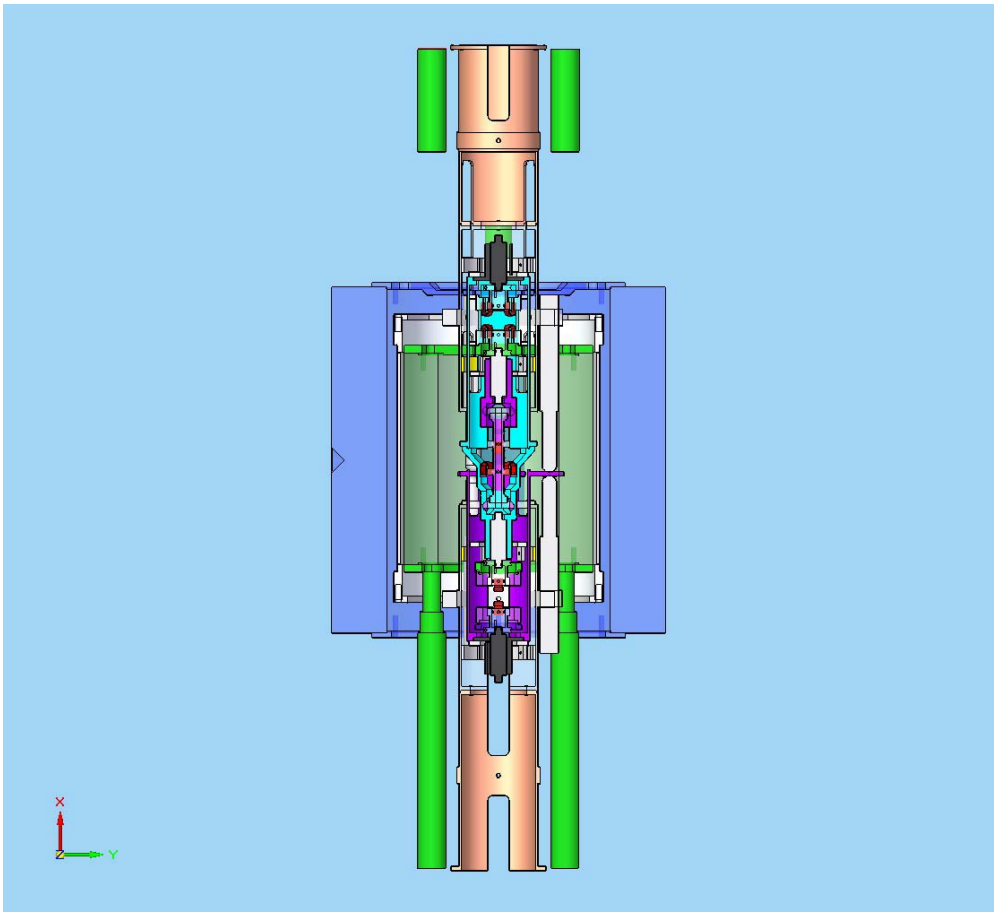

Figure 4.2-6: Inner differential measuring devices locking concept (section 1)

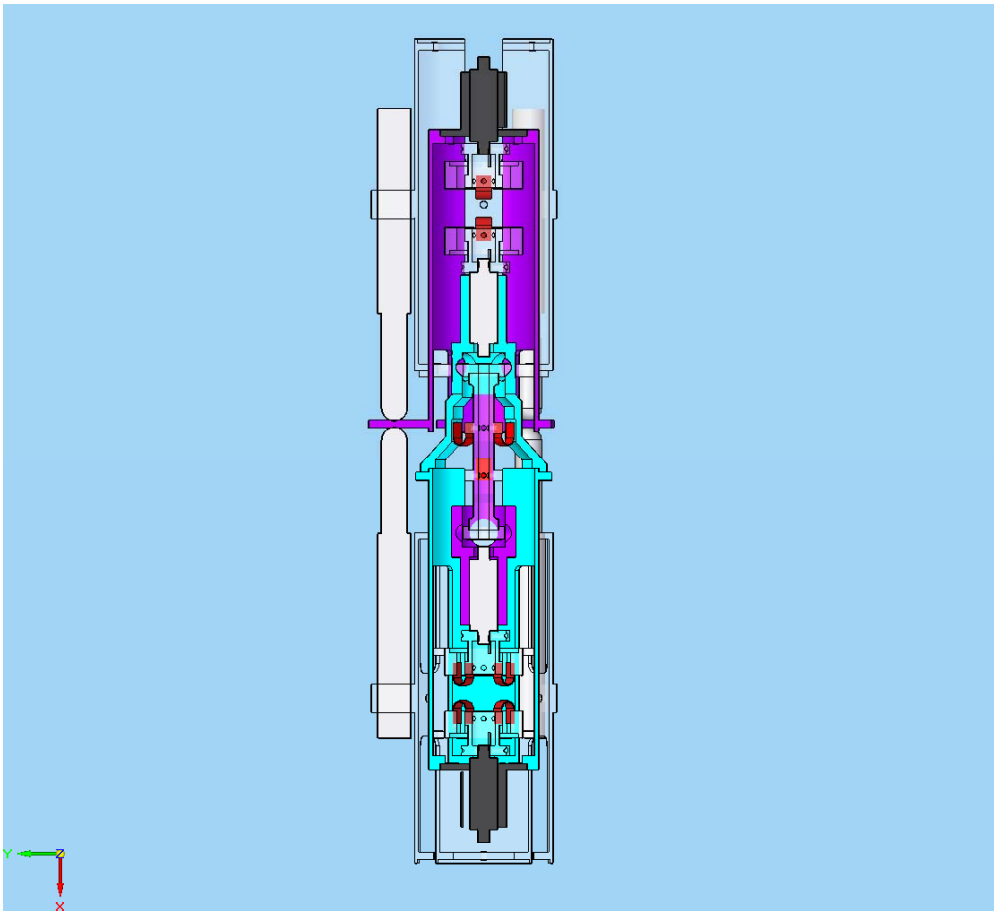

Figure 4.2-7: Inner differential measuring devices locking concept (section 2)

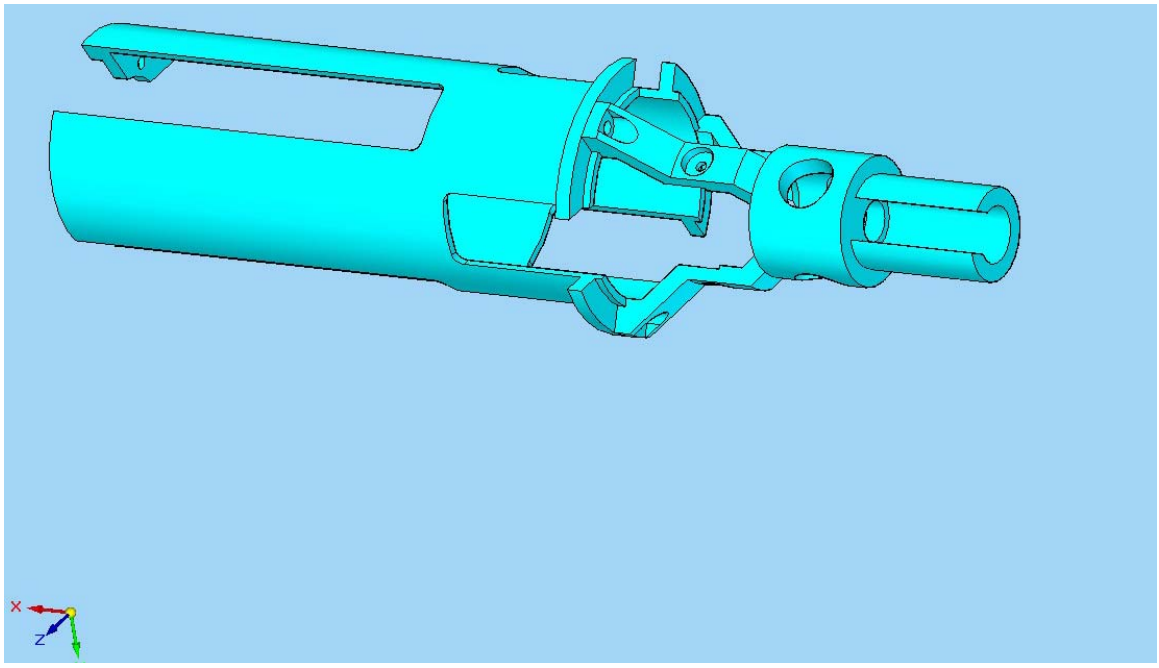

Figure 4.2-8: Inner differential measuring device main body

Figure 4.2-8 is the original configuration of the main body which is the core-element of the inner differential measuring device. The system has be rigidly locked for launch, and in order to use the simple locking system envisaged for GG, we proposed to slightly shift the load path by introducing a so called “bunny ear” tern of cantilevers, in order to fully respect the necessary axial-symmetry.

The following Figure 4.2-9 shows the modification introduced for this reason.

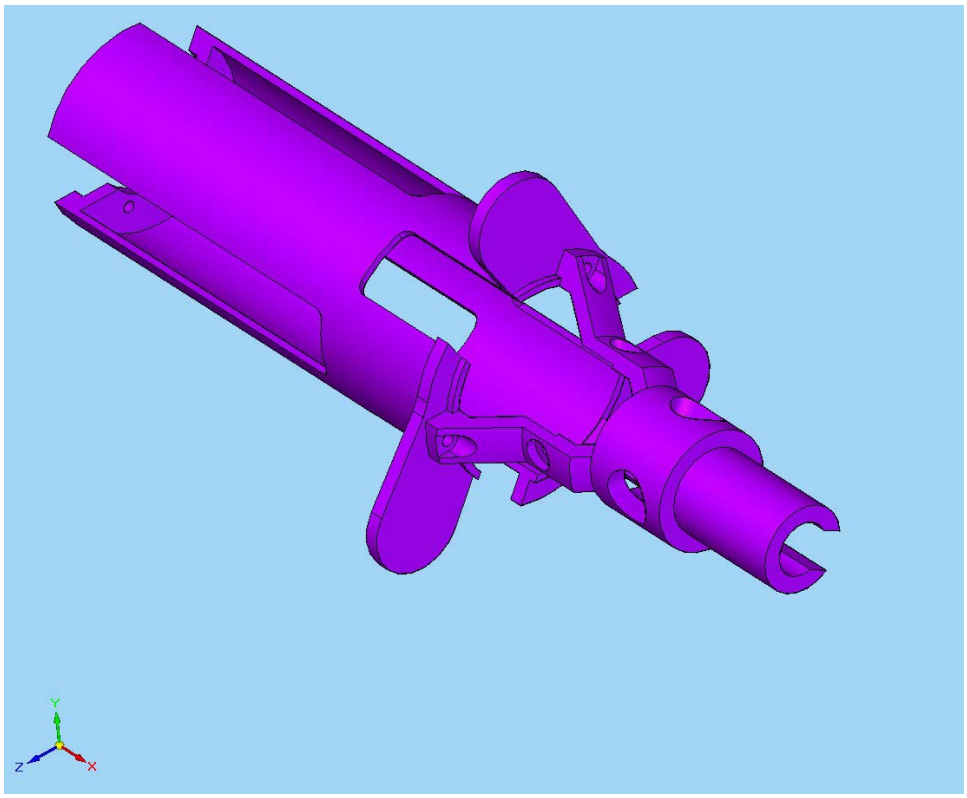

Figure 4.2-9: Inner differential measuring device main body modification for locking devices accommodation

The “bunny ear” configuration of the three cantilevers protruding in radial direction is the most simple, light, reliable and efficient way to by-pass the “crowded” mechanical system of the measuring device, allowing this device to be safely locked during launch phase.

In Figure 4.2-10 the system is shown in its integrity, with measuring devices (two of them), and the two corresponding sets of non-magnetic actuators. The overall configuration requires twelve actuators; also if this number is not negligible, we have been forced to go this way in order to satisfy failure mode analysis criteria (a must for the next design phase of the project). This design solution has been also dictated by geometrical needs, due to the complex and quite articulated shape of the sensors and their accessories.

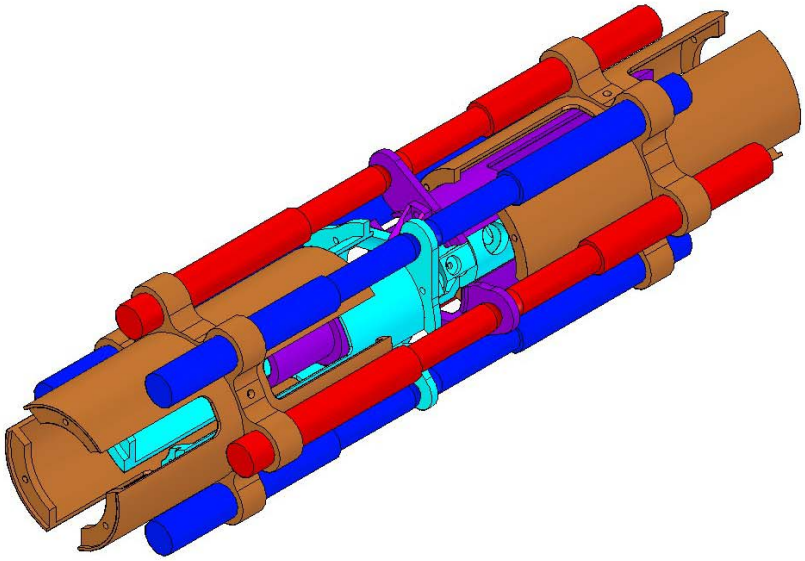

Figure 4.2-10: Inner differential measuring devices locking iso view

The last view of the locking systems (Figure 4.2-11) shows how all the main parts are nested together and in particular the twelve axial actuators locking the inner science devices.

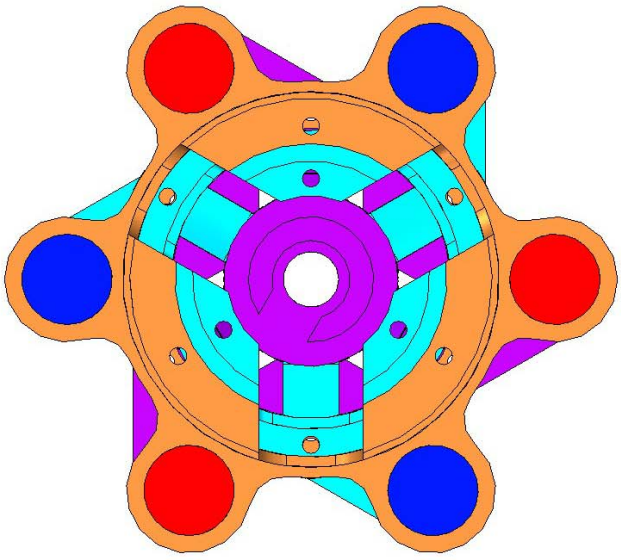

Figure 4.2-11: Inner differential measuring devices locking axial view

4.2.4 Dynamic behaviour of the differential measuring device

The differential measuring device is definitely light (less than 200 grams if made in titanium, or only 100 grams if in light alloy); this is a very important feature in terms of dynamic response, but in the same time its shape is not exactly “compact”. Its geometry, in fact, is quite spread, and this could be in principle negative, since one can fear that the device masses, being located far from its centre of gravity, could generate low-frequency vibrations, if coupled with corresponding excitations coming from the launcher motors and acting as dynamic disturbances.

Due to this fact, a finite element dynamic analysis ahs been carried out in order to verify if the above could be a potential problem or not.

The data coming form the NASTRAN runs are quite convincing about the situation, which is good. The dynamic response of the measuring device is in fact completely de-coupled from the VEGA launcher excitation, and this guarantees about the design approach proposed and developed by DTM, that can be considered solid and safe.

Here below a sequence of NASTRAN outputs is reported, showing in deformed mode the investigated device.

The first “normal mode” analysis, with the component locked at the tips of the three “bunny ear” cantilevers shows a value well above the VEGA User Manual’s prescriptions (above 400 Hz), and the same apply to the second performed analysis, the one dealing with the so called “free free” mode, which corresponds to the operating phase, when the satellite is in its correct orbit performing science.

Both investigations are repeated twice, first considering titanium as construction material, and after high-performing space qualified light-alloy. The results, as can be seen from the images, are very similar and in both cases satisfactory. The almost equivalent results are due to the fact that titanium is more rigid than light alloy in terms of elastic modulus, but also its density is correspondingly higher. The two effects are perfectly balances. So the NASTRAN output is practically the same.

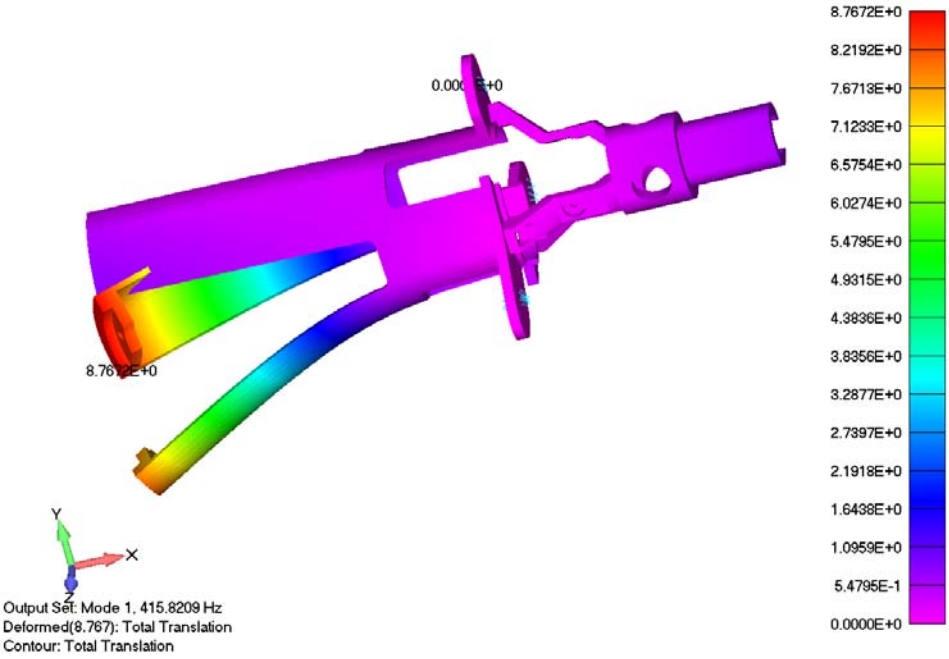

Figure 4.2-12: Differential measuring device locking mechanism - Titanium - First normal mode

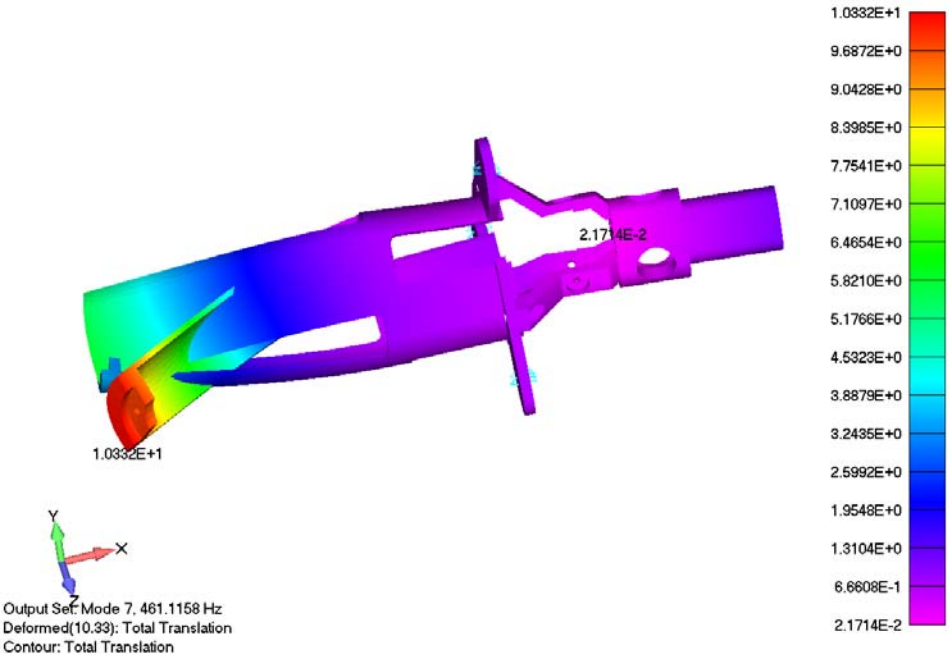

Figure 4.2-13: Differential measuring device locking mechanism - Titanium - First "free-free" mode

The result is very good and representative of the operating microgravity conditions in orbit. Apparently this is the seventh free-free mode, but the first six modes have to be discarded since they are corresponding to component's rigid translations and rotations with respect to the x,y,z system reference axes.

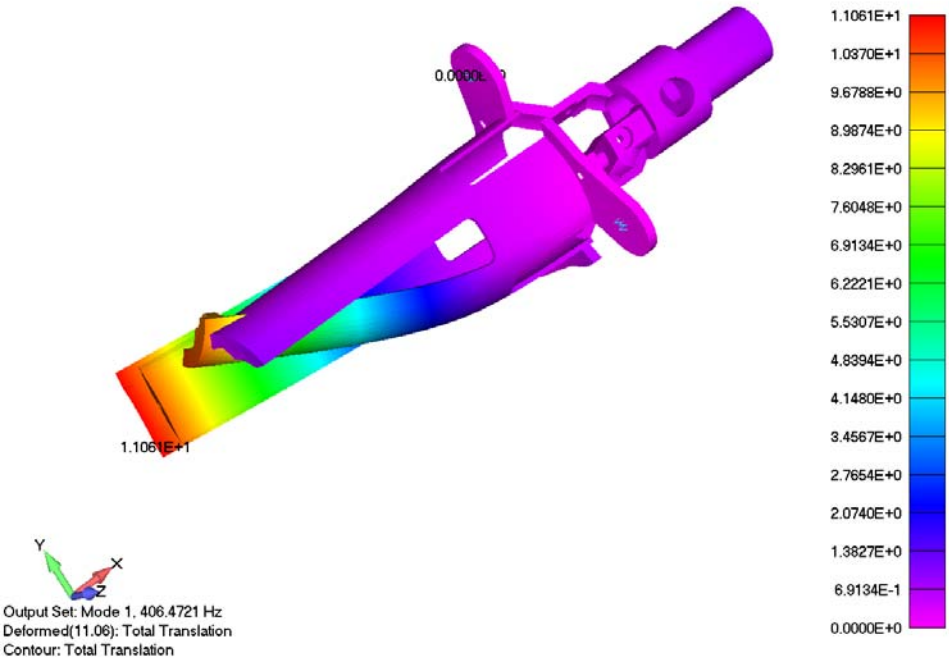

Figure 4.2-14: Differential measuring device locking mechanism - Light alloy - First normal mode

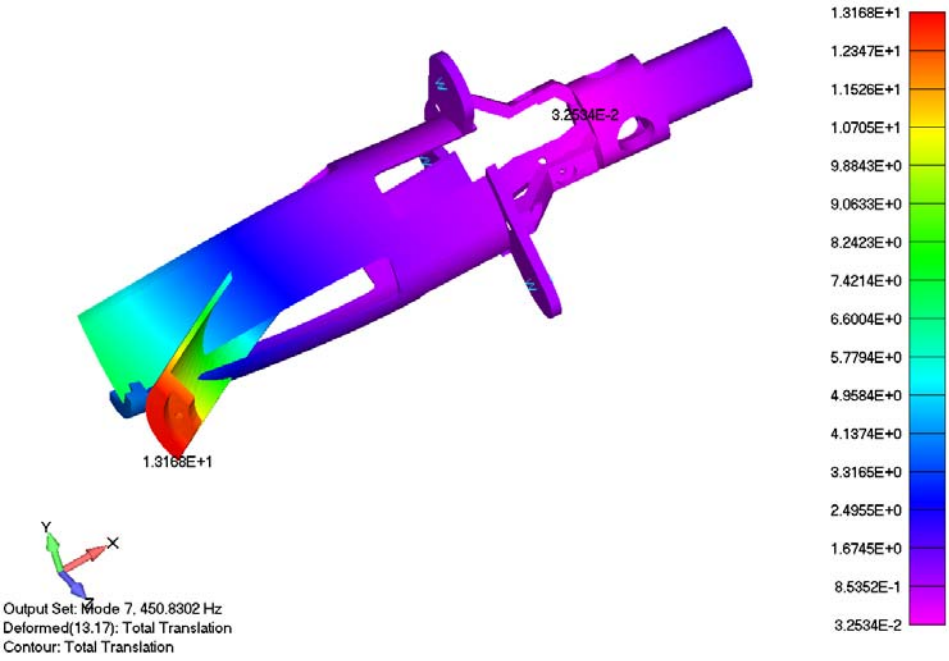

Figure 4.2-15: Differential measuring device locking mechanism - Light alloy - First "free-free" mode

The result is very good and representative of the operating microgravity conditions in orbit. Apparently this is the seventh free-free mode, but the first six modes have to be discarded since they are corresponding to the component's rigid translations and rotations with respect to the x,y,z system reference axes

4.3 Thermal Stabilization and Co-Rotation

Thermal stability of the GG accelerometer is very important as temperature induced distortions may unbalance the test masses, unbalance the capacitance bridge transducers, displace the test masses along the axis direction. The high symmetry of the entire system and its rapid rotation help considerably in reducing such effects (most importantly the radiometer effect).

However, the low equatorial orbit causes a strong thermal stress on the GG satellite as it goes in and out of the Earth shadow every orbit. This orbit has been selected, instead of a high-inclination sun-synchronous orbit, in order to avoid re-aligning the spin axis of the satellite with the orbit normal during the mission, so as to perform a more passive and less disturbed experiment, and also to reduce the complexity and cost of the mission. It definitely turns out to be the best choice with the availability, in the near future, of the VEGA launcher.

Considerable effort has therefore been devoted to the thermal stabilization of the GG payload. The thermal control shall provide a suitable thermal conditioning of the PGB environment, in terms of high stability in time of the test mass temperatures, and low axial as well longitudinal temperature gradients of the test masses themselves.

The thermal control subsystem is entirely designed on material-standard equipments and a classical passive approach is used to counter the external (direct Sun, albedo, Earth infrared radiation) as well internal (equipment power dissipations) thermal loads and their oscillations, aiming at maintaining as constant and uniform as possible the thermal environment around and inside the PGB.

MLI blankets are used to decouple loads and attenuate oscillations. They are used both to protect the external surface of S/C from external environment and to decouple the PGB from inside of S/C where the electronic units are installed. The connections of dissipating equipment to equatorial radiators are provided (all the boxes are located around the equatorial cylinder surfaces), via thermal fillers, to increase their contact conductance at the boxes radiator contact baseplates; heaters are employed when necessary to trim or maintain the necessary temperature levels.

The “spinning top” structure will be made from carbon fibre composite to reduce thermal distortions. It is worth stressing that so far no need has arisen for active heaters.

An issue has arisen about co-rotation of the PGB with the outer spacecraft. The spin rate of the outer shell will change if the moment of inertia of the shell changes while the spin angular momentum remains constant. This happens due to temperature variations of the outer shell as the GG satellite gets in and out of the Earth shadow, which is not the case for the PGB since it is very well insulated and thermally de-coupled from the spacecraft. The resulting phase difference is very large, because of the rapid rotation. However, the absolute change in the moment of inertia is indeed very small.

Note that no such phase lag will take place between the PGB and the test bodies because of the very good thermal insulation; spring coupling will take care of eliminating residual small phase lags (e.g. left out by the unlocking procedure) during the initial phase of the mission.

Two methods have been put forward to compensate the effect causing motion of the PGB with respect to the outer spacecraft.

(i) As the change in the moment of inertia is very small, it can be balanced by a small compensation mass. This compensation can be passive; the idea is to have a mass which expands and contracts in anti-phase with respect to the outer shell of the spacecraft so as to keep the total moment of inertia (of the outer shell plus the compensation mass) essentially constant.

(ii) In an alternative, active concept, co-rotation between the PGB and the spacecraft shell with be sensed by placing a small mirror on the PGB tube and a photo-detector on the spacecraft (it adds no wire to the PGB). Should a residual phase lag be detected, it will drive the thrusters of the drag free control loop for compensation.

The active method is the preferred one as it requires no additional hardware. The extra propellant mass required is small provided that the fractional change of the moment of inertia is $\leq 10^{-5}$, and this can be ensured by proper design of the spacecraft structure [RD 16] [RD 6].

4.4 Test mass materials

The choice of the test masses composition should be made in order to maximize the possibility that an EP violation may occur.

Since one does not expect that hypothetical EP violations can depend on such macroscopic properties of matter like density, and on chemical, mechanical, electric or magnetic characteristics, one should look for other properties of matter for deciding what substances to choose for the test. In [RD 32], for all the elements of the periodic table, are calculated and plotted the three properties that are considered as the most likely sources of a possible EP violation, namely

- B / μ ($B = N + Z$ being the number of barions, N the number of neutrons, Z the number of protons, μ the mass in units of the mass of the H atom)
- L / μ (L the lepton number; for neutral atoms $L = Z$)
- $|z| / \mu$ ($|z| = |N - Z|$ the z component of Isospin).

Figure 4.4-1, Figure 4.4-2 and Figure 4.4-3 are adapted from the corresponding plots reported in [RD 32]. According to Figure 4.4-1 and Figure 4.4-2, CH_2 and Pb are the best possible choice, while from Figure 4.4-2 this choice is about equivalent to the typical choice of Be for one mass and Cu or Ti for the other.

With CH_2 we indicate all solid polymers like polyethylene $(C_2H_4)_n$, polypropylene $(C_3H_6)_n$ etc., all with the same proportion of Protons and Neutrons as CH_2. It is very important to stress that in GG, due to the fast rotation of the test masses there is no need to manufacture them to need to very high precision, as small anomalies would give DC effects not competing with the signal. This is also why the GG test bodies can be 10 kg each, that is, considerably more massive than test masses typically used for ground experiments or proposed for space. The case for larger masses is obviously to reduce thermal noise.

We are therefore considering using CH_2 and Pb (or Tungsten, W, with similar characteristics for our purposes but of easier practical use) since this choice would maximize the possibility for an EP violation for the same target sensitivity of the GG experiment.

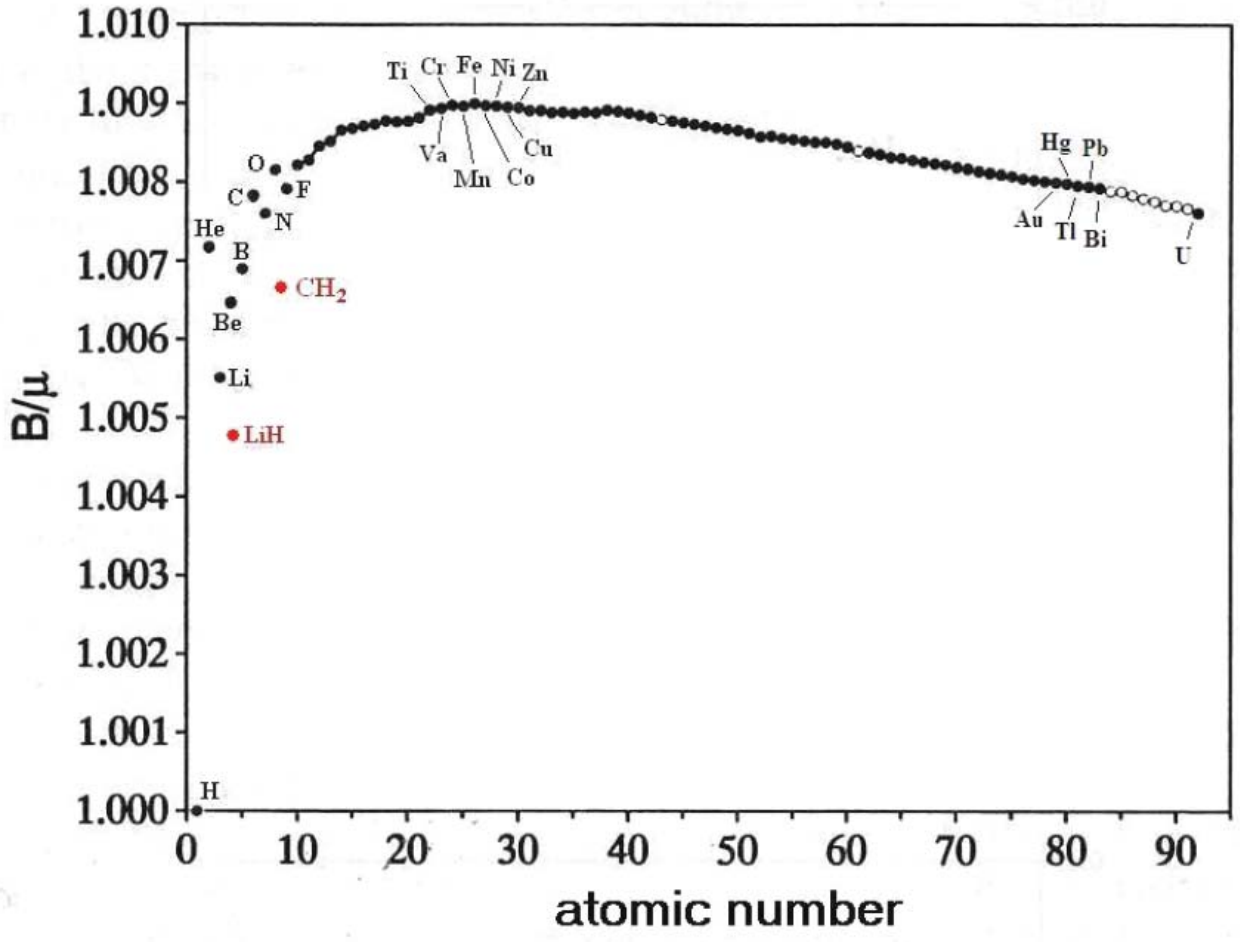

Figure 4.4-1: B/μ as function of the atomic number (the red dots have been added to the original plot in [RD 32])

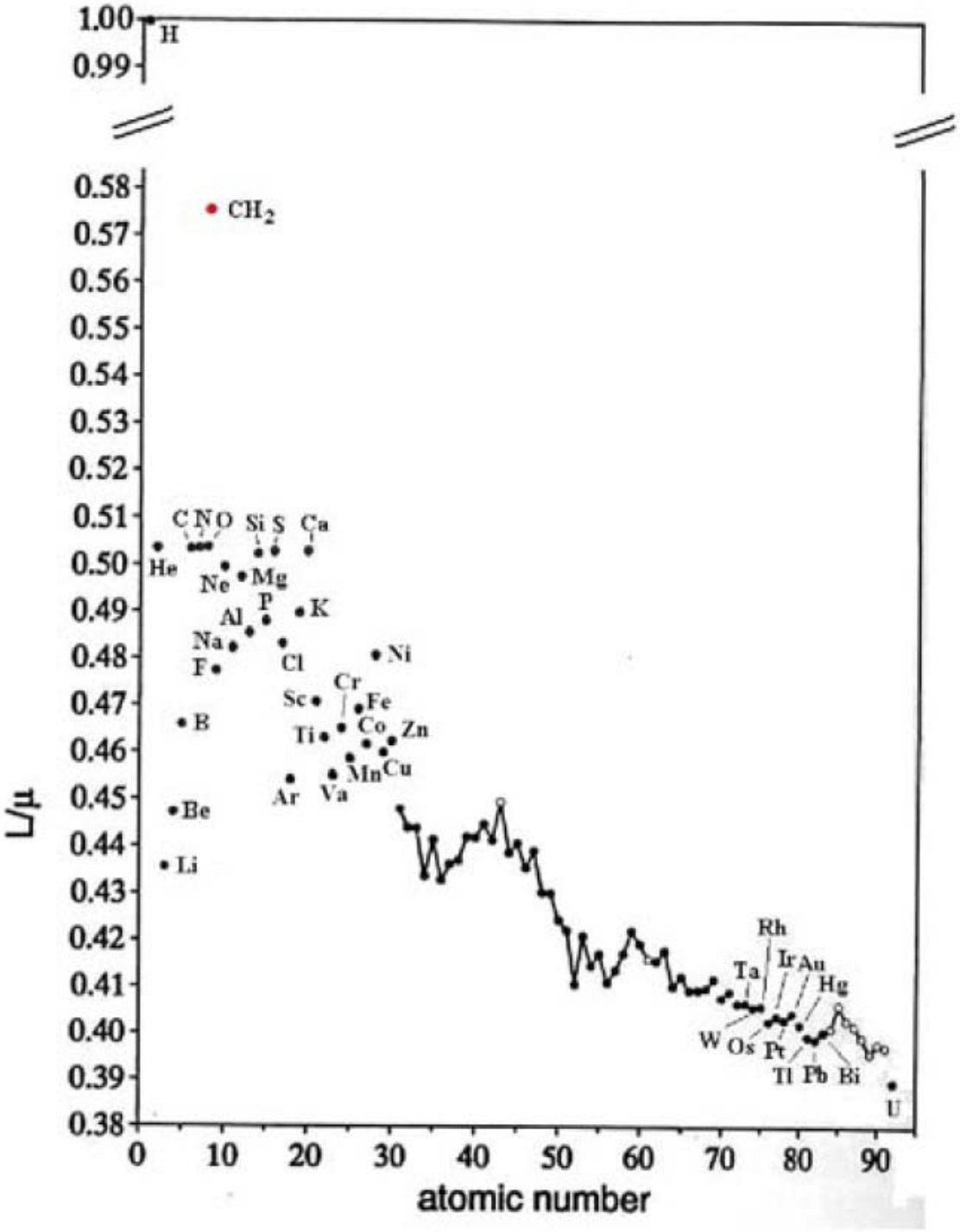

Figure 4.4-2: L/μ as function of the atomic number (the red dot has been added to the original plot in [RD 32])

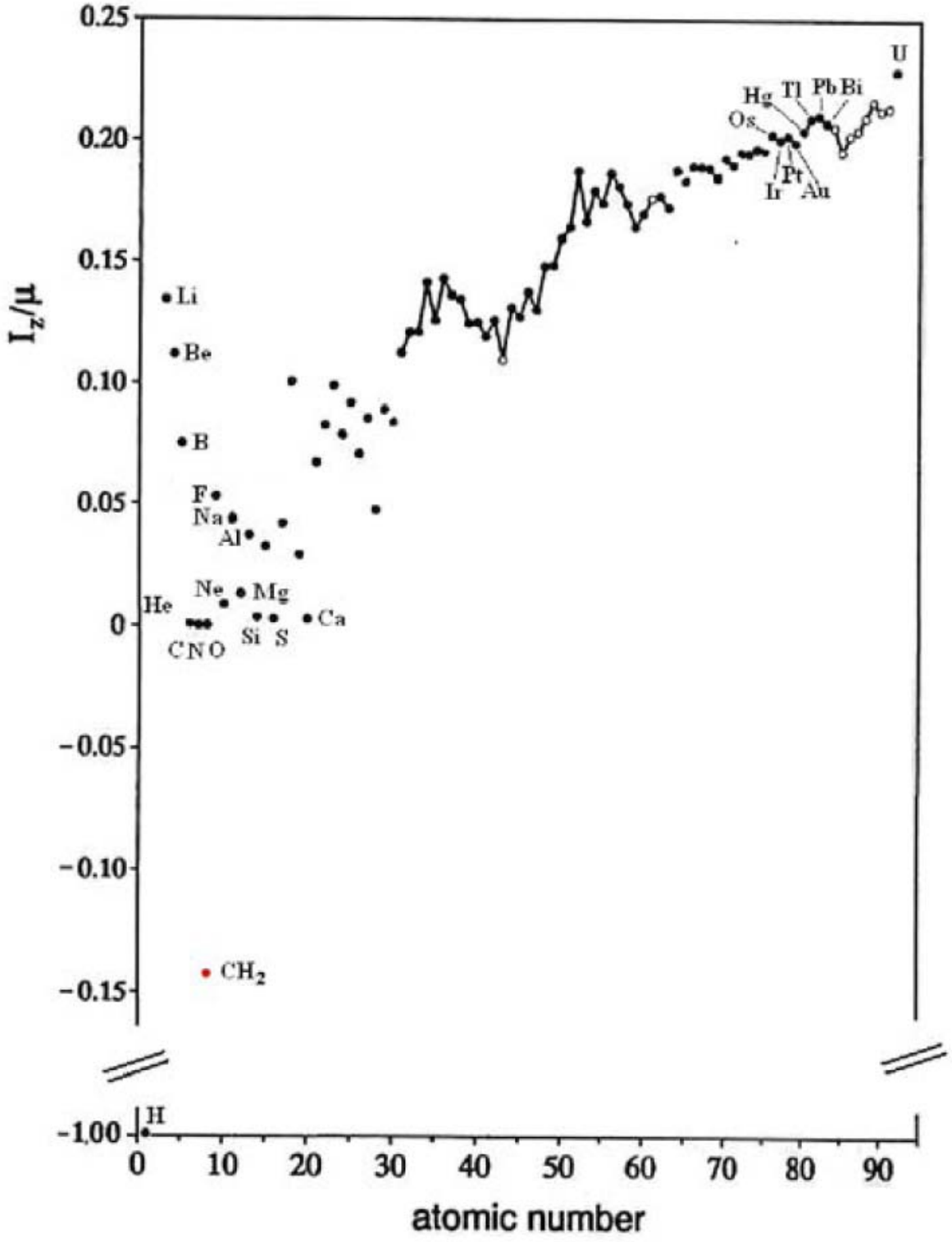

Figure 4.4-3 : I_Z/μ as function of the atomic number (the red dots have been added to the original plot in [RD 32])

5. SATELLITE, ORBIT AND THE VEGA LAUNCHER

5.1 Launcher and mission

The satellite will be launched directly into near-circular, near-equatorial orbit by a small / medium launcher such as Vega (baseline) or PSLV (backup). Both launchers have capability much in excess of a small spacecraft such as GG, and a dual launch might be taken into consideration (Figure 5.1-1).

The design launch altitude will be between 600 km and 700 km, according to the strategy discussed below. No orbit maintenance is planned, and the spacecraft altitude will be allowed to decay gently in time, with negligible impact on the satellite mission and operations.

A preliminary sequence of events is in Table 5.1-1. Once set up and initialized, the experiment will run in a regular way without any changes to either orbit or attitude. Given the near-equatorial orbit, the satellite will experience a regular once-per-orbit sequence of eclipses (35 minutes) and passes above the equatorial ground station of San Marco near Malindi, Kenya (about 10 minutes, with small variations depending on the selected altitude).

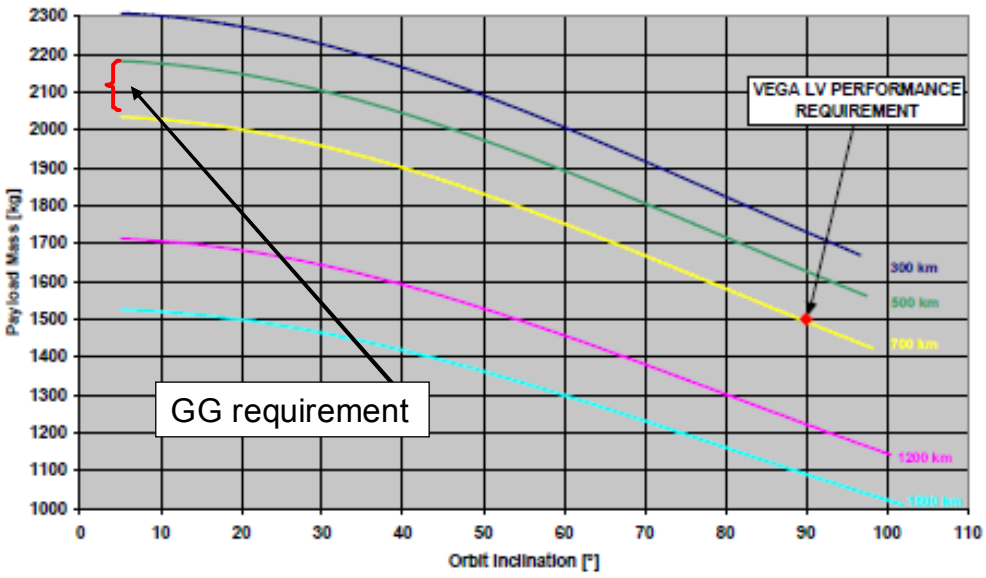

Figure 5.1-1: VEGA performance for circular orbits.

The launcher requirement is 1500 kg in a 700-km altitude polar orbit. The lower limit to the orbit inclination is about 5°, and is set by the latitude of the Kourou launch site (5°N). For such a near-equatorial orbit, as required by GG, the VEGA performance is in excess of 2000 kg, much above the needed spacecraft mass.

Launch and Ascent Phase	
duration: ≈1 hour	3-axis stabilized release by the launcher satellite off on lift-off; activation of OBDH and RF by separation switch
Early Orbit Phase	
duration: ≈1 day	sun acquisition, rate damping and coarse spin attitude stabilization (autonomous) satellite acquisition by the EOP ground station network satellite health check
Satellite Commissioning	
duration: ≈1 week	satellite control handed over to the dedicated ground station subsystem commissioning satellite spin-up (semi-autonomous, assisted by the ground station)
Payload Switch-on and Calibration	
duration: ≈3 weeks	FEEP thruster switch on (pre-calculated thrust profile) Coarse thruster calibration Activation of electrostatic dampers common-mode sensing PGB unlocking Activation of common-mode sensing Activation of drag-free control Activation of spin rate control Test mass unlocking Test mass centering & alignment Fine test mass set-up / iteration
Scientific Mission	
duration: 1 year	Routine data collection Calibration
Scientific Mission Extension (optional)	
duration: until consumables are exhausted	Same sequence as in the Scientific Mission

Table 5.1-1: Sequence of events in the GG mission

The magnitude of the drag acceleration experienced by the satellite is a key to its performance, via the common-mode rejection ratio of the experiment and the drag-free control. As is well known, the scale height of the Earth's upper atmosphere (and thus the drag on low Earth orbit satellites) is very sensitive to the intensity of the short-wavelength solar radiation and the level of geomagnetic activity. Both parameters are function of epoch and are routinely forecast by a number of organizations, with sufficient accuracy for satellite lifetime and perturbation studies. In this study, we have used the 95% confidence level NASA forecast of the solar activity index F10.7, and of the daily global index of geomagnetic activity Ap, for the time period [2013, 2020], which encompasses atmosphere conditions ranging from near-solar maximum to solar minimum (see Figure 5.1-2).

In order to design the on-board systems independently of the epoch, a maximum acceleration threshold of 2×10^{-7} m/s^2 is specified, and the launch altitude is selected in such a way that the threshold will not be exceeded, in the time span of interest for the mission, at the 95% probability level. Given the downward trend of the solar flux from 2012 on, this criterion shows (Figure 6-3) that the mission design altitude needs to be >600 km if the launch occurs before 2015, and can be 550 km or lower if the launch occurs in 2016 or after. This range of variation of the altitude is of no consequence to either the launch mass or the scientific mission performance.

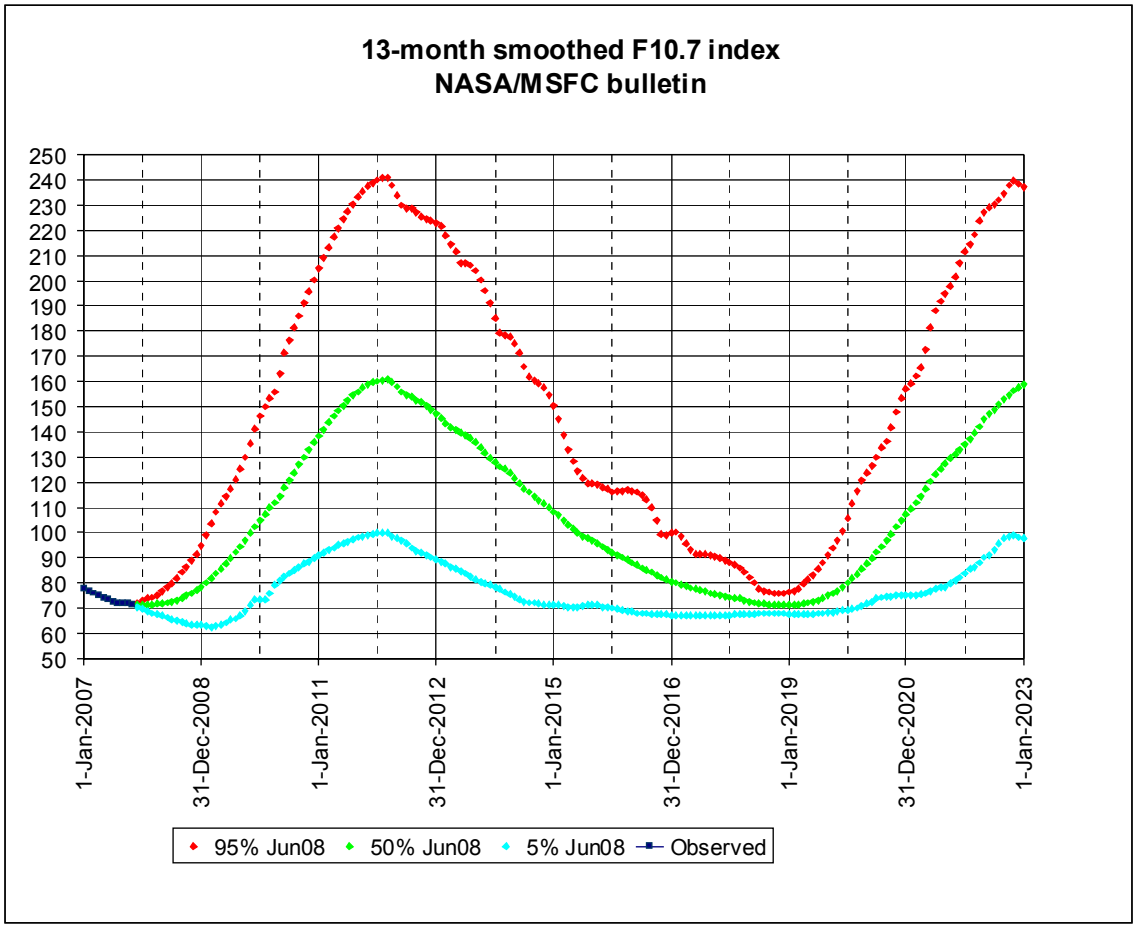

Figure 5.1-2: NASA forecast of F10.7 solar flux index [June 2008 NASA MSFC bulletin]

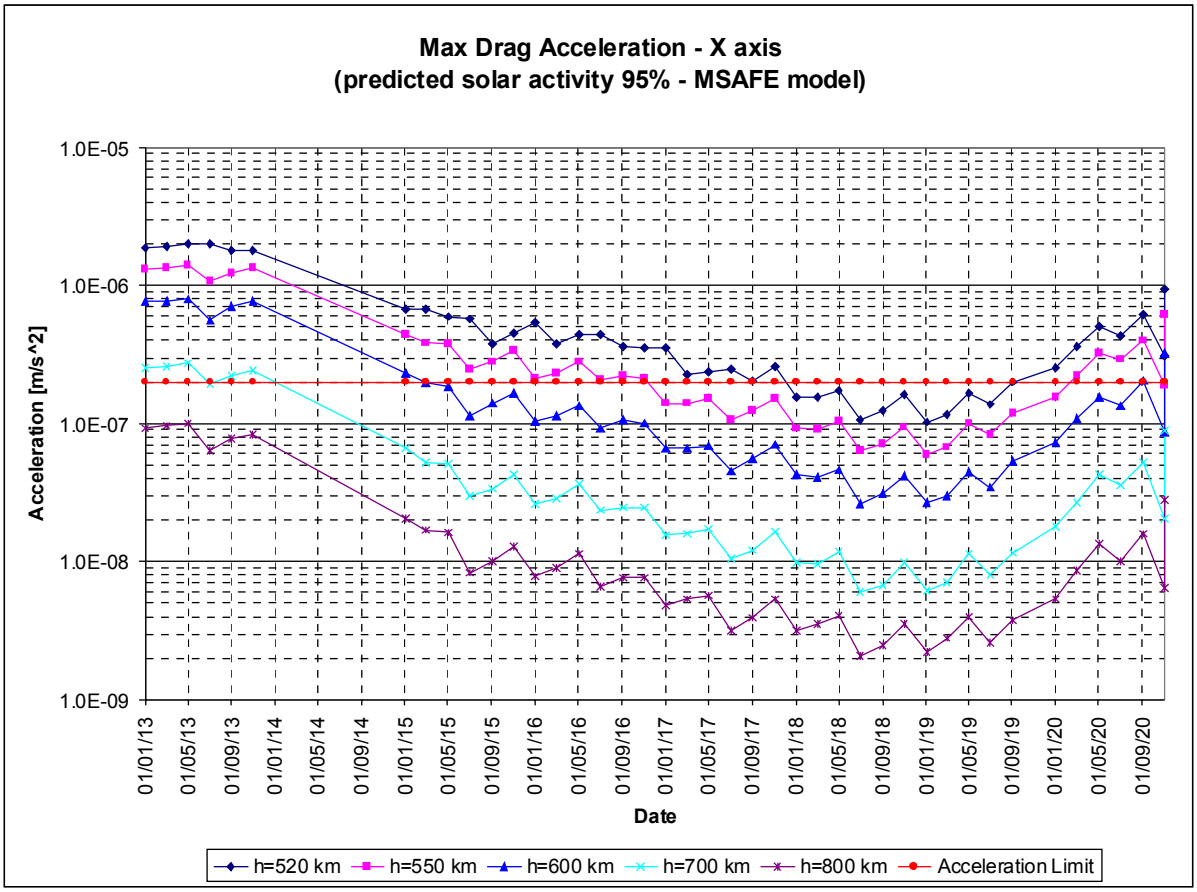

Figure 5.1-3: Parametric analysis of the drag acceleration.

The atmospheric density is taken at the 95% probability level according to the NASA forecast of June 2008. The area-to-mass ratio is 0.0046 m²/kg. A maximum drag acceleration level < 2.0E-7 m/s² first becomes available at mean orbit altitude < 600 km in January 2015.

5.2 Satellite mechanical configuration

5.2.1 GG configuration description

The cylindrical symmetry of the test masses and their enclosure, the Pico-Gravity Box, and the spin required to provide high frequency signal modulation, lead to a spacecraft of cylindrical symmetry, stabilized by rotation about the symmetry axis.

The main configuration requirements of the GG spacecraft are as follows.

- The GG experiment implies an ad-hoc configuration; reuse of an existing platform cannot be proposed. Conversely, many pieces of equipment may be inherited from the PRIMA complement.
- The spacecraft must be made compatible with the Vega launch vehicle (the previous design exercise was focused on Pegasus). In particular, the configuration shall fit the Vega fairing envelope, and the standard Vega 937 B adapter shall be used for launcher separation.
- The configuration shall allow easy integration of the PGB, with mounting/dismounting possible even during the last steps of the satellite integration.
- Low area-to-mass ratio is required ($\leq$ 0.005 m²/kg). The spacecraft shape and its mass distribution must have a degree of cylindrical symmetry. The spin axis must be a principal axis of inertia, with the following constraints
- $J_{spin} > J_{trans}$
- $\beta = (J_{spin} - J_{trans})/J_{trans} \sim 0.2 \div 0.3$.

The proposed solution is therefore a dedicated “spinning-top” structure supporting the PGB and equipment, plus two cylindrical solar panels; sensors and electric thrusters are mounted to a central belt, while the two S-band antennas, both fixed, are mounted on booms aligned with the spin axis.

The GG structural configuration is depicted in Figure 5.2-1. The external structure, completely enclosing the PGB laboratory, is made from CFRP, for minimum thermal distortions, and is made up of three parts:

- central cylinder with 1.45 m diameter, with thermal radiators cutouts;
- upper truncated cone, with the dismountable interface to the PGB suspension system;
- lower truncated cone, symmetrically placed, hosting the launcher interface ring.

The upper cone is removable to allow PGB integration. Equipment items are mounted internally to the central belt; thrusters and sensors are mounted externally. The solar array is made of two cylinders separated by a central belt for mounting equipment, including thrusters and sensors; this solution also allows a convenient distribution of thermal covers and radiators to achieve an efficient thermal control.

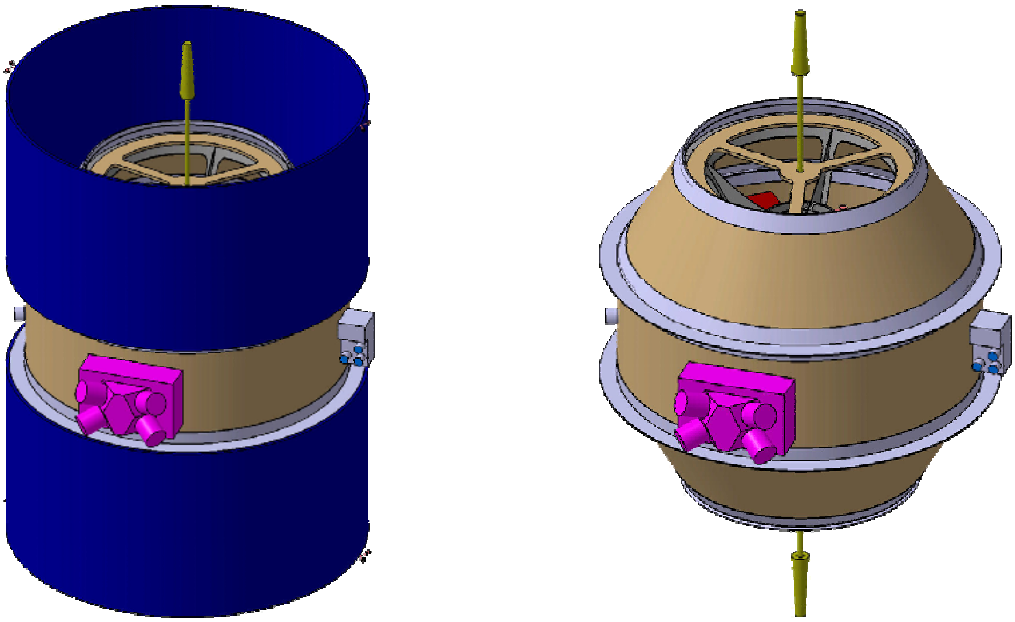

Figure 5.2-1: GG Spacecraft Configuration.

Left: integrated configuration. Right: solar panels removed to show underlying structure.

The details of the configuration are listed below, from bottom to top, together with their component materials:

- interface ring with the launcher (7075 Al-alloy TBC);
- lower payload support cone (CFRP structure);
- lower circular plate with cut-outs, to support the lower LGA antenna;
- lower truncated cone (Al honeycomb with CFRP skins);
- lower cylindrical solar panel;
- central cylinder for mounting the equipment (Al honeycomb with Al skins);
- the equipment (see relevant s/s);
- upper truncated cone (Al honeycomb with CFRP skins);
- upper payload support cone (CFRP structure);
- upper circular plate with cut-outs, to support the upper LGA antenna;
- upper cylindrical solar panel;
- PGB assembly with the on-orbit suspension springs devices;
- two PGB launch-lock mechanism sets, released after launch;
- two antennas aligned with the spin axis, both fixed.

Figure 5.2-3 shows a 3D view of the satellite. The spacecraft body is about 1.45 m in outer diameter and about 1.42 m high. The experimental apparatus is accommodated in a nested arrangement inside the body, as shown in outline in the transparent view of Figure 5.2-3. As shown by Figure 5.2-2, there is plenty of mass and volume available for double launch with Vega, should it become possible.

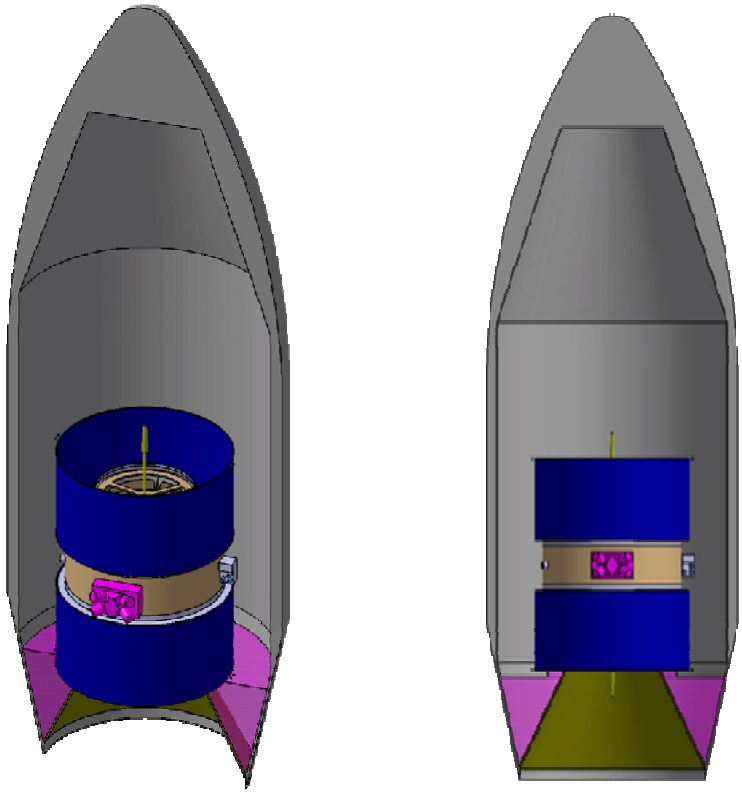

Figure 5.2-2: View of GG Spacecraft beneath Vega fairing

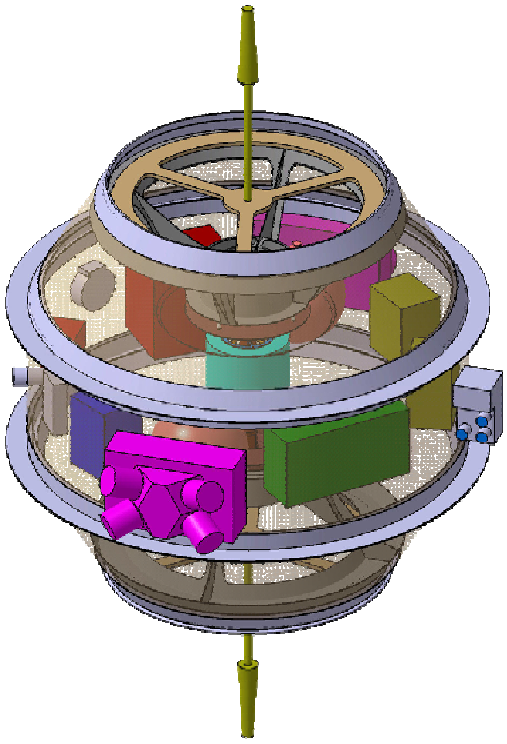

Figure 5.2-3: View of GG Spacecraft (transparent view)

In Figure 5.2-4a, a section of the spacecraft under launcher showing the additional mechanical adapter needed to accommodate sufficient solar array surface avoiding adapter forbidden area is shown, while in Figure 5.2-4b the same section on flight is provided.

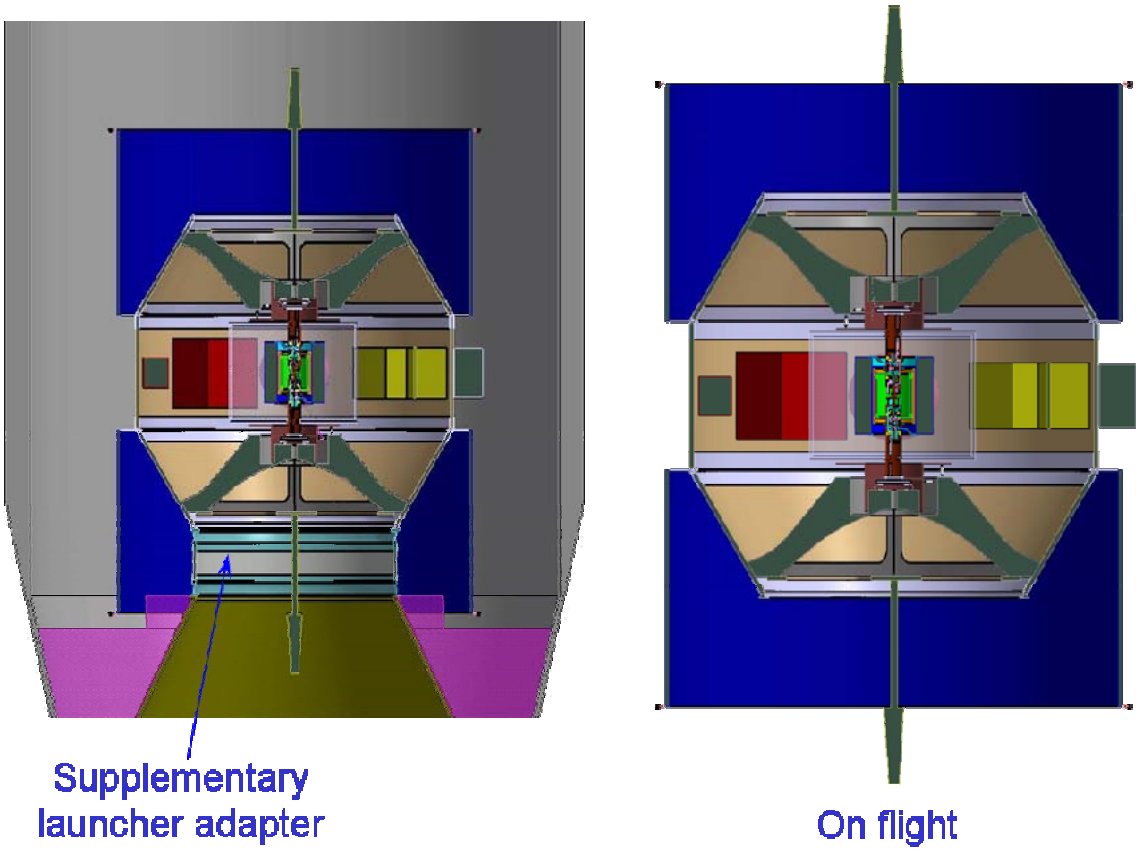

Figure 5.2-4: GG Spacecraft sections beneath fairing (a) and on flight (b)

In Figure 5.2-5 the spacecraft main dimensions are reported.

Details about the equipment layout experiment mechanical interface concepts are provided in Figure 5.2-6 and Figure 5.2-7 respectively.

PGB interfaces exploded view is depicted in Figure 5.2-8, showing all items in detail; in particular, two couples of grids are placed on top and bottom of PGB shaft in order to prevent the space plasma from entering the PGB enclosure, following the example of SAX [RD 33].

The current design maximizes the moment of inertia J_{spin} with respect to the symmetry axis, thereby providing passive spin stabilization around it, and meets the requirement with a $(J_{spin} - J_{trans})/J_{trans}$ ratio of ~ 0.23.

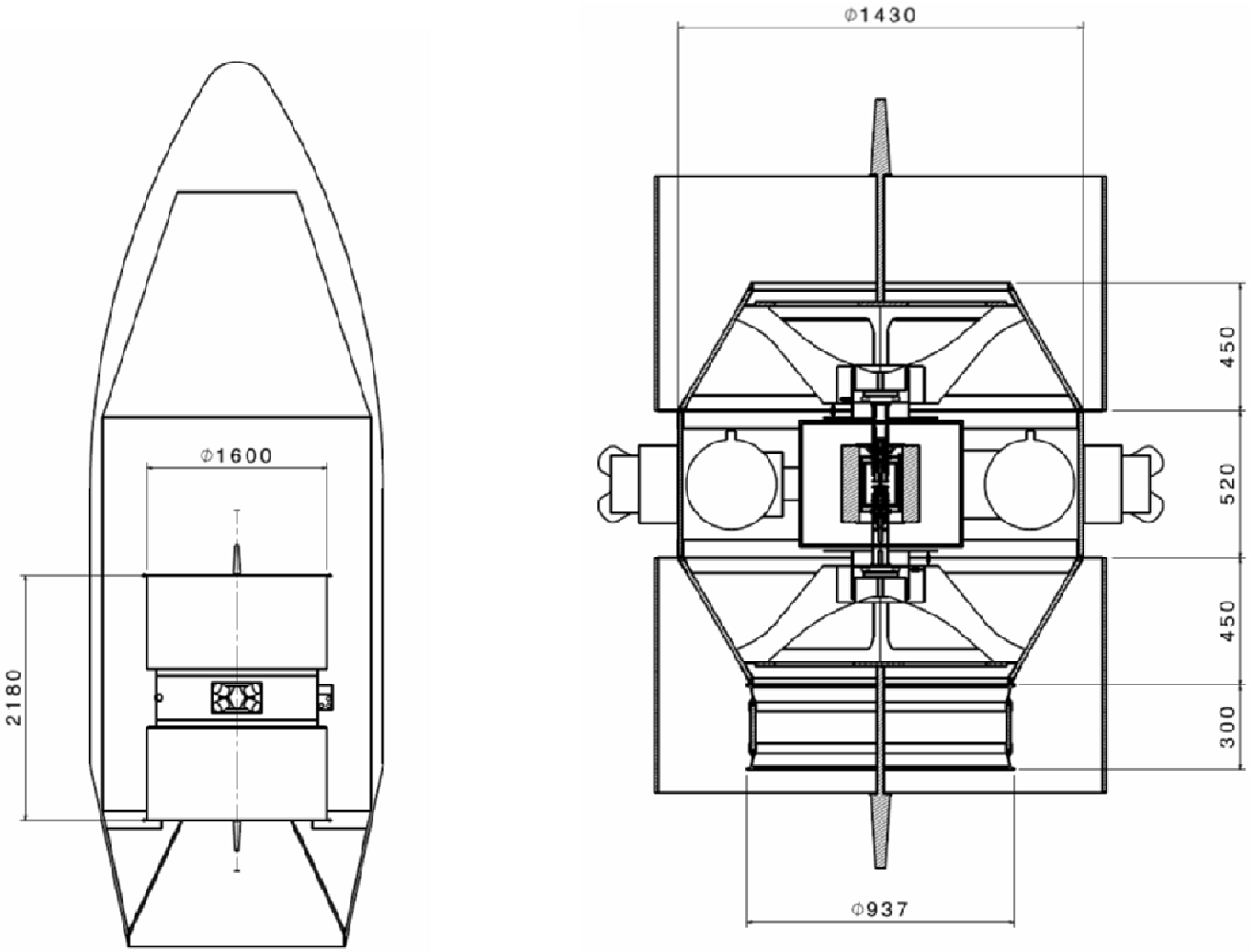

Figure 5.2-5: GG Spacecraft main dimensions

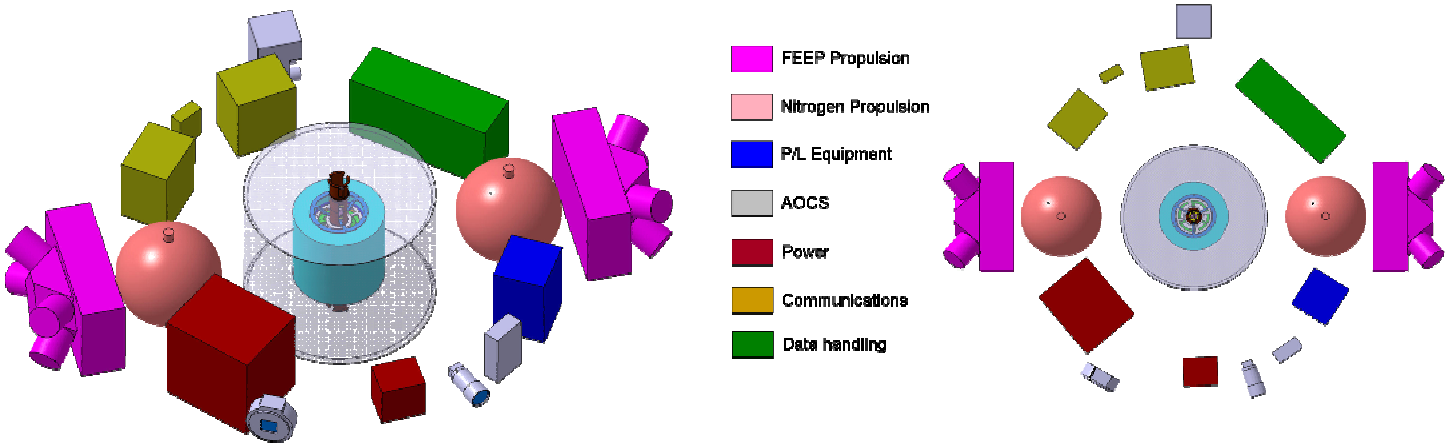

Figure 5.2-6: GG Spacecraft Preliminary Layout

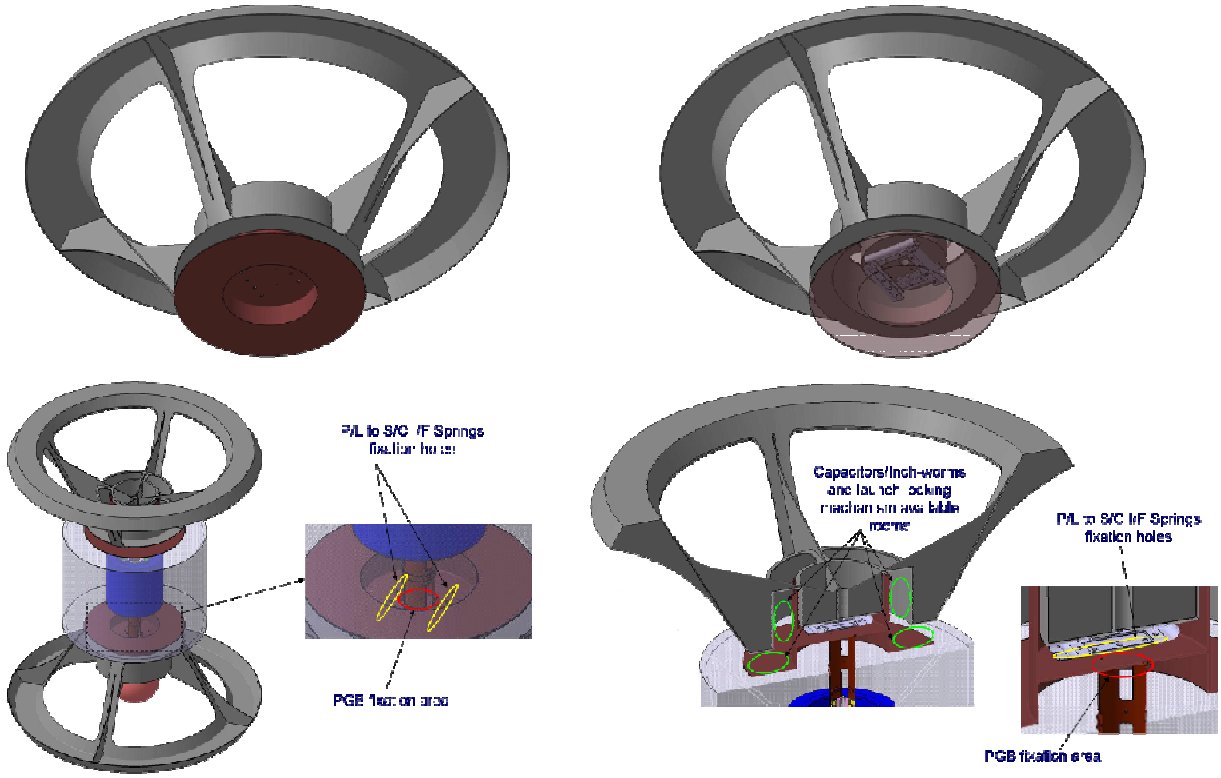

Figure 5.2-7: GG Experiment mechanical interface concept

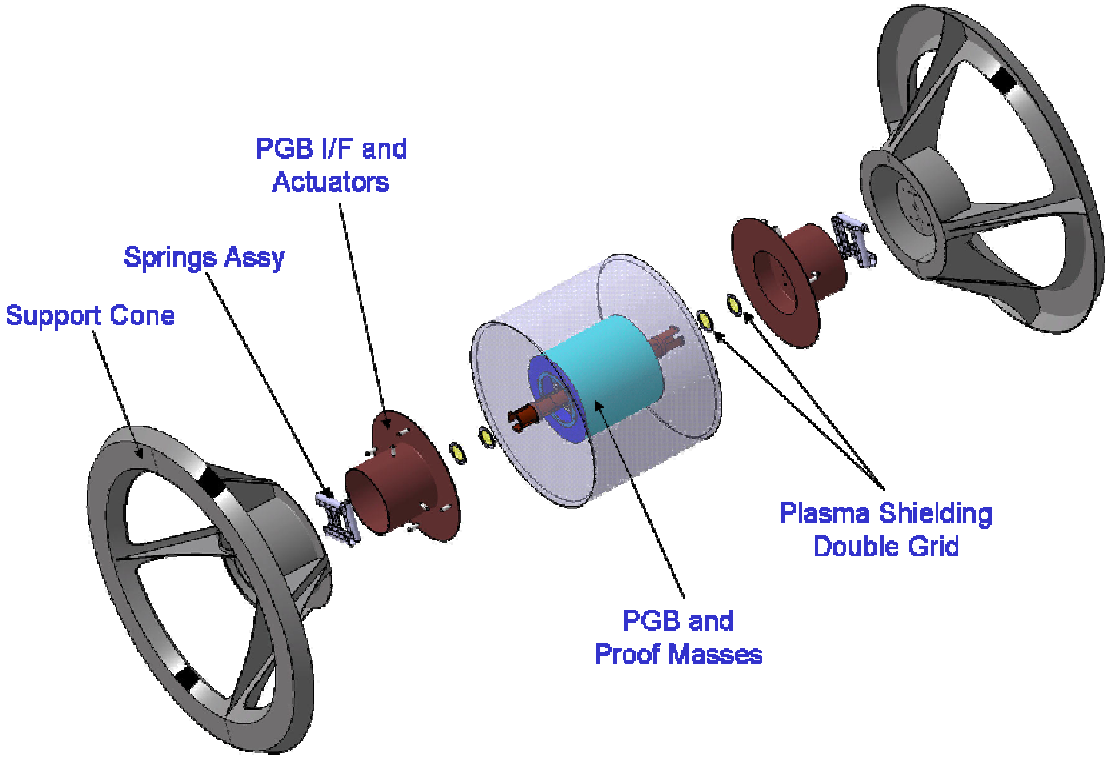

Figure 5.2-8: PGB interfaces with GG Spacecraft exploded view

5.2.2 GG spacecraft mechanical design and FEM model

The spacecraft structure, similar to a spinning top, is exceptionally compact and stiff. Carbon fibre is used to the maximum extent to minimize thermal distortions. The central belt alone is composed of Aluminium honeycomb with aluminium skins for accommodation of the thermal radiators.

A preliminary FEM model (see Figure 5.2-9 and Figure 5.2-10) has been developed by DTM [RD 13] in order to verify the compliance of the spacecraft mechanical design with the Vega stiffness requirement as follows:

- The cantilevered fundamental mode frequencies of a spacecraft hard-mounted at the interface with an off-the shelf adapter must be:
  - In lateral axis: ≥ 15 Hz for spacecraft mass ≤ 2500 kg
  - In longitudinal axis: 20 Hz ≤ f ≤ 45 Hz for spacecraft mass ≤ 2500 kg
- The cumulated effective mass associated to the longitudinal modes within the above frequency range must exceed 60% of the total mass.

The total structural mass is 123.5 kg, including 20% subsystem margin and 10 kg ballast mass allocation. The launcher stiffness requirements are fulfilled with a satisfactory margin. The calculated first axial mode with the structure constrained at launch is 43.76 Hz (against > 20 Hz and < 45 Hz required by the launcher, see Figure 5.2-11). The first lateral mode is 24.07 Hz (>15 Hz required, see Figure 5.2-12); good and comfortable margins are hence reached.

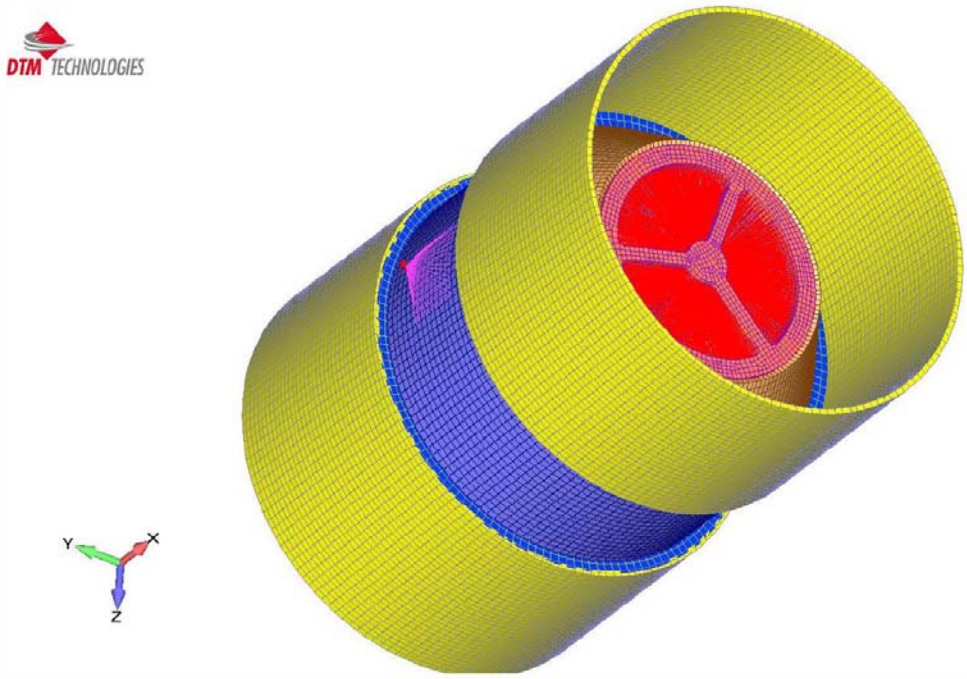

Figure 5.2-9: GG Spacecraft FEM model used for stiffness verification

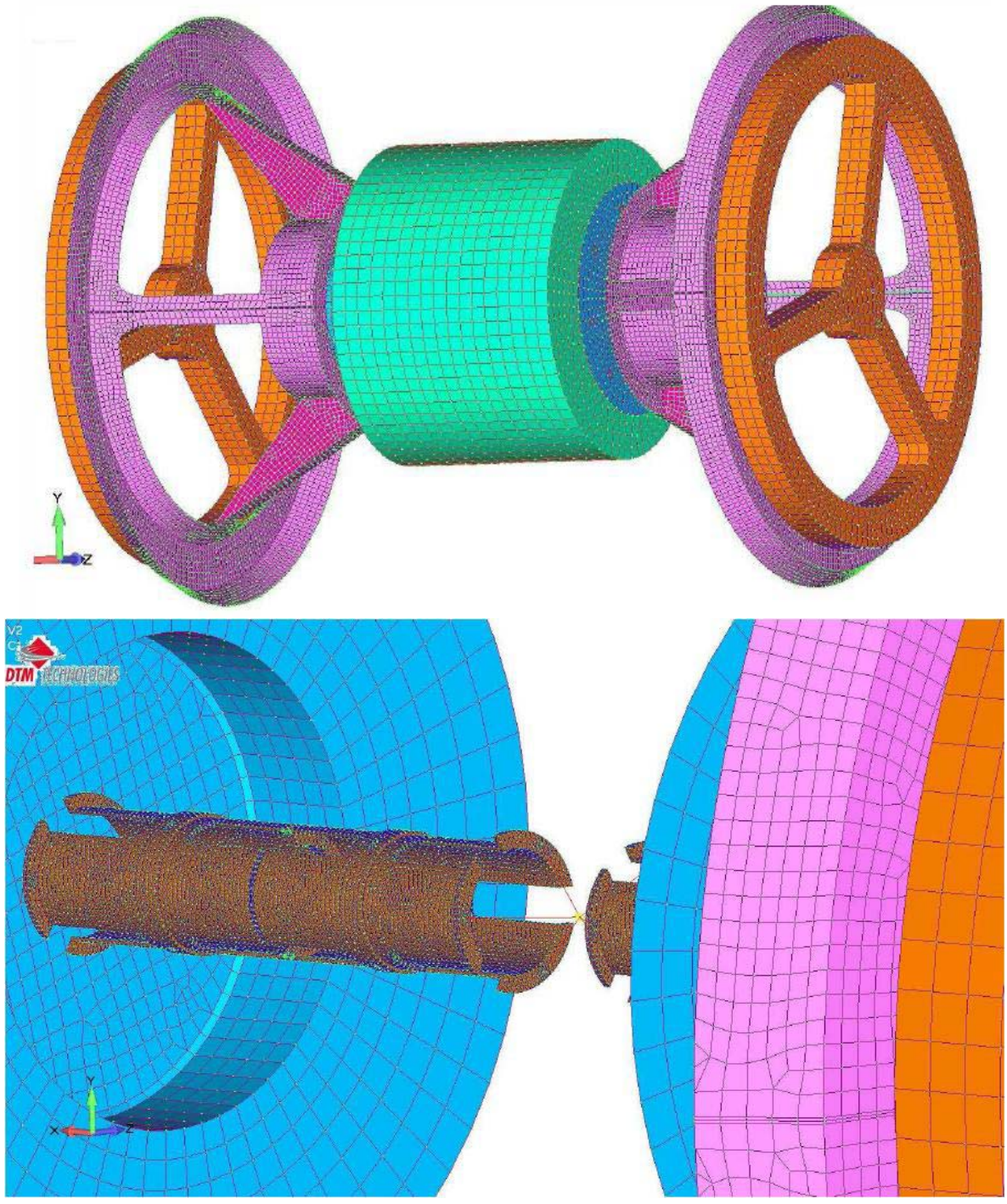

Figure 5.2-10: GG Spacecraft FEM model details

(a) PGB box and Spacecraft I/F (b) PGB shaft detail at proof masses location

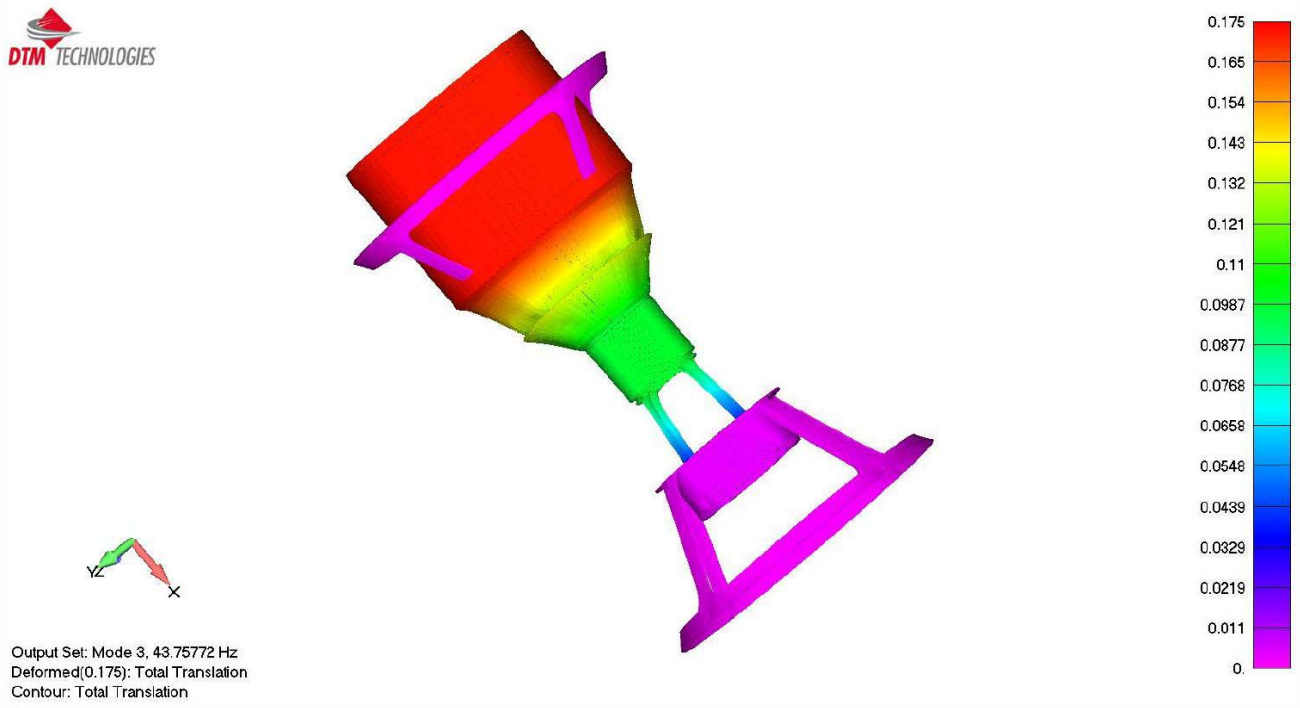

Figure 5.2-11: GG FEM Model first axial eigenfrequency (43.76 Hz)

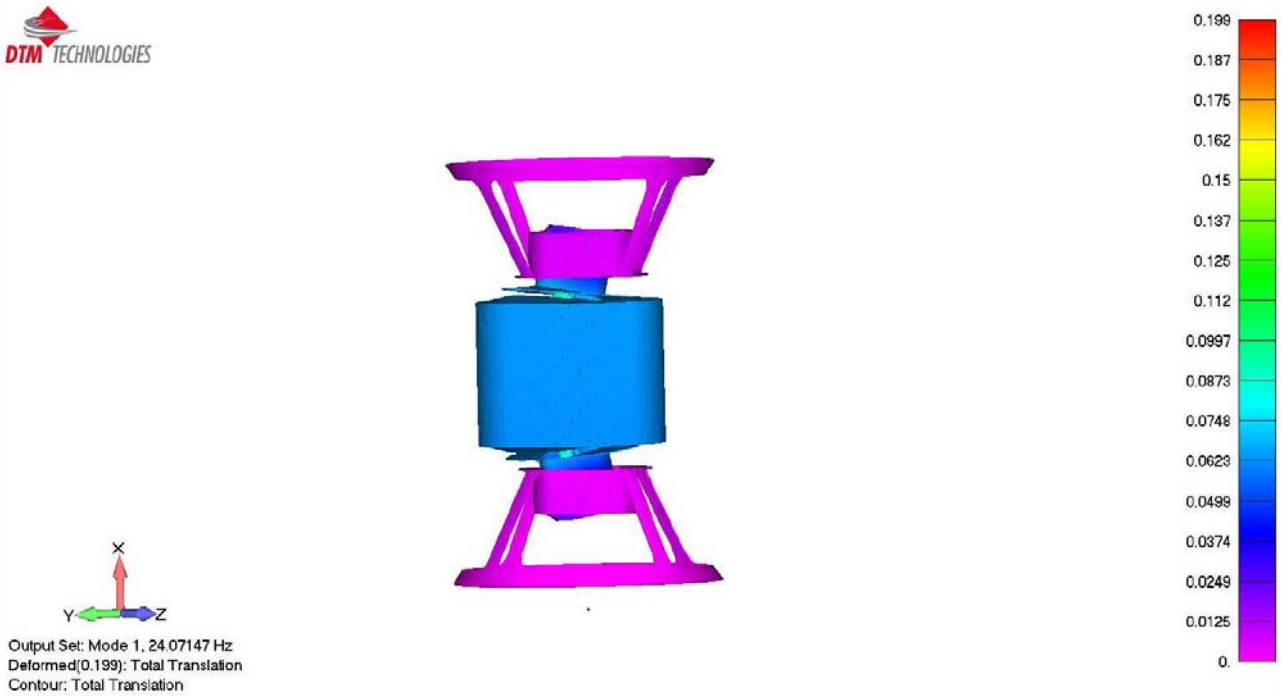

Figure 5.2-12: GG FEM Model first lateral eigenfrequency (24.07 Hz)

The dynamic behaviour of solar panels is also an important issue to be verified, due to their particular conformation (cylindrical shape, cantilevered on one side only); Figure 5.2-13 plots their first eigenfrequency, showing a significant stiffness (> 90 Hz), which is a very comfortable output at this stage of the GG program.

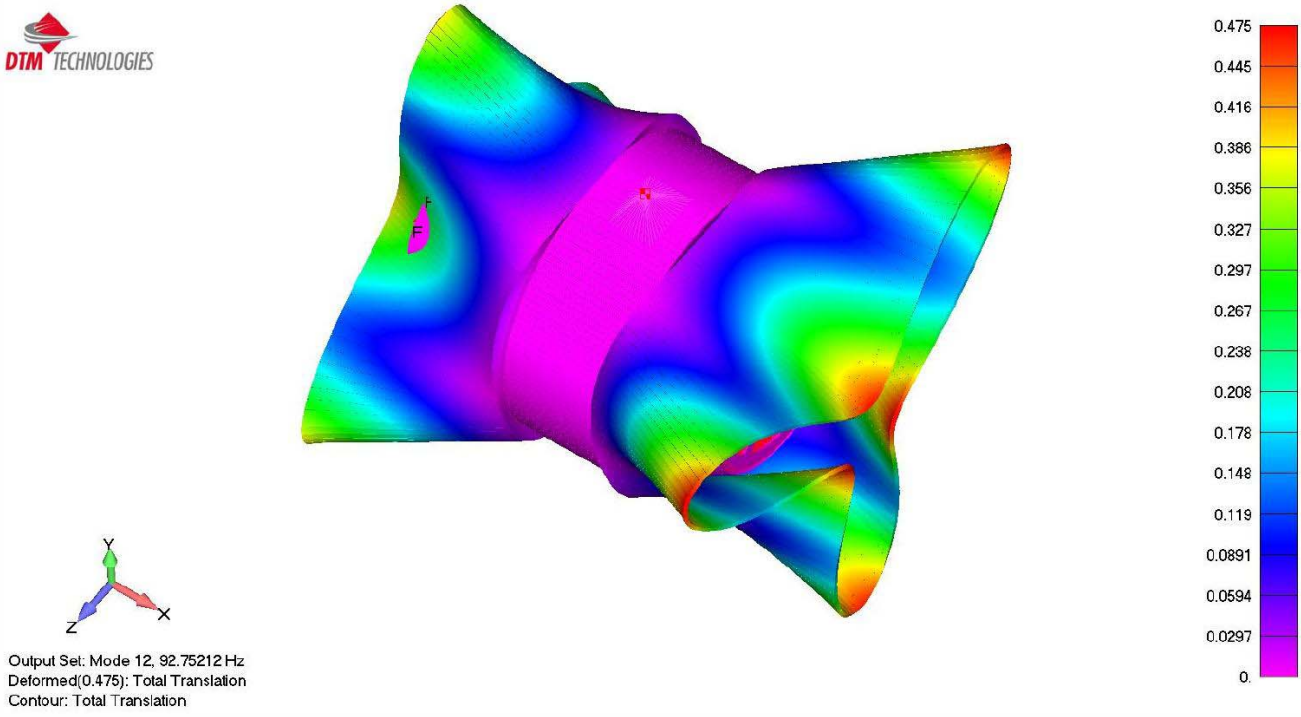

Figure 5.2-13: GG FEM model first solar panels eigenfrequency (92.75 Hz)

5.3 Thermal design and analysis

5.3.1 TCS requirements

The thermal requirements derive from the goal to maintain a thermal configuration able to perform the needed scientific measures. The high spin frequency value makes negligible the azimuthal temperature difference, while the axial effect shall be limited. Moreover it is important to maintain the temperature stable. The mechanical suspensions are sensitive to the temperature variation and this variation shall not degrade the common mode rejection of the mechanical suspension.

The following temperature requirements shall be met:

- test mass mean temperature stability better than 0.1°C/day;
- Axial temperature gradient at the level of the proof masses shall not exceed 1 °C/arm length;
- Temperature fluctuations in the proof masses shall not exceed 0.2 °C in 1 day;
- Linear temperature drift in the proof masses shall not exceed 0.2 °C/day.

As for the electronic units, the following temperature requirements were assumed:

- -20/+50 °C operating temperature;
- -30/+60 °C non operating temperature.

5.3.2 TCS description

A classical passive approach plus heaters has been selected:

The external side of the S/C will be covered by MLI blankets to counter the environment loads; painted radiators areas are distributed on the cylindrical structure following the footprint of the electronic boxes mounted inside the structural cylinder; solar arrays cells are placed on two dedicated cylindrical sections.

The internal side of the S/C will be black-painted as much as possible where power is generated (internal cylindrical section and electronic boxes) in order to minimize temperature gradients, while a low emissivity surface finish has been selected for both the external and the internal side of the PGB in order to radiatively decouple the payload from the remaining parts of the S/C.

Electronics are mounted on the internal cylindrical structure via thermal doublers/fillers to increase the baseplate contact conductance; the PGB is conductively decoupled as much as possible from the remaining parts of the S/C, and the core of the payload is connected to the support structures via Copper-Beryllium springs.

The use of standard electrical heaters to trim or maintain the necessary temperature levels; this solution will be limited to the electronic boxes area since no heaters are envisaged inside the PGB enclosure in order to limit oscillation and temperature disturbances to the test masses.

5.3.3 Mathematical model description

Geometrical Mathematical Model (GMM)

Esarad 6.2 has been used to build up the Geometrical Mathematical model and to run the radiative analysis. The GMM includes all the main structural elements, the payload components, and the equipments both inside and outside the S/C:

- Structural main cylinder, cones, flanges and payload support structures
- Internal electronic boxes
- PGB protective cylinder, I/F flanges and springs
- Payload internals: Mass 1, Mass2, Capacitive Plates, and support cylinders brackets and flanges
- External MLI blankets, sensors, antennas and Solar Arrays.

The following figures depict the modeled elements.

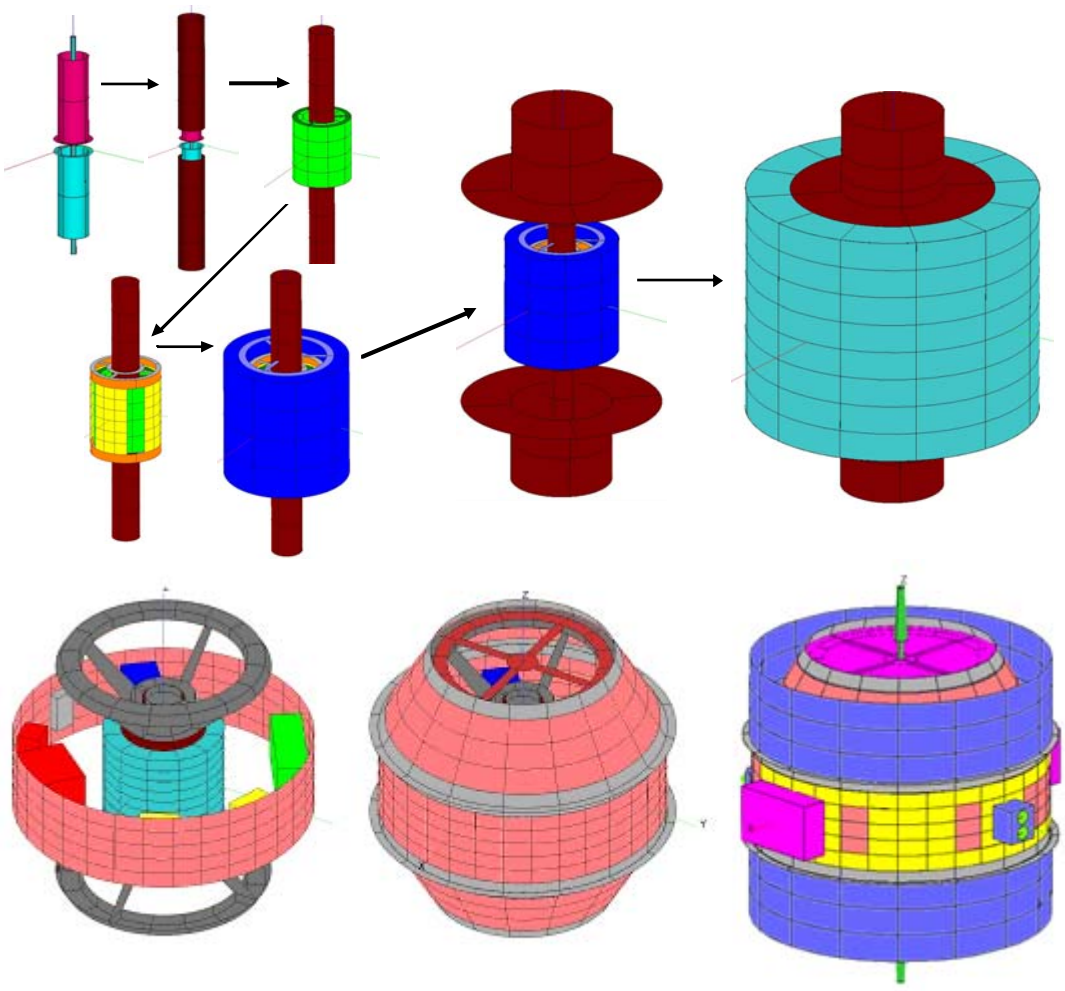

Figure 5.3-1: Overall GG Geometrical Mathematical Model component breakdown

The external radiative areas have been covered with a Silver Teflon tape and positioned only on the outer cylindrical structure panel in correspondence of the internal boxes arrangement.
The current radiative areas implemented in the geometrical model for each unit are reported in the following table.

Unit	Radiator area [m^2]
Battery	0.0222
PCE	0.0334
CDMU	0.1001
TRANSP 1	0.0334
TRANSP 2	0.0334
PCU	0.1557
Tot Radiative area [m^2]	**0.378**

Table 5.3-1: Radiator areas

A summary of the thermo-optical properties related to the surface finishes used in the Geometrical model is presented in the following table; solar absorptivity degradation due to cumulative exposition to external orbit environment has been taken into account

Surface finish	Solar Absorptivity Beginning of Life α BOL	Solar Absorptivity End of life α EOL	Emissivity ε	Note
MLI ITO Kapton	0.30	0.43	0.77	External Structure (Cylinder panel)
MLI Aluminised Kapton	0.14	0.14	0.05	External Structure (Cone panels)
Black paint Z306	0.96	0.96	0.88	Internal structure (panels), Units, Solar Array back side
Silvered Teflon tape	0.14	0.30	0.75	External Radiator
Bare aluminium	0.21	0.21	0.05	Internal Structure support
Solar Array Cell Side	0.75	0.75	0.82	Solar Array Cell
White Paint	0.23	0.65	0.88	Antenna
Gold finish	0.04	-	-	Test Masses 1 & 2 Capacitive Plates

Table 5.3-2: Thermo-optical properties

The GG mission analysed is a circular equatorial orbit around the Earth with an altitude of 520km and an orbit inclination of 0°.

The satellite spins around its Z-axis at a rate of 1Hz and the attitude considered is with Z-axis (spin axis) normal to orbit plane.

The orbital cases analysed have been essentially selected through the variation of the environmental parameters and in particular:

- Sun Aspect Angle
- Solar Fluxes
- Albedo coefficient
- Earth emitted Infra Red

The SAA aspect angle considered varying from 0° (spin axis normal to Sun direction) to 28.5°, which includes the maximum Solar declination (23.5°) and the maximum angle of the spin axis to the orbit normal, estimated in 5°.

Solar Fluxes are computed considering the extreme values of Solar constant over the year, that correspond to 1315 W/m² at Summer Solstice, and 1420 W/m² at Winter Solstice.

Albedo and Earth IR have been assumed for a typical orbit inclination of 0°.

Orbit case	Cold Case Beginning of Life	Hot Case End of Life	Hot Case End of Life
Earth-Sun distance	152.1 E06 Km	149.6 E06 Km	149.6 E06 Km
Sun temperature	5770 K	5770 K	5770 K
Solar Aspect Angle	0°	0°	28.5°
Inclination	0°	0°	0°
Orbital altitude	520 Km	520 Km	520 Km
Orbital period	5699.35 s	5699.35 s	5699.35 s
Solar Constant	1315 W/m²	1420 W/m²	1420 W/m²
Earth albedo factor	0.18	0.28	0.28
Earth temperature	251 K	263 K	263 K
Attitude	+Z normal to orbit plane	+Z normal to orbit plane	+Z normal to orbit plane
Number of orbital positions	12	12	12
Spin rate	360 deg/s	360 deg/s	360 deg/s
Spin results averaged over	12 positions	12 positions	12 positions

Table 5.3-3: Orbit and Attitude properties

Thermal Mathematical Model (TMM)

The GG's Thermal Mathematical Model (TMM) has been built with Esatan (version 10.2) software and contains all the thermal node definition, the thermal conductivity network and the internal dissipations and thermal loads (unit power and heater dissipation) applied to the relevant thermal nodes.

Ref.	Element	Material	Thermal conductivity	Heat capacity	Density	Comments
1 2 3	Structural panels: ○ cylinder ○ cones ○ solar arrays	Honeycomb	K_{XY}=7.06 W/m/K K_Z=1.34 W/m/K	900 J/kg/K	2.5 Kg/m^2	Al skin 2*0.4 mm Al core 15 mm
4 5 6 7 8 9	Structure: ○ rings ○ flanges ○ PGB I/F ○ Payload support structures ○ S/C launcher I/F Payload: ○ brackets, flanges, support cylinders (M1, M2, Capacitive Plates)	Al 7075	150 W/K	900 J/kg/K	2700 Kg/m^3	
10	Mass 1	Tungsten	167 W/m/K	142 J/kg/K	19653 Kg/m^3	
11	Mass 2	Polyethylene	0.33 W/m/K	2301 J/kg/K	941 Kg/m^3	
12	Capacitive Plates	Cu	390 W/K	380 J/kg/K	8920 Kg/m^3	
13	Propellant tanks	Ti	10 W/K	520 J/kg/K	4500 Kg/m^3	
	MLI blankets	20-layer	temperature dependent	0	0	

Table 5.3-4: Materials thermal properties

The Unit power dissipations considered for the thermal analysis take into account, for each orbit, the maximum value of power dissipation when the S/C is exposed to Sun fluxes, while the minimum value is considered during the eclipse phase.
The operating Transponder (TRSP2) in Sun Phase is maintained at 20W of dissipation for 10 minutes per orbit and then set at 6W of dissipation for remaining orbit duration.

A summary of the configuration used is given in the following table:

Node	Unit	Power in Sun	Power in Eclipse	Remarks
		[W]	[W]	
101	BATTERY	11	0	
102	SRS	1	0	
103	PGBE	23	0	
104	CDMU	45	14.4	
105	TRSP2	20 / 6 (1)	6	(1) 20W for 10min/orb 6W for 85min/orb
106	RFDN	0	0	
107	TRSP1	6	6	
108	PCU	55	14	
74000	EPSA1+PPCU+NEUTRAL	30	0	
75000	EPSA2+PPCU+NEUTRAL	30	0	
	ECE (2)	4	4	(2) Power assigned to internal cylinder support node PGB (TMM node 2705)
	Total Power dissipation	**225 / 211**	**44.4**	

Table 5.3-5: Units power dissipations

5.3.4 Analysis results

Thermal analysis cases have been performed identifying the sizing cases in accordance to environment parameters.

The Hot case analysed to size the dimension of the radiators' area, has been computed considering the environment parameters with the Sun closest to the Earth (at Winter solstice) and Albedo and Earth radiation considered at their maximum values. In addition the thermo-optical properties of surfaces are at End of Life at their largest absorptivity.

The Cold case analysed to assess the heater power consumption needed to maintain the unit above their minimum operative limit, has been performed with Sun farthest from the Earth (at Summer Solstice), and Albedo and Earth radiation considered at their minimum values. Thermo-optical properties of surfaces are at Beginning of Life at their smallest absorptivity.

Transient analysis have been performed in order to evaluate the temperature variations along a series of orbit cycles, (sun + eclipse phase) and provide evidence that all equipments temperature remain within temperature design ranges; moreover also stability criteria on test masses temperature fluctuations and gradients shall be guaranteed within defined temperature requirements.

Two different main configurations have been considered for thermal cases, according to the finish of the PGB internal structure (support cylinders, flanges, arms) and support to the cone, that have been considered respectively with a low emissivity finish (ε ≤ 0.05) or a high emissivity value (Black Paint ε=0.88). The purpose is to assess how different thermal finish may affect the temperature stability and gradient requirements on internal masses; with a configuration considering low emissivity thermo-optical properties the PGB internal enclosure is highly isolated from the rest of the satellite, which is positive factor in terms of temperature stability on test masses regardless external environment variations, but on the other hand the high time constant of the PGB could lead to a very long time needed to reach a stable temperatures inside the PGB itself. In particular this condition could occur at the very beginning of the operative phase and anytime the satellite should recover its control from a failure case.

A summary of the analysis cases is given in the following table:

Case ID	Description	Remarks
1	BOL environment and thermo-optical properties – **SAA=0°** PGB MLI cover: Aluminium finish (ε=0.05) PGB internal structure: low emissivity (ε ≤ 0.05) Heater power applied on internal units	Heater sizing Minimum temperature verification
2	EOL environment and thermo-optical properties – **SAA=0°** PGB MLI cover: Aluminium finish (ε=0.05) PGB internal structure: low emissivity (ε ≤ 0.05)	Radiators sizing Maximum temperature verification
3	BOL environment and thermo-optical properties – **SAA=0°** PGB MLI cover: Aluminium finish (ε=0.05) PGB internal structure: Black Paint finish (ε=0.88) Heater power applied on internal units	Heater sizing Minimum temperature verification
4	EOL environment and thermo-optical properties – **SAA=0°** PGB MLI cover: Aluminium finish (ε=0.05) PGB internal structure: Black Paint finish (ε=0.88)	Radiators sizing Maximum temperature verification
5	EOL environment and thermo-optical properties– **SAA=28.5°** PGB MLI cover: Aluminium finish (ε=0.05)	Radiators sizing Maximum temperature verification

	PGB internal structure: low emissivity (ε ≤ 0.05)	
6	EOL environment and thermo-optical properties– **SAA=28.5°** PGB MLI cover: Aluminium finish (ε=0.05) PGB internal structure: Black Paint finish (ε=0.88)	Radiators sizing Maximum temperature verification

Table 5.3-6: Analysis cases for sensitivity

Typical temperature profiles of units and masses are reported in the following plots (referred to case 1).

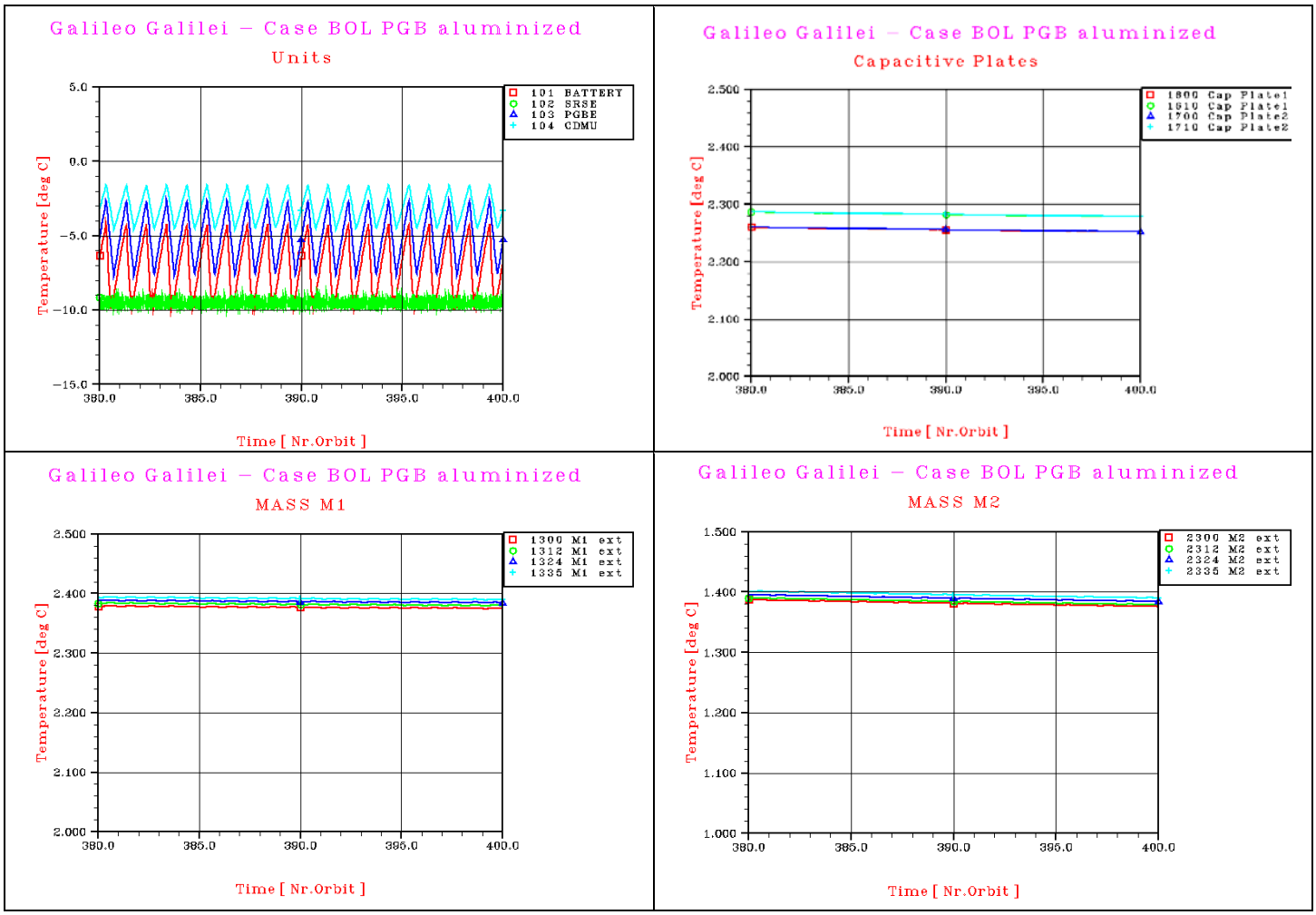

Figure 5.3-2: Thermal analysis results: typical temperature profiles

The thermal requirements are met in all cases analyzed. The maximum values are reported in the table below.

Requirement definition	Max value by analysis	Requirement value
Test Mass mean temperature stability	0.0237 °C/day	<0.1 °C/day
Temperature fluctuations in the proof masses	0.00484 °C/day	<0.2 °C/day
Linear temperature drift in the proof masses	0.02309 °C/day	<0.2 °C/day
Axial temperature gradient	0.94 °C/arm	<1 °C/arm

Table 5.3-7: Comparison of thermal analysis results with the requirements

Heater power control will be commanded through dedicated heater circuits generally controlled on a “ON-OFF logic” between temperature thresholds based on automatic control via CDMU at the minimum “operating/non operating” temperature thresholds.
The heater power request to control the unit temperature during the cold cases is around 16 W.

5.3.5 Conclusions

According to the thermal analysis results, a passive thermal control is sufficient to maintain the satellite and equipment within temperature ranges applicable to the operative status for all mission phase; moreover also the stability criteria (Mass fluctuations, drift and mean temperature requirements), and gradient temperature on Shaft arms are well satisfied within the limits required.

The temperature of all internal equipments are maintained within assumed operative temperature ranges (-20°/+50°C) in all cases analyzed with relevant margins to high limits temperature; the actual temperature level could allow to reduce the size of the radiators on the cylindrical structure still maintaining the internal equipment within their temperature limits.

At the current level of analysis the heater need is foreseen only in Cold conditions (BOL property and minimum Solar Constant level) with a requested heater load of 16 W.

The stability criteria are well satisfied within the requested limits.

Use of black paint inside the PGB (masses and plate excluded) makes the payload elements more sensitive to the external disturbances; on the other hand, black paint allows the internal components of the payload to approach the equilibrium conditions faster.

Power dissipation inside the PGB on ECE, should be minimized, as it affects the performance in terms of gradient inside PGB; with the actual thermal design the axial temperature gradients on shaft arms is still maintained below the requirement, but an eventual increase of power dissipation on the ECE will lead to exceed the requirement itself.

Due to the high decoupling of the internal payload from the rest of the S/C, long times are needed to approach the equilibrium temperatures, even if the temperature variations during this time are within the requirements. A more detailed analysis will be necessary to assess the time constant of the system.

MLI, structural elements and solar panel temperatures show normal temperature levels and are of no concern.

5.4 Electrical Architecture

Figure 5.4-1 shows the GG electrical system architecture, comprising both payload units and service module units.

The Payload Electronics is composed by two major subsystems:

- PGB Control and Processing Electronics (CPE)
- Experiment Control Electronics (ECE).

The PGB Control and Processing Electronics, located on the spacecraft platform, manages PGB motion control (whirl sensing, whirl damping) and the processing of all signals coming from the test masses (motion control and EP sensing). Moreover, the CPE performs:

- TC reception from spacecraft and decoding;
- execution of payload timelines and commands;
- Science data collection, compression and formatting;
- Formatting of TM packets and their transmission to the spacecraft.

The Experiment Control Electronics, housed inside the PGB, communicates with the CPE via an optical link. It performs readout of the EP chain and, under control by the CPE processor, manages locally the whirl sensing and damper activation.

The service module electrical architecture includes:

- On Board Data Handling
- Electrical Power System including PCDU, solar array and battery.

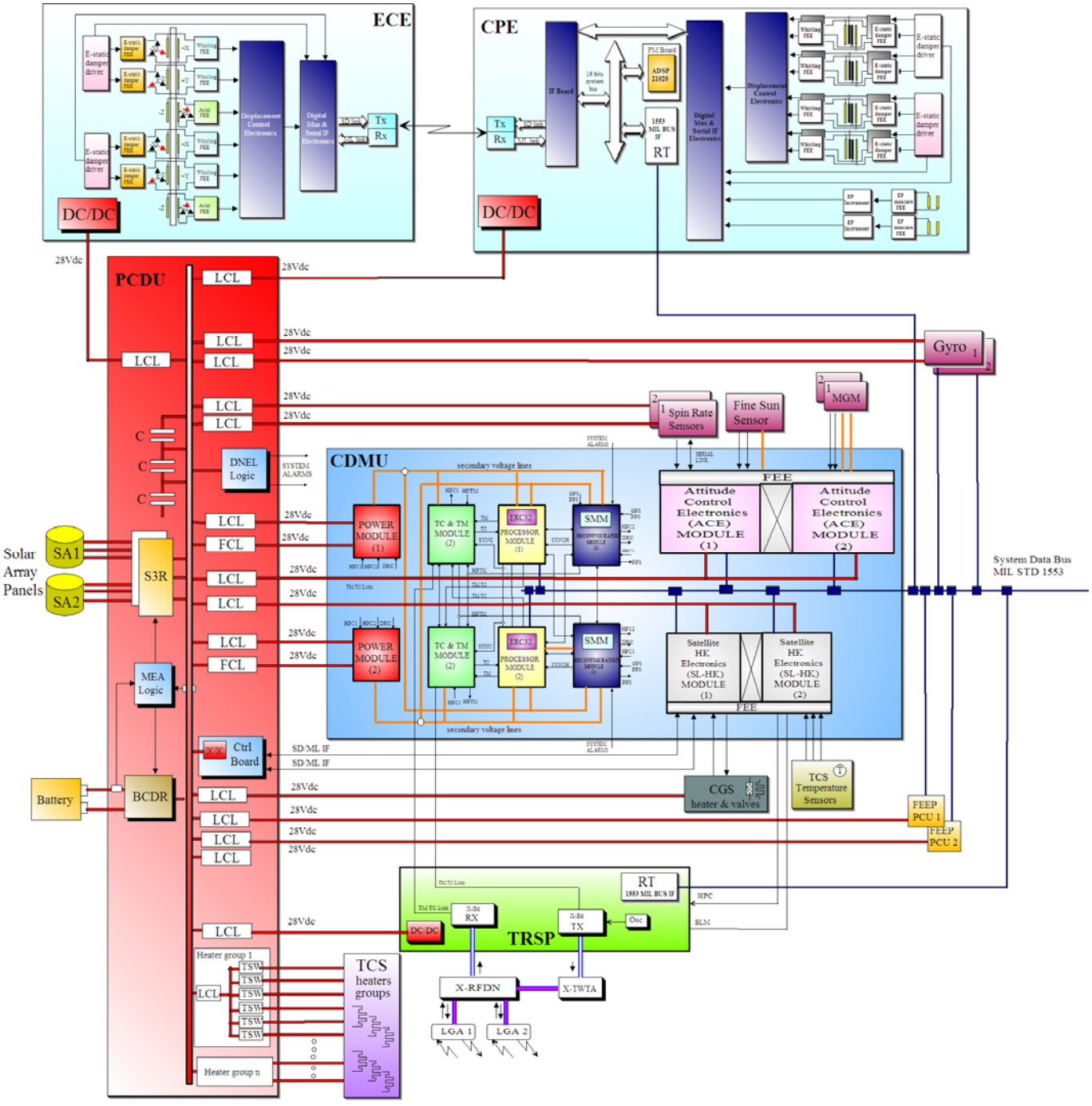

Figure 5.4-1: GG electrical architecture block diagram.

5.5 On-board data handling design

The CDMU acts as the central communication node between the Spacecraft and the active Ground Station, distributing or executing commands received from ground and collecting, formatting and transmitting the satellite telemetry.

The CDMU provides: telecommand acquisition, decoding, validation and distribution; scientific and HK data acquisition and storage; distribution of time reference signals for the Central Reference Time generator and synchronization with the local timers of the other processors; autonomy supervision and management.

Within the centralized CDMU computer, all the application software will be executed, including the software implementing the AOCS and drag free control algorithms.

The CDMU provides a number of discrete telecommand lines for reconfiguration purposes. It provides condition inputs for discrete telemetry lines which will be used for housekeeping, to acquire status monitors and temperatures from the Thermal Control sensors. Power to Thermal Control heaters is provided by the PCDU, under CDMU commands received on the 1553 bus.

Decoding and validation of telecommands uplinked from ground is performed by the TC decoder embedded in the CDMU. A set of High Priority Commands is available to command directly the end users from the decoders, by-passing any on board processor. These commands are used for time critical functions such as activation/deactivation of units, on board computers re-initialization, back-up initiation of post-separation sequences.

The CDMU includes a Reconfiguration Module, functionally independent from the Processor Module and the On Board Software, capable of processing some alarm signals via dedicated links and of commanding directly the end users via the High Priority Commands.

Moreover, the CDMU will be equipped with internal power supply dedicated boards, based on standard FPGAs (Actel RTSX), to drive all the required mechanisms and actuators. Finally, the box will implement an acquisition module dedicated the internal HK and the conditioning of the sensors and acquisition needed to control the mechanisms.

The GG on-board data handling system will be based on a single CDMU, derived from the standard LEONARDO unit, developed via the ASI PRIMA program and based on an ERC32 CPU (Figure 5.5-1 and Figure 5.5-2). A dedicated CPU board, equipped with LEON2FT processor, based on a standard ASIC, is under qualification by TAS-I. If necessary this board could replace the ERC processor board.

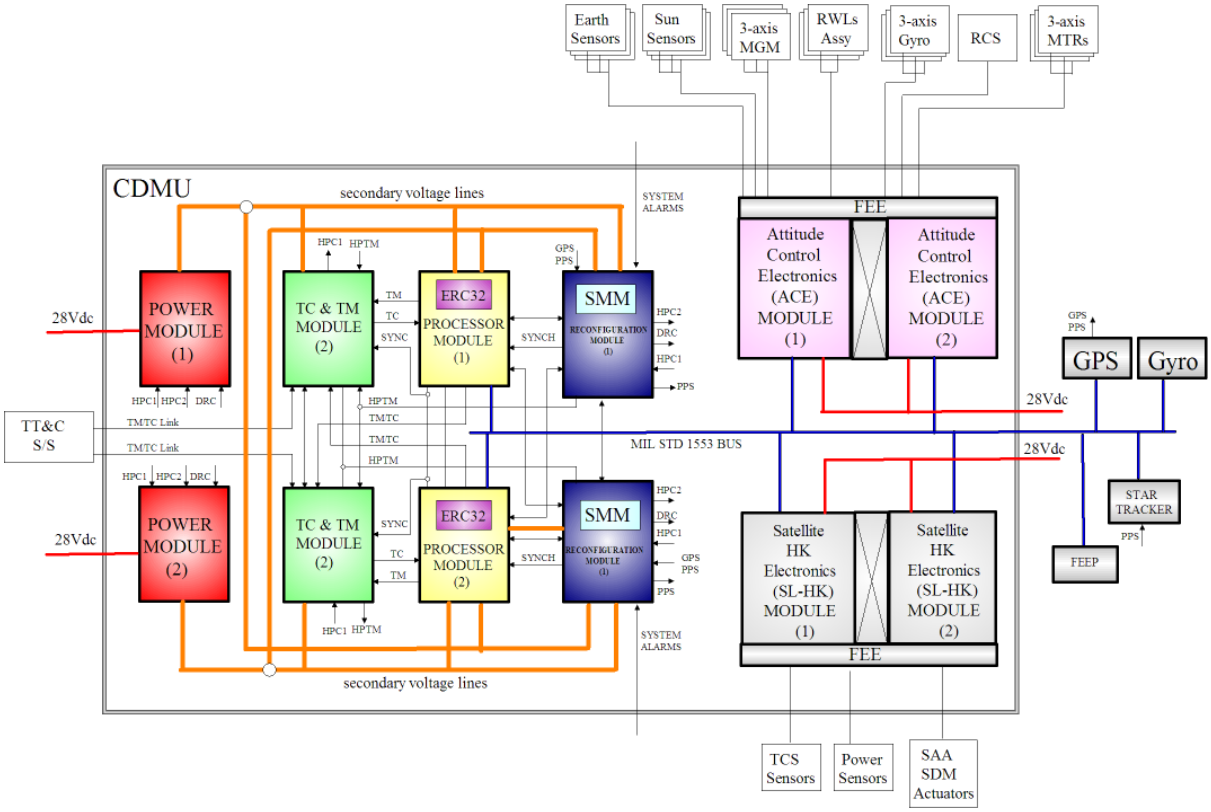

Figure 5.5-1: Functional block diagram of a generic CDMU based on TAS-I heritage.

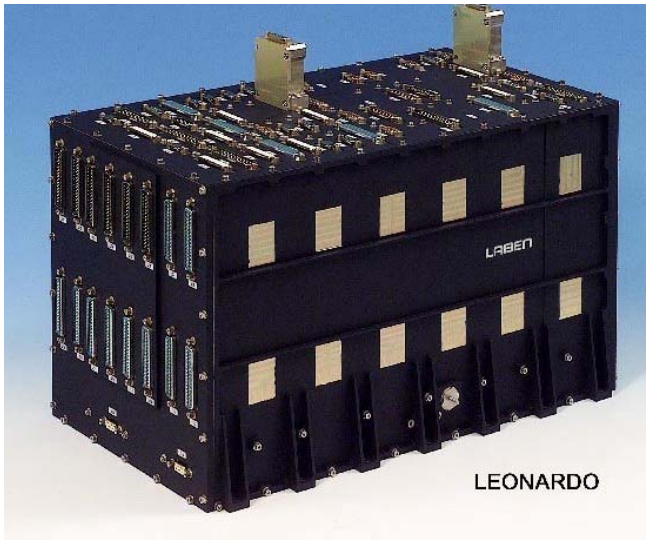

Figure 5.5-2: "Leonardo" CDMU

The CDMU includes the Mass Memory devoted to science and HK data storage.

The housekeeping data rate is estimated to be equal to 10 kbps whereas the estimated Science data rate, including payload housekeeping, is 12.7 kbps (see Table 5.8-5). The total data rate including 20% packet overhead is 27.2 kbps. The total amount of data produced in 1 orbit is 155 Mbit. An on board mass memory sized for 24-hour autonomy amounts to about 2.4 Gbit.

The mass, dimensions and power consumption of the GG CDMU are estimated from the example of the SMU-Prima computer used in Cosmo and Radarsat. The proposed CDMU for GG will include the following main components:

- 2 Processor boards (1 main + 1 cold redundant)
- 2 Reconfiguration boards (1 main + 1 hot redundant)
- 2 TMTC boards (1 main + 1 hot redundant)
- 2 ACE IF & HK boards (1 main + 1 redundant co-strapped)
- 2 Power boards (1 main + 1 cold redundant)
- 1 Mother boards
- Internal harness
- Box and connectors.

The mass memory is implemented by an optional module of the PRIMA platform family, internal to the SMU, the LMM. Each LMM implements a mass memory capability up to 2 Gbyte. Two LMM boards are used in GG.

The CDMU budgets are as follows:

- Configuration : 11 boards
- Dimensions : 380x280x220 mm
- Weight : 17 kg (including 20% contingency)
- Power consumption: 19.8 W (including 10% contingency).

5.6 Electrical power system design

The Electrical Power System (EPS) is implemented by a dedicated Power Distribution and Control Unit (PCDU), plus power generators and a battery.

The EPS is required to provide around 520W for both payload and S/C equipment, constantly along the whole mission duration of 2 years.

A fully regulated 28V power bus is adopted, compliant with the ESA power standard, under the assumption that the payload electronics only allow operation in a limited range of bus voltage variation. This design also increases the power conversion efficiency in the EPS system and reduces EMC noise.

For the Solar Array power regulation, either an S3R regulator or an MPPT regulator could be considered. An S3R regulator design is preliminarily assumed, considering its simple operation (constant attitude to the sun), the simplicity and robustness of the design and the good flight heritage. By regulating the number of SA sections connected to the bus, the bus is controlled to be at fixed voltage value.

In series to the S3R regulator there are two buck DC/DC converters, providing the required 28 V power bus voltage conversion and regulation using a majority voted Main Error Amplifier (MEA).

Taking into account the regulated bus topology, a single BCDR module can be implemented, consisting of two power regulators, a Battery Charge Regulator (BCR) and a Battery Discharge Regulator (BDR).

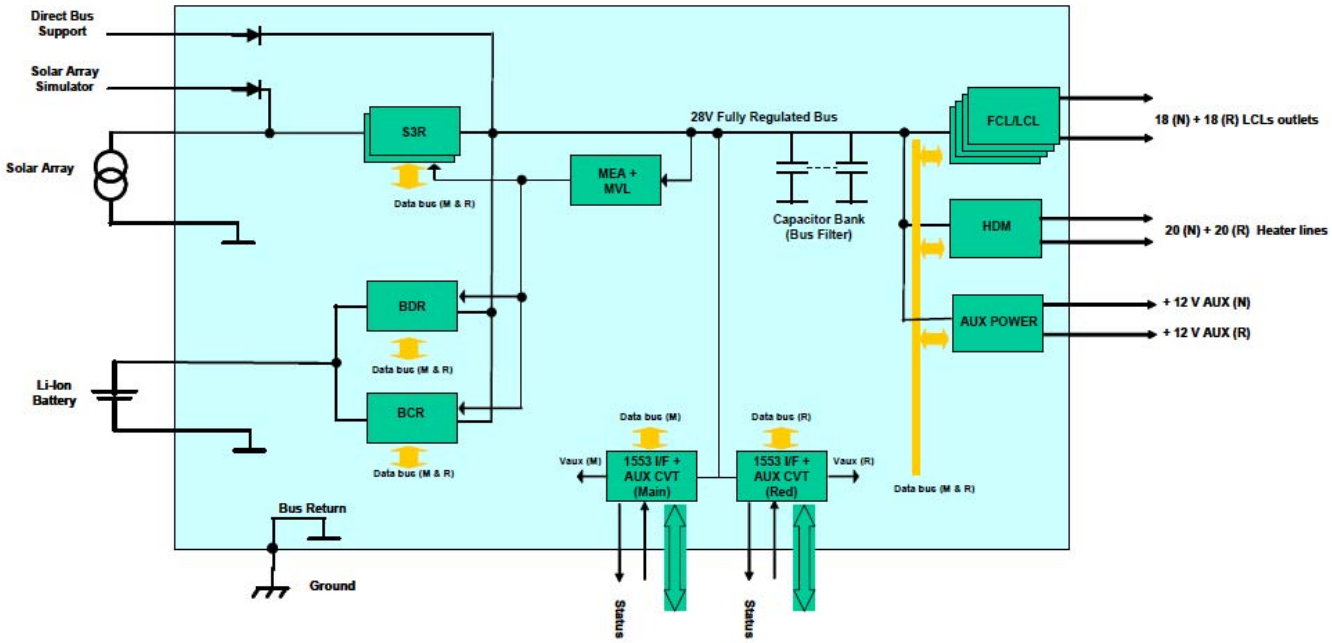

Figure 5.6-1: Functional block diagram of the proposed PCDU

5.6.1 PCDU

The functional block diagram of the proposed PCDU is reported in Figure 5.6-1. The PCDU provides the following functions:

- it controls the electrical power generated by the solar array;
- conditions the energy stored in the battery when required;
- controls, monitors and maintains the health of the EPS;
- distributes power to the scientific instruments and spacecraft equipment;
- protects the power bus from external faults and prevents failure propagation;
- provides heater switching control in response to commands;
- interfaces for AIV and Launch support EGSE.

The proposed modular PCDU, derived from the ASI PRIMA PCDU (SMU) design, has the following features.

- 28V regulated Power Bus
- Up to 700 W distributed power
- At least 4 I/F with independent Solar Array sections and 1 Li-Ion Battery
- S3R concept
- 1553 MIL bus TM/TC I/F

Outputs types: FCL (Fold-back Current Limiters), LCL (Latching Current Limiters) and Heater switches.

The foreseen PCDU redundancy concept implements a single-failure tolerant design:

- S3R sections redundant (4 diodes in series and 2 shunt transistors)
- 2 BDR regulators operating in parallel configuration (hot redundancy) dedicated to the discharge of the battery, each sized to manage the full battery power.
- 2 BCR regulators operating in parallel configuration (hot redundancy) dedicated to the charge of the Battery, each one sized to manage the full battery charge power
- 28V Bus Filter Capacitor implemented with self-healing capacitors (one capacitor failed in open circuit is considered).
- A triple redundant MEA with a Majority Voting Logic (MVL) circuit to control the 28V bus regulation control loop.
- 2 TM/TC modules with relevant Auxiliary Power Supply (APS) operating in hot stand-by redundancy (both modules ON at PCDU power up). Each interface will be capable to manage all the PCDU functions, main and redundant (full cross-strap) and it will be switched ON/OFF by direct pulse commands.

The PCDU will include the following main boards:

- 2 TM/TC I/F modules.
- 4 LCL modules.
- 1 HDM modules.
- 1 MEA + CB module.
- 2 S3R modules.
- 1 BDR modules.
- 1 BCR module.
- 1 AUX 12V module.

The following table summarizes the main characteristics of the PCDU boards.

Module / Board	Modules N°	Main Allocated Functions
TM/TC	2	1 Main + 1 Red. Each module includes: • 1553B data bus I/F. • Discrete TM/TC I/F. • Internal I/O features. • APS
LCL	4	Each module includes up 16 Low Power Latching Current Limiters (LCLs)
MEA + CB (28V)	1	28V bus filter capacitor + MEA function with 2/3 MVL.
S3R	2	4 redounded S3R sections per module.
BDR	1	2 regulators per module. Each regulator is self-standing including auxiliary power supply, input/output protections and TM/TC I/F.
BCR	1	2 regulators per module. Each regulator is self-standing including auxiliary power supply, input/output protections and TM/TC I/F.
HDM	1	Includes up to 40 switches divided into 8 groups of 5 switches.
12V auxiliary supply	1	Includes 2 independent DC\DC converters.
Mother Board	1	Interconnection of signal (TM/TC) and auxiliary voltages.

Table 5.6-1: PCDU boards

The PCDU budgets are as follows:

- Configuration : 13 boards
- Dimensions : 246 (H) x 358 (W) x 265 (L) mm
- Weight : 13,5 kg (+/-10% kg of contingency)
- Power Consumption : 22,2 W without SA regulation and 39,2 W with SA regulation.

Figure 5.6-2 shows a typical unit, similar to the proposed PCDU.

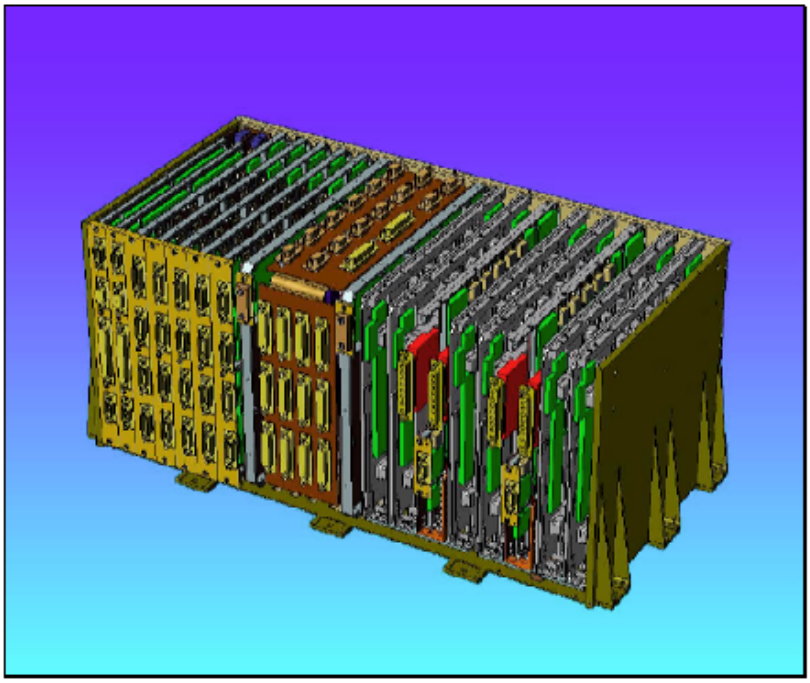

Figure 5.6-2: PCDU unit considered for GG

5.6.2 Battery

The battery provides a store for the excess solar array energy, and a source of energy whenever there is insufficient power from the array (e.g. during launch, transient power demands and eclipse periods). The selected equatorial orbit leads to eclipse on every orbit with duration of about 36 minutes over a period of 95 minutes.

The Sony 18650HC Li-Ion cell technology is considered for the battery (see Table 5.6-2).

Parameter	Value
Sony Cell Type	18650
Dimensions	∅ 18 mm 65 mm
Mass	40.5 grams
Maximum Cell Voltage	4.2 V
Minimum Cell Voltage	2.5 V
Total Cell Capacity	1.5 Ah
Nameplate Cell Energy	5.4 Wh
Nameplate Specific Cell Energy	133 Wh/kg
Nameplate Volumetric Cell Energy	318 Wh/litre
Typical standard deviation of capacity within a batch	*< 0.4% of cell total capacity*

Table 5.6-2: Characteristics of the Sony 18650HC Li-Ion cell

The proposed concept for the battery of GG uses small cells each with a total capacity of 1.5 Ah. These are assembled into units that we refer to as modules. The basic electrical concept for a modular battery consists of an array of cells connected in series strings to achieve the correct operating voltage range. Multiple strings are then wired in parallel to produce a specific battery capacity. This series then parallel arrangement of cells is known as 's-p' topology. Due to the low cell capacity of the Sony mass produced cells, the capacity of the battery can therefore be incremented in small stages to optimise a battery performance to suit specific applications.

The following figure shows the concept proposed.

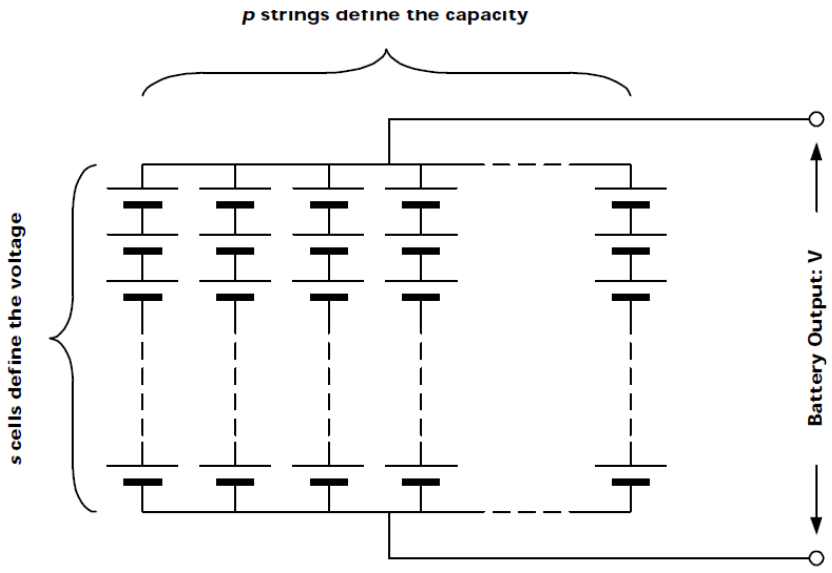

Figure 5.6-3: 's-p' battery cell topology

Additionally, each Sony Li-ion cell contains in-built safety mechanisms that prevent hazardous results from severe battery abuse, or cell failures. The safety mechanisms consist of an overcharge disconnect device, a pressure release vent and a Poly-switch Positive Temperature Coefficient (PTC) element. The following figure shows the overcharge protection mechanism design.

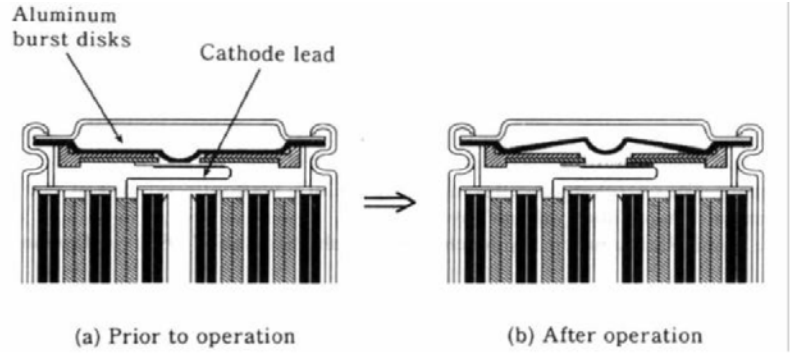

Figure 5.6-4: Battery overcharge protection mechanism

The battery sizing case is satellite supply during the eclipse phases. The selected equatorial orbit implies the presence of an eclipse at every orbit with duration of about 36 minutes for each orbit period of 95 minutes.

The battery has been sized limiting the DoD within 30% and assuming during the charge and discharge phases the following worst case power scenario:

- **288 W** of power demand (including BDR efficiency of 95%) during the eclipse period of 36 minutes
- **180 W** of available power (including BCR efficiency of 95%) during the sun period of 59 minutes.

The calculated battery characteristics under the assumptions listed above are the following:

- Capacity of 60 Ah
- Energy 1728 Wh @3,6V
- Configuration: 40p8s
- Mass: 18 kg (including 10% maturity margin)
- Dimensions: 200mm x 220mm x200mm.

5.6.3 Solar array

The GG Solar Array consists of two identical cylindrical panels, each connected to the satellite structure by means of mounting inserts. The panels are used to generate the power necessary to supply the S/C and P/L electronic units and heaters during the sunlit period, while spinning at 1 Hz.

The Solar Array is based on 3G GaAs/Ge Triple Junction solar cells, produced by AZUR Space, with 28% class efficiency (Table 5.6-3). The cell protection diode used is Si planar by-pass diode (SIBD) as reported in Table 5.6-4.

The substrate of each solar panel will be a cylindrical panel composed by Carbon Fibre skin and Aluminium honeycomb. It will includes a film polymide layer (Kapton) bonded to the front side to provide electrical isolation of the solar cells circuits. Grounding between front and rear sides will be ensured.

The Solar Array panels have been sized to sustain with some design margin the load power demand of 509 W during the sun period, including a power request of 180 W for recharging the battery, and assuming 95% BCR efficiency.

AZUR SPACE 3G28 – Covered Interconnected Cell				
Configuration of the Power Generating Element	**Unit**	**Selected solar cell**		
Type of cell		InGaP/GaAs/Ge MOCVD growth. Every solar cell is protected against reverse bias by an external Si diode		
Selected Dimensions	mm	40 × 80 with cropped corners		
Solar cell active area	cm^2	30.18		
Thickness	µm	140 ± 20		
Interconnect		Ag plated Invar		
Protection cover		CMG 100 AR		
Glass adhesive		DC 93-500		
MAX weight	g	3.7		
Electrical characteristics AM0, 28°C, 1353 W/m²				
I_{SC}	mA/cm²	16.57		
V_{OC}	mV	2685		
I_{PMP}	mA/cm²	15.93		
V_{PMP}	mV	2389		
Remaining factors (qualification data)				
		BOL	5.0E13 1MeV e^-/cm^2	1.0E14 1MeV e^-/cm^2
RV_{OC}	[#]	NA	0.989	0.980
RI_{SC}	[#]		0.997	0.994
RV_{PMAX}	[#]		0.990	0.981
RI_{PMAX}	[#]		0.999	0.997
RP_{MP}	[#]		0.989	0.978
Temperature coefficients (qualification data)				
		BOL	5.0E13 1MeV e^-/cm^2	1.0E14 1MeV e^-/cm^2
dI_{SC}/dT	µA/°C	0.30	0.34	0.34
dV_{OC}/dT	mV/°C	-5.9	-6.03	-6.05
dV_{PMAX}/dT	mV/°C	-6.1	-6.13	-6.15
dP_{max}/dT	µW//°C	-2.5	-2.6	-2.6

Table 5.6-3: Solar cell characteristics

AZUR SPACE SIBP diode		
Electrical characteristics @ 28°C		
V_{DTO}	V	< 0,8 @ 1.2 A direct current
I_{LEAK}	µA	< 10 @ dark conditions, 3.5 V

Table 5.6-4: By-pass protection diode characteristics

The cells are organized in strings to achieve the required voltage, but as the current delivered by each string is limited by the least illuminated cell, it is necessary to grant constant illumination over the entire string in order to both optimize the power conversion efficiency and minimize cell degradation. Cells shall be stacked vertically on the cylinder surface to form strings. The length of a single cell determines how many such stripes can be disposed while the height limits the number of cells per string.

The Solar Array Panels consists of two identical cylindrical panels each equipped with 74 strings of 15 cells connected in series as shown in Figure 5.6-5.

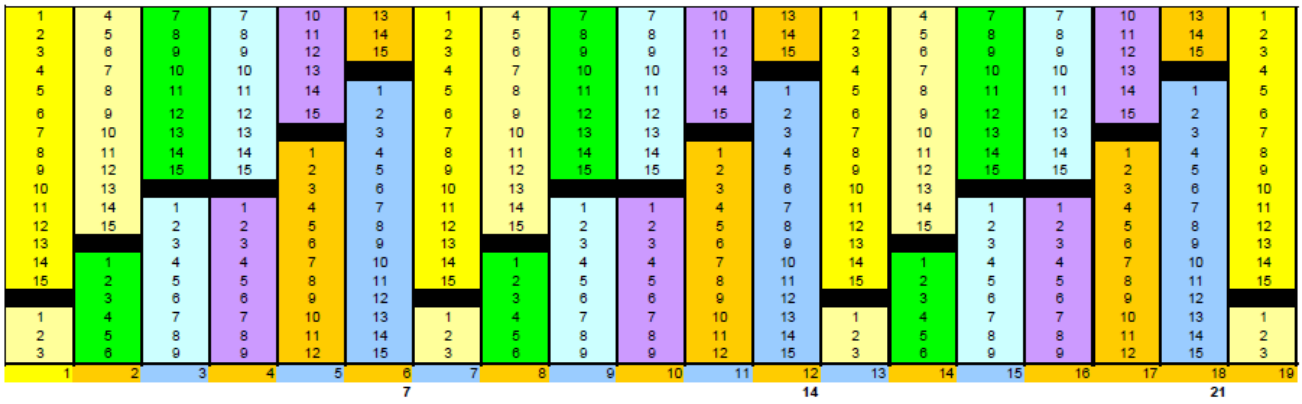

Proposed Layout				
15 series cells	74 parallel	1110 cells per panel	62 sectors	19 cells per row

Figure 5.6-5: Proposed solar panel string layout

The cells will be integrated onto the cylindrical surface as reported in the figure below. The correspondent deflection is compatible with TJ SCA cell bending properties.

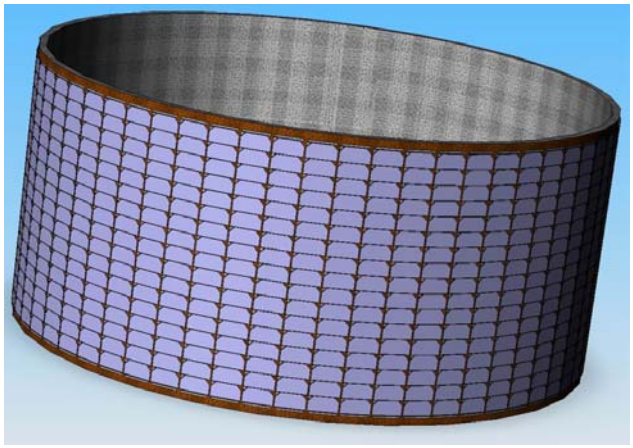

Figure 5.6-6: Solar panel drum configuration

The total number of installed cells is 2040.

As first approximation the collected solar flux of the cylindrical surface can be approximated by its projection:

$$\eta_{area} = \frac{\Pr ojectedsurface}{HalfLateralSurface} = \frac{2Rh}{\pi Rh} = 2/\pi \cong 0.637$$

However this approximation is not conservative as below specific incidence angles the conversion efficiency degrades more than the cosine projection and becomes negligible around 85°. The relative power of solar cells has therefore been calculated by applying a correction for the real physical behaviour of the solar generator. The so called 'cosine-correction' has been introduced. This correction reflects the fact that the energy transferred does not exactly follow the cosine function with lower angles but has an inward deformation with an overall integrated value of 2.5% less than the area under the real cosine function.

The formula for the corrected cosine-value (Vcos,corr) calculates from the mathematical value (Vcos) as:

$$\text{Vcos} < 0.707: \qquad V_{\cos,corr} = V_{\cos} \cdot \left[\sin\left(V_{\cos} \frac{\pi}{2} \frac{1}{0.707}\right) \right]^{0.416}$$

$$\text{Vcos} \geq 0.707: \qquad V_{\cos,corr} = V_{\cos}$$

The adapted cosine function as correction factor is given in the following figure.

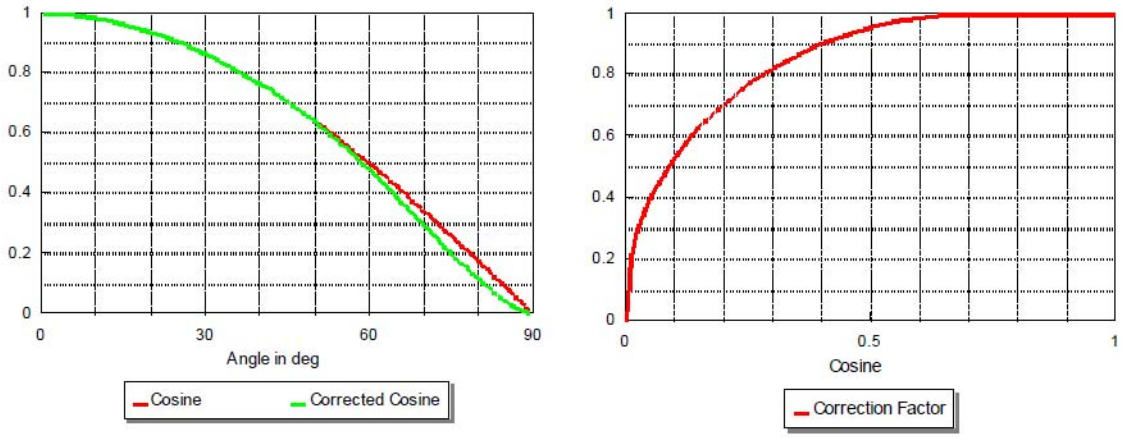

Figure 5.6-7: Corrected cosine loss factor

The collected and usable solar flux on the exposed cells area results in order of 420 W/m^2. This value is a worst case value because it does not take into account any contribution of Earth radiation and albedo.

The following operating conditions and design characteristics have been considered.

- Mission life of 6 years
- Solar Array cylindrical panel of 4 m^2 (with radius of 800 mm)
- Cell technology 3G GaAs/Ge Triple Junction
- Loss factors
    - Direct Losses :
        - Sun Intensity = 0,967
        - UV plus micrometeorites = 0,988
        - Cover-glass loss = 0,985
        - String loss = 0,985
    - Random losses:
        - Current cell mismatch = 0,99
        - Calibration error = 0,98
- Operating temperature = 50°C
- Equivalent Solar Flux = 429 W/m²
- Maximum Sun Aspect Angles = 23°
- Current degradation due to Radiation = 1*e14 MeV
- 1 string loss
- S3R an equivalent efficiency of 96%
- Area of about 4 m² (Diameter =1600 mm, Height =810 mm).

The calculated power delivered by the two solar array panels is provided in Figure 5.6-8 (Beginning of Life) and Figure 5.6-9 (End of Life).

Delivered power at BOL, 28°C						
V_{oc} [V]	I_{sc} [A]	V_{mp} [V]	I_{mp} [A]	P_{max} [W]	Pload (28V) [W]	T [°C]
37.7	19.6	31.7	18.7	591.5	544.9	28

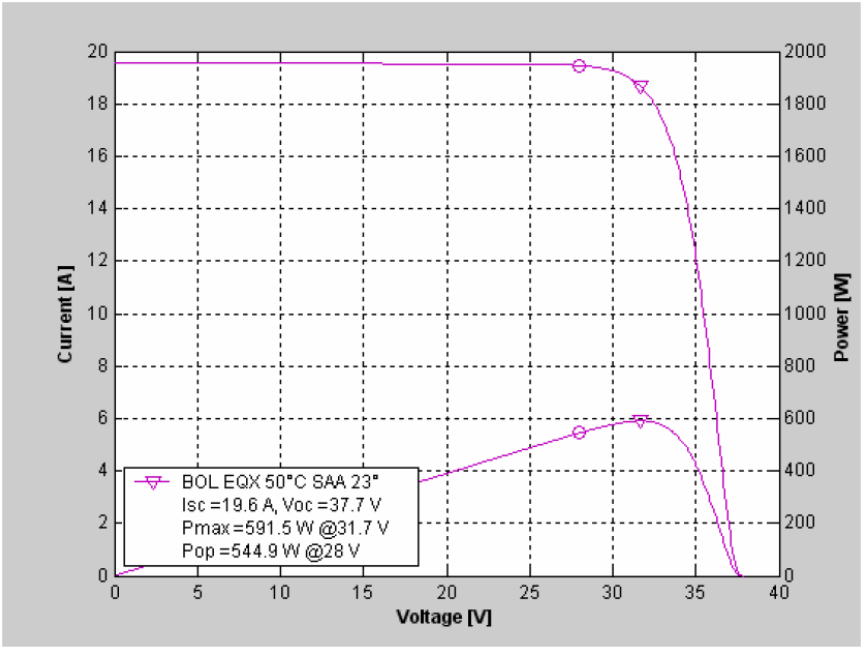

Figure 5.6-8: Calculated solar array power (BOL)

Delivered power at EOL SS, 50°C with 1 string loss, 23° SAA						
V_{oc} [V]	I_{sc} [A]	V_{mp} [V]	I_{mp} [A]	P_{max} [W]	Pload (28V)	T [°C]
36.8	18.3	31	17.5	543.8	510	50

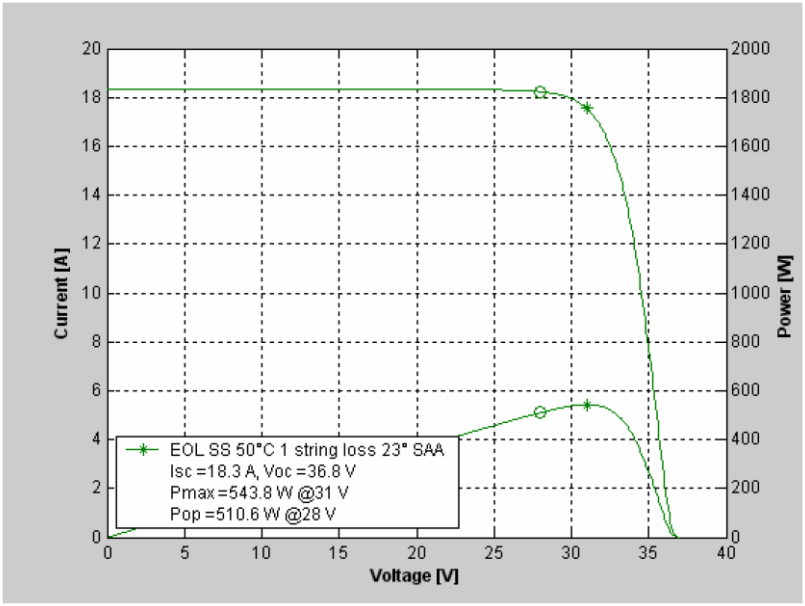

Figure 5.6-9: Calculated solar array power (EOL)

5.7 Telecommunications

An S-Band architecture derived from the PRIMA platform is proposed for the Galileo Galilei TT&C. Some modifications in the RF distribution network have to be implemented because of the different mission scenario and attitude. The architecture, shown below, consists of:

- 2 transponders with low output power (23 dBm, i.e., 200 mW) and diplexer embedded;
- RFDN miscellanea in coaxial technology:
- 2 RF switches
- Connection cables
- 2 LGAs with circular polarization (LHCP or RHCP) and hemispherical coverage (gain = -3 dBi at ±95° boresight offset angle as in Figure 5.7-3)

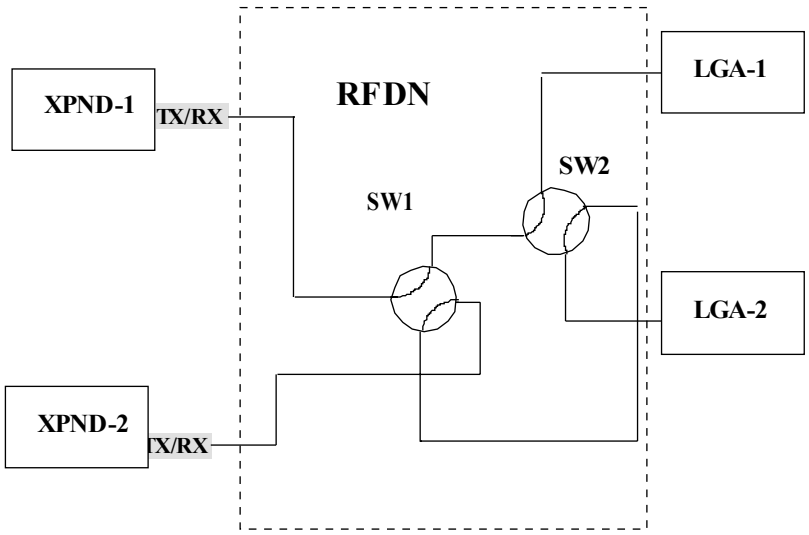

Figure 5.7-1: GG TT&C block diagram

The telemetry data generated by the GG system, including overheads and margins, is 2350 Mbit/day (see §5.8). This amount of data may be downloaded on each ground station pass, once per orbit, minimizing the telemetry rate, or with higher data rate in order to decrease the number of contacts per day and Malindi ground station occupation time consequently. The guideline for re-use of PRIMA hardware limits the TM symbol rate to 512 kbps, and leads to adoption of Reed-Solomon coding and SP-L modulation only.

Assuming the data volume generated in one day of science operations must be downloaded within the next day, Table 5.7-1 shows, as function of number of contacts per day, the minimum TM data rate allowing data volume downlink. The values in red exceed the limit of 512 kbps, so they are not allowed.

Number of contacts/day	No data compression		Compression factor 1.5 (zip		Compression factor 2.8	
	TM data rate [kbps]	TM symbol rate [kb/s]	TM data rate [kbps]	TM symbol rate [kb/s]	TM data rate [kbps]	TM symbol rate [kb/s]
1 / orbit	259	295	172	196	92	105
10	392	447	261	298	140	159
9	435	496	290	331	155	177
8	490	558	326	372	175	199
7	560	638	373	425	200	228
6	653	744	435	496	233	266
5	783	893	522	595	280	319
4	979	1116	653	744	350	399
3	1306	1489	871	992	466	532
2	1959	2233	1306	1489	700	797
1	3917	4466	2612	2977	1399	1595

Table 5.7-1: TM data rates with limitation to 512 kbps

The conclusions from the table above are that:

- without data compression 9 contacts per day are necessary;
- with “zip file” technique (compression factor = 1.5) this number can be reduced to 6;
- using a Rice algorithm (compression factor = 2.8), 4 contacts per day are enough to download the whole mass memory content.

A reduced TM data rate shall be considered in case of ranging operations. According to a preliminary ranging tone determination, fixing TM symbol rate to 256 kbps, tone frequency can be 1024.1 kHz.

Link budget calculations have been performed for the worst case, i.e. no data compression, with and without ranging. With the architecture proposed, margins are such that ranging operations are guaranteed as well (Table 5.7-2). The TC link will be established at 4 kbps following the PCM/PSK/PM modulation scheme as described in the standard ECSS-E-50-05A. Ranging too will be implemented in accordance with standard ECSS-E-50-02A.

Distance [km]	UP-LINK				DOWN-LINK						
	Data Rate [kbps]	Nom. Margin [dB]			Information Rate	TM Coding	TM symbol rate [kbps]		Nom. Margin [dB]		
		RX power	Carrier Rec.	TC Recovery				Flux	Carrier Rec.	TM Recovery	Ranging
520	4	39.96	59.08	49.69	225	R-S	257	3.25	38.78	10.53	49.43
520	4	39.96	59.88	50.49	450	R-S	513	2.70	39.33	8.07	No RG
520	4	41.96	61.88	52.49	450	R-S	513	1.20	40.83	9.57	No RG

Table 5.7-2: Link budget summary

To reach the Link budget results of Table 5.7-2, following units have been taken into account:

- S-Band PRIMA transponder
- RFDN with switches in order to avoid interferences between the signal caught by the two antennas at the same transponder receiver

- S-Band low gain antennas as ATV with maximum gain limited to 0 dBi in order not exceeding power flux density at the Earth limitation imposed by ITU

5.7.1 S-Band transponder

The transponder identified is designed to support uplink and downlink in S-Band and to ensure cold redundancy in downlink and hot redundancy in uplink. It's able to work both in non-coherent mode and in coherent mode with turnaround ratio as 240/221.

Transponder shall ensure following uplink operating modes:

- Carrier only (for lock acquisition purpose)
- Carrier + TC
- Carrier + RNG
- Carrier + TC + RNG

whilst the downlink operating modes shall be:

- Carrier only (at least for test purposes)
- Carrier +TM
- Carrier + RNG
- Carrier + TM + RNG.

The operating modes defined above can be supported by following transponder configurations:

- TX OFF + Rx ON:
  - Uplink Carrier only
  - Uplink carrier + TC
  - Uplink carrier + RNG
  - Uplink carrier + TC + RNG
- TX ON + Rx ON:
  - Uplink functions as above
  - Downlink carrier only
  - Downlink carrier + TM
  - Downlink carrier +TC + TM
  - Downlink carrier +TM + RNG
  - Downlink carrier + TC + TM + RNG

Depending on RX lock status, functions requiring TX powered, can be performed in both coherent and non-coherent mode. The "coherent mode" function shall be selectable by dedicated TC as well as ranging and TM functions.

TM modulation scheme SP L/PM is envisaged: it is compatible with ranging modulation and shall support TM bit rate of 16, 128 and 512 kbps.

Since uplink budget allows the maximum TC bit rate foreseen by ECSS Standard ECSS-E-50-05A for TC modulation scheme PCM/PSK/PM, i.e. 4 kbps, this bit rate has been selected as baseline for Galileo Galilei.

According to Link budget calculation, transmitter output power shall be 23 dBm, this value ensures the required TM data rate and meet the requirement on power flux density at the Earth.

The considered transponder is the S-band transponder with diplexer embedded.

The characteristics desired for such a transponder are summarized in Table 5.7-3 and Table 5.7-4.

Parameter	Performance
Frequency (S-Band) range	2025 – 2110 MHz
Baseband Modulation	PCM(NRZ-L)/PSK
Carrier Modulation	PM
TC Bit Rate	4000 bps
BER	10^{-5}
RF Input PWR	-50 ÷ -125 dBm
Ranging	ESA Standard

Table 5.7-3: Transponder RX Characteristics

Parameter	Performance
Frequency (S-Band) range	2200 – 2290 MHz
Telemetry data format	NRZ-L
Carrier Modulation	Split-Phase Modulated (SP L/PM)
Frequency Stability	$\pm 2 \times 10^{-5}$ all $\pm 2 \times 10^{-6}$ 24 h
RF Unit Output PWR	23 dBm
Ranging	ESA Standard

Table 5.7-4: Transponder TX Characteristics

In order to estimate the physical properties and power consumption, TAS-I transponder mounted on PRIMA platform has been taken as reference.

- S-band transponder dimensions: 230x150x190 mm
- Mass estimation: 3.9 kg.
- Power consumption:
  - RX only: 7 W
  - RX+TX: 20 W
- Power dissipation:
  - RX only: 7 W
  - RX+TX: 19.5 W

5.7.2 RFDN

Radio Frequency Distribution Network function is to connect transponders to antennas. It's a passive microwave equipment in charge of routing and distributing the signals with the aid of switches and interconnecting coaxial cables.

Galileo Galilei RFDN is aimed to be designed in coaxial technology; architecture is simple, consisting of two RF coaxial switches and connection cables only, since diplexers are part of transponders.

It shall have two interfaces to/from transponders and two interfaces to/from LGA's.

The RF coaxial switches position shall be changeable by TC's only. Dedicated HKTM will be provided to CDMU by bi-level signal status.

Being the RFDN architecture very simple, it could be decided to procure directly the single items instead of specifying RFDN as unique equipment.

In this case, switches and cables mass only shall be taken into account. One single RF switch mass could be as 120 g and half a kg of coaxial cables could be a realistic estimation, based on these assumptions, the RFDN mass could be as 700 g.

5.7.3 S-Band Antenna

S-Band omnidirectional quadrifilar helix antenna design is based on RIMSA heritage for ATV.

Radiation pattern is provided in Figure 5.7-3: the coverage as -3 dBi minimum up to ±95° off boresight is ensured. The picture of ATV S-Band antenna is shown in Figure 5.7-2.

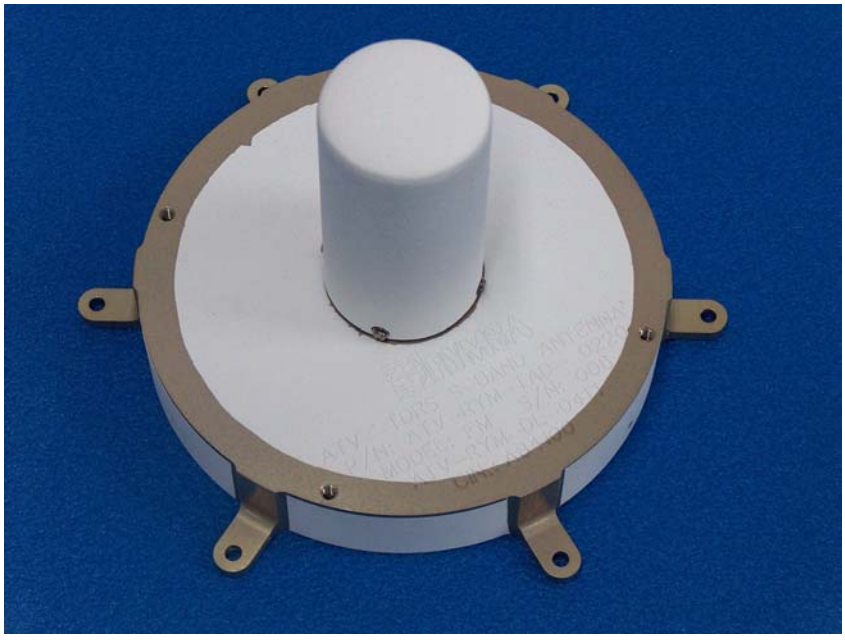

Figure 5.7-2: ATV S-Band quadrifilar antenna picture (RIMSA courtesy)

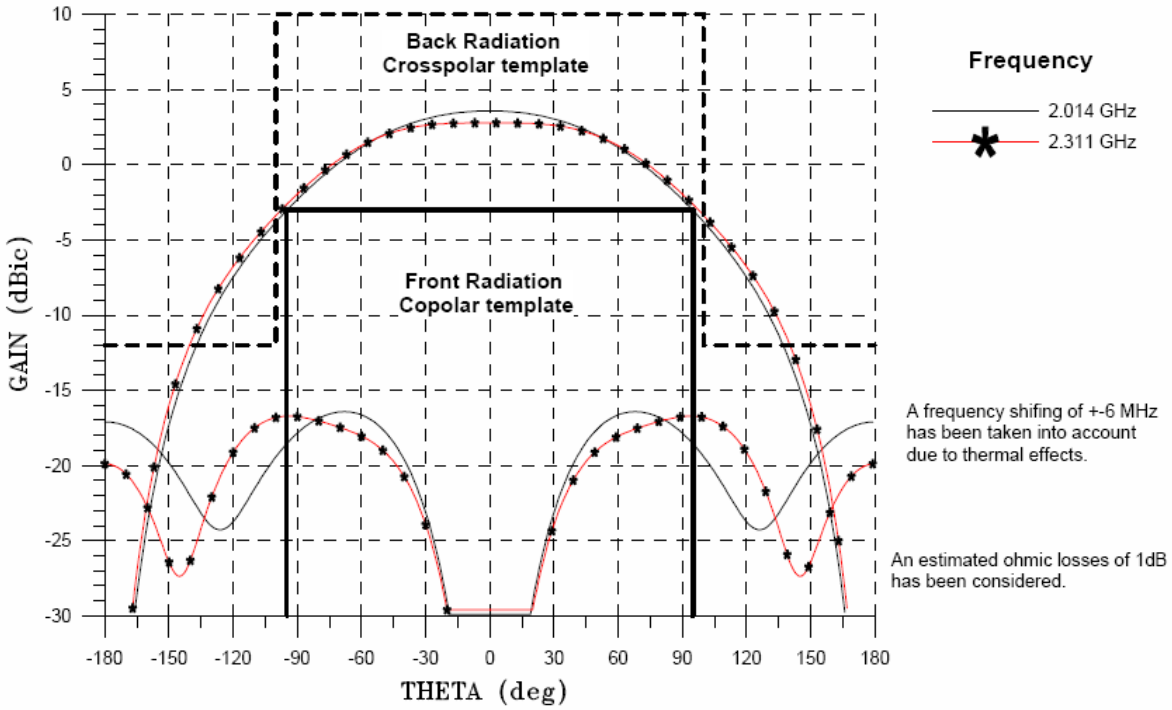

Figure 5.7-3: ATV S-Band quadrifilar antenna radiation pattern (RIMSA courtesy)

Mass and dimensions

The preliminary expected mass and dimensions are:

- Mass: < 300 g
- Dimensions: diameter <150 mm and length < 110 mm.

5.7.4 Interfaces to other subsystems

- CDMU / CPDU (Figure 5.7-4)
  - High power command for Transmitter ON/OFF, Coherent Mode ON/OFF, Ranging ON/OFF, TM ON/OFF
  - Extended High Power command for RF switches
  - Digital TM:
    - TX ON/OFF, TM ON/OFF, Ranging ON/OFF, Coherent Mode ON/OFF
    - TM switch status for RF switches position
    - Transponder receiver Lock and Squelch status: RS-422 and/or bi-level
  - Thermistors TM for TX and RX Temperatures monitoring
  - Analogue TM for transponder
    - Receiver Automatic Gain Control (AGC), Static Phase Error (SPE) and DC/DC converter secondary voltage
    - Transmitter DC/DC converter secondary voltages

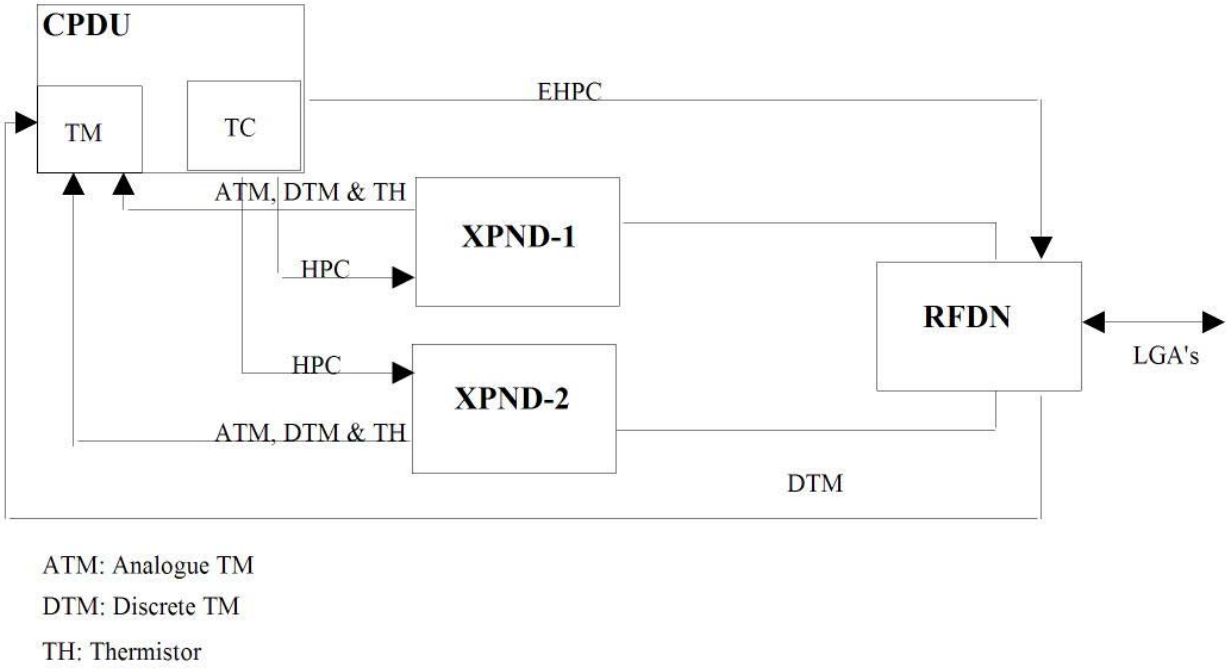

Figure 5.7-4: TT&C interfaces to CDMU CPDU

- CDMU / Encoder and Decoder (Figure 5.7-5)
  - TC stream to CDMU Decoder: RS-422
  - TM stream from CDMU Encoder: RS-422

It's envisaged a direct point to point link between transponder receivers and CDMU decoders, no cross-coupling in order to avoid problems in TC decoding; cross-coupling will be implemented inside the CDMU.

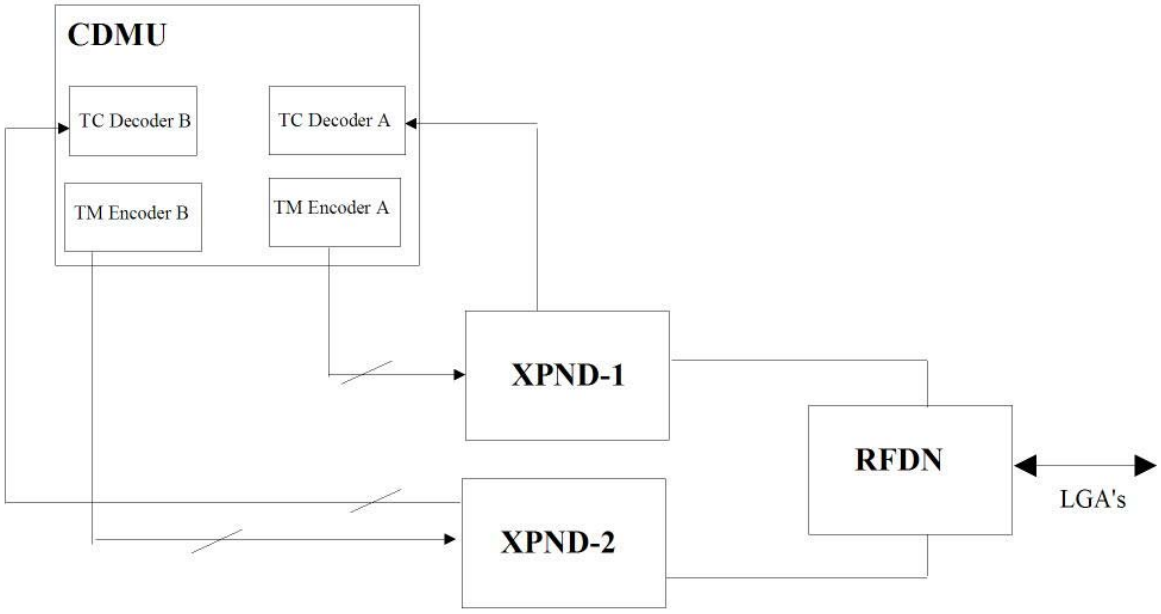

Figure 5.7-5: TT&C interfaces to CDMU Encoder and Decoder

- EPS (Figure 5.7-6)
  - 2 Fold-back Current Limiters (FCL) for transponder receivers
  - 2 Latching Current Limiters (LCL) for transponder transmitters

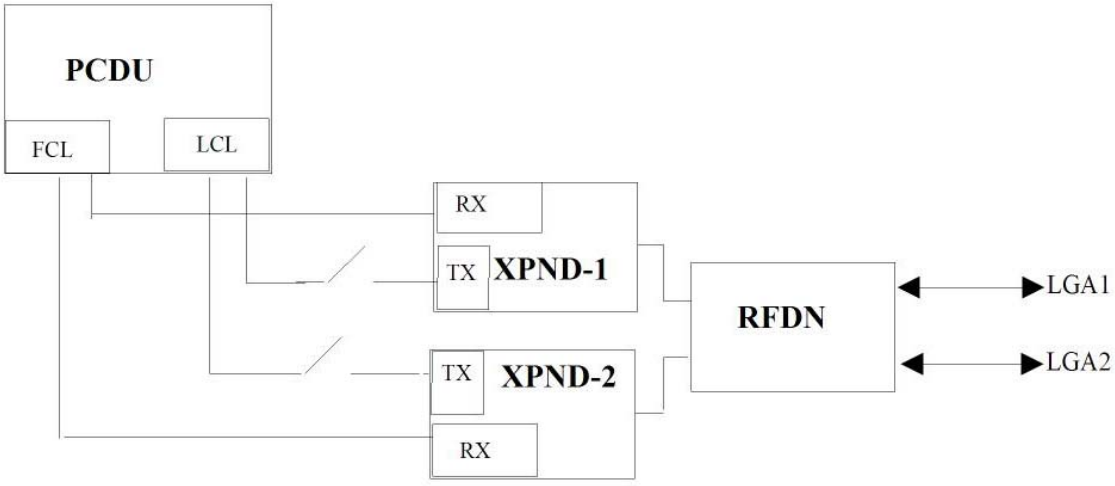

Figure 5.7-6: TT&C interfaces to EPS

5.8 System Budgets

5.8.1 Mass properties

In the following, mass and inertia tables are provided, as follows.

- CoG, MoI and Products of Inertia budgets in Figure 5.8-1;
- GG Experiment mass budget in Table 5.8-1;
- GG Spacecraft Subsystems Mass Budget in Table 5.8-2;
- GG Spacecraft System Mass Budget in Table 5.8-3.

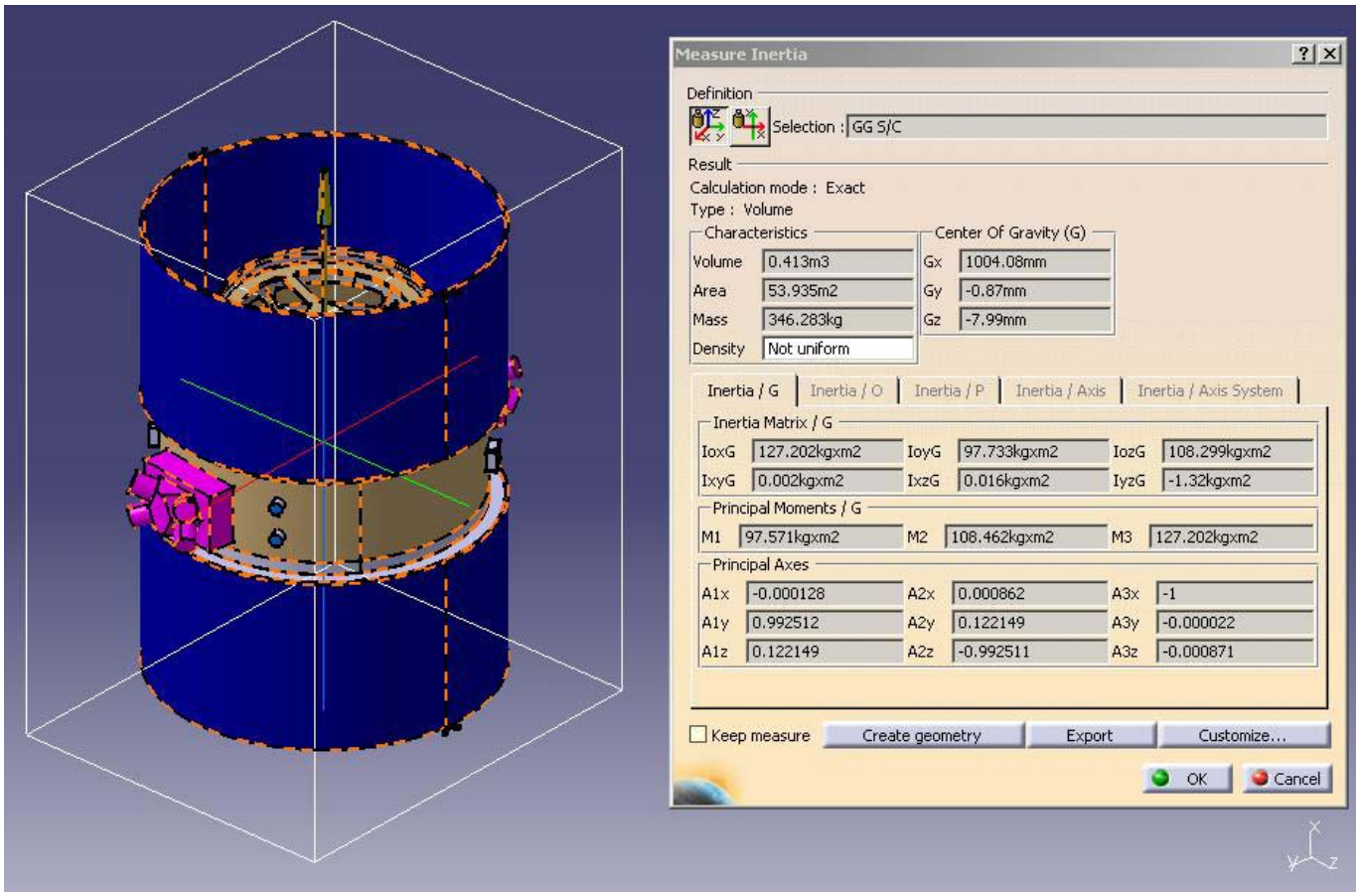

Figure 5.8-1: GG Spacecraft CoG, MoI and PoI budgets

Name	No.	Unit Mass [kg]	Total Mass [kg]	Margin [%]	Margin [kg]	Total Mass with margin [kg]
Inner Test Mass	**1**	**10,000**	**10**	**0**	**0,00**	**10,00**
Outer Test Mass	**1**	**10,000**	**10**	**0**	**0,00**	**10,00**
PGB Shaft			**2,879**	**20**	**0,58**	**3,45**
Mollette giunto 1	1	0,102	0,102			
Mollette giunto 2	1	0,071	0,071			
Mollette supporto piezo 1	1	0,098	0,098			
Mollette supporto piezo 2	1	0,030	0,03			
Assy supporto centrale	1	0,060	0,06			
Cilindro Giunto interno 1	1	0,161	0,161			
Cilindro Giunto interno 2	1	0,049	0,049			
Cilindro portante	1	1,082	1,082			
Piastre capacitive	1	1,164	1,164			
Piastrine capacitive	1	0,062	0,062			
PGB Shell allocation (TBC)	***1***	***7,60***	***7,60***	***20***	***1,52***	***9,12***
µmetal on PGB shell	**1**	**1,76**	**1,76**	**20**	**0,35**	**2,11**
PGB interface spring	**8**	**0,11**	**0,86**	**20**	**0,17**	**1,04**
Plasma shielding grid allocation	**4**	**0,01**	**0,04**	**20**	**0,01**	**0,05**
Locking mechanisms allocation (TBC)	***1***	***8,40***	***8,40***	***20***	***1,68***	***10,08***
Inch Worm	**16**	**0,10**	**1,60**	**20**	**0,32**	**1,92**
		PAYLOAD TOTALS	**43,14**	**10,7%**	**4,63**	**47,77**

Table 5.8-1: GG Experiment Mass Budget

Element 1 - Galileo Galilei						
FUNCTIONAL SUBSYSTEM	nr	ass (kg) per u	otal Mass (kg	Margin (%)	Margin (kg)	Mass (kg) with Margin
Structure			**104,61**	**18,09**	**18,92**	**123,53**
Upper Platform	1	1,23	1,23	20,00	0,25	1,48
Upper Cone	1	7,08	7,08	20,00	1,42	8,50
Outermost Cylinder	1	11,35	11,35	20,00	2,27	13,62
Lower Cone	1	7,08	7,08	20,00	1,42	8,50
Lower Platform	1	1,23	1,23	20,00	0,25	1,48
Cone to Cylinder I/F ring	2	14,58	29,16	20,00	5,83	34,99
Cone to Platform I/F ring	2	4,03	8,06	20,00	1,61	9,67
PGB shell lock/unlock mech.	2	2,50	5,00	20,00	1,00	6,00
Separation system ring	1	2,50	2,50	20,00	0,50	3,00
Miscellaneous (inserts. cleats. etc.	1	9,00	9,00	20,00	1,80	10,80
Ballast mass	1	10,00	10,00	0,00	0,00	10,00
Payload support cone	2	4,80	9,60	20,00	1,92	11,52
PGB interface	2	1,66	3,32	20,00	0,66	3,98
Thermal Control			**8,70**	**20,00**	**1,74**	**10,44**
MLI thermal blanket	1	4,30	4,30	20,00	0,86	5,16
Paints & tapes	1	1,20	1,20	20,00	0,24	1,44
Heating line	1	0,20	0,20	20,00	0,04	0,24
Doublers	1	2,00	2,00	20,00	0,40	2,40
Miscellanea	1	1,00	1,00	20,00	0,20	1,20
Communications			**9,60**	**10,00**	**0,96**	**10,56**
XPDN S-Band 1	1	3,60	3,60	10,00	0,36	3,96
XPDN S-Band 2	1	3,60	3,60	10,00	0,36	3,96
RFDN S-Band	1	1,20	1,20	10,00	0,12	1,32
S-Band Antenna 1	1	0,60	0,60	10,00	0,06	0,66
S-Band Antenna 2	1	0,60	0,60	10,00	0,06	0,66
Data Handling			**16,00**	**20,00**	**3,20**	**19,20**
CTU+RTU	1	16,00	16,00	20,00	3,20	19,20
AOCS			**5,92**	**13,11**	**0,78**	**6,69**
Smart Sun Sensor	2	0,33	0,66	5,00	0,03	0,69
Spin Rate Sensor	2	0,70	1,40	20,00	0,28	1,68
Spin Rate Sensor el.	2	0,90	1,80	20,00	0,36	2,16
Magnetometer	3	0,19	0,56	5,00	0,03	0,58
Gyroscope	2	0,75	1,50	5,00	0,08	1,58
Propulsion			**37,66**	**13,95**	**5,26**	**42,92**
EPS Assembly	2	9,27	18,54	20,00	3,71	22,25
EPS Miscellanea	1	2,14	2,14	20,00	0,43	2,57
Nitrogen Thrusters	8	0,10	0,80	5,00	0,04	0,84
Nitrogen Tank	2	7,19	14,38	5,00	0,72	15,10
Lines & Valves	1	1,80	1,80	20,00	0,36	2,16
Power			**57,68**	**14,82**	**8,55**	**66,23**
Solar Array	2	13,91	27,82	20,00	5,56	33,38
PCDU	1	13,50	13,50	10,00	1,35	14,85
Battery	1	16,36	16,36	10,00	1,64	18,00
Harness			**12,50**	**20,00**	**2,50**	**15,00**
Power Harness	1	12,50	12,50	20,00	2,50	15,00
Payload			**55,34**	**12,77**	**7,07**	**62,41**
Inner test mass	1	10,00	10,00	0,00	0,00	10,00
Outer test mass	1	10,00	10,00	0,00	0,00	10,00
PGB Shaft	1	2,88	2,88	20,00	0,58	3,45
PGB Shell allocation	1	7,60	7,60	20,00	1,52	9,12
ECE	1	5,40	5,40	20,00	1,08	6,48
CPE	1	7,20	7,20	20,00	1,44	8,64
Locking Mechanisms allocation	1	8,40	8,40	20,00	1,68	10,08
Inch Worms allocation	12	0,10	1,20	20,00	0,24	1,44
Plasma shielding grids allocation	4	0,01	0,04	20,00	0,01	0,05
mumetal on PGB shell	1	1,76	1,76	20,00	0,35	2,11
PGB interface spring	8	0,11	0,86	20,00	0,17	1,04
Propellant						**4,75**

Table 5.8-2: GG Spacecraft Subsystems Mass Budget

Galileo Galilei

	Target Spacecraft Mass at Launch			1000,00	kg
	Below Mass Target by:			482,18	kg
	Without Margin	Margin		Total	% of Total
Dry mass contributions		%	kg	kg	
Structure	**104,61 kg**	**18,09**	18,92	**123,53**	23,86
Thermal Control	**8,70 kg**	**20,00**	1,74	**10,44**	2,02
Communications	**9,60 kg**	**10,00**	0,96	**10,56**	2,04
Data Handling	**16,00 kg**	**20,00**	3,20	**19,20**	3,71
AOCS	**5,92 kg**	**13,11**	0,78	**6,69**	1,29
Propulsion	**37,66 kg**	**13,95**	5,26	**42,92**	8,29
Power	**57,68 kg**	**14,82**	8,55	**66,23**	12,79
Harness	**12,50 kg**	**20,00**	2,50	**15,00**	2,90
Payload	**55,34 kg**	**12,77**	7,07	**62,41**	12,05
Total Dry(excl.adapter)	**308,01**			**356,98**	**kg**
System margin (excl.adapter)		**20,00**	**%**	**71,40**	**kg**
Total Dry with margin (excl.adapter)				**428,38**	**kg**
Other contributions					
Wet mass contributions					
Propellant	**4,75 kg**	**100,00**	4,75	**9,50**	1,83
Adapters mass (including sep. mech.), kg	**79,94 kg**	**0,00**	0,00	**79,94**	15,44
Total wet mass (excl.adapter)				**437,88**	**kg**
Launch mass (including adapter)				**517,82**	**kg**

Table 5.8-3: GG Spacecraft System Mass Budget

5.8.2 Power budgets

The power demand of the satellite is computed taking into account the design maturity of each unit (power contingency). The reference configuration used to compute the power budget includes the utilization of the FEEP organized in two clusters with 4 thrust each and assuming an average total thrust of 350 μN.

Power Budget (Configuration with 2 FEEP clusters)					Sunlit	Eclipse	
Equipments	No. Of active	Unit Power [W]	Contingency [%]	Power with Contingency [W]	Nominal Power [W]	Nominal Power [W]	LEOP phase [W]
ECE	1	9	20	10.8	10.8	0	0
CPE	1	18	20	21.6	21.6	0	0
Total P/L [W]					**32.4**	**0.0**	**0.0**
CDMU	1	18.0	10	19.8	19.8	19.8	19.8
TRSP1 (Tx + Rx)	1	20.0	3	20.6	20.6	20.6	20.6
TRSP 2 (Tx + Rx)	1	6.5	5	6.8	6.8	6.8	6.8
PCDU	1	25.0	10	27.5	44.5	27.5	27.5
Battery (max charging)	-	-	-	-	180.0	0.0	0.0
TCS (heaters)	1	12.0	20	14.4	14.4	30.0	30.0
Fine Sun sensor	1	1.3	10	1.4	1.4	1.4	0.0
Gyro	0	19.8	10	21.8	0.0	0.0	21.8
Rate Sensor	1	6.0	10	6.6	6.6	6.6	0.0
Magnetometer	3	0.8	10	0.9	2.6	2.6	2.6
FEEP (2 cluster option)	1	133.0	20	159.6	159.6	159.6	0.0
Total Service Module [W]					**456.4**	**275.0**	**129.1**
Total Satellite [W]					**488.8**	**275.0**	**129.1**
PCDU loss [2%]					9.8	5.5	2.6
Harness loss [2%]					10.0	5.6	2.6
GRAND TOTAL w/o system margin [W]					**508.5**	**286.1**	**166.5**

Table 5.8-4: Satellite power budget

5.8.3 Data budgets

The mass memory budget and hence the telemetry data rates depend on the data collection mode. The total science data rate in the normal scientific mode is about 158 Mbit/orbit including all overheads and margins (Table 5.8-5).

An on board mass memory sized for 24-hour autonomy would amount to about 1.6 Gbit. The whole 24-hour memory contents could be downloaded to the ground station in one single pass of 10' duration at a rate of about 186 kbps that is compatible with the maximum data rate permitted by the ESA S-band stations.

Data description	Variable list	Number of variables	Freq. [Hz]	Record length [bit]	Data rate [kbit/s]
Diff. TMs displacement	Δx, Δy	2	50	16	1.6
Tme/PGB displacement	Δx, Δy, Δz	3	50	16	2.4
Tmi/PGB displacement	Δx, Δy, Δz	3	50	16	2.4
PGB/Spacecraft displac.	Δx, Δy, Δz	3	50	16	2.4
ω_{SPIN}	ω_x, ω_y, ω_z	3	50	16	2.4
Reference time	t	1	50	16	0.8
Science data					**12.0**
PGB whirl monitoring	Sensing + actuation	6	1	16	0.096
Tme whirl monitoring	Sensing + actuation	6	1	16	0.096
Tmi whirl monitoring	Sensing + actuation	6	1	16	0.096
ADC monitoring	Number of ADC	9	1	16	0.144
Inchworm monitoring	Number of inchworms	6	1	16	0.096
Piezo monitoring	Number of piezo	6	1	16	0.096
PGB Inner temperature monitoring	Number of temperature sensors	20	0.10	16	0.03
Capacitance bridge monitoring	Number of capacitance bridges	9	0.10	16	0.01
Payload HK					**0.7**
Commands to FEEP	Number of commands	6	1	16	0.096
PGB/Spacecraft phase lag	Number of lag sensors	1	0.10	16	0.0016
Commands to actuators	Number of commands	6	50	16	4.8
Sun sensor	1 (2 in case o redundancy)	2	50	16	1.6
FEEP monitoring	Number of FEEP	6	1	16	0.096
SVM (DFACS + other sub-systems)					**10.0**
			Total Data Rate	kbps	**22.7**
			Overhead		**20.0%**
			Total Data Rate with margins	kbps	**27.2**
			Altitude	km	**520**
			Period	s	**5702**
			Data volume	Mbit/orbit	**155**
			Pass duration	minutes	**10**
			Telemetry rate	kbit/s	**259**
			Passages/day		**15**
			Telemetry data volume	Mbit/day	**2350**

Table 5.8-5: Satellite data budgets

6. DRAG-FREE AND ATTITUDE CONTROL ARCHITECTURE

6.1 Functional description

The Drag-Free and Attitude Control (DFAC) is responsible for:

- before PGB unlock:
  - the spacecraft attitude control after launcher separation, in order to guarantee safe power and communication conditions;
  - spacecraft spin-up to achieve the spin rate required by scientific observation (360deg/s);
- after PGB unlock:
  - the stabilization of whirl control;
  - drag compensation with very high rejection to permit the detection of the EP violation (if any);
  - the control of the spacecraft spin-rate and of the PGB-spacecraft relative spin angle. This is necessary for PGB suspension, sensors and actuators integrity.

6.2 Operating modes organization

Depending on the separation conditions (pre-defined attitude, spin-rate, attitude and angular rate errors) different scenarios may be envisaged for the starting operating phase of the spacecraft. According to [RD 31], two separation options are available using Vega launcher:

- 3-axis stabilisation;
- spin stabilization around the upper composite longitudinal axis.

The accuracy provided by launcher in terms of orbital parameters and attitude accuracy is given in Table 6.2-1. The DFAC mode organization has been designed to be compliant with both separation options in order to permit different launch opportunities.

Considering a spin stabilized separation, the spacecraft Z-axis may be considered close to required one with errors lower than 5÷10deg half-cone. The separation conditions with a spin rate close to the maximum allowed (30deg/s) gives enough gyroscopic stability achieving safe power and communication operating conditions.

No	Parameter	Unit	Value	Comments
	Injection accuracy (700km altitude, 3σ)			
1	Altitude error	km	15	
2	Inclination	deg	0.15	
3	Argument of perigee	deg	-	
4	RAAN	deg	0.3	
	Three-axis stabilized mode (3σ)			
5	Longitudinal axis de-pointing	deg	1	
6	Transversal axis de-pointing	deg	1.5	
7	Angular tip-off rates along longitudinal axis	deg/s	0.6	
8	Angular tip-off rates along transversal axis	deg/s	1.0	
	Spin stabilized mode (3σ)			
9	Max spin rate	deg/s	30	
10	Spin rate accuracy	deg/s	1	@ 30 deg/s
11	Transverse angular tip-off rates	deg/s	0.6	@ 30 deg/s
12	Nutation	deg	5	@ 30 deg/s, half angle

Table 6.2-1: Vega launcher performances [RD 31]

In the three axis stabilized separation option, the attitude control system shall provide:

- rate damping;
- Sun acquisition and slow-spin up of the spacecraft around Z-axis, to provide a slow but effective spin-stabilization for fuel saving.

After separation, the residual angular rate is damped to be lower than 0.1deg/s. Then, the spacecraft is slewed in order to have the spacecraft z-axis close to the final required pointing (Earth Z-axis). The rate-damping may be obtained by using a coarse gyroscope. The pointing close to the Earth z-axis may be obtained by a magnetometer thanks to the almost equatorial orbital plane. The spin-axis pointing may be improved after early ground contacts and orbit determination, using an on-board orbit propagator and Earth magnetic field model.

Taking into account the spacecraft geometry, any attitude providing the spacecraft Z-axis almost normal with the orbit plane may be considered safe for power and communications.

In order to permit higher accuracy with respect to what may be expected by using only a magnetometer, also after in-flight calibration (key procedure), it has been considered convenient to consider another sensor (fine Sun sensor) to improve the spin-axis pointing. Using such equipment, determination of satellite spin-axis pointing will be possible all along the spacecraft mission.

Separation occurs with AOCS in Stand-By Mode (SBM). After separation in stabilized three-axis mode, the Rate Damping Mode (RDM) is activated to reduce the angular rate, and then the Coarse Pointing Mode (CPM) is autonomously activated to steer the spacecraft Z-axis toward the local magnetic field, and to introduce a weak spin stabilization to save propellant. In such a way, taking into account the satellite shape, safe power and communication conditions will be met. After on-ground orbit determination, the pointing may be improved thanks to an on-board Earth Magnetic Field model.

After separation in spin stabilized mode, the spacecraft kinematics condition are almost the same as the exit condition from CPM (FPM entry conditions). Improving the pointing conditions is the responsibility of Fine Pointing Mode (FPM) using the Sun sensor.

In Spin-Up Mode (SUM), the angular rate around spacecraft Z axis will be increased up to 360deg/s (±10%). Satellite Z-axis pointing direction is estimated starting from magnetometer, Sun sensor, on-board Sun propagator, orbit propagator and Earth magnetic model. Before starting SUM, the three-axis flux-gate magnetometers shall be calibrated to recover bias, scale factor, non-orthogonality errors.

When the required angular rate is achieved (spin rate equal to 360deg/s, transversal angular rate close to zero), transition to Spin Stabilized Mode (SSM) is commanded.

In SSM, after PGB unlock, the DFAC shall guarantee PGB integrity, by stabilization of PGB-satellite relative movement (whirl control, spin rate and PGB-satellite rotation around spin axis control).

In Drag-Free Mode (DFM), the drag compensation in the XY plane and Z axis is done in parallel with whirl control, spin rate and PGB-satellite rotation control. The drag is captured by capacitive sensors (CapS) as relative motion between PGB and satellite. The drag compensation and the spin-rate control are done by micro-propulsion (μProp); whirl stabilization actuators are capacitive actuators (CapA). DFM is quite complex, due to the spin. In order to meet the very demanding requirement on drag attenuation (greater than 50000), very accurate measurement of the satellite spin rate is needed. A Spin Rate Sensor (SpRS) is used for such purpose.

The transition between SSM and DFM is commanded any time the scientific observation is required. Back-transition from DFM to SSM is convenient for fuel saving (no-drag compensation).

No attitude control for spin-axis re-pointing has been foreseen during scientific phase. Analysis executed in the frame of the study shows that limiting the mission to two years and managing carefully system aspects like residual magnetic dipole and residual unwanted torque, the expected de-pointing is still acceptable for scientific purpose. This aspect will be re-considered in early phase B.

Table 6.2-2 shows the equipment used during each operating mode by control loop (•), or for satellite monitoring and on-ground spin-axis pointing reconstitution (×).

Figure 6.2-1 shows the preliminary AOCS mode organization, considering the two options for the separation.

In SSM the spacecraft will be left without any additional attitude control action. The active control action starts again in Drag-Free Mode (DFM). In SSM the whirl control only is active.

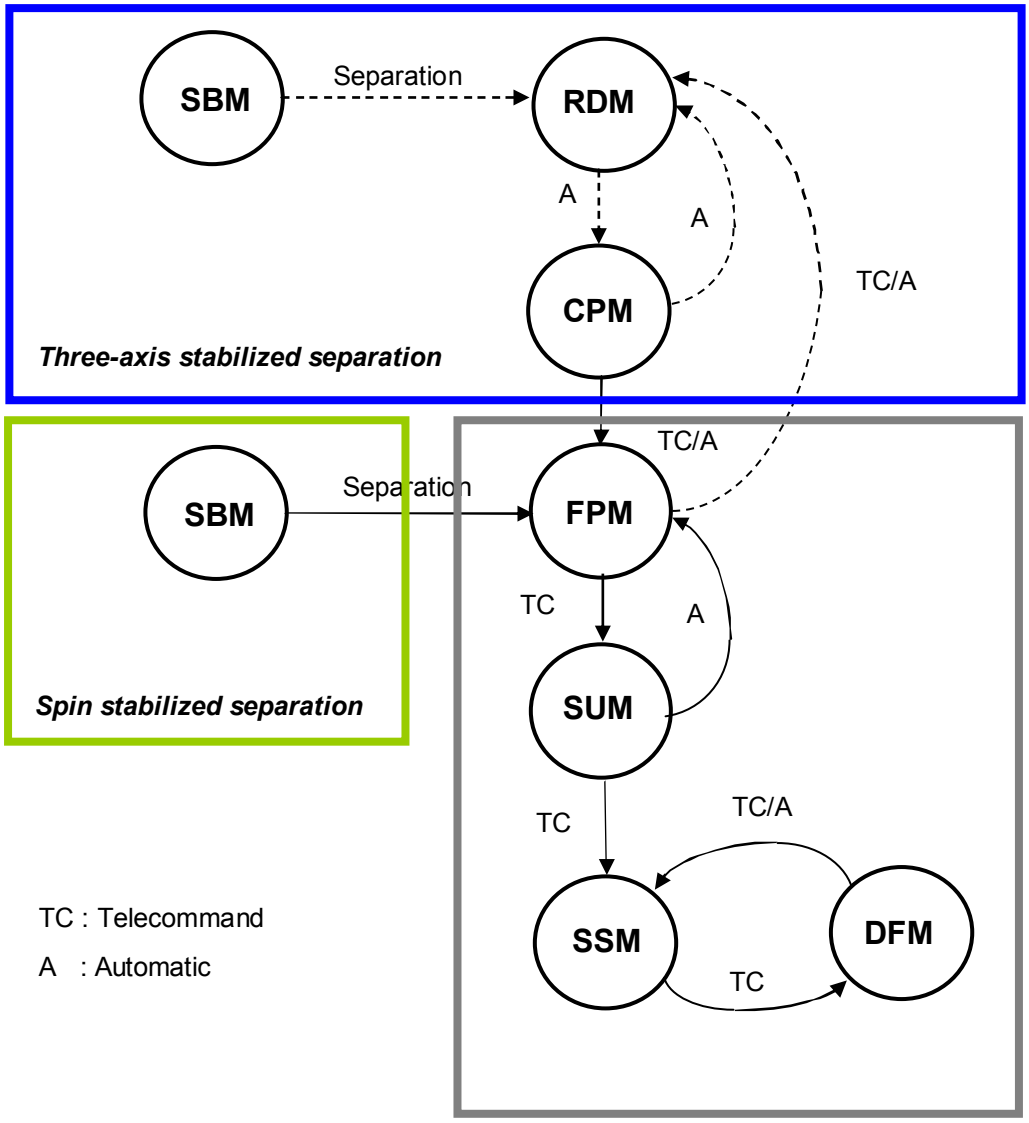

SBM	Stand-By Mode
RDM	Rate Damping Mode
CPM	Coarse Pointing Mode
FPM	Fine Pointing Mode
SUM	Spin-Up Mode
SSM	Spin Stabilized Mode
DFM	Drag-Free Mode (scientific mode)

Figure 6.2-1: DFAC mode organization.

Mode	GYRO	MGM	SSS	SpRS	CapS	RCS	µProp	CapA
Stand-By								
Rate Damping	•					•		
Coarse Pointing	•	•				•		
Fine Pointing	•	•	•			•		
Spin-Up	•	•	•			•		
Spin Stabilized	×	×	×		•		•	•
Drag-Free	×	×	×	•	•		•	•

Table 6.2-2: Equipment versus operating mode

6.3 Drag compensation control

6.3.1 The model of the plant

The model to be considered for the control design (control law, equipment requirement specification) starts from the following assumptions:

- the spacecraft is a rigid body;
- the PGB is a rigid body;
- coupling between spacecraft and PGB is provided by suspension.

Let be:

x, y, z : the coordinates of the PGB COM with respect to the spacecraft COM;

m_S : the spacecraft mass

m_{PGB} : the PGB mass

m_r : the reduced mass

$$m_r = \frac{m_S\, m_{PGB}}{m_S + m_{PGB}}$$

F_P : perturbing force (drag, solar pressure, thruster's noise)

F_T : thruster assembly control force

F_C : capacitors' control force

Q : quality factor of the PGB suspension

ω_S : spacecraft spin rate

ω_0 : natural frequency of the suspension

The following differential equations describe the dynamics of the PGB-spacecraft COMs relative motion with respect to an inertial observer positioned at the orbital reference frame at the initial time:

$$\ddot{x} = -\omega_0^2 x - \left(\frac{\omega_0^2}{Q\omega_S}\right)\dot{x} + \left(\frac{\omega_0^2}{Q\omega_S}\right)\omega_S y - \frac{F_{PX}+F_{TX}}{m_S} - \frac{F_{CX}}{m_r}$$

$$\ddot{y} = -\omega_0^2 y - \left(\frac{\omega_0^2}{Q\omega_S}\right)\dot{y} - \left(\frac{\omega_0^2}{Q\omega_S}\right)\omega_S x - \frac{F_{PY}+F_{TY}}{m_S} - \frac{F_{CY}}{m_r}$$

$$\ddot{z} = -\omega_0^2 z - \left(\frac{\omega_0^2}{Q\omega_S}\right)\dot{z} - \frac{F_{PZ}+F_{TZ}}{m_S} - \frac{F_{CZ}}{m_r}$$

The model shows coupling between the movements on the XY plane, while the movement on Z axis is independent. The coupling occurs by the parameter $\left(\frac{\omega_0^2}{Q\omega_S}\right)\omega_S$ that is equal to about $2\ 10^{-5}$ (weak coupling).

The poles of the 4th order system describing the dynamics on XY plane are:

$$p_{1,2} = -0.000234 \pm j0.0419 = -0.000234 \pm j\omega_0$$

$$p_{3,4} = 0.000231 \pm j0.0419 = 0.000231 \pm j\omega_0$$

The poles of the 2nd order system describing the dynamics along Z-axis are:

$$p_{5,6} = -1.551\ 10^{-6} \pm j0.0419 = -1.551\ 10^{-6} \pm j\omega_0$$

Without any external control action the movement on the plane X-Y is unstable (in the literature known as *whirling motion*). Figure 6.3-1 shows the magnitude of the transfer function between the force applied in X axis (Y axis) and the movement along X (along Y).

The following equations describe the dynamics of the PGB-spacecraft COMs relative motion with respect to an observer fixed with the spacecraft body frame:

$$\ddot{x} = -\left(\omega_0^2 - \omega_S^2\right)x - \left(\frac{\omega_0^2}{Q\omega_S}\right)\dot{x} + 2\omega_S\dot{y} - \frac{F_{PX}+F_{TX}}{m_S} - \frac{F_{CX}}{m_r}$$

$$\ddot{y} = -\left(\omega_0^2 - \omega_S^2\right)y - \left(\frac{\omega_0^2}{Q\omega_S}\right)\dot{y} - 2\omega_S\dot{x} - \frac{F_{PY}+F_{TY}}{m_S} - \frac{F_{CY}}{m_r}$$

$$\ddot{z} = -\omega_0^2 z - \left(\frac{\omega_0^2}{Q\omega_S}\right)\dot{z} - \frac{F_{PZ}+F_{TZ}}{m_S} - \frac{F_{CZ}}{m_r}$$

As in previous reference frame, the model shows coupling between the movements on the X and Y, while the movement on Z axis is independent. The coupling occurs by the parameter $2\omega_S$ that is equal to about 12.6 (strong coupling).

The poles of the 4th order system describing the dynamics on XY plane are:

$$p_{1,2} = -0.000234 \pm j6.3251 = -0.000234 \pm j(\omega_S + \omega_0)$$
$$p_{3,4} = 0.000231 \pm j6.2413 = -0.000231 \pm j(\omega_S - \omega_0)$$

The poles of the 2nd order system describing the dynamics along Z-axis are (same for inertial reference frame):

$$p_{5,6} = -1.551\ 10^{-6} \pm j0.0419 = -1.551\ 10^{-6} \pm j\omega_0$$

Without any external control action the whirl motion is unstable. The stabilization of whirl motion can be implemented by building in a rotating frame a damping command proportional to the relative velocity between bodies in the inertial (non-rotating) reference frame.

Figure 6.3-2 shows the magnitude of the transfer function between the force applied in X axis (Y axis) and the movement along X axis (Y axis). Figure 6.3-3 provides a zoom around spin rate (1 Hz) of the magnitude of the above transfer function: it is possible to recognize the effect of frequency shift of the suspension transfer function due to spacecraft and PGB spin rate. The disturbances at spinning frequency are not attenuated by the PGB suspension (natural frequency around 6.7 mHz). This is the reason why so fine drag compensation is required to the drag-free controller: drag is not attenuated by the PGB suspension but only by CMRR of the balance connecting the proof masses.

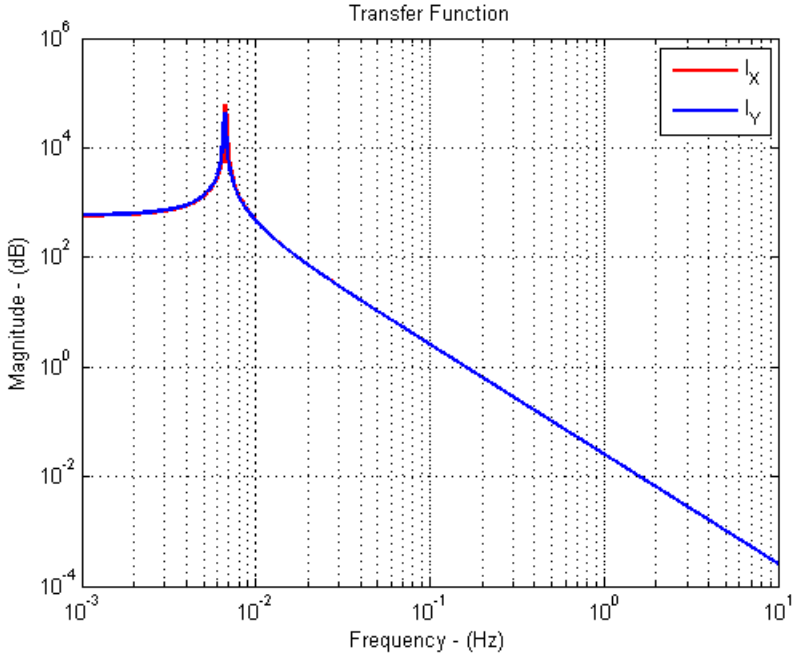

Figure 6.3-1: Force-displacement transfer function in the Inertial Reference Frame

Magnitude of the transfer functions between X force and X displacement (red), Y force and Y displacement (blue) in Inertial reference frame.

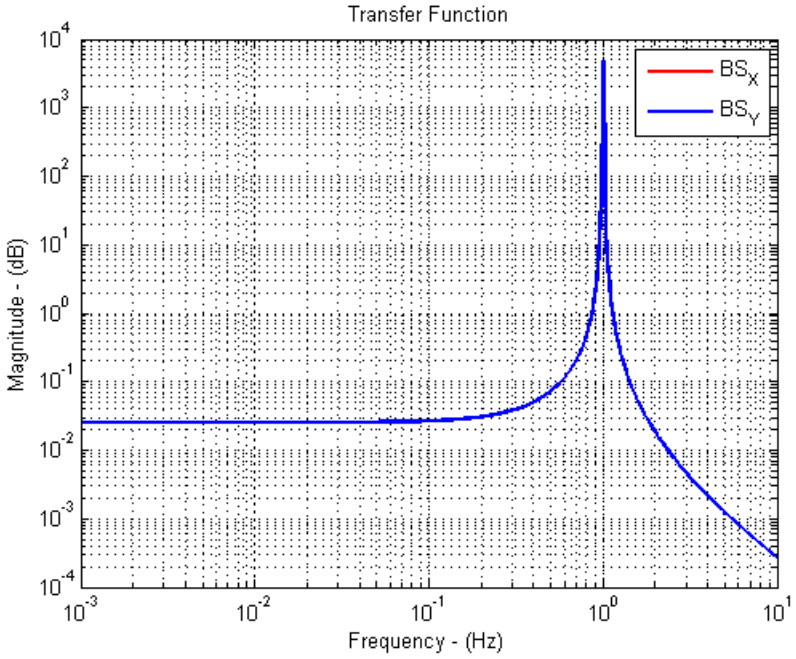

Figure 6.3-2: Force-displacement transfer function in the Body Reference Frame

Magnitude of the transfer functions between X force and X displacement (red), Y force and Y displacement (blue) in the Body reference frame.

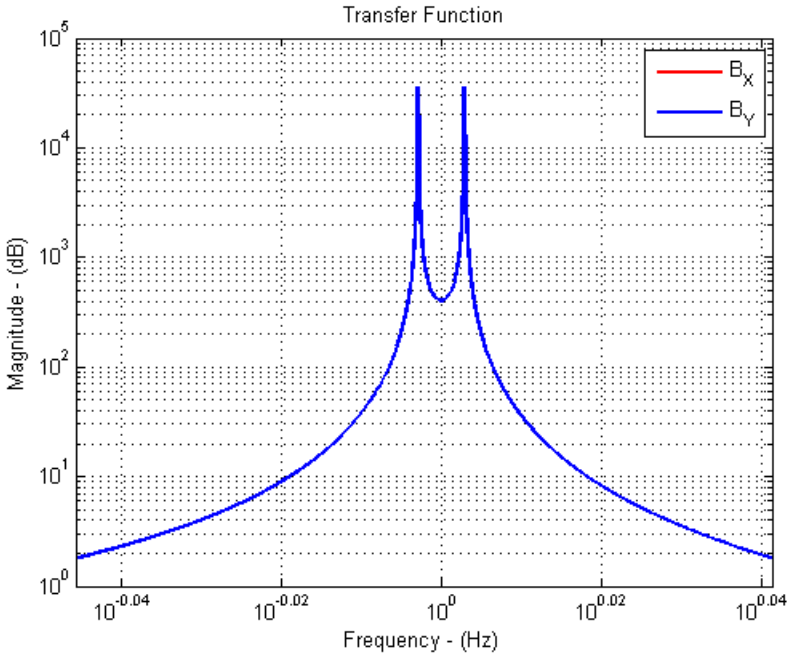

Figure 6.3-3: Force-displacement transfer function in the Body Reference Frame (zoom)

Zoom around 1 Hz of the magnitude of the transfer functions between X force and X displacement (red), Y force and Y displacement (blue) in the Body reference frame.

6.3.2 Architecture and algorithms

According to previous analysis, the designed controller has in charge:

- the stabilization of the relative displacement in the plane XY, limiting the magnitude;
- the rejection of any disturbances (drag is the expected major one, but others are solar pressure, thrusters noise, etc.) at spinning rate (1Hz) on overall axis;
- the stabilization of the spin rate versus variation of the spacecraft inertia moment due to thermo-elastic deformations. It is necessary to preserve the integrity of the suspension and sensors.

The controller has been organized according to the architecture provided in Figure 6.3-4.

There are three independent controllers:

- *XY drag-free controller* for drag compensation on the XY plane. The controller shall reduce the drag disturbances at spinning rate providing a rejection lower than $2\ 10^{-5}$;
- *XY whirl controller* for the stabilization of the movement in the plane XY. The controller shall stabilize the movement introducing a low-frequency action.
- *Z drag-free controller* for drag compensation and displacement reduction along Z axis.
- *Spin-axis angular rate controller*, to limit the relative rotation between PGB and satellite for suspension integrity.

XY drag-free controller is feed by measurement on relative XY displacement between PGB and spacecraft COM provided by capacitors sensors. The fine compensation occurs thanks to micro-thrusters assembly.

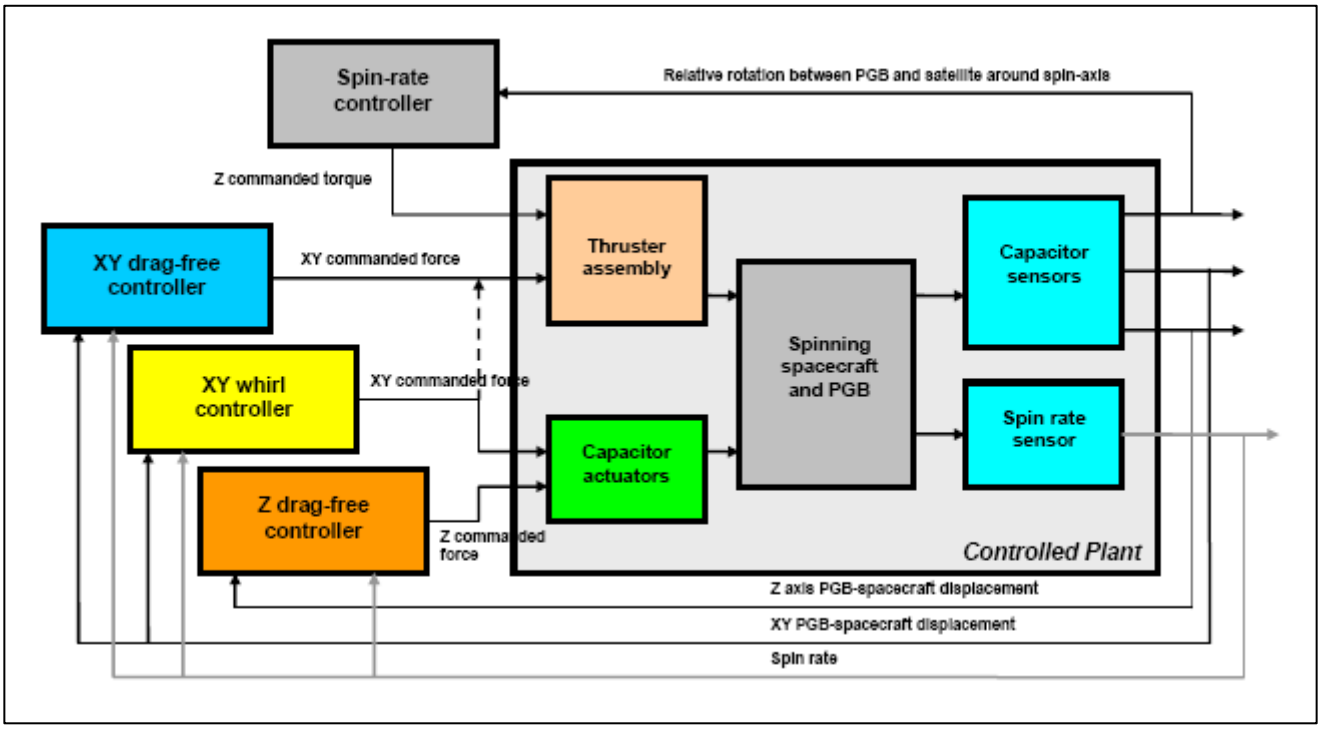

Figure 6.3-4: Linear axis control architecture

Also XY whirl controller is feed by measurement on relative XY displacement between PGB and spacecraft COM as for XY drag-free controller, and the actuation is realized by capacitors (out from DFM, when PGB is released by mechanism and micro-thrusters assembly disabled) and/or micro-thrusters assembly (during DFM, as alternative).

Z drag-free controller is feed by measurement on relative displacement along Z axis between PGB and spacecraft COM provided by capacitors sensors. Actuation is realized always by capacitors.

The spin-rate controller is driven by measurement on relative rotation around Z axis between PGB and spacecraft provided by capacitor sensors. Actuation is realized thrusters.

XY drag-free and XY whirl controllers are Multi Input Multi Output (MIMO) controller, and Z drag-free controller is a Single Input Single Output (SISO) controller.

All controllers have been designed according to the state variable approach building four lower level functions:

- state variable observer;
- control law;
- command distribution.

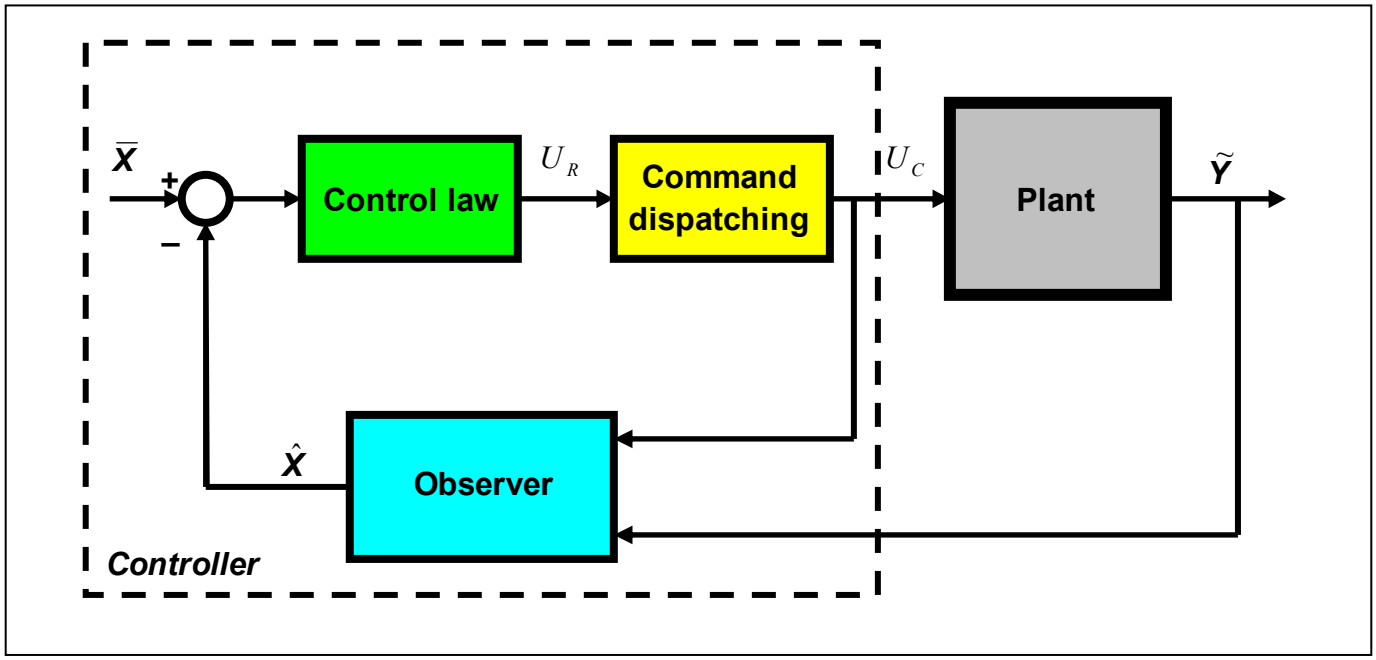

Figure 6.3-5: Block diagrams and functions considered for the algorithm design.

State observer has in charge the reconstitution in real-time of all relevant plant state variables. It embeds:

- the dynamic and kinematics plant models with acceptable and/or convenient simplifications;
- relative disturbance force/torque model acting on the spacecraft and PGB;
- feed-forward by commanded force/torque.

It is realized as a discrete dynamic system, according to the following state equation:

$$\hat{\boldsymbol{X}}(i+1) = \boldsymbol{A}\hat{\boldsymbol{X}}(i) + \boldsymbol{B}_U \boldsymbol{U}_C(i) + \boldsymbol{B}_Y \tilde{\boldsymbol{Y}}(i)$$

where

$\hat{\boldsymbol{X}}$: estimated state variables;
$\tilde{\boldsymbol{Y}}$: measured variables;
$\boldsymbol{A}$: state evolution matrix;
$\boldsymbol{B}_U$: command input matrix;
$\boldsymbol{B}_Y$: measure input matrix;
$\boldsymbol{U}_C$: command send to the actuator;
i : current sample step;
$i+1$: next sample step.

XY drag-free observer has been designed neglecting the coupling between X and Y axes obtaining two one-axis observers. This is possible since the design has been done considering the inertial reference frame and the high observer bandwidth. The model state variables are 5 for X axis observer and 5 for Y axis observer. They are the relative position and velocity, disturbance acceleration constituted by an integrator preceded by a harmonic oscillator. Each observer embeds the model given in Figure 6.3-6.

Z drag-free observer has been designed as for X and Y axes. The general model embedded in the one-axis observer is shown in Figure 6.3-6. X_0 represents the relative position, X_1 the relative velocity, X_2 the disturbance acceleration. Depending on the considered axis and the reference frame, specific values have been considered for α, β, ω_X and m_X.

Z spin rate observer embeds the double integration dynamics and a simplified disturbance torque model. The number of model state variables is 4; the observer is a 5^{th} order discrete model due to the introduction of a dynamic feed-back.

Usually, the control law function computes the required force based on the sum of the following terms:

- proportional to the difference between reference relative position and estimated one;
- proportional to the difference between reference relative velocity and estimated one;
- estimated disturbance force.

The general model is a linear combination of all estimated state elements, i.e.:

$$\boldsymbol{U}_R(i+1) = -\boldsymbol{K}\hat{\boldsymbol{X}}(i+1)$$

.

In the XY and Z drag-free controllers the above approach has been totally followed. Instead in the XY whirl controller, the commanded force is proportional to the actual linear velocity in the inertial reference frame and it takes into account the estimated disturbance force.

Starting from the required force provided by control law the command distribution computes:

- the command to be send to each actuator in the assembly;
- the resultant commanded force taking into account actuator resolution, saturations, etc. Resultant commanded force is fed to the observer.

Observers' gains and control law gains have been computed according to pole placement approach. Controllers sampling frequency has been fixed to 10Hz (1 order of magnitude higher than the spacecraft spin rate).

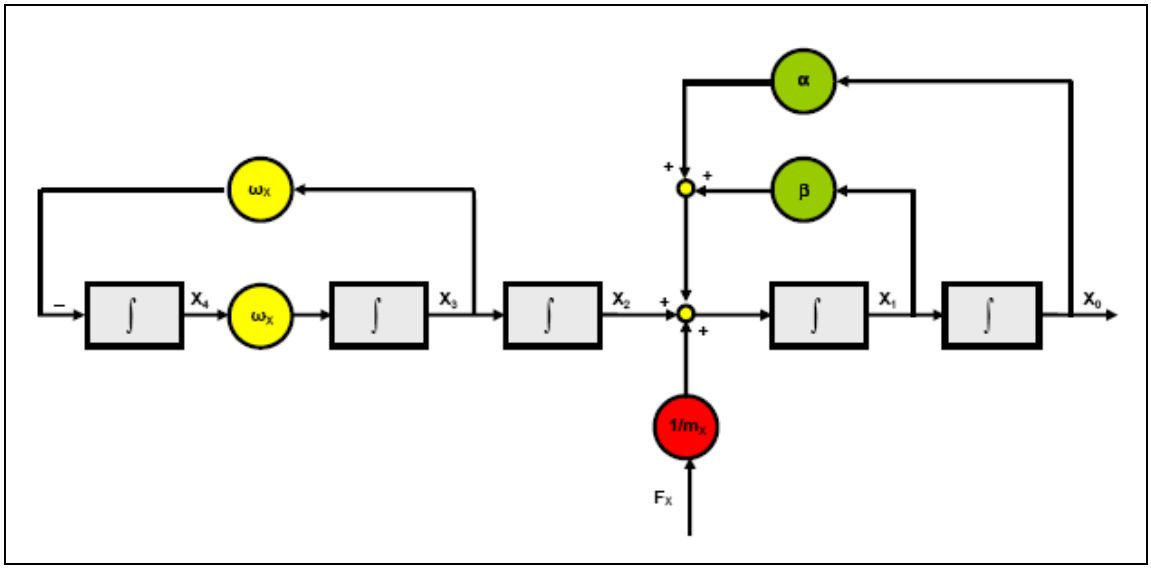

Figure 6.3-6: Model embed in the one-axis observer (X , Y and Z axes).

The dispatching is a non-linear function that computes the thrust to be applied to each thruster in order to provide the required forces and torques. Formally

$$\boldsymbol{U}_C(i+1) = \boldsymbol{Dispatching}\left(\boldsymbol{U}_R(i+1)\right)$$

$\boldsymbol{U}_R$: required command (force and torque);

$\boldsymbol{U}_C$: command send to the actuator.

Depending on the available computation capabilities, the dispatching function may be based on different algorithms. Correct design of such a function is a key point for fuel saving. Here, the application of simplex like algorithms (linear programming for the solution of an optimization problem) will be considered.

The observer embeds an harmonic oscillator to achieve the very high required disturbance rejection taking into account the sampling frequency limitations. As well known from literature, the rejection is very high only in an interval of frequencies very little around the value considered for the design. Rejection greater than 25000 may be achieved only for if $\left|\frac{\tilde{\omega}_S - \omega_S}{\omega_S}\right|$ is lower than 10^{-4}. The angular rate shall be well known also for whirl controller but with less stringent accuracy.

6.4 Actuators for fine drag compensation

The capability to compensate the disturbances at spinning rate strongly depends on the actuator performances. Low thrust, low noise and resolution thrusters are required.

Two technologies have been considered, both leaded by Italian industries:

- Field Emission Electrical Propulsion (FEEP) from ALTA S.p.A.;
- Cold gas propulsion system (CGPS) from TAS-I S.p.A.

FEEP is an electrostatic propulsion concept based on field ionization of a liquid metal and subsequent acceleration of the ions by a strong electric field. They are characterized by high specific impulse, very low noise and resolution, fast response time (tens of milliseconds) but also high electric power consumption.

Cold gas micro-propulsion is based on the well-know cold-gas technology, with significant improvements and new concepts on pressure regulation stage, mass flow-sensor, thrust valve, control algorithms. They are characterized by low specific impulse (about two orders of magnitude lower than FEEP), very low noise and resolution, slow response time (hundreds of milliseconds).

The status of both technologies with respect to the requirement reported in Table 6.2-2 will be provided in the next chapters.

6.4.1 FEEP thrusters

FEEP Thrusters are being developed for the ESA Lisa Pathfinder (LPF) mission and the CNES Microscope mission (see Figure 6.4-1).

Thruster development is nearly completed, and the preparation of the Lisa Pathfinder FEEP Cluster Assembly (FCA) Qualification Model is ongoing. Manufacturing of FM parts for LPF was also released. Microscope programme is currently on hold, pending completion of thruster development.

During thrusters development phase, the following results were achieved:

- demonstration of priming principle and repeatability (6 thrusters in a row were successfully activated and fired);
- full performance characterization;
- demonstration of endurance up to more than 1000 Ns (> 3200 hours firing);
- successful performance of environmental testing (sine + random vibration, thermal balance);
- direct thrust measurement (ongoing at TAS-I Turin);
- neutral flow measurement characterization (ongoing at ONERA Palaiseau).

Table 6.4-1 permits the comparison of the Galileo Galilei requirements with the currently available FEEP performances. It is possible to see that the major not compliant of already available Lisa Pathfinder equipment are related to the response time and the centrifugal accelerations. Both are not considered critical by manufacturer, pending additional activities to be executed during phase B. ALTA has already outlined possible design solutions.

LISA Pathfinder (ESA – Technology demonstration for LISA)

Microscope (CNES - Equivalence principle)

Figure 6.4-1: ESA missions based on FEEP micro-propulsion.

No	Parameter	Unit	Value	FEEP status
1	Maximum thrust	µN	>=150	Thruster is designed and currently being qualified for a maximum thrust of 150 µN. Command capability is, at present, greater than 204.8 µN, and thrust up to 540 µN was recorded during one test
2	Max thruster response time	ms	40	Current response time (for 60 µN step from 0 to 60 µN) is about 80 to 150 ms, (depending on thrust and up or down command), with command frequency at 10 Hz. Step response can be improved up to 30-40ms reducing internal delay, fall time, by biasing minimum thrust (e.g. working with thrust higher than 70 µN) and/or adding some internal dissipation.
3	Resolution (quantization)	µN	24	Thruster/PCU are designed and currently being qualified for a thrust resolution of 0.1 µN
4	Max noise	µN/√Hz	18	The thruster is being qualified for 0.03µN/√Hz (range 0.006 to 5 Hz)
5	Scale factor error	%	12	PCU allows scale factor correction and re-calibration with a 12 bit resolution (individual command correction). Requirement is not deemed critical.
6	Update command rate	Hz	10	Already available for Lisa Pathfinder
7	Total impulse	Ns	4500	Thruster is designed vs. a requirement of 2900 Ns (Lisa Pathfinder). Life test (on QM) will be performed up to 1100 Ns (with possible extension to higher total impulse). Analysis will be performed to predict EOL performance. At present, > 1000 Ns were verified at EM level.
8	Minimum thrust	µN	<=10	Thruster is designed and currently being qualified for a minimum thrust of 0.3 µN.
9	Vector stability	rad	0.17	For thrust greater than 10 µN is always met.
10	Centrifugal acceleration	g	<4.4	Not met by current design. Modification of thruster design, and, in particular, of tank position and shape, to minimize hydrostatic head will permit to achieve the requirement.

Table 6.4-1: Status of FEEP thrusters with respect to GG requirements

Figure 6.4-2 shows the FEEP cluster assembly designed for Lisa Pathfinder and representatives for the GG design. Each cluster consists of:

- 4 thrusters;
- the supporting and interface structure;
- the required thermal control hardware;
- the necessary harness, including low voltage connectors and high voltage flying leads.

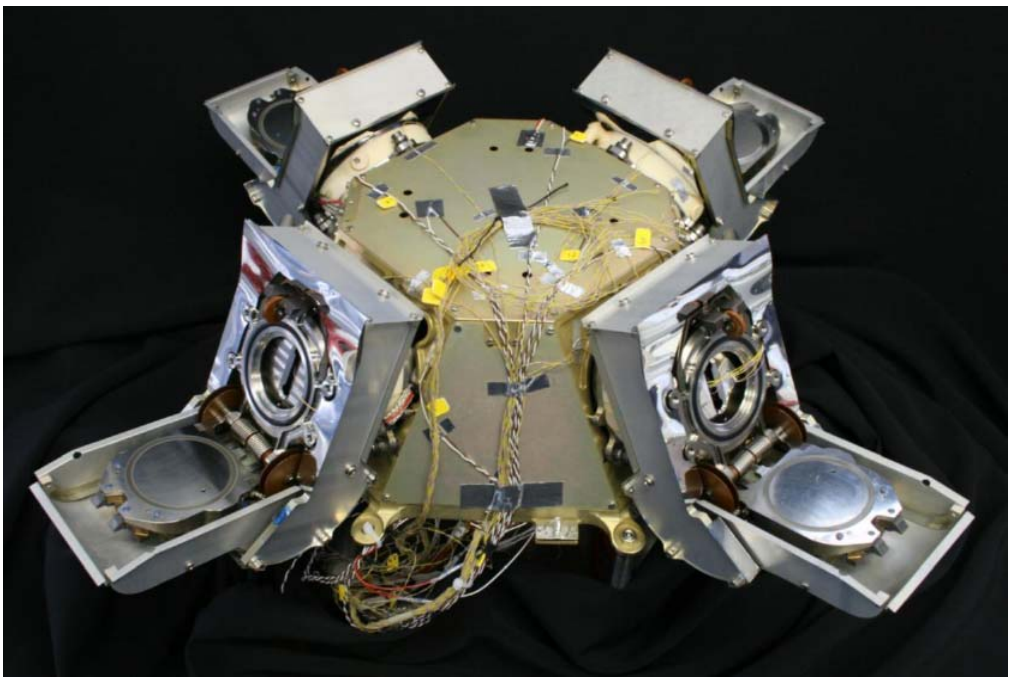

Figure 6.4-2: FEEP cluster assembly for Lisa Pathfinder.

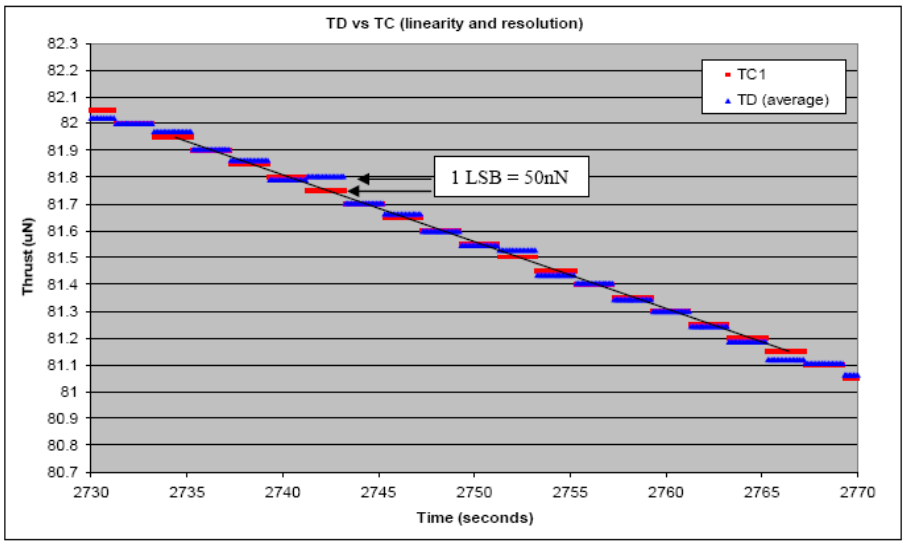

Figure 6.4-3: FEEP thrusters resolution.

As every ion thrusters, FEEP is prone to arc discharge events (arcing). Arc discharge occurs usually between emitter and accelerator electrodes (i.e., it is an event internal to the thruster). The discharge event lasts between 2 and 10 µs. After that, voltage drops down and thrust is temporarily interrupted. Thrust is recovered after the capacitors of PCU are recharged. Typical time is that of thrust command response (for a 0 to nominal thrust step).

Figure 6.4-4 shows the observed percentage of sparks versus time between sparks. Figure 6.4-5 shows the spark rate versus the thrust level. Taking into account the frequency of arcing occurrence and the duration, the expected effect will be the introduction of a transient in drag-compensation that will increase the noise to be considered for post-processing. In a case, this aspect will be considered in the next study phase.

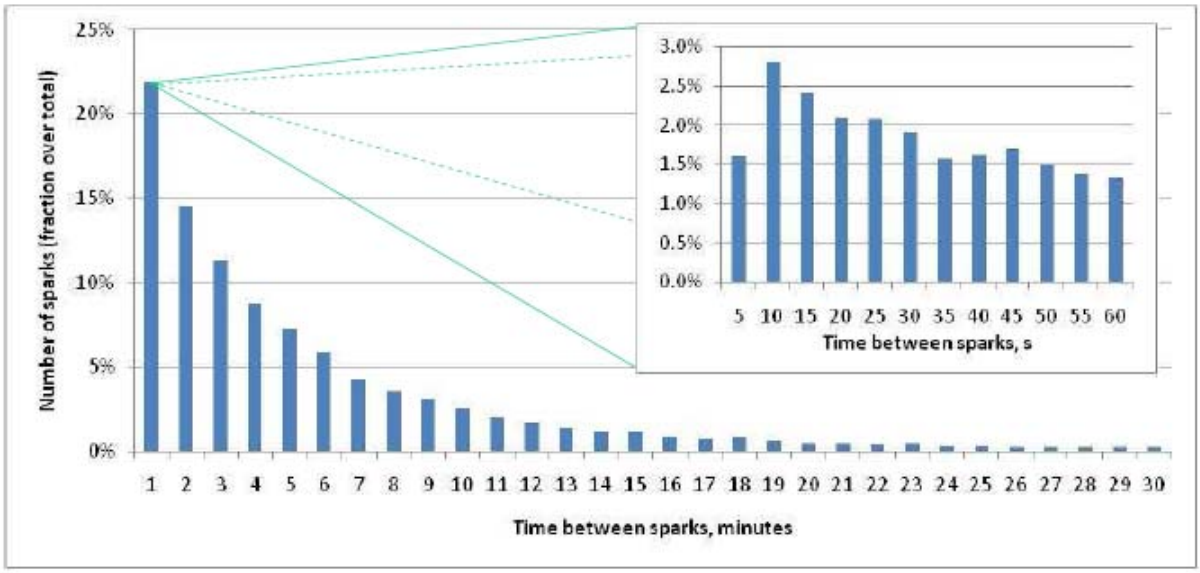

Figure 6.4-4: Percentage of sparks vs. time between sparks

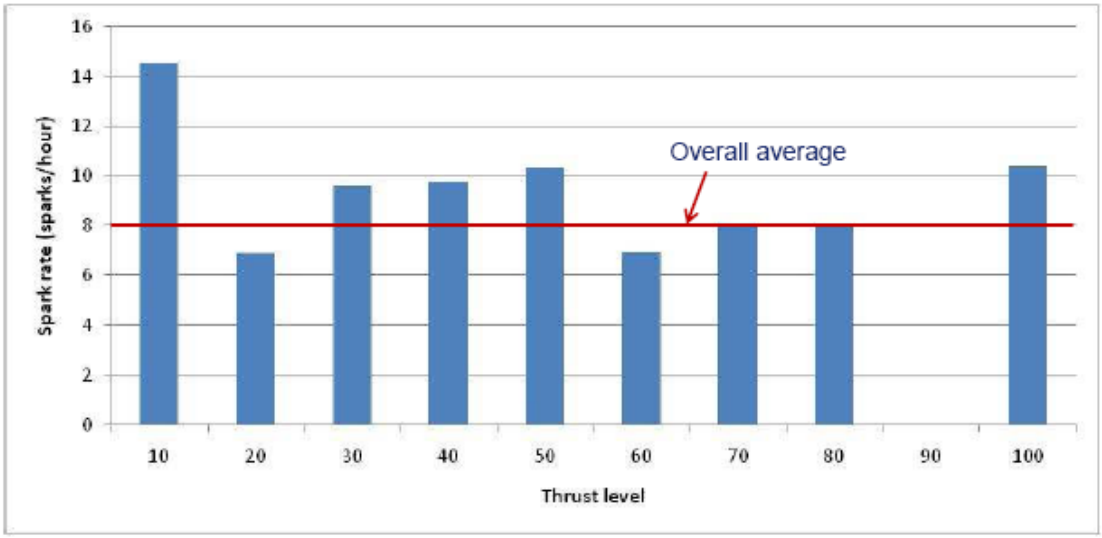

Figure 6.4-5: Spark rate vs. thrust level.

6.4.2 CGPS thrusters

GAIA Micro Propulsion system (MPS), currently under qualification at TAS-I, represents the reference design and technology starting points for configuring/realizing both Microscope and Galileo Galilei.

Improvement will be provided using an EPR (Electronic Pressure Regulator) instead then a MPR (Mechanical Pressure Regulator) for realizing the PRS (Pressure Reduction & Regulation Stage)

The main advantages of an EPR based on regulation valves as actuating elements are.

- fully European technology (key components are TAS-I products);
- no ITAR exportation/importation problems;
- extremely low leakage (at least one order of magnitude better than the MPR);
- very low ripple in the regulated low pressure;
- high degree of flexibility (regulated low pressure selectable according to a specified set point);
- contained mass and dimensions.

Table 6.4-2 permits the comparison of the Galileo Galilei requirements with the currently available CGPS performances. It is possible to see that the major not compliant of already available GAIA equipment are related to the response time and the command rate. Both are not considered particularly critical by manufacturer, pending additional activities to be executed during phase B for electronic box and control algorithm re-design.

Figure 6.4-6 shows the spectral density of the thruster noise measured by Nanobalance facility in Torino. Figure 6.4-7 reports pictures of key devices used by the MPS.

No	Parameter	Unit	Value	CGPS Status
1	Maximum thrust	μN	>=150	Thrust levels up to 500 mN achievable
2	Max thruster response time	ms	40	about 100 ms: commanded thrust level below 50 mN: 100 to 200 ms: commanded thrust level in the 50 to 500 mN range
3	Resolution (quantization)	μN	24	1 μN achievable with the current GAIA Design
4	Max noise	μN/√Hz	18	1 μN/√Hz from 0.01 Hz to 1 Hz 0.045 μN/√Hz from 1 Hz to 150 Hz achievable with GAIA design
5	Scale factor error	%	12	1 for GAIA
6	Update command rate	Hz	10	1 Hz for GAIA
7	Total impulse	Ns	4500	Same Total impulse figure required for GAIA 700 million cycles at 10 Hz, in open loop, performed on the TV EM
8	Minimum thrust	μN	<=10	1 μN achievable with the current GAIA Design
9	Vector stability	rad	0.17	No data available at the moment, not critical
10	Centrifugal acceleration	g	<4.4	No risk of valve opening induced by the centrifugal force has been recognized. In fact, the centrifugal force (0.174 kg) is lower than the spring strength (1 kg).

Table 6.4-2: Status of Cold Gas Propulsion System with respect to GG requirements

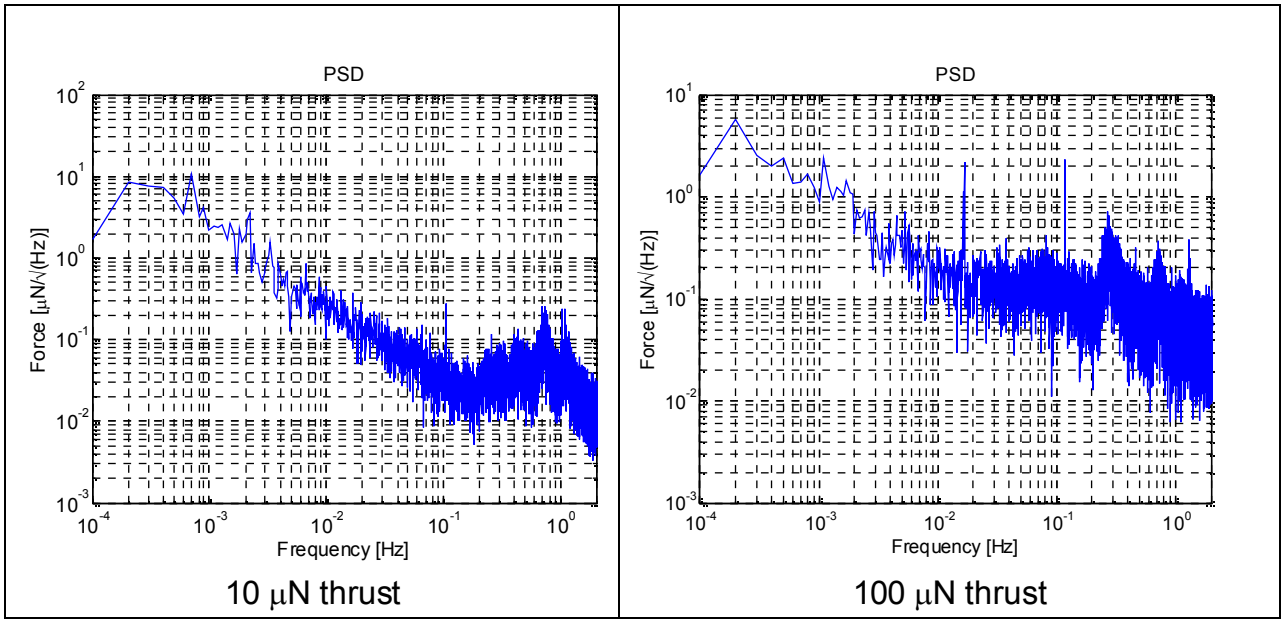

Figure 6.4-6: Spectral density of the cold gas thrusters noise measured by the Nanobalance facility (TAS-I).

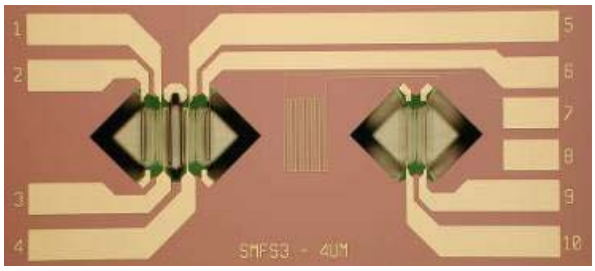

Mass Flow Sensor implemented in a Si Chip (new layout)

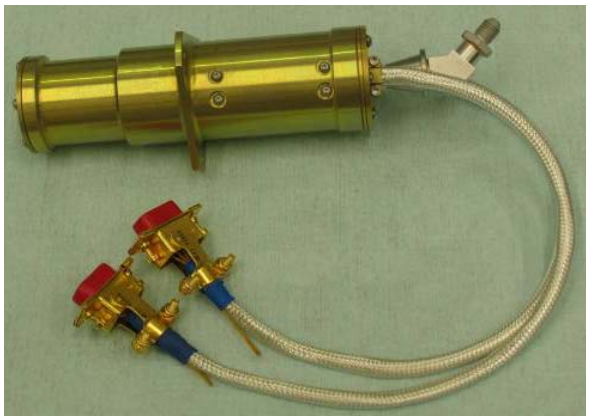

Micro Thruster EQM model assembled in view of qualification Campaign vs. GAIA requirements

Thrust Valve EQM for GAIA MPS

Low Pressure Regulation Valve with Nozzle (cutaway) close up

Figure 6.4-7: Pictures of the major CGPS component.

6.5 Spin rate sensor

Taking into account the unavailability of off-the-shelf equipment due to high relative accuracy and high angular rate (at beginning of Phase A2 the required angular rate was 720deg/s), specific equipment has been designed by TAS-I in cooperation with SILO. During the Phase 2 the design has evolved, and, taking into account the lower spin rate, other solutions may be considered too. In early Phase B, the use of such sensor will be addressed again, to provide the most effective solution (cost, performances).

A small telescope endowed with Position Sensing Detectors (PSD) as focal plane detects Sun position from the position of the light spot focused on the PSD.

Sensor main features are:

- square camera design to detect Sun for the whole year
  - Field Of View (FOV) corresponding to Sun annual declination range i.e. ± 25°
- optical system focusing light spot on PSD sensing area
- PSD outputs:
  - Optical power of detected light source i.e. Sun
  - Coordinates of light spot focused on PSD sensing plane, translating into angular measurement of Sun position.

The sensor accommodation will be normal to the satellite spin axis.

The internal section view is provided in Figure 6.5-1.

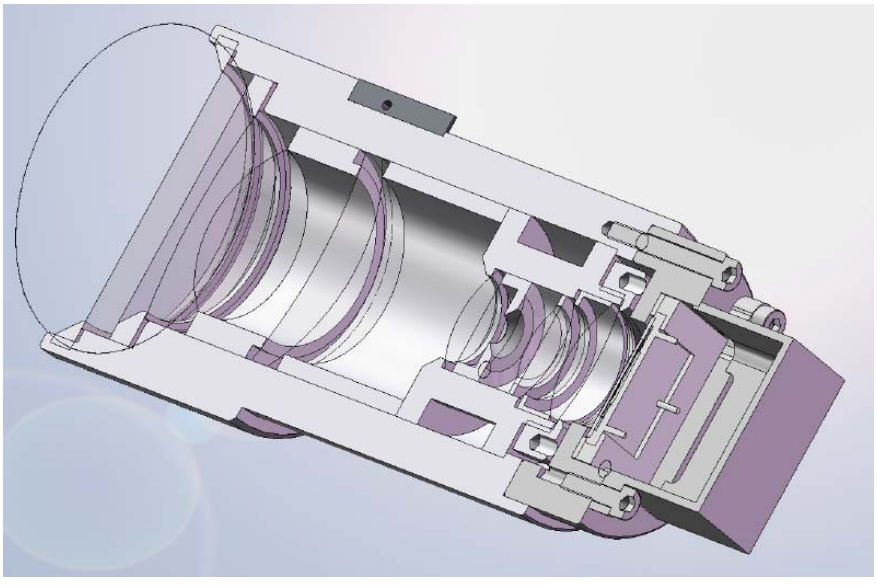

Figure 6.5-1: Spin rate sensor - Internal section view

6.6 Simulation results

In the following, the major results related to most challenging XY drag-free and XY whirl controllers will be provided. Equipment parameters have been considered in agreement with the specified values.

The presentation has been organized in lower level chapters devoted to:

- simulated perturbing force;
- XY state variables trajectory without whirl and drag controls;
- XY state variables trajectory with whirl control and without drag control;
- XY state variables trajectory with whirl and drag controls.

6.6.1 Simulated perturbing force

The simulated perturbing force takes into account the drag only. The drag force profile time series and its amplitude spectrum both given in the inertial reference frame are shown in Figure 6.6-1 and in Figure 6.6-2 respectively. Figure 6.6-3 shows the drag force in body reference frame with spacecraft spin rate equal to 1Hz.

Drag force amplitude has been scaled in order to provide a maximum linear acceleration equal to 0.2 10^{-6} m/s². The orbital period is about 5800s (600km).

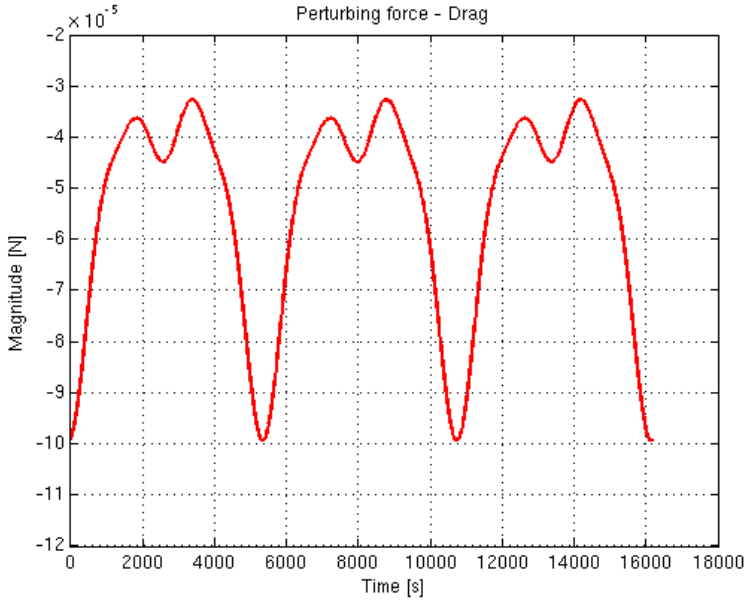

Figure 6.6-1: Time series of the XY plane perturbing force (inertial reference frame)

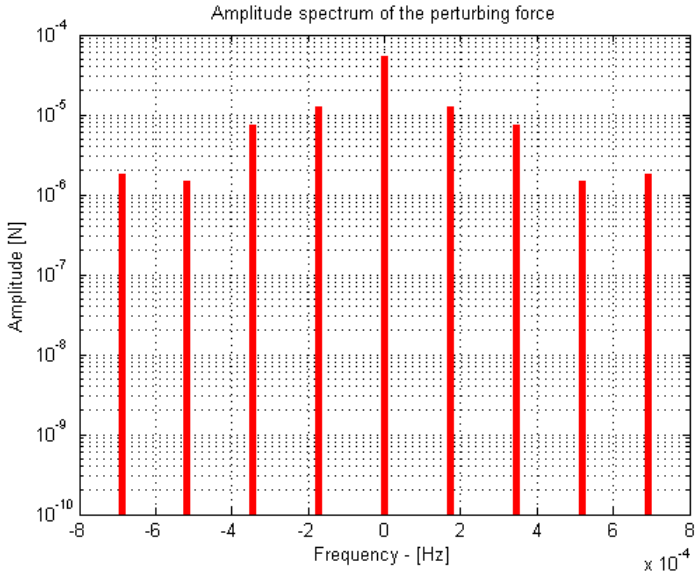

Figure 6.6-2: Spectrum of the XY plane perturbing force (inertial reference frame)

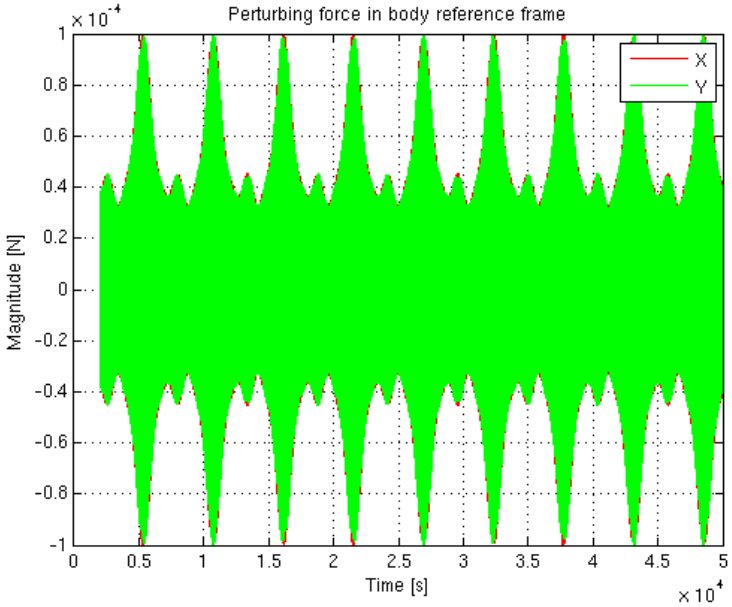

Figure 6.6-3: Time series of the XY plane perturbing force (body reference frame)

6.6.2 XY state variable trajectory without whirl and drag controls

Figure 6.6-4 shows the XY displacements as function of time without whirl and drag-free controllers. The growing of magnitude of X and Y relative positions due to instability is evident. Figure 6.6-5 shows a zoom of the XY movements.

Figure 6.6-6 and Figure 6.6-7 provide the XY displacements in phase diagram.

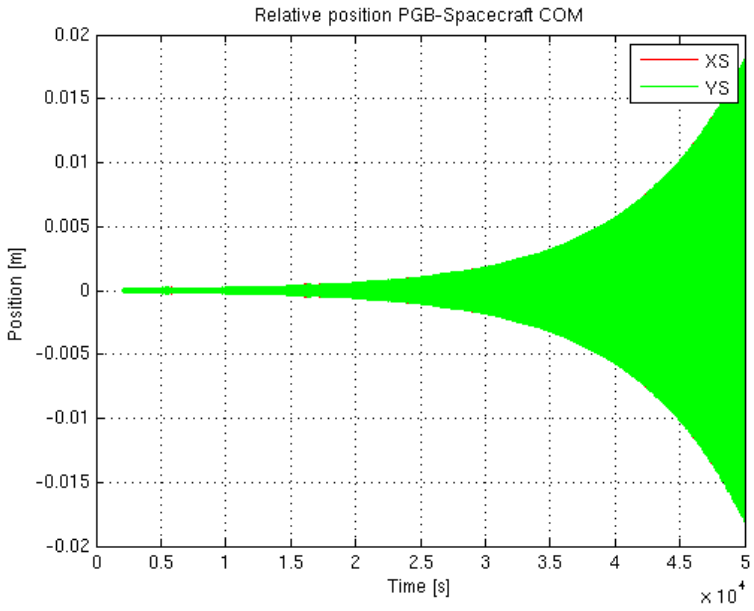

Figure 6.6-4: Time evolution of the PGB- spacecraft COMs relative position

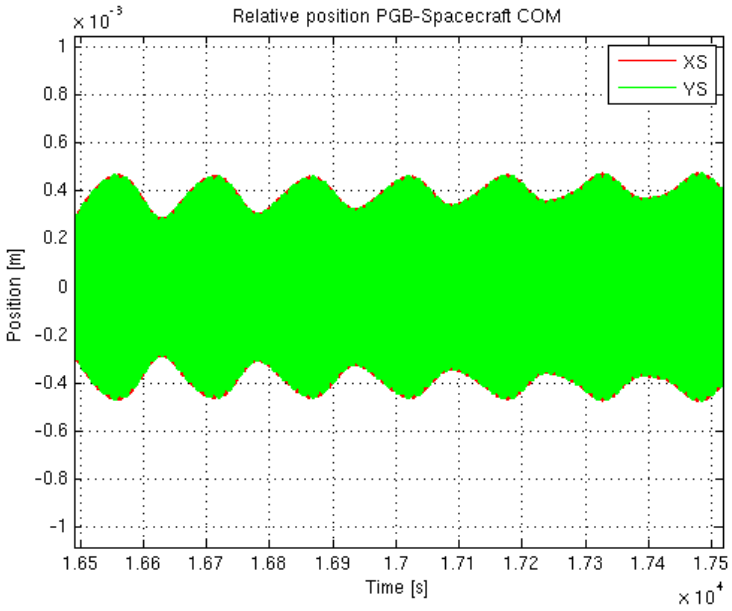

Figure 6.6-5: Time evolution of the PGB- spacecraft COMs relative position (zoom)

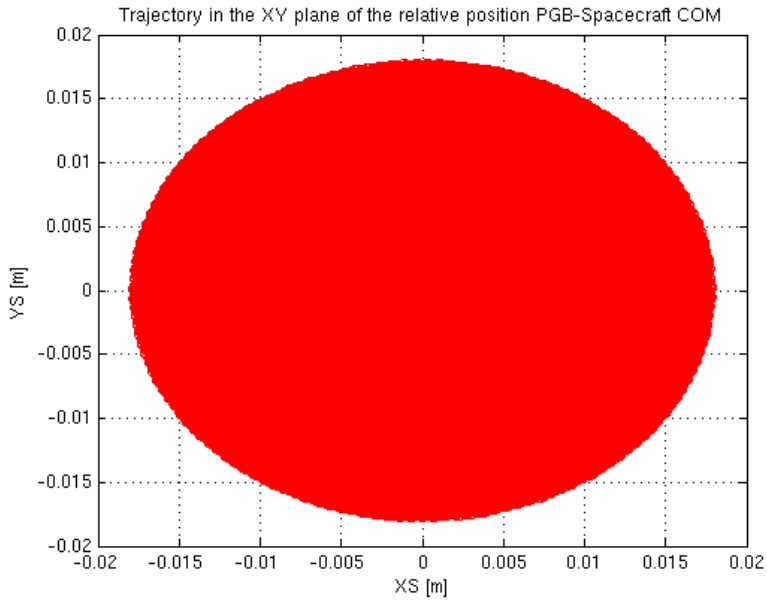

Figure 6.6-6: Phase diagram of the PGB- spacecraft COMs relative position

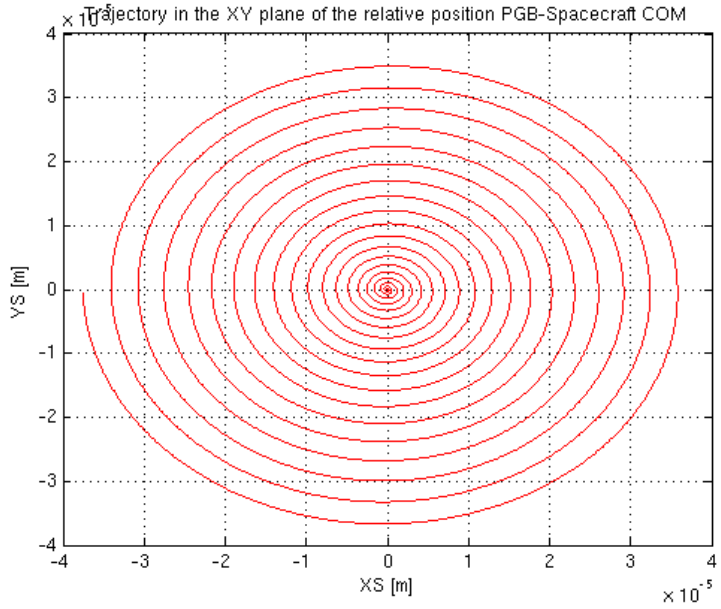

Figure 6.6-7: Phase diagram of the PGB- spacecraft COMs relative position (zoom)

6.6.3 XY state variables trajectory with whirl control and without drag control

Figure 6.6-8 and Figure 6.6-9 show the XY displacements as function of time with whirl control and without drag-free control. The pictures show the effectiveness of the stabilization introduced by control law.

Figure 6.6-10 and Figure 6.6-11 show the one-side spectral density of the XY PGB-spacecraft relative position given in the body reference frame. It is possible to recognize around 1 Hz the lines due to the perturbing force spectrum (see also Figure 6.6-2). The maximum value of the relative position spectral density around 1Hz, computed with a frequency resolution equal to about 2 10^{-5} Hz, is 7 10^{-3} m/√Hz.

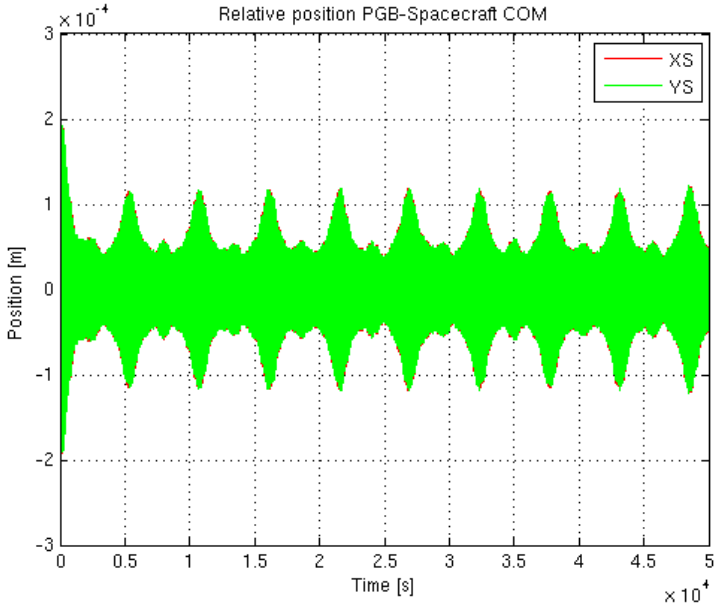

Figure 6.6-8: Time evolution of the PGB- spacecraft COMs relative position (body reference frame)

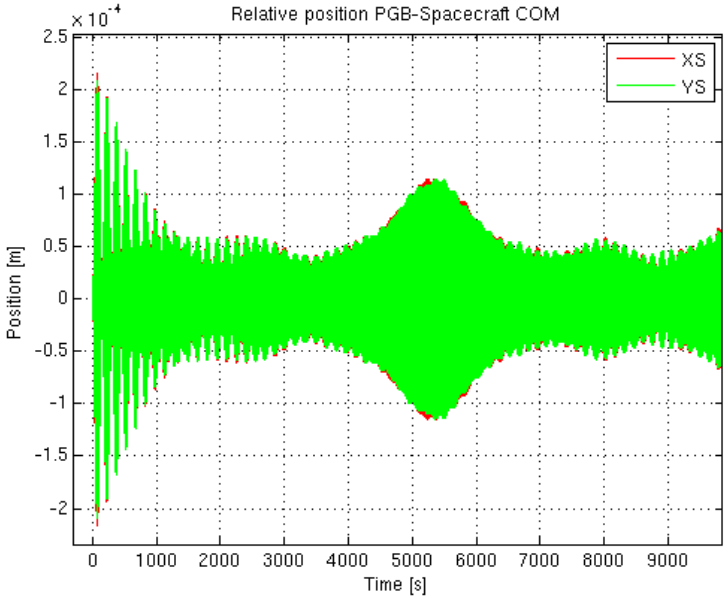

Figure 6.6-9: Zoom of the PGB- spacecraft COMs relative position (body reference frame)

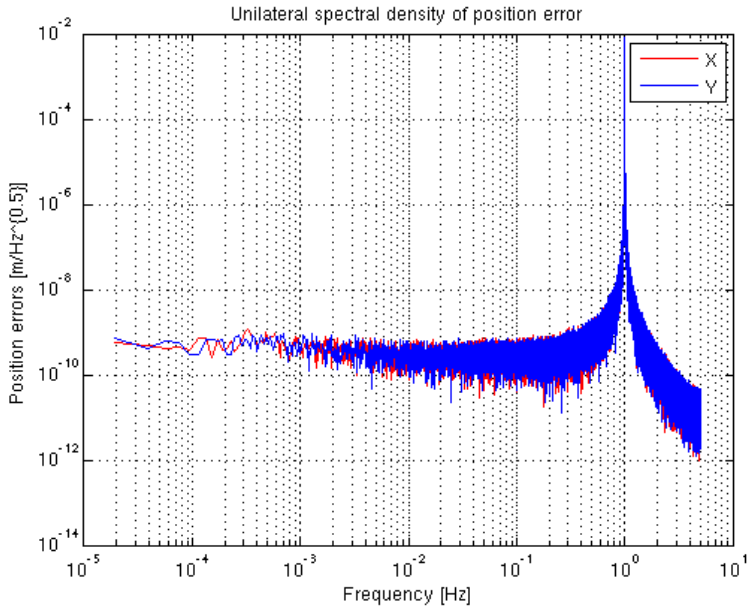

Figure 6.6-10: One-sided spectral density PGB-spacecraft COMs relative position (body reference frame)

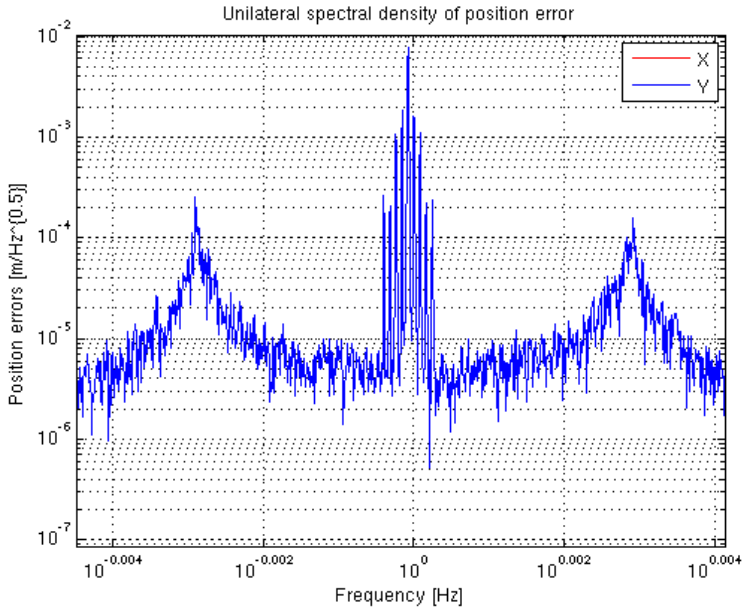

Figure 6.6-11: Zoom around 1Hz of the previous figure

Zoom around 1Hz of the one-side spectral density PGB-spacecraft COMs relative position (body reference frame)

6.6.4 XY state variables trajectory with whirl and drag controls

Results provided in the pictures below have been obtained considering a relative uncertainty on spacecraft spin rate equal to 10^{-4} Hz (one order of magnitude worse that the required value).

Two cases have been considered:

- without capacitor sensors measurement noise (Figure 6.6-12, Figure 6.6-13, Figure 6.6-14 and Figure 6.6-15). This case is relevant to appreciate the drag compensation capabilities provided by the designed control;
- with capacitor sensors measurement noise (Figure 6.6-16 and Figure 6.6-17). It permits to see the end performances, to be considered for scientific post-processing.

Comparing the maximum spectral density around 1Hz given in Figure 6.6-11 and Figure 6.6-15, it is possible to observe that the rejection of drag disturbances provided by the XY drag-free controller is better than 1/150,000 with a relative uncertainty on angular rate knowledge equal to 10^{-4}.

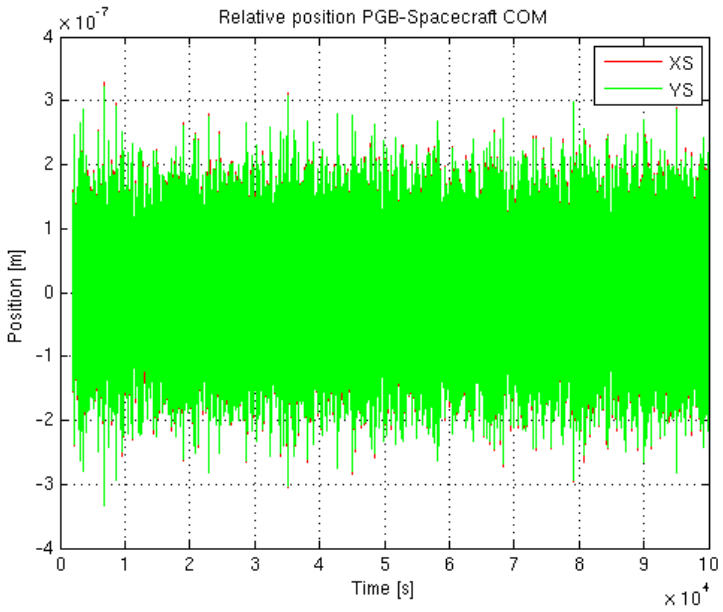

Figure 6.6-12: Time evolution of the PGB- spacecraft COMs relative position (body reference frame, without measurement noise)

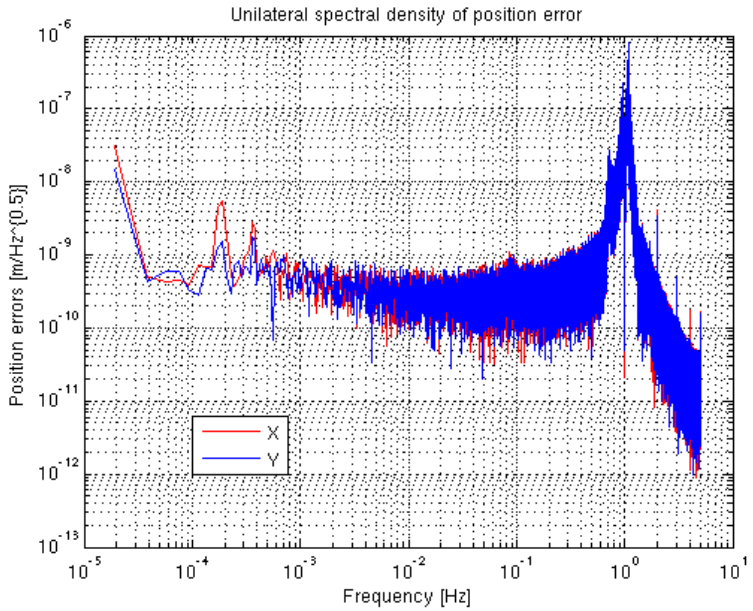

Figure 6.6-13: One-side spectral density PGB- spacecraft COMs relative position (body reference frame, without measurement noise)

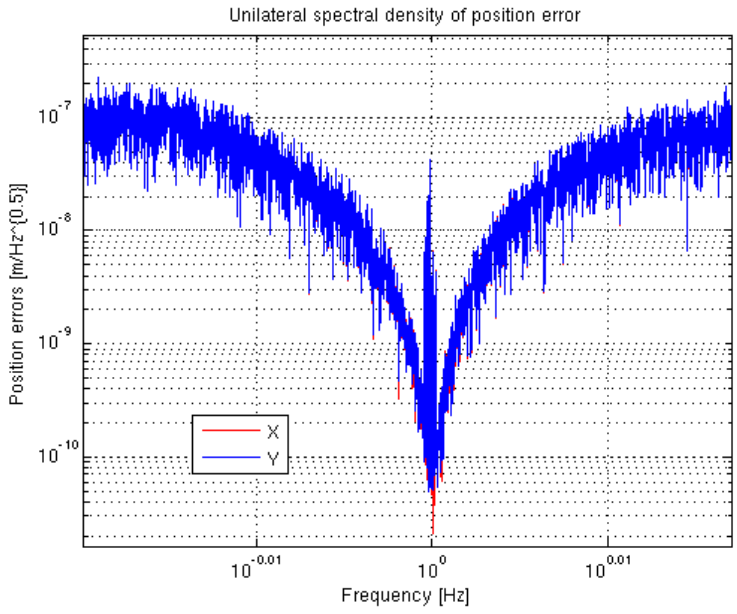

Figure 6.6-14: Zoom around 1Hz of the one-side spectral density PGB- spacecraft COMs relative position (body reference frame, without measurement noise)

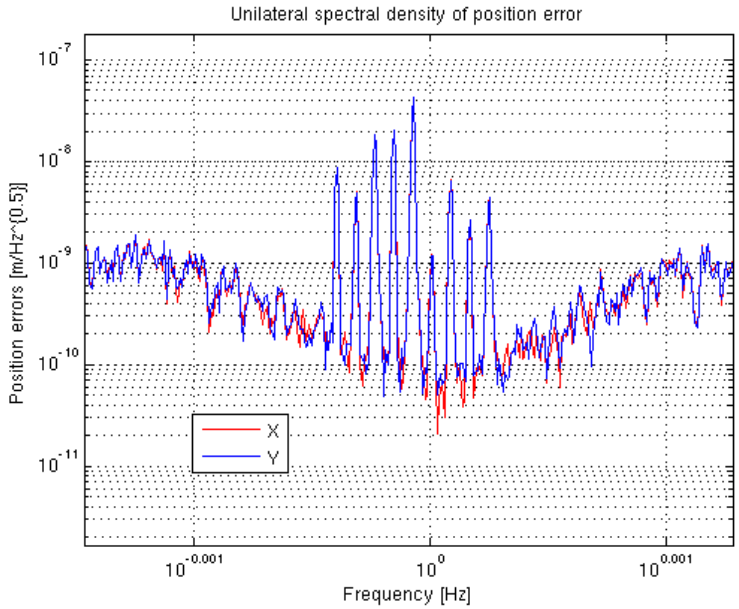

Figure 6.6-15: Zoom around 1Hz of the one-side spectral density PGB- spacecraft COMs relative position (body reference frame, without measurement noise)

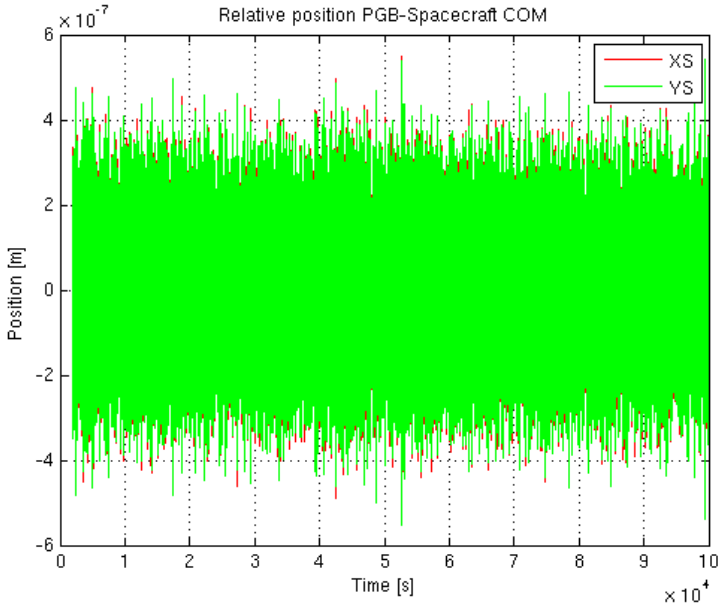

Figure 6.6-16: Time evolution of the PGB- spacecraft COMs relative position (body reference frame, with measurement noise)

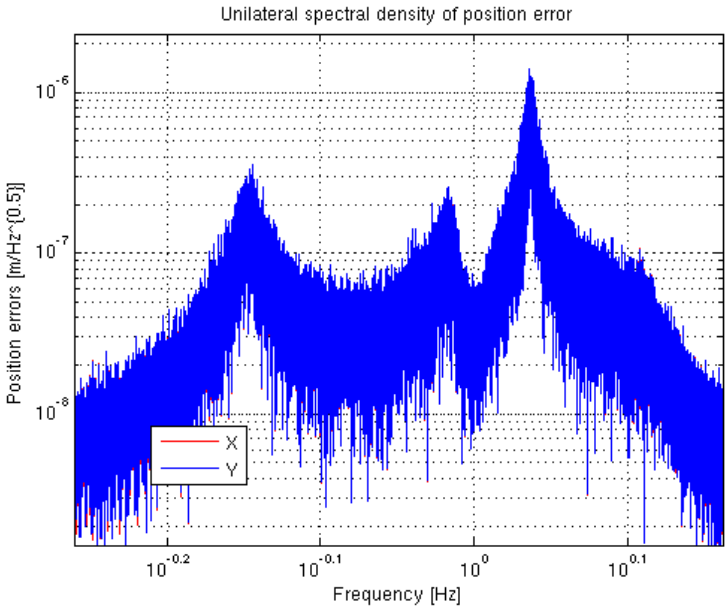

Figure 6.6-17: Zoom around 1Hz of the one-side spectral density PGB- spacecraft COMs relative position (body reference frame, with measurement noise)

7. SPACE EXPERIMENT SIMULATOR

7.1 Motivation and Background

Space missions in Fundamental Physics like GG require high precision experiments to be performed in space with no direct access to the apparatus once in orbit. Though this is commonplace for all space missions, space missions at large do not rely on weightlessness as a key feature for the experiment performance. To the contrary, GG as well as other missions in this field (e.g. GP-B, Goce, μScope, Lisa-PF, Step, Lisa …), are designed to perform experiments in absence of weight. Therefore, the experimental apparatus is designed and built to work at zero-g, not at 1-g, and the issue arises as to how effectively such an apparatus can be tested in the lab before launch, and what are the chances for the space mission to perform as expected.

Since flight opportunities are scarce –especially for basic science– and flying a mission, even in Low Earth Orbit, is typically as expensive as large ground projects, it is a must to provide firm evidence before launch that chances to succeed are high.

Considerable effort has been devoted during several years in order to provide strong evidence for the success of the GG mission.

This is done by proceeding along the following three lines:

- Build up a numerical Space Experiment Simulator of the GG mission in space based on the best know-how available to the most advanced space industries, particularly those with direct expertise in missions which fly zero-g designed payloads
- Build up a prototype in the lab which is demonstrated to have the key physical features of the payload to fly, and provide experimental evidence that the major requirements of the space mission are met
- Feed the values of the physical parameters measured in the lab into the Space Experiment Simulator to assess the overall performance of the GG mission.

It is apparent that this is a very challenging plan. Space industry should have the capability required; the payload should have been designed so that a 1-g version of it can be built which maintains its key features; the scientific and industrial teams should be able to work in very close collaboration.

All such conditions are met in GG, in terms of space industry specific know-how, of physical design of the experimental apparatus for it to be significantly tested in the lab, as well as for what concerns a well established tradition of close collaboration between scientists and space industry.

Thales Alenia Space Italy (To) is well equipped to perform the task of building a GG Space Experiment Simulator. In its capacity as prime contractor of the GOCE mission of ESA, TAS-I designed, built, tested and demonstrated the performance of, a complete Space Experiment Simulator for this mission, which has considerable commonalties with GG.

GOCE, launched successfully on March 17th from the Plesetsk cosmodrome in northern Russia, is a very challenging high-tech mission devoted to measuring the gravitational field of the Earth to very high degree and order. It is therefore equipped with very sensitive accelerometers arranged in diamond configuration to accurately measure gravity gradient effects. The accelerometers –designed and built by ONERA (Chatillon, France)– are based on a "free floating" test mass with electrostatics bearing and pick up. Though a tiny mechanical connection is added in order to provide passive electrostatic grounding, the accelerometers as such can work only at zero-g and no full test is possible in the lab. ONERA –with the support of CNES– has indeed already flown similar accelerometers (onboard the Space Shuttle, as well as in previous satellite geodesy missions such as CHAMP and GRACE). However, being the tasks of GOCE more challenging, a Space Experiment Simulator was built by Thales Alenia Space in Torino to check the consistency of spacecraft and payload specifications with the overall system requirements, to support trade-off, sensitivity and worst-case analyses, to support design and pre-validation testing of the Drag-Free and Attitude Control (DFAC) laws, to prepare and test the on-ground and in-flight gradiometer calibration concepts, to prototype the post-processing algorithms, and to validate the performance of the mission. The GOCE simulator has been extensively used during the design and construction of the spacecraft and payload and is the centrepiece of the flight commissioning and calibration activities being carried out at this time.

A delay in the readiness of the launcher has postponed the launch of GOCE by several months, but the satellite is now flying in its low Earth orbit, thus allowing in particular putting the numerical Simulator itself under the most stringent test.

The GG Space Experiment Simulator was initiated –with ASI support– since the first study of the mission, precisely because it was immediately rated as a crucial validating tool. This preliminary simulator allowed the basic physical features of the GG system to be identified and checked; however, it was still too simplified (e.g., it was mostly a 2-dimensional model).

Building up on the expertise acquired with the GOCE Simulator, the GG Space Experiment Simulator could be raised to a very advanced level in the very short time of the GG Phase A2 study. Furthermore, by incorporating in it the physical parameters as experimentally measured in the lab with the Payload Prototype, the accuracy of the simulation was correspondingly enhanced. The combination of (a) flight validation of the orbit and spacecraft environment simulation and (b) lab validation of the experiment parameters, makes the GG simulator an extremely reliable performance validation tool, the like of which was seen in no other similar mission.

7.2 GG Simulator Architecture

The GG simulator solves for the satellite dynamics along an orbit resulting from the application of the Earth's gravity field, the non-conservative environmental disturbances (atmospheric drag, wind, solar radiation pressure, coupling with Earth's magnetic field, etc.) and the DFAC control forces and torques.

The GG simulator is based on three different main modules: the Environment, the Dynamics and the Post-Processing ones. Figure 7.2-1 shows a description of the GG simulator logical breakdown, highlighting the main data sets exchanged.

The *Environment Module* is in charge of computing the gravity field, the gravity gradient and the non-gravitational forces/torques acting on the spacecraft. These forces and torques are added to the forces of the DFAC and AOCS actuators, in order to realize the GG orbit.

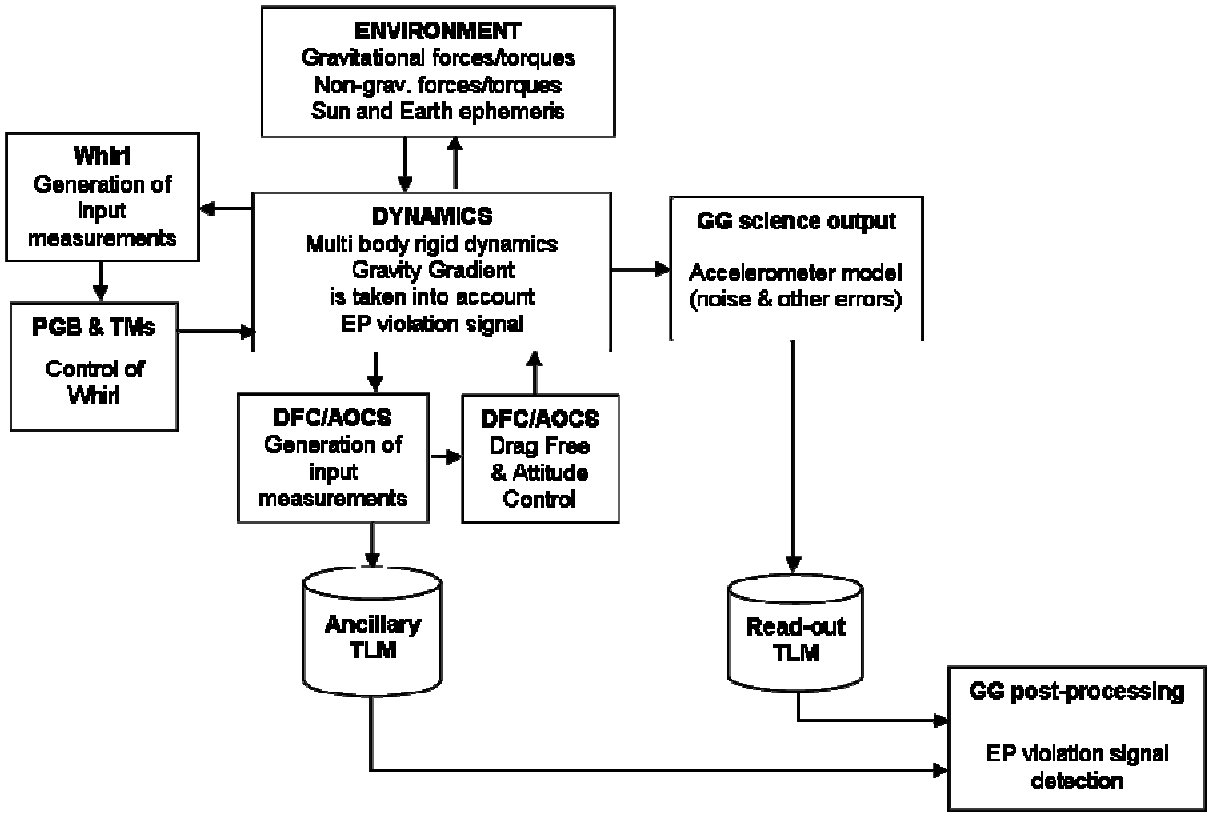

Figure 7.2-1: GG simulator block-diagram.

The three main modules of the simulator are the Environment, the Dynamics and the Post-Processing modules. The blocks containing the controllers for the damping of the whirling motion of PGB and of the test masses, the Drag Free and the Attitude and Orientation of the satellite are components of the Dynamics module.

The *Dynamics Module* is in charge of computing the GG orbit and the relative dynamics of PGB w.r.t. the spacecraft, and of test masses w.r.t. PGB. This module has to take into account the gravity gradient acting on each body inside the GG spacecraft, and of the EP violating signal acting on the test masses. The control laws for the damping of the PGB and test masses whirling motion, for the drag free and the AOCS are also dedicated blocks of the dynamics module. It is also in charge of computing:

- the capacitance measurements used to feed the Whirl control of the PGB and of the test masses (simulation of the capacitance sensors, which feed the whirl controller)
- the forces necessary to damp the PGB and test masses whirl motions (simulation of the actuators, which realise the whirl controller commanded forces)
- the effects due to temperature variations on the inertia properties of spacecraft, PGB and test masses
- the effects due to temperature variations on the mechanical suspension (degrade of the $CMRR_{xy}$ and $CMRR_z$) and on the mechanical balancing of the read-out capacitance bridge
- the effects of the temperature gradients on the mechanical suspension (degrade of the $CMRR_{xy}$ and $CMRR_z$) and on the mechanical balancing of the read-out capacitance bridge
- the DFAC and AOCS sensors' measurements
- the DFAC and AOCS actuators' forces and torques (simulation of the FEEP/cold gas thrusters)
- the ancillary telemetry data and the other spacecraft data
- the GG science output (simulation of the science capacitance sensors measurements, which feed the post-processing module).

The *Post-Processing Module* is a self standing off line post-processor, which is in charge of detecting the EP violating signal in terms of differential test mass displacement starting from the science output (and ancillary telemetry if needed). It is also used to compute accelerations, displacements and other useful vectors in the hereafter defined different reference frames.

7.2.1 Simulator Reference Frames

The GG simulator describes the satellite orbit w.r.t. the most relevant reference frames for the science mission, which have been also used for the assessment of the Scientific Requirements and of the Error Budget: the Inertial Reference Frame, the Local Vertical Reference Frame and the Body Fixed Reference Frame.

7.2.1.1 Inertial Reference Frame

The fundamental Inertial Reference Frame (IRF) of the mission is currently realised by the J2000 Equatorial Reference Frame (JERF), which is a Cartesian frame defined as follows (see Figure 7.2-2):

- Origin, O_{J2000}, located at the centre of the Earth
- X_{J2000} axis at the intersection of the mean ecliptic plane with the mean equatorial plane at the date of 01/01/2000 and pointing positively towards the vernal equinox
- Z_{J2000} axis orthogonal to the mean equatorial plane at the date 01/01/2000
- Y_{J2000} axis completing a right-handed reference frame

The satellite initial conditions (position, velocity and attitude) are defined w.r.t. the Inertial Reference Frame. At t= 0 s, the satellite is lying along the X_{J2000} axis, and its velocity is along the Y_{J2000} one.

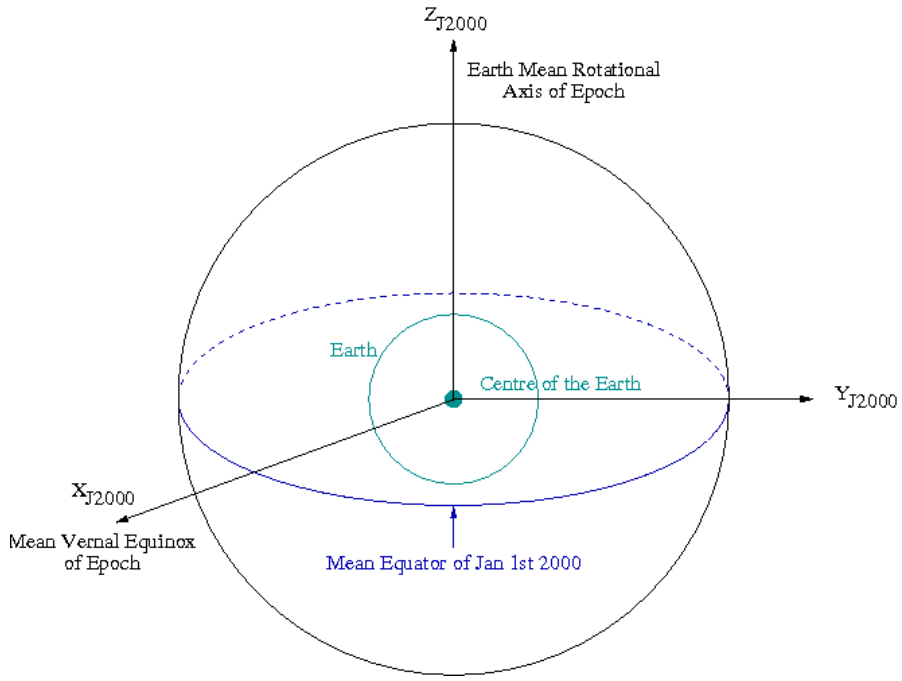

Figure 7.2-2: The Inertial Reference Frame is the J2000 Equatorial Reference Frame.

The centre is coincident with the Earth centre, the X axis is at the intersection of the mean ecliptic plane with the mean equatorial plane (at the date Jan 1st 2000), the Z axis is perpendicular to the mean equatorial plane (at the date Jan 1st 2000), and the Y axis completes a right-handed reference frame.

7.2.1.2 Local Vertical Local Horizontal Reference Frame

The Local Vertical Local Horizontal Reference Frame (LVLH) is the second fundamental frame: in this frame the EP violating signal always appears along a fixed direction (in case of a perfect circular orbit, the Earth is fixed in this reference and the EP violating signal appears as a DC effect). In order to have the EP violating signal along the X_{LVLH} axis, this reference frame is so defined (see Figure 7.2-3):

- Origin, O_{LVLH}, located at the satellite centre of mass (COM)
- X_{LVLH} axis directed from the centre of mass of the Earth to the satellite centre of mass (X_{LVLH} axis identifies the local vertical from the point of view of the satellite COM)
- Y_{LVLH} axis points toward the direction of motion (it identifies the local horizontal projection of the velocity)
- Z_{LVLH} axis is perpendicular to the orbital plane and completes the right-handed coordinate system.

Notice that because the spacecraft velocity vector rotates, to remain tangential to the orbit, the LVLH system also rotates about the Earth. The LVLH does not take into account the GG spinning about its symmetry axis.

The Post-Processing module of the GG simulator aims to compute the test masses differential displacement due to the EP violating signal w.r.t. the X_{LVLH}, while the main component of the non-gravitational accelerations acting on the spacecraft external surface is along Y_{LVLH}, i.e. 90° out of phase.

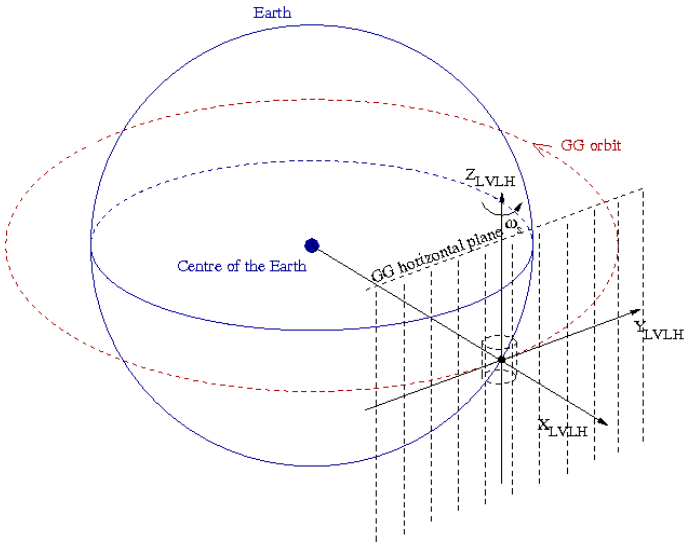

Figure 7.2-3: The Local Vertical Local Horizontal Reference Frame (LVLH)

The LVLH is a frame co-rotating with the spacecraft. Its origin is coincident with the satellite COM, its X axis is always from the Earth centre of mass to the satellite centre of mass, Y is pointing in the direction of orbit motion (it identifies the local horizontal plane) and its Z axis is perpendicular to the orbital plane and completes the right-handed coordinate system.

7.2.1.3 Body Fixed Reference Frame

The Body Fixed Reference Frame (BF) is the frame "attached" to the spinning satellite and defined by means of physical markers on the true structure. The necessity of assuming one spacecraft fixed reference frame is dictated by the fact that DFC sensors and actuators are fixed with respect to the satellite structure (PGB and test masses are mechanically suspended and during science operations are not fixed with respect to the satellite structure). The BF frame is defined according to the following prescription:

- The Z_{BF} axis corresponds to the central axis of the PGB connecting cylindrical tube (when the PGB is locked to the satellite). It is nominally the spinning axis of the satellite, and the positive direction is the same of the angular rate vector. In the GG simulator the Z_{BF} axis is the satellite spin axis and it is coincident with the PGB symmetry axis at t=0 s.
- The reference origin, O_{BF}, is located on the Z_{BF} axis. When PGB and test masses are locked with respect to the satellite, the origin marker is placed in order to individuate the position along the Z_{BF} axis of the test masses equatorial plane. O_{BF} is nominally coincident with the satellite centre of mass (when PGB and proof masses are locked). In the GG simulator, O_{BF} is coincident with the satellite centre of mass.
- X_{BF} and Y_{BF} axes lie on the plane containing O_{BF} and perpendicular to the Z_{BF} axis. Each axis passes through the median plane of the two pairs of capacitance plates in between the test masses. A dedicated marker identifies the axes X_{BF} and Y_{BF}, which are chosen to complete with the Z_{BF} axis a right-handed coordinate system. In the GG simulator, it is assumed that the capacitance plates defining the X_{BF} axis are the ones on the X_{J2000} at t = 0.

7.2.2 Simulator Environment Module

This block is dedicated to the computation of the forces and torques acting on the spacecraft and resulting from the interaction with the orbital environment. As such, this module computes the gravity force, the gravity gradient torque, the aerodynamic force and torques, the magnetic torque, the solar radiation pressure force and torque. It includes:

- the Earth gravity field, with gravitational constant GM = 3.986004418·1014 m^3/s^2, according to the EGM96 Earth Gravity field solution, and Earth Mean Radius = 6378144 m. The gravity gradient torque taking into account for J2 effect is also applied on each body.
- the MSIS86 atmospheric model for the computation of the air density, temperature and chemical composition along the satellite orbit. The F10 and F10.B indexes related to the Solar activity and the Geomagnetic indexes Ap and Kp are used to feed the MSIS model.
- a model of the Earth's magnetic field derived from the Oersted satellite measurements
- the celestial bodies ephemerides computation.

The solar radiation pressure and Earth albedo are computed by modeling the satellite surface as a set of one cylinder and two simple flat surfaces. The pressures due to the solar and Earth albedo, which depend mainly on the distance from the Sun, on the altitude of the satellite during its orbit, and on the angle between the Sun direction and the local-vertical direction, is computed

for each elementary surface. Once the pressures have been computed, the corresponding forces for each surface are obtained considering the normal and tangent components depending on the surface extension and on the aspect angle of the surface with respect to fluxes direction. The force is computed for each surface and applied to the surface's centre of pressure. The resulting force and torque on the centre of mass of each body is then computed.

7.2.3 Simulator Dynamics Module

The complete GG system, which takes into account the spacecraft, the Pico Gravity Box, the inner and outer test masses, has been simulated by using the DCAP (Dynamics and Control Analysis Package) software package developed by Thales Alenia Space under ESA contract. An additional dummy body has been introduced in order to solve for the orbit without introducing numerical errors due to the high spinning frequency of the spacecraft itself (the orbit is solved in the reference frame of the first body of the kinematics chain). The dummy body is a massive point coincident with the spacecraft centre of mass: its motion w.r.t. the Inertial Reference Frame is defined by the degrees of freedom (3) of the Hinge 1, which connects it (Node 1) to the origin of the IRF. Moreover, the dummy body identifies the origin of the LVLH reference frame: the vector pointing towards the Earth identifies the X-axis, its velocity identifies the Y-axis (along-track direction), and the orbit angular velocity is along the Z-axis. The bodies are characterized by the up-to-date values of the mass and inertia properties, while the dummy body – Body 1 - is a unitary massive point coincident with the spacecraft centre of mass (Node 10). The bodies of the GG dynamical model (schematically represented in Figure 7.2-4) and the degrees of freedom (summarised in Table 7.2-1) are defined as follows:

- Body 1 is the dummy body. Its representative node (Node 1) is coincident with the spacecraft centre of mass. The Hinge 1, which connects the IRF to Node 1, has 3 degrees of freedom: its translation completely describes the orbit motion of the spacecraft.
- Body 2 is the spacecraft. The satellite has its centre of mass (Node 10) coincident with the dummy body (Node 1). The null-length Hinge 2, which connects the LVLH origin to the s/c centre of mass, permits satellite rotations only. In particular, the rotation about the Z axis defines the spin w.r.t. the LVLH.
- Body 3 is the Pico-Gravity Box (PGB). The Hinge 3, which connects the s/c centre of mass (Node 10) to the PGB centre of mass (Node 20), provides the 6 degrees of freedom (3 rotations and 3 translations) of the PGB-s/c relative motion.
- Body 4 is the outer (external) test mass (TMe). The Hinge 4, which connects the PGB centre of mass (Node 20) to the TMe centre of mass (Node 30), provides the 6 degrees of freedom (3 rotations and 3 translations) of the TMe-PGB relative motion.
- Body 5 is the inner test mass (TMi). The Hinge 5, which connects the PGB centre of mass (Node 20) to the TMi centre of mass (Node 40), provides the 6 degrees of freedom (3 rotations and 3 translations) of the TMi-PGB relative motion.

This type of multi-body connection grants an open-loop kinematics topology, with no need for cut-joint hinges. All hinges are described by a Euler sequence Type 1, x-y-z. The active degrees of freedom (DoF) defined by hinges can be differently set depending on the required type of simulation.

Hinge Id.	Transl. Dofs (x,y,z)	Rotational Dofs (x,y,z)
1	F, F, F	L, L, L
2	L, L, L	F, F, F
3÷5	F, F, F	F, F, F
Note : L = Hinge DoF Locked F = Hinge DoF Free		

Table 7.2-1: Hinge degrees of freedom

Translation and rotational degrees of freedom of the hinges defining the kinematics chain of the GG system. Hinge 1 connects the IRF to the dummy body, and the null-length Hinge 2 connects the dummy body to the spacecraft centre of mass.

The Hinge 1 defines also the initial condition for the GG orbit (w.r.t. the IRF), with the convention that at t = 0 the satellite position is ($R_\oplus$ + h, 0, 0) and the satellite velocity is (0, v_y, 0), with $R_\oplus$ the Earth equatorial radius and h the GG orbit altitude. The Hinge 2 defines instead the satellite spin w.r.t. the IRF: initially it has been assumed to be 2 Hz, but it is going to be updated to 1 Hz, according to the last analyses, which have been performed in order to verify the capability of FEEPs and cold gas thrusters for the drag free compensation.

The mass and inertia properties used in the simulator have been fixed at the beginning according to the last Phase A Report description (2000); then, they have been updated according to the March review mass budget. At the end they shall be updated according to the last mass budget. The mass and inertia properties are not continuously updated in order to make more efficient the “growth” of the simulator (the main job is adding all the possible spurious effect masking or competing with the EP signal).

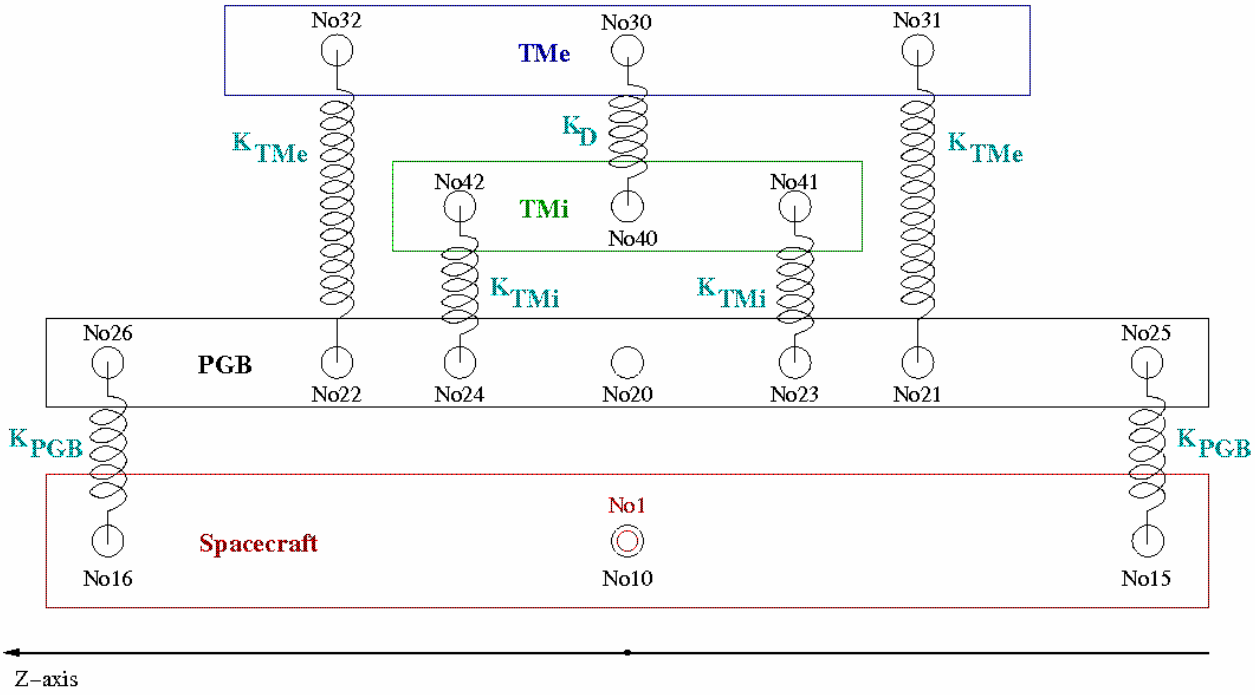

Figure 7.2-4: Schematic model of the GG dynamics system.

Logical scheme of the dynamical model implemented within DCAP software code for finite element simulation of the space experiment. The z axis is the spin/symmetry axis of the system; all elastic connections along z are very stiff; the plane of sensitivity is perpendicular to z. The model encompasses all bodies (spacecraft, PGB and 2 test masses), each one with its 6 degrees of freedom in 3D (3 for translation and 3 for rotation), mass and moments of inertia. All non rigid components of the system (sketched as springs) are implemented with their designed stiffness (in the sensitive plane as well as in the z direction) and mechanical quality factors Q for simulation.

The mechanical suspensions connecting the PGB to the spacecraft and the test masses to the PGB, which are schematically represented by springs in Figure 7.2-4, are implemented in order to provide realistic suspension modes (according to the GG on the Ground measured values) and transfer function (see Table 7.2-2). The PGB-s/c suspension is also characterised by its realistic dissipative term, corresponding to a mechanical quality factor $Q_{PGB} \cong 90$, in order to provide the most realistic representation of the PGB-s/c dynamics behaviour: the PGB-s/c relative motion not only must be measured in order to feed its control of the whirl motion, but provides also the input of the DFAC control, which is a key point for the GG science performance.

GG sub-system	Planar oscillation period [s]	Axial oscillation period [s]
s/c-PGB	360	30
PGB-TMe	$30 < T_{CMxy} < 120$	30
PGB-TMi	$30 < T_{CMxy} < 120$	30
TMe-TMi	540	0

Table 7.2-2: Oscillation periods

Oscillation periods of the GG subsystems along the satellite spin axis and in the plane perpendicular to it.

The dissipation of the PGB-test masses suspensions is instead assumed to be greater and greater than the true one, by adopting a corresponding mechanical quality factor $Q_{TM} \cong 500$ (vs. a true value of $Q_{TM} \cong 20000$): this choice is necessary in order to have a whirl-radius doubling time t_{rw2} of the order of $t_{rw2} \approx 10000$ sec (vs. a true value of $t_{rw2} \approx 500000$ sec). This shorter t_{rw2} permits to carry out simulations covering a mission time duration not longer than 200000÷300000 sec, but which cover all the relevant aspects in terms of disturbing effects and science performance (the EP signal is in fact detected). The adoption of the true value for the mechanical quality factor of the PGB-test masses suspension would force the length of one science performance simulation to several millions of seconds, just to verify the growth of the whirling motion! It is apparent that there is nor loss of generality, neither a “favourable” assumption in this choice.

The EP violating signal is simulated with a force with amplitude $F_{EP} = m_{TM} \cdot g(h) \cdot \eta$ N, which is directed from the Earth centre of mass to the centre of mass of the outer test body only (it is a pure differential force for the test masses). This mean that the EP violating force is always directed along the X_{LVLH} axis. The mass of the proof body is 10 kg, the value of the local gravity sensed from the test mass depends on the GG altitude, and it is about 8÷8.4 m/s^2. The Eötvös parameter η is an input value for the simulator, with η in the range of $10^{-17} \div 10^{-13}$.

High-fidelity models represent sensors feeding the control algorithms and the actuators (FEEPs/cold gas thrusters and spinning-up gas thrusters), which are in charge of generating the DFAC and AOCS commanded forces and torques. The high-fidelity models for sensor and actuators have to account for intrinsic noises, transfer functions, non linearity, mounting errors, sensor/actuators inner geometrical imperfections (see Figure 7.2-5), temperature fluctuations, quantization and all the other effects which can degrade the scientific performance of the sensors/actuators, since the goal of the simulation is predicting the realistic mission scientific performance.

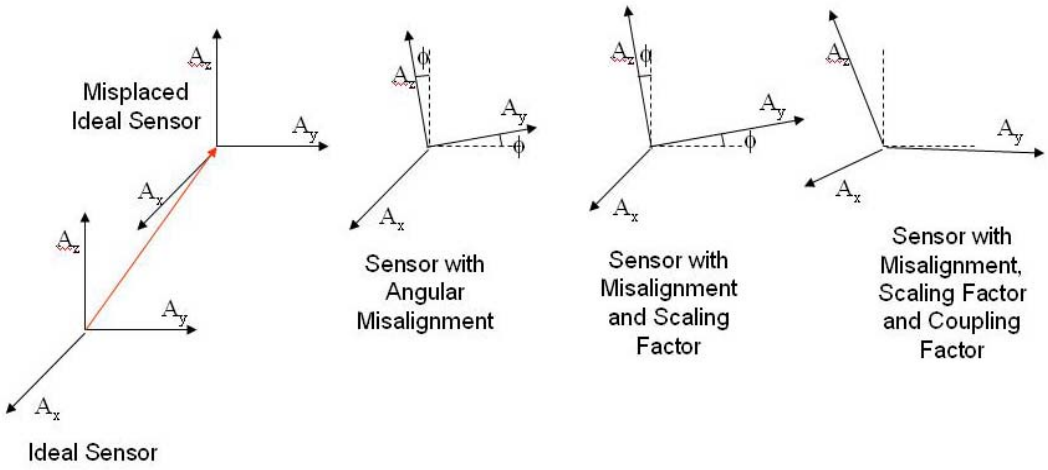

Figure 7.2-5: Sensor/actuator geometrical imperfections

Imperfections include mispositioning, misalignment, scale factor error and coupling error.

The simulation of sensor/actuator noise and of temperature fluctuation is based on the superposition of deterministic noise (implemented by sinusoidal terms) and of stochastic noise (implemented by noise shaping technique). With the noise shaping technique, a properly devised (in the frequency domain) noise shaping filter is used to provide the desired shape to its feeding unitary band limited white noise. The block-diagram of the white noise shaping technique is reported in Figure 7.2-6: a unitary (one-sided) white noise is passed through an analog/digital filter that builds up the requested noise Spectral Density and which integrates also an anti-aliasing filter (if necessary). The output of the filter is then decimated (if requested) and saved into a dedicated variable.

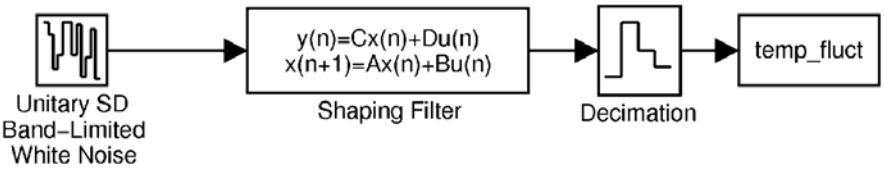

Figure 7.2-6: Block diagram of the white noise shaping technique.

A white noise with unitary (one-sided) Spectral Density is passed through a shaping filter (applying also the anti-aliasing, if necessary) and decimated (if required) before saving the output into a dedicated variable.

Figure 7.2-7 shows as example the time histories of the fluctuating temperature, temp_fluct, realized according to the white noise shaping technique. Figure 7.2-8 shows the Spectral Density (SD) as computed from the simulated time history, vs the desired analytic SD: the desired analytic SD can be superimposed to the computed one.

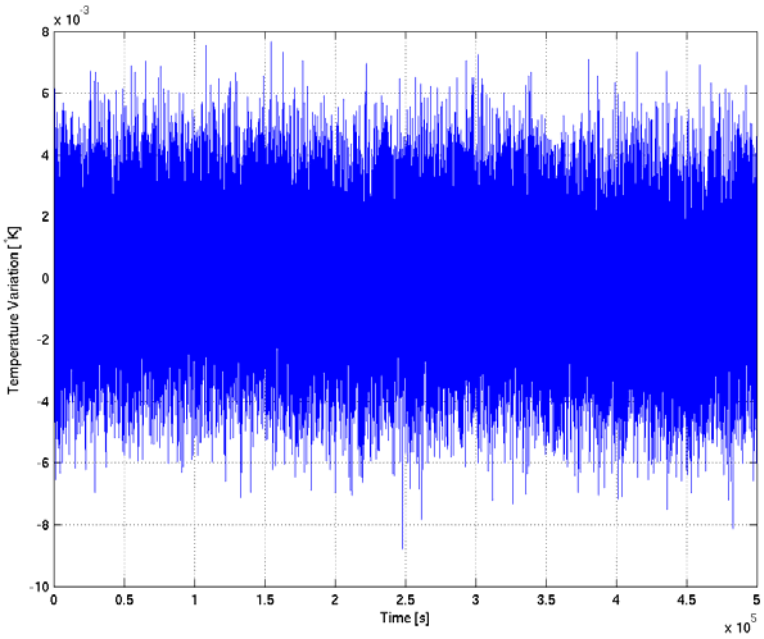

Figure 7.2-7: Time history of the fluctuating component of temperature obtained with the white noise shaping technique

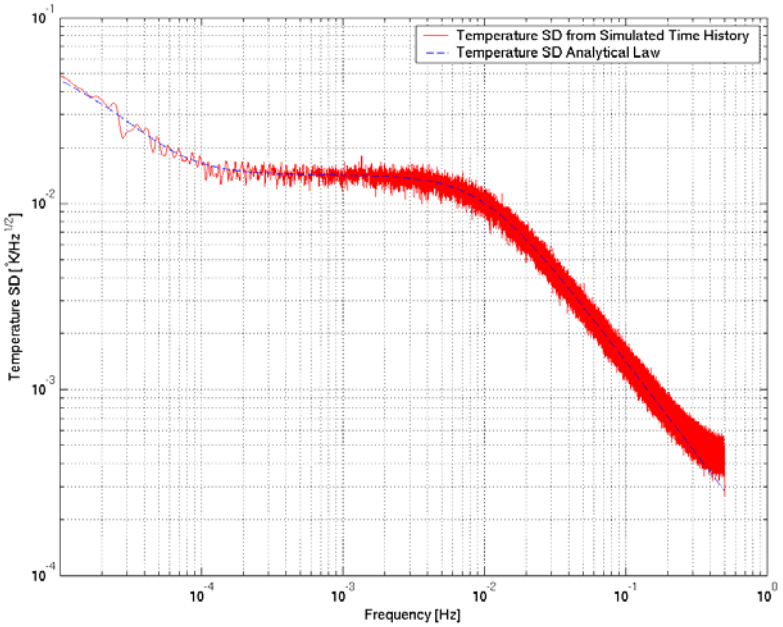

Figure 7.2-8: Spectral density of the temperature fluctuation computed from the simulated time history vs. the Spectral density desired analytic law.

The above cited technique provides the capability of adding the temperature effects sensed at the level of the test masses (thermal noise, temperature fluctuation), of the mechanical balancing of the science read-out, and of the $CMRR_{xy}$ and $CMRR_z$ variation due to temperature.

An analytic function for the temperature variation sensed from spacecraft and PGB shall be instead modelled in order to introduce their inertia variations.

The simulator architecture allows easy incorporation of models generated by a wide range of software tools, such as DCAP-RT (Dynamics and Control Analysis Package for Real Time, TAS-I developed dynamics package), and commercial off the shelf tools like Matlab/Simulink and Real Time Workshop.

7.2.4 Post-Processing Module

The GG sensor and actuators are fixed w.r.t. the spinning satellite: this means that the detection of the EP violation signal and of the other interesting information (non-gravitational acceleration, whirling motion, temperature effects, gravity gradient contributions, etc.) is completely masked by the GG spinning frequency.

The Post-Processing module, which is in embryonic status (Phase A level), consists of a Matlab macros package, which has been implemented in order to allow the transformation of all the sensor measurements from the BF to the IRF and to the LVLH reference frames. Also the ancillary information about the satellite, PGB and test masses dynamics is provided in all the reference frames, in order to allow the science performance check by using the time histories generated by the simulator. The implemented macro package requires the Signal Processing and Statistics Matlab Toolboxes. The coding of this module is such that it should be easy a full porting to the GNU Octave environment, which is a free Matlab clone providing also packages equivalent to the Signal Processing and Statistics Toolboxes.

The Post-Processing module allows the analysis on both the time and frequency domain, providing results in terms of Amplitude Spectrum and Spectral Density of the interesting signals (e.g. Fourier analysis of the non-gravitational accelerations w.r.t to IRF and Spectral Density accelerations and displacements).

A further development of this module is foreseen in case of advance in Phase B of the GG science mission.

7.3 Science Performance Simulation

The results of one science performance simulation are hereafter reported in order to validate the GG simulator and to show its capabilities and usefulness. This simulation was carried out in order to check the real basis of the experiment, i.e. the capability to detect the EP violating signal, taking into account:

- the gravity field and the gravity gradient acting on the spacecraft
- the non gravitational forces acting on the spacecraft surface
- the dissipation of the mechanical suspensions (whirling motions and whirl controls of PGB and test masses)
- the gravity gradient acting on the proof masses.

For this exercise, the sensors' and actuators' noise and imperfections have been neglected, in order to compare the simulator's results vs. the analytical predictions. Moreover, it is assumed a perfect Common Mode Rejection Ratio of the mechanical suspensions ($\chi_{CMRRxy} = 0$, $\chi_{CMRRz} = 0$), and a perfect mechanical balancing of the science capacitance bridge ($\chi_{bridge} = 0$). Due to the perfect rejection of the common mode by means of the mechanical suspension, the DFC for the partial compensation of the non-gravitational disturbances is not working in this simulation. The satellite spin frequency has been updated to the new default value: 1 Hz. For this exercise the oscillation periods of the test masses and of PGB have been modified (compare Table 7.3-1 vs. Table 7.2-2) in order to largely amplify the displacements due to the inertial acceleration sensed by the bodies (this is due to the fact that the adopted environment cannot be considered a worst case scenario).

GG sub-system	Values of simulated Planar oscillation period [s]	Values of simulated axial oscillation period [s]
s/c-PGB	295.04	295.04
PGB-TMe	$T_{CMxy} = 113$	113
PGB-TMi	$T_{CMxy} < 113$	113
TMe-TMi	500	0

Table 7.3-1: Oscillation periods adopted in the simulation

Oscillation periods of the various GG subsystems along the satellite spin axis and in the plane perpendicular to it adopted for this science performance simulation.

The orbit altitude for this simulation has been chosen to be 520 km, which is not the reference altitude of the science mission, but the one for which the local gravity is 8.4 m/s^2: this value of local gravity was the driver for the EP violating signal for this simulator run. The implemented EP violating signal is the minimum detectable one, i.e. it is due to $\eta=10^{-17}$. Such a signal is simulated with a force with amplitude $F_{EP} = m_{TM} \cdot g(h) \cdot \eta = 8.4 \cdot 10^{-16}$ N, always directed along X_{LVLH} and acting on the outer test mass only. The initial time for the orbit has been assumed to be 2013 July 7th, 6 a.m.: the solar radiation indexes used for this simulation are F10 = F10.B = 120, the geomagnetic index is 8: Figure 7.3-1 shows the GG orbit and the initial conditions of the simulation (satellite on the X_{IRF} axis). The solar radiation pressure has been taken also into account. The spacecraft area to mass ratio used for the simulation is 0.0032 m^2/kg, which is slightly better than the up-to-date true one (0.005 m^2/kg), but still representative.

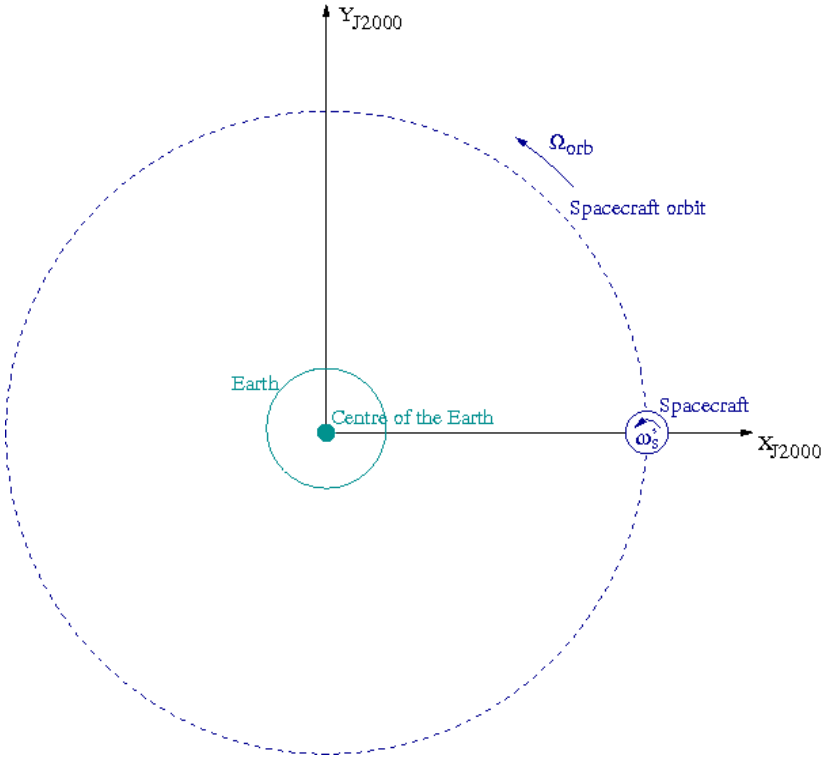

Figure 7.3-1: Scheme of the initial conditions for the satellite orbit of this simulation.

At t = 0 Hinge 1 locates the satellite w.r.t. the IRF with the position vector r = ($R_\oplus$ + h, 0, 0), with $R_\oplus$ the Earth equatorial radius and h the GG orbit altitude. The satellite velocity is so v = (0, v_y, 0).

The continuous controllers of the whirling motion of the PGB and test masses are fed by ideal capacitance sensors and realized through ideal capacitance actuators.

7.3.1 Satellite acceleration in the LVLH reference frame

One of the main features of the simulator is the capability to compare the accelerations that have to be compensated/rejected and the acceleration that has to be detected: the non gravitational forces acting on the external surface of the spacecraft provides an inertial acceleration that is several orders of magnitude bigger than the EP violating signal. The LVLH components of the spacecraft non gravitational acceleration have been computed by using the Post-Processing module and shown in Figure 7.3-2, Figure 7.3-3 and Figure 7.3-4 below.

Figure 7.3-4, which shows a zoom of the time histories of the spacecraft acceleration along the Z_{LVLH} axis, highlights also the oscillating term due to the mechanical coupling with the PGB. It has to be pointed out here that the realized simulation is not yet the worst case scenario for the environment, and that it is just one possible representation for the satellite dynamics. The worst case scenario for the environment shall be taken into account once the satellite configuration and the possible launch date will be frozen. The short eclipse periods are also visible: during the eclipse the mean value of acceleration is zero.

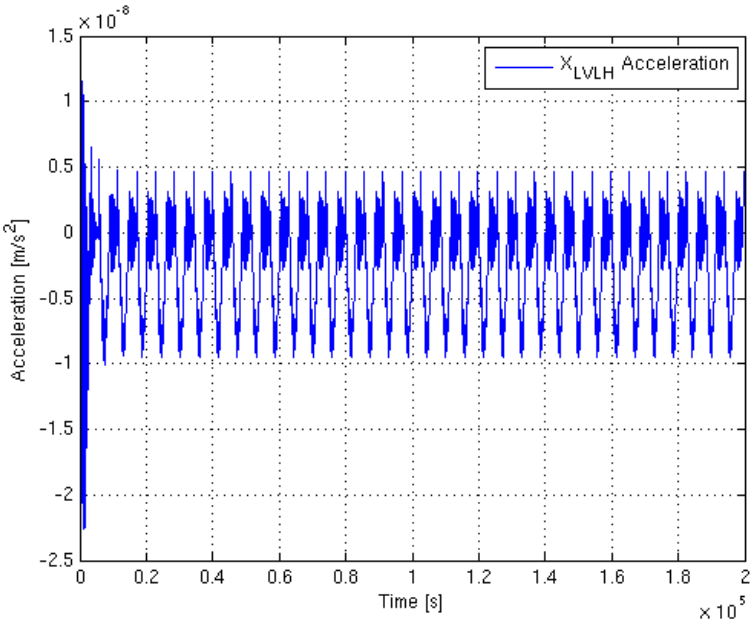

Figure 7.3-2: Time history of the spacecraft non gravitational acceleration along X_{LVLH}

The X_{LVLH} axis is the direction of the EP violating signal, whose amplitude is $8.4 \cdot 10^{-17}$ m/s².

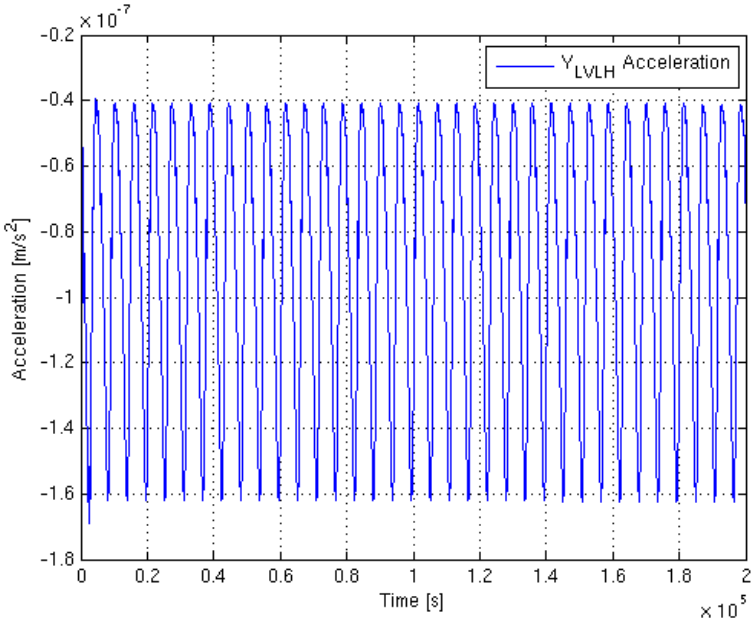

Figure 7.3-3: Time history of the spacecraft non gravitational acceleration along Y_{LVLH}

Y_{LVLH} is the axis perpendicular to the direction of the EP violating signal, whose amplitude is $8.4 \cdot 10^{-17}$ m/s².

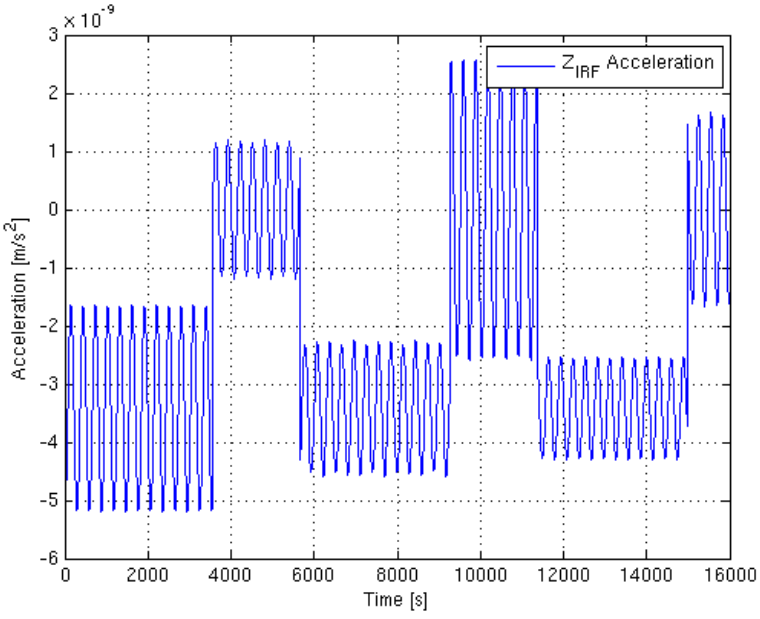

Figure 7.3-4: Time history of the satellite non gravitational acceleration along Z_{IRF}

Zoom of the time history of the satellite non gravitational acceleration along the Z_{IRF} axis (Z_{LVLH} is parallel to it, there is only translation of the origin), i.e. perpendicular to the orbit plane. The relative motion of PGB w.r.t. the spacecraft is represented by the oscillations of the signal. The short eclipse periods are also visible (acceleration mean value is zero).

7.3.2 PGB-s/c displacement

The PGB-s/c displacement is analyzed in the Drag Free control document [RD 16].

7.3.3 Common mode motion of the test masses

The displacement of each test mass w.r.t. the PGB provides the information about the required overall rejection of the common mode acceleration. The overall external non-gravitational force affecting the spacecraft motion is sensed from the test masses as inertial force: in principle it is a pure common mode for them, such as in this simulation. In true life, it is anyway necessary to reduce this common mode acceleration for mainly three reasons:

- the common mode acceleration displaces each test mass, and this displacement has a limited range: the gap of the science capacitance plates
- the common mode rejection of the test masses mechanical suspension is not 0 (i.e. a fraction of the common mode acceleration is transformed into differential acceleration, which competes with the interesting signal to be detected)
- the capacitance read-out, which is in charge of detecting the test masses relative displacement due to an EP violation, is sensitive to both common and differential mode. Hence (a) Its dynamic range must be not saturated; (b) Its rejection of the common mode is limited.

In order to have a very small gap for the capacitance plates of the science read-out (i.e. high sensitivity), the external non-gravitational acceleration is partially compensated by means of an active Drag Free Control, which reduces the inertial acceleration sensed from the PGB and test masses at the orbit frequency. The remaining common mode acceleration is rejected from the mechanical suspension. In the IRF, the residual common mode acceleration sensed from the PGB and test masses at the orbit frequency is $a_{CMxy} = \chi_{DFCxy} \times a^{ext}_{NG\,xy}$. The a_{CMxy} acceleration is responsible of the elongation of the “springs” connecting the PGB to the spacecraft and the test masses to the PGB in the test masses equatorial plane XY.

In this simulation, whose main objective is the simulator validation, $\chi_{DFCxy} = 1$ (no DFC) and so $a_{CMxy} = a^{ext}_{NG\,xy}$. The inertial acceleration, which becomes a differential term due to the mechanical balance suspension imperfections, is $a^{iner}_{DM} = a_{CMxy} \times \chi_{CMRRxy}$, wih χ_{CMRRxy} the suspension Common Mode Rejection Ratio. As already mentioned above, in this simulation $\chi_{CMRRxy} = 0$, instead of $\chi_{CMRRxy} = 10^{-5}$ (perfect common mode rejection): so, $a^{iner}_{DM} = 0$. This means that the PGB-test mass displacement is the largest possible one, but that at the same time the differential displacement is not affected by this large value. In other words, in such a configuration the simulator can be used at the same time to check the level of violation of the requirements on the test masses common mode displacement in case of non drag free mode, and at the same time it can be used to detect the EP violating signal.

The Post-Processing module provides the time histories of the satellite position, velocity and acceleration in both the IRF and LVLH reference frames. It also provides the s/c-PGB and the PGB-test masses displacement, velocity and acceleration in both the IRF and LVLH reference frames, thus removing the high frequency components, which would make figures of BF time histories almost useless.

The following pictures show the time histories of the TMe common mode displacement along the three axes of the LVLH reference frame, as computed from the post-processing module.

Figure 7.3-5 shows the displacement of the outer test mass w.r.t. the PGB along X_{LVLH}: the maximum displacement (some tens of microns) is by far smaller than the gap between the science capacitance plate and the inner surface of the outer proof body (2.5 mm). While in this simulation the only difference of proof masses displacement is due to the EP violating signal and to gravity gradient (the differential displacement due to EP violation is $\Delta x_{EP} = F_{EP} \times (T_{diff})^2/(4 \times m_{TM} \times \pi^2) \cong 0.5$ pm), in true life a fraction $\chi_{CMRRxy} = 10^{-5}$ of the observed common mode displacement is detected as differential displacement.

Figure 7.3-5 shows also that there is an offset on the X_{LVLH} displacement, whose value is 1 micron, which means 10 pm of differential displacement with the same frequency and phase of the EP signal: the necessity of the DFC for the compensation of the orbital component (in the IRF) of the non gravitational acceleration is here clearly stated. The larger displacement of the proof mass, i.e. the oscillation with amplitude of about 5 microns, generates (through $\chi_{CMRRxy} = 10^{-5}$) a differential displacement which is about 2 orders of magnitude bigger than Δx_{EP}. Also this term benefits from the action of the DFC, since the drag at orbit frequency in the IRF, i.e. the main drag component, shall not contribute to the orbit frequency term of non-gravitational acceleration in the LVLH reference frame. This differential displacement, anyway, has not the same frequency of the EP violating signal and does not affect the science performance of the experiment.

Figure 7.3-6 shows the displacement of the outer test mass w.r.t. the PGB along Y_{LVLH}: the maximum displacement (one hundred of microns) is smaller than the gap between the science capacitance plate and the inner surface of the outer proof body (2.5 mm). Moreover, the largest part of this displacement is an offset, i.e. it is due to the orbital term (in the IRF) of the non-gravitational forces acting on the spacecraft: the presence of the DFC would reduce this displacement to about 30 microns. In this not realistic situation (absence of DFC) it is anyway demonstrated that the gap of the science capacitance read-out is not saturated. The offset along Y_{LVLH}, when "converted" into differential displacement through χ_{CMRRxy}, provides a $\Delta Y_{LVLH} = 500$ pm, i.e. a huge displacement having only a phase difference of 90° w.r.t. the EP violating signal. Again, the usefulness of the DFC is transparent and underlined.

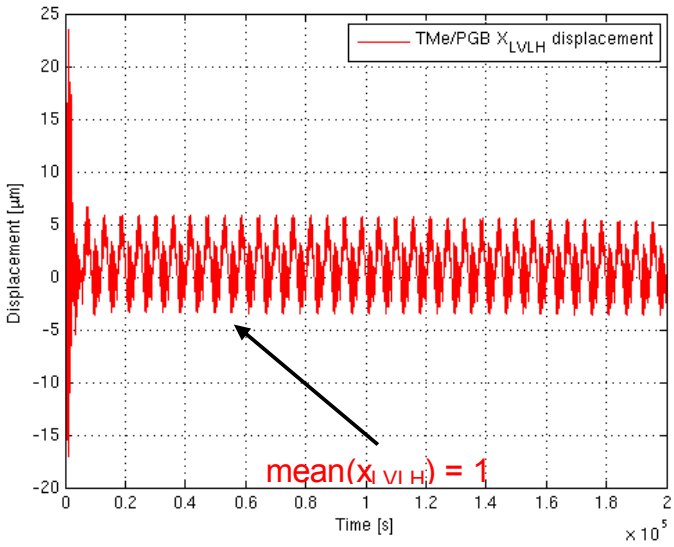

Figure 7.3-5: TMe-PGB displacement along the X_{LVLH} axis

Part of the initial transient has been removed from the picture. The displacement along X_{LVLH} is not a problem from the point of view of the gap of the science capacitance plates. The offset (mean value) of the displacement, which is about 1 micron, has the same signature of the EP violating signal. In real life, without the Drag Free control, the fraction of common mode offset along X_{LVLH} transformed into differential mode due to the imperfect CMRR ($\chi_{CMRRxy} = 10^{-5}$, i.e. not zero) of the mechanical balance, would completely mask the EP violating signal, being about 20 times greater than Δx_{EP}.

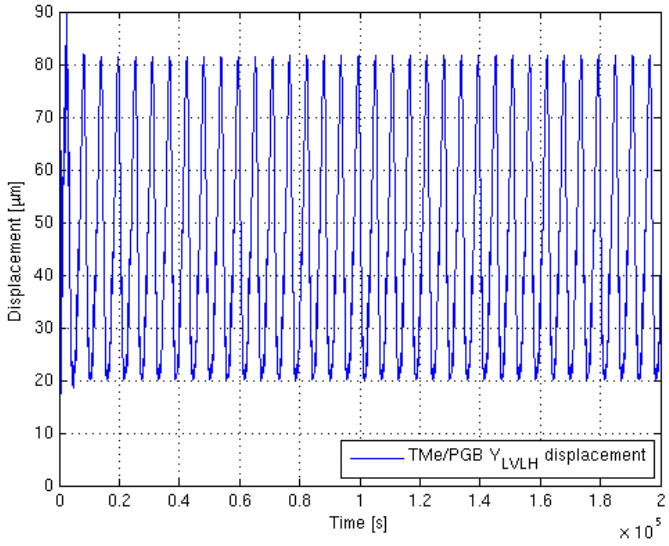

Figure 7.3-6: TMe-PGB displacement along the Y_{LVLH} axis

Part of the initial transient has been removed from the picture. The displacement along Y_{LVLH} is not a problem from the point of view of the gap of the science capacitance plates. The offset (mean value) of the displacement, which is about 1 micron, has the same signature of the EP violating signal. In real life, without the Drag Free control, the fraction of common mode offset along X_{LVLH} transformed into differential mode due to the imperfect CMRR ($\chi_{CMRRxy} = 10^{-5}$, i.e. not zero) of the mechanical balance, would completely mask the EP violating signal.

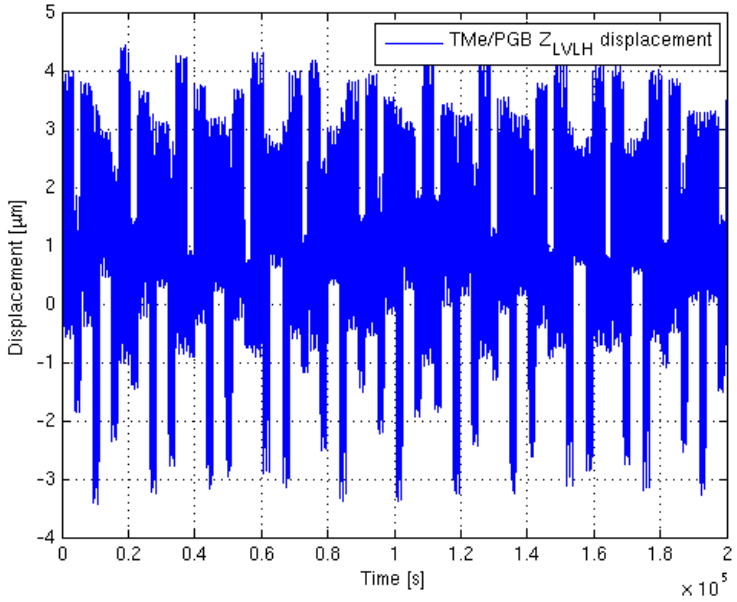

Figure 7.3-7: TMe-PGB displacement along the Y_{LVLH} axis

Part of the initial transient has been removed from the picture. The displacement along Y_{LVLH} is not a problem from the point of view of the gap of the science capacitance plates. The offset (mean value) of the displacement, which is about 1 micron, has the same signature of the EP violating signal. In real life, without the Drag Free control, the fraction of common mode offset along X_{LVLH} transformed into differential mode due to the imperfect CMRR ($\chi_{CMRRxy} = 10^{-5}$, i.e. not zero) of the mechanical balance, would completely mask the EP violating signal.

Figure 7.3-7 shows the displacement of the outer test mass w.r.t. the PGB along Z_{LVLH}: the maximum displacement (about 5 microns) is smaller than the gap (2.5 ÷ 5 mm) of the capacitance sensors devoted to measure the proof masses displacement along the symmetry axis. In true life, the offset along Z_{LVLH}, which is about 1 micron, when "converted" into differential displacement through $\chi_{CMRRz} = 2 \cdot 10^{-2}$, provides a ΔZ_{LVLH} = 20 nm. This differential displacement along the symmetry axis, due to the gravity gradient tensor, gives rise to a differential acceleration in the test masses equatorial plane, at a frequency that is two times the orbit one (w.r.t. IRF). The requirement on the test masses differential displacement along the symmetry axis at the orbit frequency (w.r.t. IRF) is $\Delta z^* = 0.5$ nm. The maximum displacement along the symmetry axis is about $200 \cdot \Delta z^*$. The DFC is in charge of reducing by a factor 500 the non-gravitational forces acting at the orbit frequency along the satellite spin axis: it is transparent that taking into account the DFC compensation, the differential displacement along Z_{LVLH} becomes smaller and smaller than Δz^*. The science target of being capable of measuring $\eta = 10^{-17}$ requires the DFC compensating action on both the orbit plane and the symmetry axis.

7.3.4 Differential mode motion of the test masses

The test masses differential displacement due only to the EP violating signal is $\Delta x_{EP} = a_{EP} \times (T_{diff})^2/(4 \times \pi^2) = 0.531936$ pm (this value is obtained by using the same parameters feeding the simulator, i.e. $T_{diff} = 500$ s, $a_{EP} = 8.4 \cdot 10^{-17}$ m/s^2). The science read-out does not provide directly the displacement due to the EP violation only, but the overall differential displacement, which takes into account also the gravity gradient contribution. The overall expected differential displacement along X_{LVLH} is in fact:

$$\Delta x_{LVLH} = \frac{F_{EP}}{m_{TM} \cdot \left(\omega_{DM}^2 - 3 \cdot \frac{GM_{\oplus}}{(R_{\oplus} + h)^3} \right)} = 5.4449 \cdot 10^{-13} m$$

The time histories of the test masses differential displacement w.r.t. the IRF (after synchronous demodulation at the spin frequency) shown in Figure 7.3-8, highlight the orbit frequency of the expected signal. The EP violating signal is a rotating vector (at orbit frequency) w.r.t. IRF, so that X_{IRF} and Y_{IRF} are out of phase of 90°: the time delay between a maximum for the X_{IRF} component and the following Y_{IRF} one is about 1425 s (one quarter of the orbital period), as shown in Figure 7.3-8.

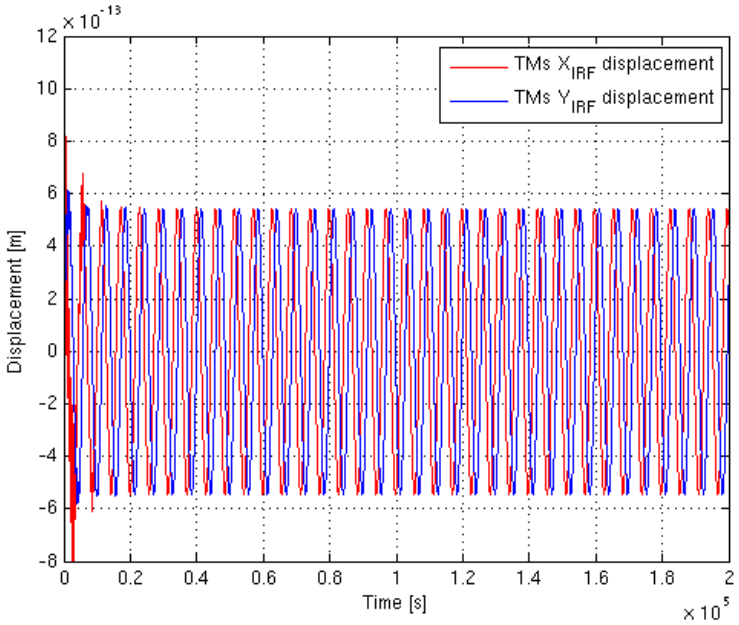

Figure 7.3-8: Test mass differential displacement w.r.t. the IRF.

The signal signature at orbit frequency is apparent: the oscillation period of the signal is the orbit one, and the time span between a maximum for the X_{IRF} component and the following Y_{IRF} one is about 1425 s (one quarter of the orbital period).

The test masses differential displacements have to be observed in the LVLH frame in order to clear understand the test bodies' behavior and to validate the simulator (at lhe level of pm!). At first, the ΔX_{LVLH} and ΔY_{LVLH} differential displacements can be plotted in the same figure, to check their values w.r.t. the expected ones. Since the $CMRR_{xy}$ in this science performance simulation is 0, and there are not differential forces acting on the test masses along Y_{LVLH}, the expected test masses differential displacement along Y_{LVLH} is $\Delta Y_{LVLH} = 0$. Figure 7.3-9 shows the perfect match between the predicted differential displacements and the measured ones (accuracy is better than 1 femtometer): it has to be noticed that the gravity gradient contribution to ΔX_{LVLH} is correctly taken into account by the GG simulator.

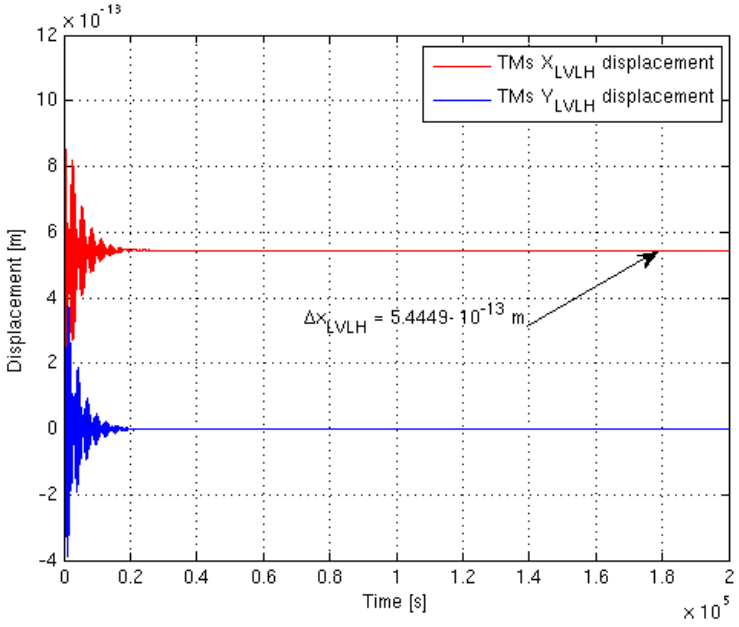

Figure 7.3-9: Test masses differential displacements in the LVLH frame.

The measured ΔX_{LVLH} and ΔY_{LVLH} differential displacements match the predicted values with accuracy better than 1 femtometer. The gravity gradient contribution to ΔX_{LVLH} is correctly taken into account by the GG simulator.

The above describes results show a perfect match of the simulator vs. the expected results in the boundary conditions selected for this validating simulation. The switch-on of the imperfections, noises and of all the spurious effects, which can affect the experiments, shall be carried out with particular care, in a step by step approach, in order to check each contribution w.r.t. the overall science performance and w.r.t. the budgeted error.

7.3.5 Dynamic range of the simulator

The first version of the GG simulator was essentially devoted to check the experiment performance taking into account the supercritical rotation (i.e. PGB and test masses whirling motion, and whirl motion control) in the 3-dimensional space, a good model of sensors and actuators, the EP violating signal, and an ad hoc implemented environment. The GG orbit did not exist, i.e. Earth gravity field (and also gravity gradient) was not implemented in the simulator. For this reason the drag was introduced as a force with a DC term and two sinusoidal components at the nominal orbit period and at nominal half orbit period w.r.t. the IRF. At the initial time t_0, the GG satellite was coincident with the IRF origin.

The introduction of the Earth gravity field (and of gravity gradient), i.e. of the GG satellite orbit, in the simulator was not cost free. A huge dynamical range has now to be covered: from half a pico-meter differential displacement of the test masses with some significant decimal digits ($\leq 10^{-14}$ m), to the orbital radius of the satellite around the Earth ($\approx 10^{7}$ m). The dynamics range required to the default implementation of the DCAP software package is so $\geq 10^{21}$ m, which is beyond the double precision capability.

It has been verified that the double precision is still useful when the effort of the simulation is focused on the DFC and or whirl control performance, i.e. if it is not required to explore the test mass behaviour at the sub nano-meter level.

When the simulations are carried out in order to explore the GG mission science performance, it is required to run the simulator in quadruple machine precision. This requirement has a huge cost in terms of the CPU time: the simulator speed slows down by a factor ≈ 20 vs. the double precision run. A quadruple precision run on a Dual Xeon @3.4 GHz has almost the real time speed: the simulation of a time span of $2 \cdot 10^{5}$ s requires 205704 s of real CPU time.

The simulation results presented in Section 7.3 above have been carried out by a quadruple precision run of the GG simulator.

7.4 Conclusions

The development of the GG simulator will be a continuous process all along the life of the project. The current activity focused on the integration of the DFC and PGB whirl motion control as described in [RD 16]. This integration needs a particular care due to the necessity of running the added code in quadruple precision in case of science performance simulations.

Future development of the simulator will focus, in particular, on the following aspects:

- Implementing high-fidelity models of the selected DFC actuators
- Accurately representing the test masses properties (inertia, magnetic, thermal) according to the final selection of the materials
- Updating the modeling of the science capacitance-read-out sensor according to the final specific design for the space experiment
- Updating the representation of CMRR degradation due to mechanical unbalancing (stiffness variation vs. temperature, etc.)
- Updating of the disturbing terms depending on the test mass materials
- Consolidating the Post-Processing module.

The current version of the GG simulator is capable of exploring the sub-picometer world while the satellite is orbiting at an altitude of about 7000 km. This is an astonishing capability, due to the huge dynamic range ($\geq 10^{21}$ m) required to the simulating tool. The simulator is now already capable to extract the EP violating signal with $\eta = 10^{-17}$ taking into account:

- Earth gravity field and gravity gradient
- Non-gravitational forces acting on the satellite surface due to atmospheric drag, solar radiation pressure and Earth albedo
- EP violating signal
- PGB and test masses supercritical rotation with whirl motion due to the mechanical suspension dissipation
- PGB and test masses whirling motion control by means of capacitance actuators co-rotating with the satellite
- Science capacitance read-out.

The current available simulator is far more mature than any usual Phase A simulator, due to the previous experience on the GG project and the GOCE End-to-End simulator heritage. This powerful tool shall support the GG science team for the entire duration of the design phase, as a means for determining the achievable mission performance, and, consequently, trade off implementation options. In this way, specifications for all system elements can be derived, consistent with the overall goal and mutually balanced. Its Post-Processing module shall suggest/support realistic procedures for scientific data reduction, based on fully representative 'raw' data. In the future, during the verification phase, it shall be used as a means to establish the expected system performance, given the measured performance of all elements, tested separately and together, as far as viable.

8. THE GROUND SEGMENT

8.1 Key GG Operations Requirements

The GG mission is devoted to a single experiment that, once initialized, runs to the end of the scientific data collection. In the Launch and Early Orbit Phase, operators control the correct spacecraft activation and perform attitude and spin-up maneuvers. Experiment set-up and first calibration operations follow. Thereafter the Science Phase starts and the experiment is run in 7-day (TBC) long data collection intervals. Spacecraft health checks will be cadenced at regular intervals to monitor the correct data acquisition and spacecraft status.

The nominal duration of the mission is two years. No orbit change maneuvers are required after insertion into operational orbit by the launcher. De-orbiting at end of life is not envisaged. Orbit determination is performed by using range and Doppler data from the Ground Station, no localization systems are foreseen on board.

The processing of scientific data is done in bulk; therefore no scientific quick-look is required. All satellite operations are autonomous, executed on the basis of time-tagged operation sequences that are loaded at least one day in advance. The minimum integration time of the experiment is determined by the experimental noises and is about 7 days. Hence, examination of the scientific data at shorter intervals is, strictly speaking, not significant. Therefore, quick look procedures are not needed and the scientific data can be routed to the Scientific Data Centre within a couple of days of reception. On the other hand, for the purposes of checking the health of the scientific payload and the correct execution of the measurement procedures, shorter reaction times may be desirable. Tests based on consistency checks, threshold parameter values etc. may be elaborated and implemented in automatic self-check procedures that can be run periodically by the onboard computer, and can be used to alert the ground control of any non-nominal state of the scientific payload. Data affected by anomalies of any sort will be rejected on post-processing and will have no effect but a shortening of the data collection period.

There are no requirements for real-time interaction between the satellite and the MOCC during a communication pass over the ground station. Because of that, and given the high level of on-board autonomy, the tasks of the ground control are essentially limited to:

- commanding and monitoring of the initial attitude maneuvers (spin axis orientation and spin-up);
- performing orbit determination and propagation and scheduling spacecraft/ ground station contacts;
- analyzing satellite data to establish that the satellite is operating correctly;
- generating and transmitting command sequences and parameters in accordance with science needs.

8.2 Ground Segment Description

The ground segment comprises the following functional blocks (Figure 5.4-1):

- Ground Stations System (GSTS)
- Ground Communication Subnet (GCS)
- Mission Operations Control Center (MOCC)
- Launcher Operations Control Center (LOCC)
- Science Operations Control Center (SOCC)
- Support Facilities (SF).

The GSTS supplies the required space to ground communication for telemetry reception and telecommand uplink. It includes a dedicated ground station for the normal operations, supplemented by additional stations during the LEOP. The nominal ground station is the ASI Station in Malindi, Kenya. Among the additional ground stations which can be employed to support the initial mission phases, the ESA/CNES Station at Kourou, French Guyana, is particularly well suited because of its near-equatorial location.

The Ground Communication Subnet (GCS) interconnects the ground stations with the functional blocks providing management of the satellite operations (the MOCC), and the science operations (the SOCC). This network can be largely realized using the existing ASI multi-mission operational network (ASINET).

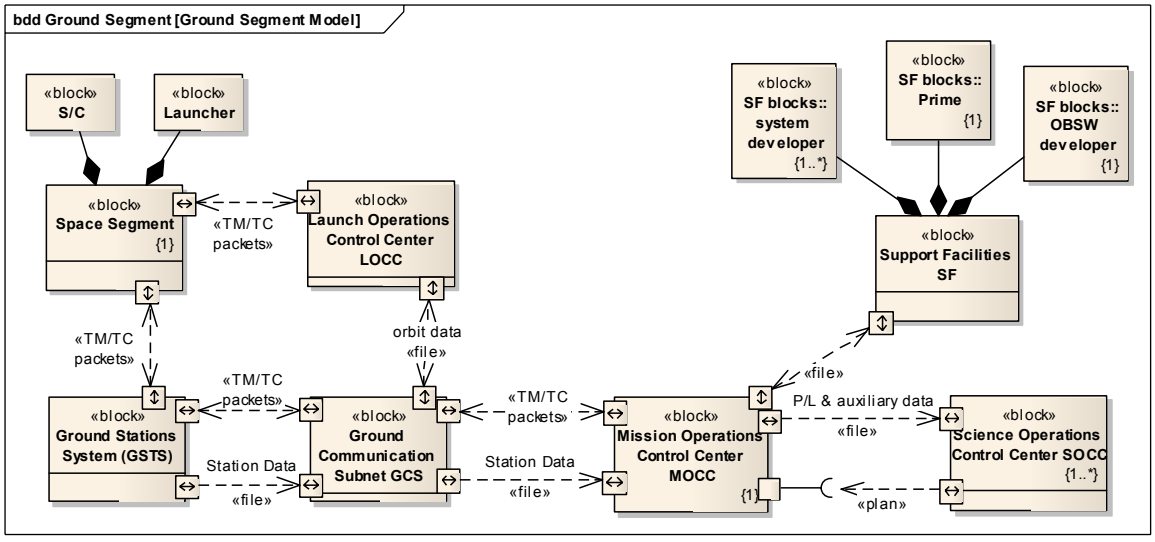

Figure 8.2-1: Functional model of the GG ground segment.

Each block is a logical unit and/or a physical unit. The fundamental building blocks comprise the Ground Stations System (GSTS) with the Ground Communications Subnet (GCS), the Mission Operations Control Center (MOCC), the Launcher Operations Control Center (LOCC), the Science Operations Control Center (SOCC) and Support Facilities (SF).

The MOCC is responsible for the execution of all GG mission operations. It provides mission planning, orbit and attitude determination for both operational purposes and science data processing applications, spacecraft monitoring and control and payload monitoring and control. The MOCC will route the scientific telemetry to the SOCC and will receive the payload command requests from the SOCC to be subsequently processed and uplinked to the satellite.

Launch operations are managed by the LOCC. In the pre-launch and launch phases, until satellite separation, the MOCC provides the interface to the LOCC.

The SOCC is responsible for the generation of the scientific operations sequences to be executed on board, as well as for the scientific data processing and analysis. In the GG mission, real-time involvement of the SOCC in the mission operations is not a requirement. Therefore both science data and science operations sequences can be exchanged between MOCC and SOCC in an “off-line” mode.

The SF is a collection of facilities usually involved in the spacecraft development and providing engineering support during the mission, such as software or system developers for thrusters. During Commissioning and Calibration phases, the SF teams could be partly co-located at the MOCC.

Physically, the MOCC functions as well as most SF functions will reside in an operations control center provided by ASI. The specific program needs do not require the SOCC to be logistically separated: both functions may be co-located in the same facility. Anyway, the engineering and science teams will have web access to the necessary MOCC functionalities, whatever their physical location.

8.3 User Segment Description

GG is a mission devoted to a single experiment and has one single User Group led by the PI. Co-PIs are selected to become members of the GG User Group on the basis of:

- His/her specific contribution to hardware and/or software components of the payload and/or spacecraft;
- His/her knowledge of specific scientific topics of the science addressed by the mission;
- His/her specific expertise on: data analysis in the field of fundamental physics in space; GG full scale numerical simulations; recovery of scientific information from numerically simulated GG data;
- His/her contribution to key instrumental aspects of the mission which are known to affect the scientific outcome of the mission.

GG mission data will remain in the hands of the User Group for the entire duration of the mission and up to a maximum of 2 years after mission completion. After that, data will be made public via free internet access to a dedicated GG Mission Data Webpage. It has to be noted that the scientific outcome of the GG mission as to the Equivalence Principle being confirmed or

violated, as well as in relation to the sensitivity achieved, will be of extreme importance and therefore it has to be established beyond any possible doubt. This requires other scientists and scientific collaborations outside the mission team to be in a position to independently check the results, starting from original data. To this end, the GG Mission Data Webpage will freely provide:

- Full GG science raw data with appropriate description and format specification for use from anyone interested in checking the User Group analysis;
- Full GG mission operation data with appropriate description and format specification to be used in combination with science data for completeness of information whenever needed;
- Reduced science data set as created by the GG User Group for signal search and analysis of relevant physical effects. Information on how the set has been created will be provided along with it;
- Data analysis software and codes developed and used by the GG User Group, including all the software tools which typically are not published on scientific journals along with the results.

8.4 Science Operations and Science Management Plan

After the launch and early orbit phase, experiment set-up and first calibration operations are executed. Thereafter, the experiment is run in 7-day long data collection intervals. Calibration sessions are regularly interspersed with the measurement intervals. Continuation of the mission improves the measurement accuracy with the square root of the measurement time. The nominal duration of the mission is two years.

The processing of scientific data is done in bulk; therefore no scientific quick-look is required. All scientific operations are autonomous, executed on the basis of time-tagged operation sequences that are loaded at least one day in advance. Given the high level of autonomy, the science operations are essentially limited to:

- Command and monitoring of the initial experiment set-up;
- Analysis of satellite data to establish that the experiment is operating correctly;
- Generation and transmission of command sequences and parameters for experiment tuning.

After commissioning at the beginning of life, the main operational modes of the satellite are:

- Experiment Set-up and Calibration Mode
- Normal mode (scientific operation of the experiment)
- High-rate Data Collection Mode
- Safe (Hold) Mode.

The experiment set-up phase will be based on semi-autonomous procedures, with intermediate checks by the ground after each phase before the next operation is executed. The experiment set-up includes the balancing of the test masses and the mechanical balancing of the

capacitance read-out sensors. Both operations need to be repeated at regular intervals. Automatic procedures for such operations will be elaborated, possibly with some interaction with the ground control.

In the science measurements phase, the operation will be essentially autonomous. The Normal Mode is characterized by the drag-free control, executed by proportional milli-Newton thrusters. However, the survival of the mission does not depend on the drag-free control, since the maintenance of the operational attitude is guaranteed by the gyroscopic stability. In case of malfunctions, the scientific operations will be put on hold and housekeeping data will be collected and transmitted to ground on the next station passes; resumption of the operations will be commanded by the ground.

Generally, the command and parameter sequences of the Normal mode will need to be updated on a time basis of several weeks, except in the set-up phase when the frequency will be higher (some hours).

The scientific telemetry data stream consists of:

- Test mass differential displacements (in-plane, 2 axes)
- External test mass displacement w.r.t. PGB (3 orthogonal axes)
- Internal test mass displacement w.r.t. PGB (3 orthogonal axes)
- PGB to spacecraft displacement (3 orthogonal axes)
- Spin velocity vector
- On board reference time.

All such data are collected as 16-bit words at high rate (50 Hz). Payload housekeeping data (monitors, temperatures, …) are collected at lower rates, depending on the time constant of the phenomena to be kept under control. Finally, a complete record of the drag-free control operation (commands as received, actuator response, auxiliary variables, monitors and controls) is collected to enable reconstructing the time history of the disturbance rejection performance.

A preliminary budget of the telemetry data is in Table 8.4-1.

Data description	Variable list	Number of variables	Frequency [Hz]	Record length [bit]	Data rate [kbit/s]
Diff. TMs displacement	$\Delta x, \Delta y$	2	50	16	1,6
Tme/PGB displacement	$\Delta x, \Delta y, \Delta z$	3	50	16	2,4
Tmi/PGB displacement	$\Delta x, \Delta y, \Delta z$	3	50	16	2,4
PGB/Spacecraft displacement	$\Delta x, \Delta y, \Delta z$	3	50	16	2,4
ω_{SPIN}	$\omega_x, \omega_y, \omega_z$	3	50	16	2,4
Reference time	t	1	50	16	0,8
Science data					**12**
Payload Housekeeping					**1**
Drag-free control					**7**

Total Data Rate	**kbps**	**20**
Period	**s**	**5702**
Data volume per orbit	**Mbit/orbit**	**112**
Telemetry rate	**kbit/s**	**186**

Table 8.4-1: Telemetry data rate budget

9. DEVELOPMENT APPROACH AND PROGRAMMATICS

9.1 Satellite development approach

9.1.1 Development objectives and elements

The objectives of the GG program are:

- To carry out a test of the Equivalence Principle with sensitivity of a least 1 part in 10^{17}, in low, near-equatorial, near-circular Earth orbit, for a duration of at least 2 years;
- To design, develop, and test a small satellite, devoted to the above objectives, over a time span (Implementation Phase) not exceeding 3 years (TBC), within a level of resources commensurate with that of a small satellite program of ASI;
- To launch and operate the satellite using as much as possible the infrastructure and resources at the disposal of ASI;
- To use this opportunity to advance the implementation and use of Italian technology and know-how in the service of an outstanding scientific project.

The space segment, the GG Satellite, is defined as a modular product consisting of two modules: the Platform (or Service Module) and the Payload (Pico Gravity Box). At lower level each module is composed of subsystems, and each subsystem can be composed of one of more units plus auxiliary parts.

A number of elements support the project during its life cycle.

- The GG Payload ground prototype (GGG). GGG is an experiment to test the Equivalence Principle, at lower sensitivity, with an apparatus very close to a prototype of the payload designed for the GG space experiment. The experiment is carried out at the University Of Pisa and can be used as a development model for the flight model.
- Software simulators. Satellite and Payload simulators, both HW and SW, will be used during the project lifecycle to consolidate the design, verify requirements in advance respect to the HW manufacturing, execute tests not performable on real HW.
- Standard engineering mathematical tools will be used to support the project development.
- Ground Support Equipment (GSE). The GSE comprises all the test equipment needed to support the ground activities on GG and its components. The GSE includes Electrical and Mechanical Ground Support Equipment.
- Standard laboratory equipment and special tools used during the GG integration and test activities.

- Test facilities. Along its ground lifecycle GG and its flight components will use different test facilities such as thermal vacuum chambers, shakers, acoustic chambers, anechoic chambers. A dedicated facility will be selected to perform the environmental test campaign. All flight items will be subjected to a Cleanliness Control Plan and to a Quality Control. Consequently the facility used by the prime contractor and its subcontractors shall conform to these requirements. In particular all the items qualified to flight shall be maintained in a qualified clean room (typically class 8).
- The VEGA facilities in Kourou to support the Launch Campaign.
- The GG Ground Segment: it provides all the necessary features to ensure satellite control during the mission and scientific data acquisition, storage and analysis. It comprises as subsystems the ground station network, the Operations Control Center (OCC), responsible for the execution of the mission operations, and the Science Operation Center (SOC), responsible for the scientific data processing and analysis.

9.1.2 Program flow

The GG project will be implemented in the following steps:

- System Definition Phase (Phase A/B), that includes the definition of the GG flight system and its relevant support equipment and the finalization of the System and Payload design;
- Development and Production phase (Phase C/D) that includes the detailed design, the development, production, verification and delivery of the GG flight Satellite with the Payload installed on it, the associated support equipment, and the launcher adapter;
- Launch and in orbit commissioning (Phase E/F), that include the launch preparation, the launch itself and the system checkout and calibration in the early orbit phases;
- The operating life, in which the scientific measurements will be acquired, stored, and analyzed until the end of the mission.

The GG Satellite detailed design definition will start from the preparation of high level (system level) specifications. Starting from these documents, lower level specifications (subsystem and unit level) will be prepared as input for the subcontractors. The Subcontractors will provide to the prime the requested items after completion of relevant development and validation process. All the units, subsystems, parts collected by the prime will be integrated to compose the final satellite and validated with the testing campaign at system level.

Dedicated reviews and milestones are defined in the various project phases to certify the above process.

9.1.3 Model Philosophy

At the satellite system level, a Proto Flight approach is proposed. Prior to the PFM program,

- the satellite functional performances will be validated using a dedicated End to End simulator (purely SW) plus an Avionics Test Bench where representative HW will be incrementally included in the loop. This HW will be composed of breadboards and 'Off the Shelf' components, functionally representative of the flight HW;
- the satellite-level thermo-structural performances and the compliance with the relevant requirements will be evaluated by analysis.

The Proto Flight Model will be the final product after integration, and the unit that will be launched. Since a single complete satellite model is foreseen, it will be subjected to a complete proto-flight test campaign in order to confirm the functional validation performed on simulators, and the thermo-structural performances evaluated by analysis.

At lower level (payload and platform), different model approaches apply as detailed in §9.2 and §0 below.

9.1.4 Schedule

The GG program will be phased according to the following durations and main reviews:

- Phase B 9 months KO, PDR
- Phase C/D 36 months CDR, TRR, FAR
- Phase E 3 months LRR.

Figure 9.1-1 shows the current GG master schedule for the phases B, C/D, E, and F. The Ground Segment schedule is included with the following baseline:

- 2 years of mission (including commissioning)
- 1 year of long term data archiving.

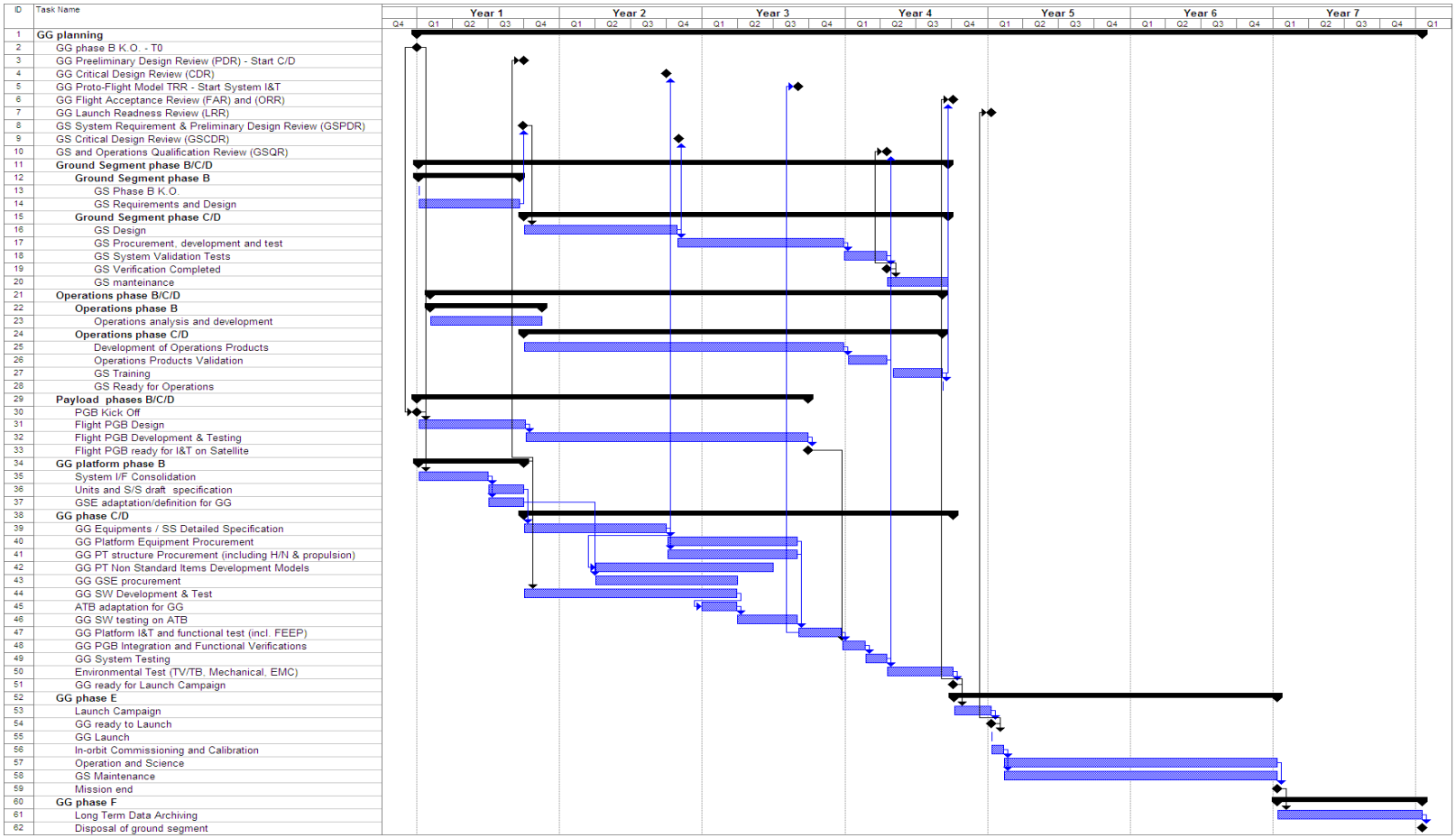

ID	Task Name
1	**GG planning**
2	GG phase B K.O. - T0
3	GG Preeliminary Design Review (PDR) - Start C/D
4	GG Critical Design Review (CDR)
5	GG Proto-Flight Model TRR - Start System I&T
6	GG Flight Acceptance Review (FAR) and (ORR)
7	GG Launch Readness Review (LRR)
8	GS System Requirement & Preliminary Design Review (GSPDR)
9	GS Critical Design Review (GSCDR)
10	GS and Operations Qualification Review (GSQR)
11	**Ground Segment phase B/C/D**
12	**Ground Segment phase B**
13	GS Phase B K.O.
14	GS Requirements and Design
15	**Ground Segment phase C/D**
16	GS Design
17	GS Procurement, development and test
18	GS System Validation Tests
19	GS Verification Completed
20	GS manteinance
21	**Operations phase B/C/D**
22	**Operations phase B**
23	Operations analysis and development
24	**Operations phase C/D**
25	Development of Operations Products
26	Operations Products Validation
27	GS Training
28	GS Ready for Operations
29	**Payload phases B/C/D**
30	PGB Kick Off
31	Flight PGB Design
32	Flight PGB Development & Testing
33	Flight PGB ready for I&T on Satellite
34	**GG platform phase B**
35	System I/F Consolidation
36	Units and S/S draft specification
37	GSE adaptation/definition for GG
38	**GG phase C/D**
39	GG Equipments / SS Detailed Specification
40	GG Platform Equipment Procurement
41	GG PT structure Procurement (including H/N & propulsion)
42	GG PT Non Standard Items Development Models
43	GG GSE procurement
44	GG SW Development & Test
45	ATB adaptation for GG
46	GG SW testing on ATB
47	GG Platform I&T and functional test (incl. FEEP)
48	GG PGB Integration and Functional Verifications
49	GG System Testing
50	Environmental Test (TV/TB, Mechanical, EMC)
51	GG ready for Launch Campaign
52	**GG phase E**
53	Launch Campaign
54	GG ready to Launch
55	GG Launch
56	In-orbit Commissioning and Calibration
57	Operation and Science
58	GS Maintenance
59	Mission end
60	**GG phase F**
61	Long Term Data Archiving
62	Disposal of ground segment

Figure 9.1-1: GG program master schedule

9.2 Payload development plan

At payload (PGB) level, a two-model approach is proposed. The PGB-STM (Structural Thermal Model) will be used to qualify the mechanical and thermal design, including the thermo-structural deformation aspects. The STM has therefore to be representative in terms of mechanics and thermal design. The PBG-PFM (Proto Flight Model) will be used to complete the acceptance from the mechanical, thermal and functional point of view, and will be the flight unit. Figure 9.2-1 summarizes the PGB test approach.

From the equipment point of view, the following units are new developments, and will be subjected to a complete qualification test campaign, including environmental testing (TV/TB, mechanical test):

- ECE and (partially) CPE
- Accelerometer
- Lock/unlock mechanisms.

The ECE and CPE will have Engineering Models, mechanically, thermally and functionally representative of the flight units. The Accelerometer is functionally covered by the GGG laboratory experiment; however an STM is needed anyway and will be provided as part of the complete PGB assembly. The mechanisms shall be completely flight representative, and shall be included in the PGB-STM. Table 9.2-1 summarizes the approach.

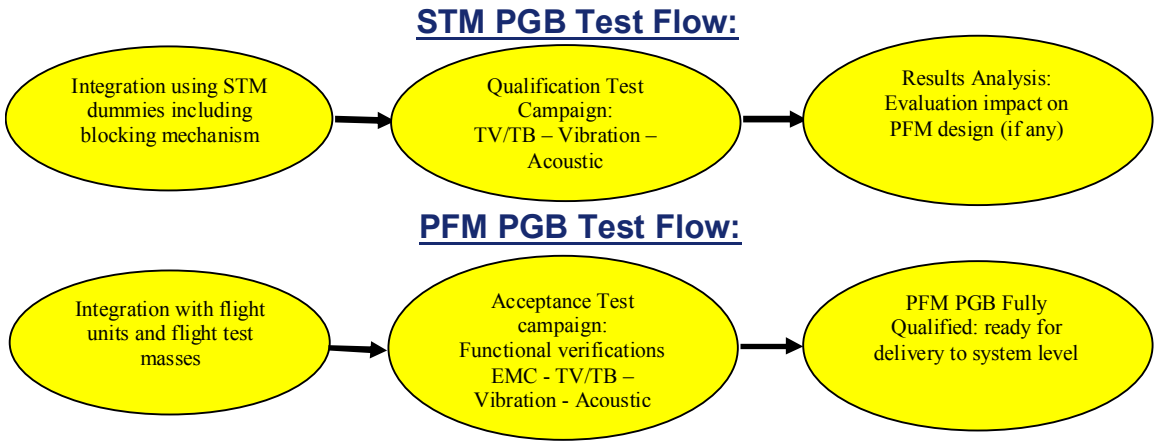

Figure 9.2-1: Two-model approach to PGB system testing

Assembly – Unit	EM / Functional model	PFM
Accelerometer Mechanics	GGG-Pisa (tbc)	1
ECE unit	1	1
CPE unit	1 (tbc)	1
Locking mechanism	n. 1 set	NN sets

Table 9.2-1: PGB unit model philosophy

9.3 Platform development plan

Different model philosophies will be applied for units and subsystems according to whether they are recurring items or not. As general rule, a protoflight approach will be defined for the recurring items. At equipment and subsystem levels, the verification approach will be defined in function of the individual unit/subsystem Technology Readiness Level (TRL). The general approach is to have a complete qualification test campaign and consequently a qualification approach on the new items, and to perform a reduced acceptance campaign on the recurring units.

The following non-recurring or (partially) new development items have been identified.

- FEEP. At least one FEEP development model will be foreseen as part of the qualification process, before the flight model.
- Spin Sensor. At least two models will be foreseen as part of the qualification process: 1) an Engineering Qualification Model (EQM), which shall be submitted to a complete qualification test campaign to assess the design and the technological solutions; 2) a Flight Model (FM), which shall be submitted to a test campaign at flight conditions before being installed on the satellite.

At platform and system level, the PFM will be subjected to a complete proto flight test campaign, including thermal testing, mechanical testing and electro-magnetic compatibility, according to the sequence depicted in Figure 9.3-1.

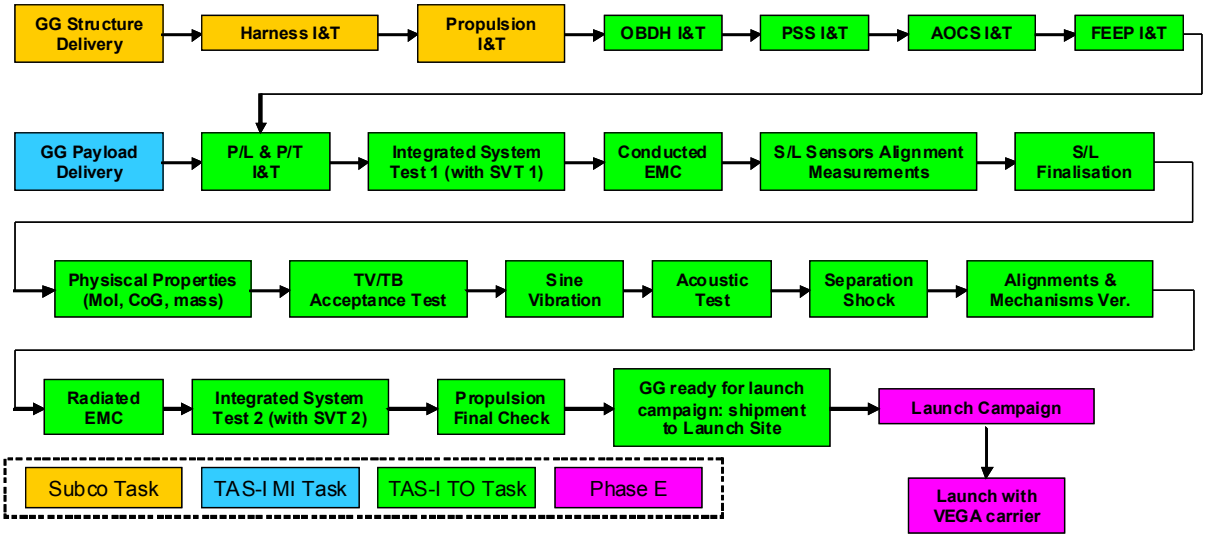

Figure 9.3-1: Development Plan at satellite level.

In the above scheme colour coding is used to mark different responsibilities. Gold stands for an item/subsystem provided by and external subcontractor. Green marks a task under Industrial Prime responsibility. Blue signals the payload and its components. Phase E is identified in a different colour since it will be probably be subjected to a different contract.

9.4 Development plan for the Ground Segment

The ground segment will be developed in step with the flight system, as shown in Figure 9.4-1.

According to the requirements assessment performed in Phase A2, all major hardware provisions and facilities may be inherited from existing ASI assets. Therefore no significant costs are envisaged for hardware/facility procurement.

The mission specific items to be designed and developed / procured as part of the GG program include all the necessary GS documentation, plans, software and procedures. Major items are listed below.

Phase B

- Ground segment requirements document (GSRD)
- Space–to–ground interface control document (SGICD)
- Mission analysis report (MAR)

Phase C

- Space–to–ground interface control document (SGICD) – final version
- Consolidated Report on Mission Analysis report (CREMA)
- Operations engineering plan (OEP)
- Mission operations plan (preliminary)

Phase D

- Validated Mission Operations Plan (MOP)
- Validated space and ground segment monitoring and control databases
- Operations training plan (OTP)
- Fully validated ground segment, including personnel and procedures, ready for in–orbit operations and exploitation.

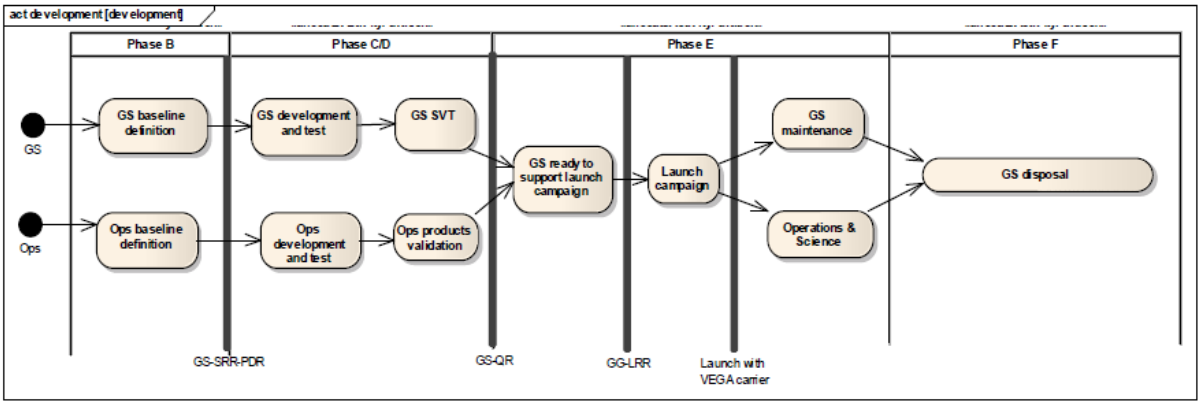

Figure 9.4-1: Ground segment development plan

9.5 Development plan for the User Segment

The GG "user segment" is constituted by the PI and the associated scientific consortium, as described in §8.3. The tools to be developed include descriptions and format specifications of Level 1 data for scientific use, and data analysis software and codes. These tools will be produced all along the life cycle of the project. Concurrently, the satellite software simulator (an early version of which is already available today) will be employed for generating simulated science data streams, to test and validate the data analysis software.

9.6 Program management

In the frame of GG Phase A2, a program organization has been established which constitutes the model for the program management of the subsequent phases, summarized below. In this organization, Thales Alenia Space Italia (Torino) is the prime contractor, in charge of the system design, and the satellite development and validation until its delivery to the customer. TAS-I Milano is in charge of the Payload development and verification until its delivery to the system. Telespazio is in charge of the Ground Segment development, validation and management, supported by ALTEC for the management of the scientific product related tasks of the ground segment.

Thales Alenia Space Italia possesses an effective management system that is the result of experience gained in more than 30 years of activity in the space domain. This management approach is routinely applied for all space-related products (platforms, payloads, ground systems…), and, among them, in scientific satellite programs. The approach was successfully exercised in the management of both large and small European industrial teams, with interfaces with the scientific communities, the ground segment and the launcher authorities. The TAS management system has obtained the ISO 9001 certification and complies with the ESA ECSS standard policies and management requirements.

To accomplish its task of Prime Contractor, Thales Alenia Space Italia will nominate a Project Team comprising the various expertises, managerial, technical and quality, necessary to carry out the relevant tasks and duties.

TAS-I will be responsible for the management and direction of the Subcontractors, controlling their programmatic and technical performances. It will provide to ASI visibility at any level of its industrial team and will make accessible and available all information generated under the GG Study.

The TAS-I project management will be exercised via:

- a Project Management Plan that defines the management rules and organization in accordance with the ASI requirements;

- standard, well proven techniques for work breakdown structuring, program planning and scheduling, risk management and control, change management, program reporting, documentation and communication exchange;
- implementation of a uniform management approach to the Subcontractors, extending to them the Prime Contractor management requirements;
- the definition of financial and cost management rules in accordance with the applied contract typologies;
- the definition of rules and procedures for contract change management, configuration management, progress and performance evaluation.

9.7 Milestones and meetings plan

The milestones associated to the GG program phases are summarized below.

9.7.1 Phase B

The objective of this phase is to consolidate and freeze the specifications and plans already initiated in Phase A2. Specifically, the Phase B activities will have the following purpose:

- To complete the review and analysis of the GG requirements and the translation of them into subsystem and unit specifications (a task already initiated in Phase A2). Special care will be put in the evaluation of possible reuse of existing and already qualified items, to reduce the cost and increase the reliability;
- To complete the trade-offs, to freeze a detailed GG design baseline compliant with the requirements and to consolidate the performance budgets;
- To establish a detailed design of the GSE needed for the AIV/AIT campaign;
- To complete the management, PA, development, integration, test and qualification plans;
- To initiate, if needed, breadboarding and test activities on critical items;
- To initiate procurement of long-lead items (if any).

The Phase B will be formally closed by the GG Preliminary Design Review (PDR).

9.7.2 Phase C/D

The main objective of Phase C will be to implement the designs, the plans and the specifications generated in Phase B into a fully integrated, qualified and tested GG proto-flight model together with all required supporting hardware and software.

Phase C will be concluded with the GG Critical Design Review (CDR), giving formal authorization to start with unit and subsystems procurement and AIT activities.

Phase D will comprise:

- development and manufacturing of all flight hardware;
- integration and testing of the satellite according to the specified model philosophy;
- execution of the functional and environmental test campaigns;
- production and delivery of the satellite user's manual;
- delivery of the GG proto-flight model.

Phase D will be concluded with the GG Final Acceptance Review (FAR).

9.7.3 Phase E

Phase E comprises the launch campaign and the satellite in-orbit commissioning.

The objectives of the launch campaign include in particular:

- final GG verification at the launch site to check the satellite performance after the shipment to Kourou for launch with VEGA;
- mating operations with the launcher;
- joint operation with the launcher authority, including final countdown.

The formal review that completes the Launch campaign is the Launch Readiness Review (LRR), held a few days before launch. A successful LRR will authorize GG to launch.

The main objectives of the commissioning phase include:

- In orbit check of all GG subsystems and functions;
- configuration of the satellite in its operating modes;
- payload set-up and first calibration;
- start of scientific data acquisition.

9.7.4 Program milestone summary

The main events of GG project until GG launch are shown in Table 9.7-1, starting from the kick-off of Phase B. The associated bar chart is in Figure 9.1-1. This preliminary sequence of program events will be consolidated as part of the GG Implementation Proposal.

	Key Events	Epoch from T0
Reviews (Satellite level)	Phase B Kick-Off	T0
	Preliminary Design Review	T0+9m
	Phase C/D Kick-Off	T0+9m
	Critical Design Review	T0+21m
	Test Readiness Review	T0+32m
	Final Acceptance Review	T0+45m
	Launch Readiness Review	T0+48m
	Launch	T0+48m
Reviews (GS level)	Ground Segment Preliminary Design Review	T0+9m
	Ground Segment Critical Design Review	T0+22m
	Ground Segment Operations Qualification Review	T0+40m

Model	Main Goals	Epoch from T0
ATB	ATB Availability for GG	T0+24m
	ATB Ready for SW Test	T0+27m
	ATB Test Completion	T0+48m
FM	FM/PFM Equipment Procurement Start	T0+21m
	Results of development models availability	T0+30m
	GSE for system activities availability	T0+30m
	FM/PFM Equipment Procurement Completion	T0+32m
	Flight PGB Availability at System Level	**T0+35m**
	S/L Ready for Environmental Test	T0+39m
	S/L Ready for Launch Campaign	T0+45m
	S/L Ready for Launch	**T0+48m**

Table 9.7-1: GG program milestones

10. LIST OF ACRONYMS AND ABBREVIATIONS

AD	Applicable Document
AIV	Assembly Integration and Test
AOCS	Attitude and Control Subsystem
ASI	Agenzia Spaziale Italiana
BCR	Battery Charge Regulator
BDR	Battery Discharge Regulator
CCSDS	Consultative Committee for Space Data Systems
CDMU	Command and Data Management Unit
CFRP	Carbon Fiber Reinforced Plastics
CGPS	Cold Gas Propulsion System
CMRR	Common Mode Rejection Ratio
CNES	Centre National d'Etudes Spatiales
COG	Center of Gravity
COM	Center of Mass
CPE	Control and Processing Electronics
CPU	Central Processing Unit
DFACS	Drag Free and Attitude Control Subsystem
DFM	Drag Free Mode
DoD	Depth of Discharge
E2E	End To End Simulator
ECE	Experiment Control Electronics
ECSS	European Cooperation for Space Standardization
EGSE	Electrical Ground Support Equipment
EOL	End Of Life
EP	Equivalence Principle
EPS	Electrical Power System
EQM	Engineering Qualification Model
ESA	European Space Agency
FEEP	Field Emission Electric Propulsion
FEM	Finite Element Model
FCA	FEEP Cluster Assembly
FCL	Fold-back Current Limiter
FOS	Factor of Safety
FOV	Field of View
G/S	Ground Station
GG	Galileo Galilei (Satellite)
GGG	Galileo Galilei on the Ground (Experiment)
GMM	Geometrical Mathematical Model
GOCE	Gravity and Ocean Circulation Explorer
HK	Housekeeping
I/F	Interface
INFN	Istituto Nazionale di Fisica Nucleare
IRF	Inertial Reference Frame

ISV	Independent Software Validation
ITO	Indium Tin Oxide
JERF	J2000 Equatorial Reference Frame
LCL	Latching Current Limiter
LEOP	Launch and Early Orbit Phase
LGA	Low Gain Antenna
LL	Limit Loads
MLI	Multi Layer Insulation
MOI	Moment Of Inertia
MRD	Mission Requirement Document
OBCP	On Board Control Procedure
OBDH	On Board Data Handling
P/L	Payload
PA	Product Assurance
PCDU	Power Control and Distribution Unit
PCE	Payload Control Electronics
PCU	Power Control Unit
PGB	Pico Gravity Box
POI	Product of Inertia
PSLV	Polar Satellite Launch Vehicle
PPRF	Payload Physical Reference Frame
QL	Qualification Loads
RD	Reference Document
RFDN	Radiofrequency Distribution Network
SA	Solar Array
SD	Standard Document
S/C	Spacecraft
STS	System Technical Specification
SEL	Single Event Latch-Up
SEU	Single Event Upset
SPF	Single Point Failure
SPRF	Satellite Physical Reference Frame
S³R	Sequential Switching Shunt Regulator
S/S	Subsystem
STB	Software Test Bed
SVF	Software Validation Facility
TAS-I	Thales Alenia Space Italia
TBC	To Be Checked
TBD	To Be Defined
TC	Telecommand
TCS	Thermal Control System
TM	Telemetry
TM	Test Mass
TMM	Thermal Mathematical Model
TRL	Technological Readiness Level

END OF DOCUMENT